Technische Universität München

Physik Department E20

Molecular Nanoscience and Chemical Physics of Interfaces

Scanning Probe Microscopy Investigation of Hybrid Nano Systems Comprising Functional Molecules and Two-Dimensional Layers

Dissertation

Jacob Steffen Ducke

Technische Universität München

Lehrstuhl E20 - Molekulare Nanowissenschaften und Chemische Physik
von Grenzflächen

Scanning Probe Microscopy Investigation of Hybrid Nano Systems Comprising Functional Molecules and Two-Dimensional Layers

Jacob Steffen Ducke

Vollständiger Abdruck der von der Fakultät für Physik der Technischen Universität München zur Erlangung des akademischen Grades eines Doktors der Naturwissenschaften (Dr. rer. nat.) genehmigten Dissertation.

Vorsitzender:	Prof. Dr. Björn Garbrecht
Prüfer der Dissertation:	1. Prof. Dr. Willi Auwärter
	2. Prof. Dr. Friedrich C. Simmel

Die Dissertation wurde am 09.07.2018 bei der Technischen Universität München eingereicht und durch die Fakultät für Physik am 15.10.2018 angenommen.

Abstract

The bottom-up approach is a promising strategy for the large scale production of nano electronic devices. Self-assembly and on-surface synthesis of molecular entities combine the potential of atomic precision and the upscalability for industrial purposes.
To achieve the implementation of molecular nanostructures in applications, several challenges still need to be overcome:
The protection of organic materials against potential reactants in the atmosphere such as oxygen is crucial. In this work we introduce a method where we cover functional molecules with a protective two-dimensional layer, applying an intercalation protocol. We show that the intercalated molecules are intact and that their intrinsic functionalities are preserved. While transferred protective layers used in alternative approaches are usually strongly contaminated, our method yields a low concentration of impurities.
A second challenge is the on-surface synthesis of stable molecular nanostructures on insulating materials. We introduce a new type of intermolecular coupling reaction, which can be used for the bottom-up synthesis of nano graphene. The intrinsic reactivity of the functional groups afford an atomically precise on-surface reaction on a two-dimensional layer without direct contact with a catalytic active metal.
A third issue is that metals, which are used to electronically contact molecules in nano electronics, typically have a strong influence on the molecule's electronic properties. We show that graphene exhibits outstanding properties as a conductive support for organic materials as it comprises high conductivity while preserving the electronic structure of molecules unlike bulk metals.

With our results we have expanded the understanding of the bottom-up synthesis for nano architectures. The self-assembly of functional molecules on and beneath different complementary materials as well as the introduced coupling reactions are important steps towards molecular electronics.

II

Contents

1 Introduction

The evolution of silicon based electronics within the last century was essential for modern societies. Starting with the invention of the transistor in 1948 [1], the subsequent miniaturization according to Moore's law [2, 3] enabled the development of for example personal computers and portable cellphones. However, Moore's law is approaching fundamental limits and new ideas to create high performance electronic devices appear [4, 5].
One promising approach is the implementation of organic molecules with intrinsic functionalities [6–11] in novel molecular electronics such as molecular switches [12–15] and organic photovoltaics [16–19]. In contrast to silicon transistors, which can switch between on and off state, functional molecules extend the scope of possible applications to for example optical devices. Furthermore, the scaling limit for molecular structures (one molecule) reaches down to the sub nanometer regime.
The self-assembly of molecules opens up ways to regularly position molecules, which is suitable for upscaling and therefore for industrial purposes [20–24]. However, a key challenge is to steer the exact adsorption positions of individual molecules in molecular networks. Another question, which has to be solved, is the contacting of the molecules for read-out and manipulation of the molecular states. And finally, organic molecules have to be protected from oxygen for stable long term operations [25, 26].
Consequently, to generally engineer molecular devices, three basic components are mandatory:

- Molecules with intrinsic functionalities (e.g. porphines)
- Conductive material to contact the molecules (e.g. graphene)
- Insulating material for protection, spacing, and decoupling purposes (e.g. h-BN)

The substrate on which the molecules adsorb can be used as a template to define the adsorption positions of the molecules and furthermore the underlying support strongly influences the electrical properties of molecules [27]. Therefore, the fundamental understanding of the interaction between molecules and different materials is of essential importance.
In this work, we investigate the interaction between a prototype functional molecule (porphine), a prototype conducting material (graphene), and a prototype insulating material (h-BN) in a well defined environment.
We brought in porphine as a functional molecule, the parent compound of all porphyrins. Porphyrins are used in nature in many essential biological processes such as oxygen transport [28] and photosynthesis [29, 30]. Furthermore, the porphine functionality can easily be adjusted to its specific purpose by modifying its core with metal or hydrogen atoms, or by changing their substituents [30].
Graphene is a two-dimensional material, with outstanding mechanical and electrical properties [31–35]. Graphene is only one atom thick and reveals exceptional electron mobilities and

therefore is already used in novel nano technology [36, 37].
h-BN is an isomorph of graphene, which is also two-dimensional with a similar lattice constant [36, 38]. However, in contrast to graphene, *h*-BN exhibits a wide band gap [39] and is consequently completely transparent for visible light. The large bandgap, the high chemical and thermal stability in combination with the similar geometry to graphene, make *h*-BN to an auspicious material for nano architectures.
The growth of both materials is easily scalable [37, 40–44] and first nano electronic devices combining graphene and *h*-BN have been designed [36, 45–48].

The structure of this thesis is as follows:
For the experiments a combined scanning tunneling microscope (STM) and non contact atomic force microscope (nc-AFM) at low temperatures and in ultra high vaccuum (UHV) is used and the corresponding fundamentals are presented in Chapter 2. The used materials in this thesis are introduced and the growth of graphene on copper and silver is described.
h-BN has already been shown to electronically decouple molecules from an underlying metal support and to be used as a template to self-assemble molecules [27, 49–54]. We start from this point of arranged molecules on *h*-BN, expanding the scope of bottom-up architecture protocols by bringing functional molecules beneath the *h*-BN. This intercalation of molecules upon moderate thermal activation is described in Chapter 3. While the self-assembly of the molecules is modified upon intercalation beneath the insulating *h*-BN layer, we show that an intrinsic molecular function (e.g. the electronic switch) is preserved. Furthermore we succeeded in the growth of graphene underneath a covering *h*-BN layer, using porphines as precursor molecules. To obtain insights to what extend the *h*-BN monolayer can protect organic molecules from reactive oxygen, we characterized the *h*-BN/molecule/metal system after exposure to ambient conditions. These experiments are described in Chapter 4.
In Chapter 5 the bottom-up synthesis of covalently bound polyaromatic chains is presented. We employed a highly reactive 1,3 dipolar cycloaddition reaction between an azomethine and a cyano group for the coupling process. Exploiting the high reactivity, we showed the polymerization process on an *h*-BN/Cu(111) support at moderate temperatures. The applied reaction protocol extends the tool box for the bottom-up synthesis of nano electronic devices as it might be feasible for insulating materials and covalently couples polyaromatic molecules, which are promising candidates for atomically precise synthesis of carbon based nano architectures.
Finally, we looked into the interaction of porphines with graphene and compared it to the porphine on *h*-BN/Cu(111) system. Therefore in Chapter 6 a comprehensive investigation of the electronic and geometric properties of the graphene/metal systems is given. The surface state characteristics of the metals are only slightly modified upon the graphene adsorption, pointing towards weakly bond graphene. Furthermore, we observe a reduction of the local work function when graphene is adsorbed and quantify the electronic and geometric corrugation of the graphene/Cu(111) system spatially.
In Chapter 7 the self-assembly and the electronic properties of porphines on graphene are pre-

sented. In contrast to the porphine/h-BN/Cu(111) case the molecules on graphene easily desorb from the surface and are not trapped to specific Moiré positions on the graphene. However, we evidence a similarly strong electronic decoupling of the molecules from the underlying metal support. This electronic decoupling is from great interest as metals are known to influence the electronic properties of molecules in a way that for example the molecules can hardly be used for optical applications. Here we show that graphene, which can be used as a highly conductive electrode, does decouple the molecules while only slightly influencing the intrinsic electronic properties of the molecules.

In Chapter 8 a small excursion from the atomically precise surface investigation to the implementation of nano science to macroscopic devices, which can be used for artificial intelligence, is illustrated. We investigated single metal-insulator-metal (MIM) junctions in terms of a four-probe STM/AFM on the microscopic scale, and in addition a nanowire network including a huge amount of (MIM) junctions macroscopically. After several training sessions the artificial neural network showed first proofs of intelligence by memorizing different trained patterns.

Finally Chapter 9 provides a summary and an outlook.

2 Experimental methods

The data shown in this work were measured with a scanning tunneling microscope (STM) and a combined STM/nc-AFM, where nc-AFM stands for non contact atomic force microscope. Both instruments are operated at low temperature around 5 K and in ultra high vacuum (UHV) at $p = 10^{-10}$ mbar.

Binnig and Rohrer invented the STM in 1982, when they experimentally evidenced tunneling electrons, which were already proposed in the 1920s [55–57]. They exploited the exponential dependence of the tunneling current on the tip-surface separation to image the surface of various materials [57–59].

The Nobel prize awarded in 1986, only four years later, shows the huge potential this invention had in the surface science community. However, the tunneling of electrons can only be used for conducting materials and therefore a complementary approach, the AFM was developed in 1986, which gave access also to non conducting surfaces [60, 61].

Again Binnig was involved in the development together with Quate and Gerber and even though the invention was not awarded with the Noble prize, the more than 18.000 quotations to date of their pioneering publication [60] prove the relevance of AFM.

In contrast to the rather simple exponential behavior of the measured tunneling current in STM, the forces between the cantilever apex and the investigated surface are more difficult to describe and therefore also more difficult to use for imaging purposes. To obtain similar performance than STM, AFM had to undergo several evolution steps and is now even outperforming STM for many systems.

While the AFM is sensitive to localized core electrons, electrons contributing to the STM current lie close to the Fermi energy E_F and can therefore be much broader distributed, for example in molecular orbitals, leading to a higher possible resolution of AFM compared to STM [62].

The best performances in AFM are achieved with oscillation driven cantilevers operating in frequency modulation mode (FM-AFM) introduced in 1991 [63].

Using FM-AFM Giessibl et. al. published the first true atomic resolution in AFM using a Silicon cantilever in 1995 [64]. In the following years Giessibl invented a new type of cantilever, the qPlus sensor [65, 66], consisting of a quartz tuning fork with high reliability, cheaply accessible from the mass producing watch industry. The introduction of the qPlus sensor gave access to subatomic resolution [67, 68] and to the imaging of chemical bonds in real space [69].

In the following the fundamentals of STM and AFM are described. As the STM/AFM applied in this work comprises a qPlus sensor, which is operated in FM-mode the description of the AFM technique is focused on this design.

2.1 Scanning tunneling microscopy (STM)

2.1.1 Theory of scanning tunneling microscopy

In this section a brief introduction to the theoretical fundaments of the scanning tunneling microscope (STM) is given and the applied tunneling current is theoretically explained. A more comprehensive description is summarized elsewhere [70, 71] and is not part of this thesis.
In classical mechanics a potential barrier can only be overcome if the energy of for example an electron is higher than the potential barrier. In contrast, in quantum mechanics even particles with lower energy have a certain probability to overcome the barrier (Figure 2.1). The wave like character of electrons can be theoretically described as a solution $\Psi(x)$ of the Schrödinger equation 2.1. This equation is used to quantify the tunneling probability of electrons:

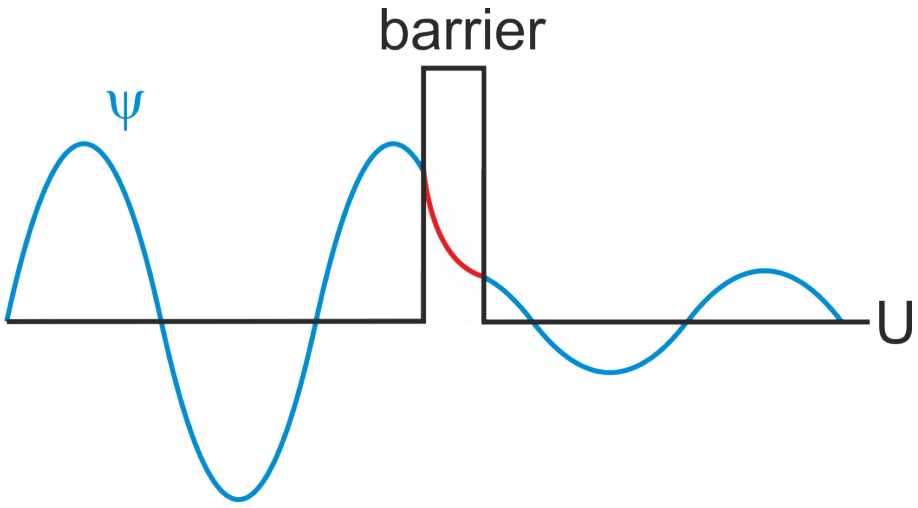

Figure 2.1: *Schematic of an one-dimensional tunneling process through a potential barrier. Oscillating wave function Ψ illustrates the solution of the Schrödinger equation on both sides of the potential barrier. An exponential decay is depicted for the wave function inside the barrier.*

$$-\frac{\hbar^2}{2m}\frac{d^2}{dz^2}\Psi(x) + U(x)\Psi(z) = E\Psi(x)$$

where m is the electron mass, E the energy of the electron, $\hbar$ the reduced Planck constant and U the potential. In the classically accessible region in Figure 2.1 where $U < E$ two solution of the Schrödinger equation are found:

$$\Psi(x) = \Psi(0)e^{\pm i\frac{\sqrt{2m(E-U)}}{\hbar}x} = \Psi(0)e^{\pm ikx} \tag{2.1}$$

The two solutions describe the electron moving in positive $(-ikx)$ and in negative $(+ikx)$ x-direction, equivalent to a classical consideration. In quantum mechanics, we also obtain a solution of the Schrödinger equation in the region where $U > E$:

$$\Psi(x) = \Psi(0)e^{-\frac{\sqrt{2m(U-E)}}{\hbar}x} = \Psi(0)e^{-\kappa x} \tag{2.2}$$

which determines a certain probability $\Gamma(x)$ to observe the electron inside the barrier:

$$\Gamma(x) = |\Psi(0)|^2 e^{-\kappa x} \tag{2.3}$$

$\Gamma(x)$ decays exponentially inside the barrier resulting in a finite amplitude of the electron wave function behind the potential barrier. The finite amplitude depends on the thickness and height of the potential barrier and causes a certain probability to observe an electron, which is tunneled through the barrier. This tunneling effect is the physical phenomena that is exploit to image structures via a scanning tunneling microscope (STM). In case of the STM electrons tunnel from the tip to the sample through a vacuum barrier or vice versa. A simple approach to describe the tunneling current from the sample to the tip (tip and sample having the same work function Φ, thermal activation of charge carriers are neglected and the applied sample bias U_b is small ($eU_b << \Phi$)) leads to an tunneling probability of an electron in the n^{th} state with an energy between the Fermi level E_f and $E_f - eU_b$ of:

$$\Gamma \propto |\Psi_n(x)|^2 = \Psi(0)e^{-2\frac{\sqrt{2m\Phi}}{\hbar}x} \tag{2.4}$$

The tunneling current is then obtained by summing up all n electron states in the sample in the energy range between the Fermi level and $E_f - eU_b$.

$$I_t \propto \sum_{E_f - eU_b}^{E_f} |\Psi_n(x)|^2 \approx U_b \cdot \rho(x, E_f) = U_b \cdot \rho(0, E_f)e^{-2\frac{\sqrt{2m\Phi}}{\hbar}x} \tag{2.5}$$

where U_b is the sample bias and $\rho(x, E_f)$ is the local density of states (LDOS) of the sample at the Fermi level, which is assumed to be constant within the considered energy range. x is the distance between sample and tip, as only electrons on the sample surface contribute relevantly to the tunneling current due to the strong distance dependence of the tunneling probability (Equation 2.4). Similar to the tunneling probability a strong dependence on the sample tip separation is obtained, which explains the high sensitivity of STMs.
For are more accurate description of the tunneling current the Bardeen formalism [72] is used. Bardeen applied Fermi's golden rule to the two wave functions of the tip (Ψ_t) and of the sample (Ψ_s):

$$\Gamma = \frac{2\pi}{\hbar} |M|^2 \delta(E_{\Psi_s} - E_{\Psi_t}) \tag{2.6}$$

Only elastic tunneling processes are considered, which is guaranteed by the δ-function. The matrix element M is given by:

$$M = \frac{\hbar^2}{2m} \int_S (\Psi_s^* \nabla \Psi_t - \Psi_t^* \nabla \Psi_s) dS \tag{2.7}$$

where S is a surface, which lies in the vacuum gap between sample surface and tip. The tunneling current I_t is then obtained by summing up all states between E_f and $E_f + eU_b$. The Fermi functions are set to their zero temperature values in the low temperature approach:

$$I_t = \frac{2\pi e}{\hbar} \int_{E_f}^{E_f + eU_b} \rho_s(E - eU_b)\rho_t(E) \left|M\right|^2 dE \tag{2.8}$$

To evaluate the matrix element M the approximation of Tersoff-Hamann [70] is applied. Tip and sample have the same work function Φ but are treated independently. The tip apex is assumed to be spherical with radius R and is modeled with a s-like wave function, leading to a tunneling current of:

$$I_t \propto U_b \cdot e^{-2kR} \rho_t(E_f) \cdot \sum_s \left|\Psi_s(r_0)\right|^2 \delta(E_s - E_F) \tag{2.9}$$

where r_0 distance between the sample surface and the center of the spherical tip and $k = \frac{2m\Phi}{\hbar}$ is the inverse decay length of the wave functions and holds the information of the barrier height Φ. The information of the exponential decay with tip-sample separation d is found in:

$$\left|\Psi_s(r_0)\right|^2 \propto e^{-2d\frac{\sqrt{2m\Phi}}{\hbar}} \tag{2.10}$$

The sum in 2.9 can also be expressed by the LDOS of the sample ρ_s at the tip position r_0:

$$\rho_s(r_0, E_F) = \sum_s \left|\Psi_s(r_0)\right|^2 \delta(E_s - E_F) \tag{2.11}$$

Summarizing equations 2.9 and 2.11 following equation for I_t is obtained:

$$I_t \propto U_b \cdot e^{-2kR} \rho_t(E_f) \rho_s(r_0, E_F) \tag{2.12}$$

Consequently, the tunneling current comprises information of the topography and the electronic properties of the investigated sample. To extract the information of the LDOS of the sample scanning tunneling spectroscopy (STS) can be used as is explained in the following.

2.1.2 Scanning tunneling spectroscopy (STS)

Scanning tunneling spectroscopy is used to measure the LDOS of the investigated sample. A schematic of the STS and typical STS spectra are presented in Figure 2.2 (c) and (d). Equation 2.12 shows the dependence of I_t on the ρ_s and the applied voltage U_b. U_b determines the energy of the electrons and additionally defines the states, which contribute to the tunneling current [73]:

$$I_t(V) \propto \int_0^{eU_b} \rho_s(r,E)\rho_t(r,E-eU)T(r,E,eU_b)dE \tag{2.13}$$

with $T(r,E,eU_b)$ is the barrier transmission coefficient. Differentiation of this integral (Equation 2.13) leads to:

$$\frac{dI}{dU_b} \propto \rho_s(r,eU_b)\rho_t(r,0)T(r,eU_b) + A(V) \tag{2.14}$$

where A(V) contains the voltage dependence of the transmission coefficient. By assuming that the LDOS of the tip and A(V) are constants, a clear correlation between the differential conductance $\frac{dI}{dV}$ and the LDOS of the sample is obtained:

$$\frac{dI}{dU_b} \propto \rho_s(r,eU_b) \tag{2.15}$$

Consequently, the differential conductance gives insights in the LDOS of the sample. To measure $\frac{dI}{dV}$ the tip is located at a certain position and the feedback is switched off. The tip is kept at the specific height while the sample voltage U_b is varied and the current is recorded. The measured I/V curve is then differentiated numerically to obtain $\frac{dI}{dV}$ and the information about the LDOS of the sample. A more practical way to extract the $\frac{dI}{dV}$ is the use of the lock-in technique. The applied DC sample bias gets overlaid by an AC voltage with a defined modulation frequency and small amplitude. The measured current signal is multiplied by a signal oscillating with the modulation frequency and by adjusting the phase and feeding the signal through an low pass filter one obtains directly the differential conductance and the LDOS of the sample.

2.1.3 STM imaging

The tunneling effect is employed to image the surface of the investigated sample, collecting topographic and electronic information. Typically two operational modes, namely *constant current mode* (Figure 2.2 (a)) and *constant height mode* (Figure 2.2 (b)) are performed. For both modes, the position of the tip is defined by the x and y coordinates and the tip is scanned over the whole image. Typically the tip moves fast along the whole range of the x-direction and subsequently jumps to the next line of the y-direction, until the complete area is covered.
In the *constant height mode* the z-position of the tip is held constant and the current is monitored. This mode is seldomly used as it comprises risks of crashing the tip and other experimental issues such as moving the tip parallel to the sample surface, which has to be adjusted. In *constant height mode* the imaged data is the measured current.
The *constant current mode* is mainly used in this thesis. Here the current and bias have to be set and a feedback loop is applied to adjust the z-position of the tip in a way that the measured current stays constant. The response speed of the feedback can be varied for the specific measurement. The z-position is imaged and holds information of the topography and

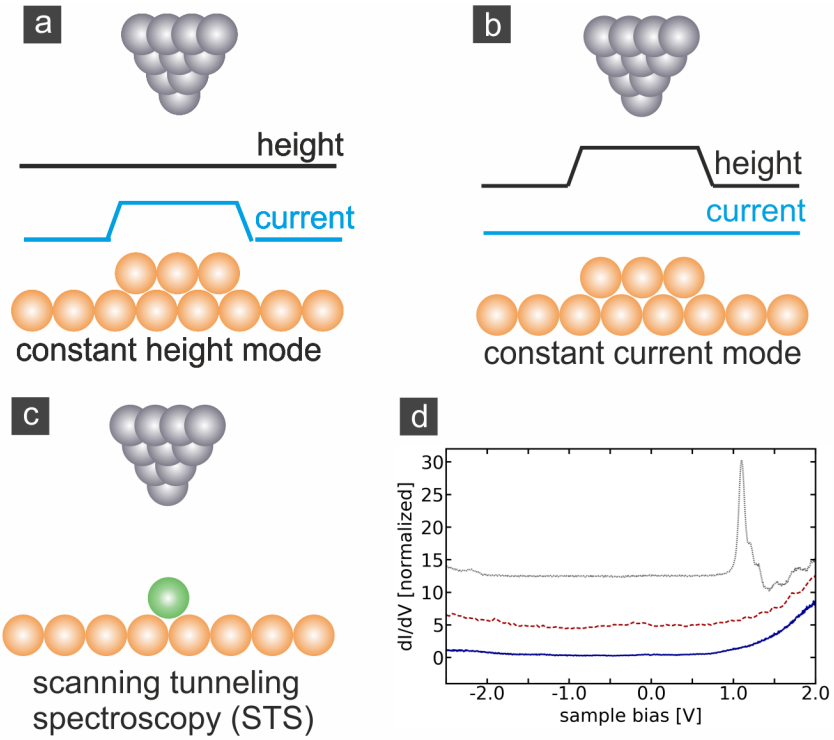

Figure 2.2: *Operational modes of STM: (**a**) Constant height mode, the tips is kept a a constant z position while the current signal is recorded.(**b**) Constant current mode, the current is kept at a set value while the z position of the tip is measured. (**c**) STS, tip is located on top of the point of interest and kept at a fixed z position. The LDOS is measured and plotted against the applied bias. Typical STS spectra are shown in (**d**). The gray graph depicts a spectra of a molecule decoupled from a metal support by an insulating layer, while the dashed red and the blue line show the LDOS of molecules in direct contact with the underlying support.*

the LDOS of the sample surface.

Furthermore, STM is used for lateral and vertical manipulation of single atoms and molecules.

2.2 Frequency modulated atomic force microscopy (FM-AFM)

2.3 Theory of frequency modulated atomic force microscopy

In this work the experimental data was recorded via a FM atomic force microscopy at UHV and low temperatures [74]. The so-called qPlus sensor is used (see Figure 2.7) to measure the surface of the investigated samples [66]. In the following a basic theoretical description of the frequency modulated AFM signal at UHV is presented. More elaborated considerations can be found elsewhere [75–77].

The interaction between the tip of the frequency modulated AFM and the sample surface can be modeled by a very easy model system as sketched in Figure 2.3 (b). The cantilever with

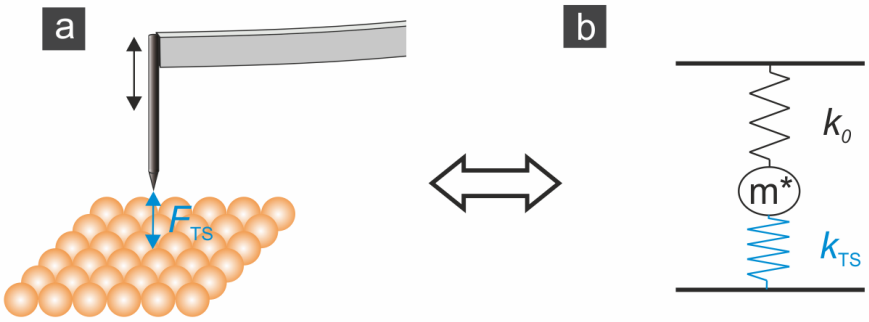

Figure 2.3: *AFM modeled via two springs and an effective mass. (**a**) Oscillating cantilever with attached tip of an AFM. The interaction between tip and sample is illustrated by F_{TS}. (**b**) The AFM is modeled by two springs and an oscillating effective mass m^*. The cantilever is represented by a spring with spring constant k_0, eigenfrequency f_0 and the effective mass m^*, whereas the information of the tip-sample interaction is modeled by the second spring with spring constant k_{TS}. Typically $k_{TS} \ll k_0$*

attached tip is symbolized as a spring with spring constant k_0 and an effective mass m^*. Before the tip apex comes in the proximity of the sample, the cantilever and accordingly m^* is oscillating with its eigenfrequency f_0. When the tip approaches the surface the interaction between tip and surface can be described by an additional spring with spring constant k_{TS} sitting between m^* and the surface as shown in Figure 2.3 (b). Accordingly to Hook's law (small oscillation amplitudes) the effective spring constant of the two spring system is given by $k^* = k_0 + k_{KS}$ and the resulting effective resonance frequency f_{res} reads as:

$$f_{res} = \frac{1}{2\pi}\sqrt{\frac{k^*}{m^*}} = \frac{1}{2\pi}\sqrt{\frac{k_0 + k_{TS}}{m^*}} = \frac{1}{2\pi}\sqrt{\frac{k_0}{m^*}}\sqrt{1 + \frac{k_{TS}}{k_0}} \tag{2.16}$$

For typical experimental settings k_0 of the macroscopic cantilever is much larger than k_{TS} resulting from the tip-sample interaction. With $k_{TS} \ll k_0$ and an first-order Taylor series approximation following frequency shift Δf of the oscillating cantilever is found:

$$\Delta f = f_{res} - f_0 = \frac{f_0}{2k_0} k_{TS} \tag{2.17}$$

By differentiating k_{TS} it becomes obvious, that the measured observable Δf carries information about the potential V_{TS} and the force F_{TS} between tip and sample:

$$\Delta f(z) = \frac{f_0}{2k_0} k_{TS} = -\frac{f_0}{2k_0}\frac{\delta F_{TS}}{\delta z} = \frac{f_0}{2k_0}\frac{\delta^2 V_{TS}}{\delta^2 z} \tag{2.18}$$

2.4 Tip-sample forces

So far with this simple spring model, however the more challenging task is now to describe the force acting between tip and sample. Three fundamental interactions between tip and sample have to be considered to model F_{TS}:

- Van der Waals (vdW) interaction
- Chemical interaction
- Electrostatic interaction

Due to the UHV conditions and the used non magnetic tips in the experiments, friction and magnetic forces are neglected here.

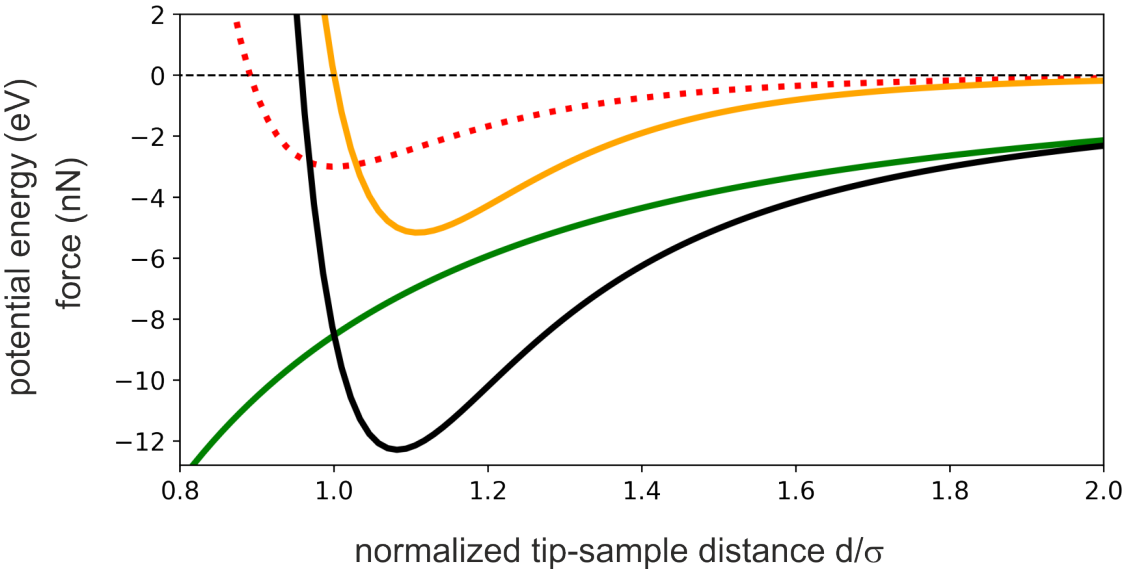

Figure 2.4: *Tip sample interactions. Lennard-Jones potential (dashed red line), Lennard-Jones forces (orange), vdW background force (green), and total force (black). Parameters:* $E_{min} = 3$ eV, $\sigma = 2.5$, $A_H = 2$ eV, $R = 20$ nm

Lennard-Jones potential The well established Lennard-Jones potential [78, 79] is a decent starting point to characterize the interactions between tip and sample. The Lennard-Jones potential (V_{LJ}) describes the potential between two neutrally charged spherical atoms or molecules and reads as:

$$V_{LJ} = E_{min}\left[\left(\frac{\sigma}{d}\right)^{12} - \left(2\frac{\sigma}{d}\right)^{6}\right] \tag{2.19}$$

with E_{min} is the global minimum of the interaction potential at a separation distance $d = 1.122\sigma$ of the two particles. The potential comprises a repulsive component scaling with the

power of twelve (**chemical interaction**) and an attractive component scaling with the power of six (**van der Waals interaction**). In Figure 2.4 the red dashed line is representing the Lennard-Jones potential. The chemical forces show such a high distance dependence for small distances that the repulsive tip sample interaction can be approximated by the Pauli repulsion of a single tip apex atom and a single surface atom. However, the long range vdW component originates from fluctuation induced dipoles, which varies by d^6 for spherical atoms [80]. Consequently, in the case of differently shaped tip and sample, a more appropriate model of the attractive long range vdW forces is needed [75]. For a spherical tip and a flat surface the vdW forces can be described by the Hamaker approach, which integrates over the volumes of tip and sample [81]. The vdW forces caused by the specific geometry of the tip and the surface can be described by an additional term in the Lennard-Jones potential [82]:

$$V_{TS} = E_{min}\left[\left(\frac{\sigma}{d}\right)^{12} - \left(2\frac{\sigma}{d}\right)^{6}\right] - \frac{A_H R}{6d} \tag{2.20}$$

with the material specific constant A_H, which is typically around 1 eV [83, 84] and the radius of the etched tip (several tens of nm). The corresponding forces can then be written as:

$$F_{LJ} = 12\frac{E_{min}}{\sigma}\left[\left(\frac{\sigma}{d}\right)^{13} - \left(\frac{\sigma}{d}\right)^{7}\right] \tag{2.21}$$

for the Lennard-Jones force and

$$F_{TS} = 12\frac{E_{min}}{\sigma}\left[\left(\frac{\sigma}{d}\right)^{13} - \left(\frac{\sigma}{d}\right)^{7}\right] - \frac{A_H R}{6d^2} \tag{2.22}$$

in the geometry corrected case. In Figure 2.4 both forces, the normal Lennard-Jones force for spherical molecules (orange) and the corrected Lennard-Jones potential for the particular case of a tip and sample geometry (black) are shown. Additionally the vdW background is plotted in Figure 2.4 in green.
In a similar way the Lennard-Jones force can be extended by **electrostatic forces**. Again for a spherical tip and a flat surface, an electrostatic potential difference $\Delta\Phi$ between tip and sample leads to an additional electrostatic force [85–87]:

$$F_{electrostatic} = -\frac{\pi\epsilon_0 R\Delta\Phi^2}{d} \tag{2.23}$$

which has to be summed to the tip sample force F_{TS}. For most of the measurements in this thesis the applied bias was set to zero and therefore the electrostatic contributions to the tip sample interaction are neglected. However, also for zero applied bias the electrostatic force can cause distortions in the AFM images due to inhomogeneous charge distributions on the sample, which has to be kept in mind.

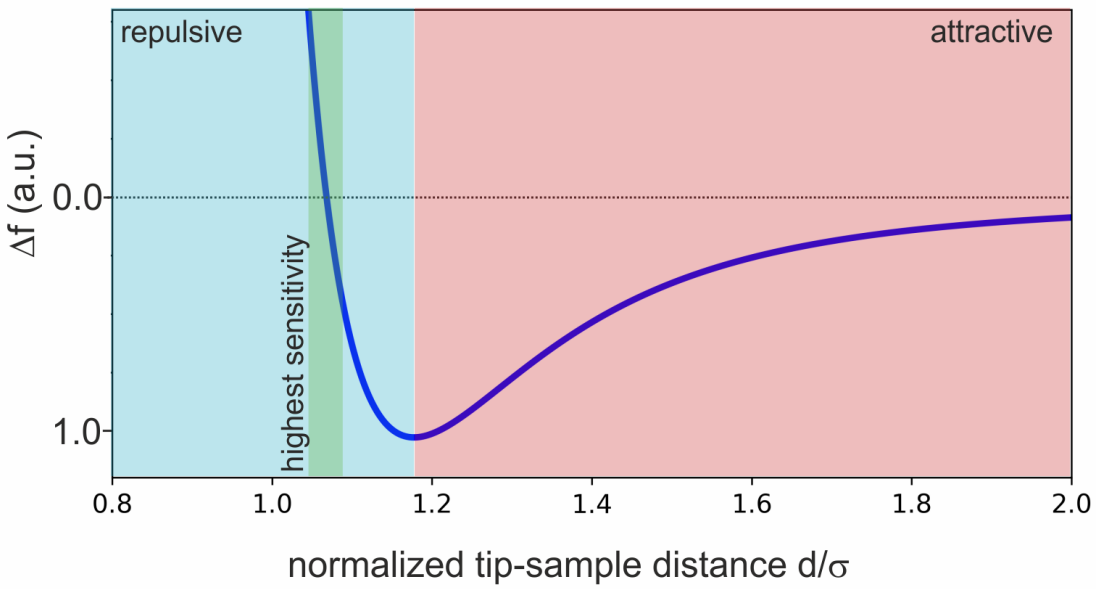

Figure 2.5: *Tip-sample distance depended frequency shift Δf. The blue curve illustrates the frequency shift Δf, which is $\propto -\frac{\delta F_{TS}}{\delta z}$. For large tip-sample separation the vdW force is dominating, leading to an attractive interaction (red region). For smaller distances the repulsive contributions causing the main interaction between tip and sample (blue region). The green region highlights the tip-sample separation with the highest sensitivity. For small deviations in distance, large changes in Δf can be imaged.*

To summarize, the measured observable Δf is plotted in Figure 2.5 against the normalized tip-sample distance. Three distinct regions are color coded.
For large tip-sample distances the tip-sample interaction is dominated by the attractive long range vdW forces and therefore corresponds to the attractive region colored in red. For smaller separations the Pauli repulsion becomes more relevant and consequently the blue colored region is referred to the repulsive regime. In the green colored region the highest sensitivity is observed [69]. In this region, small deviations in tip-sample separation cause large differences of Δf, which can be imaged.
For even smaller distances the tip tends to jump to the sample, leading to unstable imaging conditions. More stability of the measurement can be obtained by larger oscillation amplitudes, however due to a stronger averaging effect caused by the vertical tip movement, the sensitivity decreases.
Consequently the oscillation amplitudes used for this work range from about $20 - 200$ pm. Another notable aspect of Figure 2.5 is that the Δf curve exhibits a minimum. Thus, a measured Δf value can be obtained for two different tip-sample separations. This non-monotonic behavior needs to be considered for data interpretation and requires higher demands on the feedback system of the microscope as explained in the following.

2.5 FM-AFM feedback

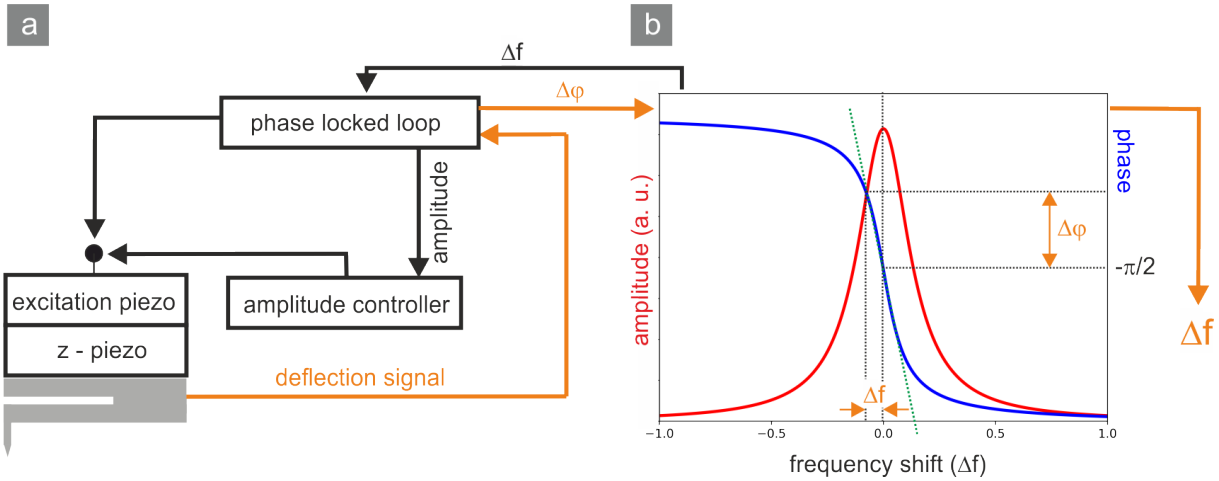

Figure 2.6: *Feedback system of the FM-AFM.* ***(a)*** *The cantilever is driven by the excitation piezo. The measured deflection signal is then fed to an phase locked loop (PLL), where the resonance frequency f_{res} of the cantilever, which interacts with the surface, is determined and the f_{exc} is adjusted to $f_{exc} = f_{res}$. The amplitude controller regulates the amplitude of the excitation signal via a PI control to keep the deflection amplitude at its setpoint.* ***(b)*** *Δf is not measured directly from the deflection signal. The phase shift $\Delta\varphi$ between excitation and deflection signal is used to quantify Δf. While $\Delta\varphi$ follows an arctan signature (blue line) it can be modeled by a linear slope in the vicinity of f_0. This slope is then used to estimate Δf from the measured $\Delta\varphi$. The red line shows the deflection amplitude for a range of f_{exc} with switched off feedback system. The red curve is used to identify f_0 of the freely oscillating cantilever.*

Δf is the wanted observable, which gives insights into the interactions between tip and sample, as explained above. To extract Δf from an FM-AFM experiment three independently working feedback systems are needed. The feedback can adjust following parameters:

- $\Delta\varphi$ between excitation and deflection signal
- Amplitude of cantilever oscillation
- z-position of tip

Figure 2.6 sketches the feedback system and the processing of the measured signal to obtain the wanted Δf values. The cantilever oscillation is driven by an external excitation, which excites the cantilever at its resonance frequency f_{res}. The excitation frequency f_{exc} is adjusted to match the resonance frequency f_{res} by keeping the phase shift between excitation signal and the measured cantilever oscillation signal at $\Delta\varphi = \pi/2$, which is realized by the first feedback system. Therefore, the deflection signal is fed into a phase locked loop (PLL) where the signal first enters a lock-in amplifier to extract the amplitude of the oscillating cantilever and the phase shift $\Delta\varphi$ between excitation and deflection signal [88, 89].

$\Delta\varphi$ is then used to derive the change of the resonance frequency f_{res} from the resonance frequency of the freely oscillating cantilever f_0, which is used to obtain Δf by:

$$\Delta f = f_{res} - f_0 \tag{2.24}$$

Figure 2.6 (b) depicts the evaluation of Δf. The graph shows a frequency sweep, of the freely oscillating cantilever with completely switched off feedback systems. While f_{exc} is ramped up the amplitude and $\Delta\varphi$ of the deflection signal are measured. The amplitude (red curve) shows a Lorentzian shaped peak at its resonance frequency f_0, whereas the corresponding $\Delta\varphi$ follows an arctan signature with $\Delta\varphi = \pi/2$ at f_0. In the vicinity of f_0 the arctan can be approximated by a linear slope $m_\varphi = \frac{\Delta\varphi}{\Delta f}$ as drawn in Figure 2.6 (b) in green.
This slope is used to quantify Δf from the measured $\Delta\varphi$ between excitation and deflection signal. The obtained Δf is then used to image the surface of the substrate and additionally fed into the PLL where f_{exc} is adapted to the current f_{res} of the interacting cantilever. The slope m_φ is very critical for the AFM imaging and depends on the shape of the tip, which is altered for example by bias pulses and changes with temperature. Consequently m_φ has to be determined frequently.
The second feedback adjusts the magnitude of the excitation amplitude and is needed to keep the oscillation amplitude at a certain set point. Differing amplitudes would lead to not wanted changes in the tip-sample distance. Here the amplitude is adjusted by a simple PI controller, which determines the amplitude of the excitation signal.
Running these two feedback to keep $\Delta\varphi$ at $\pi/2$ and the oscillation amplitude at the amplitude set point, the sample surface can be investigated within different operational modes:

Constant height mode At constant height mode the tip is fixed at a vertical position and Δf is recorded for each pixel $\Delta f(x, y)$. To avoid crashing of the tip only small flat areas can be measured, which is limiting the range of the scan frames. Furthermore a correct plane correction is essential for imaging in this mode.

Constant Δf mode Similar to the constant current mode in STM, a z-feedback is needed for constant Δf measurements in FM-AFM. In this mode crashing the tip is less likely and the plane angle of the surface has rather small influence. However compared to the constant height mode the resolution of the measurement suffers due to convolution effects of the tip apex with the surface.
Therefore, to measure more corrugated systems, which are not accessible via the constant height mode the two pass method is used to obtain higher resolution in comparison to the constant Δf mode. The imaged observable is similar to the constant current case of the STM, the z-position of the piezo.

Two pass mode [90] The two pass mode combines the advantages of the constant height and the constant Δf mode. The investigated region is first scanned in constant Δf mode to keep the tip sample distance at a safe level. In the subsequent step the tip follows the z-profile measured in the constant Δf mode and images the Δf signal. Doing this the surface can be imaged with the high constant height resolution even for strongly corrugated surfaces. Usually the second pass follows the first pass line for line. To obtain high sensitivity an offset in the vertical z-direction of the first pass can be added.

$\Delta f(z)$-spectroscopy $\Delta f(z)$-spectroscopy can be used to quantitatively determine height differences on the surface by measuring the z-dependence of $\Delta f(z)$. To compare different $\Delta f(z)$ curves the z-position of the global minima of $\Delta f(z)$ for different x, y-positions can be used. For isotropic tip-sample interactions the z-position of the $\Delta f(z)$ minima give direct access to the height distribution of the surface [91].
Furthermore, additional variables (tunneling current, excitation amplitude, $\Delta\varphi$) are measured simultaneously, which carry supplementary information.

2.6 qPlus sensor

The employed cantilever is the substantial part for high quality AFM operations. Since the beginning of the 1990s the most commonly used cantilevers are made of silicon [92–94]. However for frequency modulated AFMs, which exhibit the highest resolutions the qPlus sensor shown in Figure 2.7 reveals superior properties [66]. The qPlus sensor consists of a quartz tuning fork where one prong is glued to an heavy base plate and a conducting tip is attached the one end of the other prong. The qPlus sensor exhibits following advantages for high performance AFM operations:

- Piezoelectric effect of quartz: The deflection signal of the qPlus sensor can easily be sensed via the piezoelectric induced voltages of the cantilever movement. In contrast to a piezoresitive cantilever [95] the qPlus is feasible for low temperature operations as it exhibits only negligible dissipation [96, 97].
- High stiffness: The high stiffness is essential for the stability of FM operation to avoid *jump-to-contact* instabilities [75].
- High Q-value: The energy loss to drive the oscillation of the cantilever is extremely small.
- High thermal stability [97–99]: The temperature of the system has relatively low influence on Q-factor and resonance frequency and therefore on the imaging performance.

A tip functionalization can further improve the resolution of the qPlus sensor [69]. CO terminated tips are used to image chemical bonds in this work.

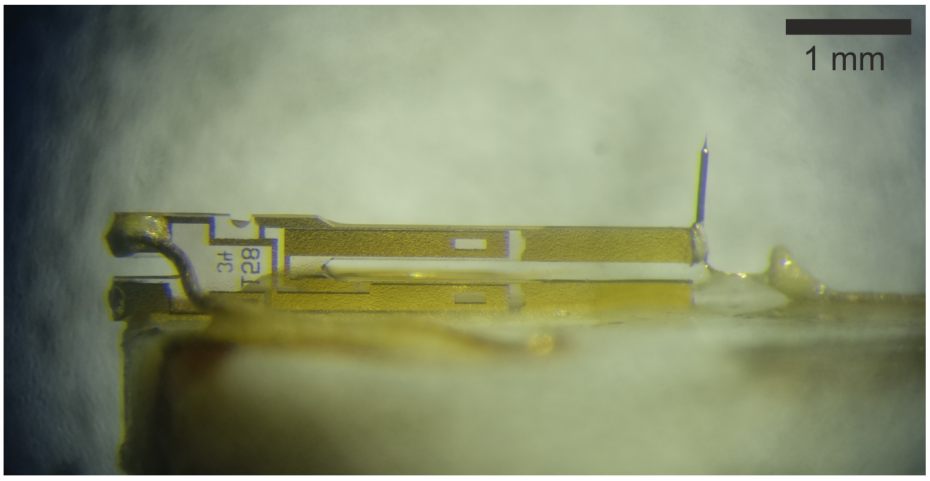

Figure 2.7: *qPlus sensor. The quartz tuning fork is glued on a heavy base plate and conducted by an gold wire. The conductive tip (here tungsten) is glued at the end of the upper prong and conducted by an additional gold wire.*

2.7 Experimental approach

The experiments presented in this work were carried out with two different microscopes. The main difference between them is that the combined STM/AFM hosts a qPlus sensor whereas the second microscope can only be used as STM.
Despite that, the design of the two microscopes is very similar and consequently the description of the experimental set up is exemplarily presented with the STM/AFM microscope. For high performance measurement ultra high vacuum and low temperatures are essential.

2.7.1 UHV system

High vacuum during sample preparation and SPM measurements is essential for our experiments. Already small contamination of the investigated surface can modify the observed results and the preparation protocols can be altered due to the gaseous environment. Therefore the preparation (light blue) and the SPM chamber (yellow) in Figure 2.8 are kept in UHV at a pressure of around $p \approx 10^{-10}$ mbar.
Both chambers are separated by a gate valve and can be kept at UHV independently. The whole system is pumped through the preparation chamber to reach UHV. A first vacuum stage is obtained by a dry diaphragm pump going down to low pressures of $p \approx 1$ mbar, which is necessary to run two successively connected turbo molecular pumps (TMP).
Furthermore, the pressure can be temporarily decreased by an titanium sublimation pump and a liquid nitrogen cooled cold trap, which are connected to the preparation chamber.
The whole set up has to be heated to 390 K for about three days to achieve the targeted UHV. Both chambers are additionally pumped by ions pumps, which are sufficient to hold the UHV

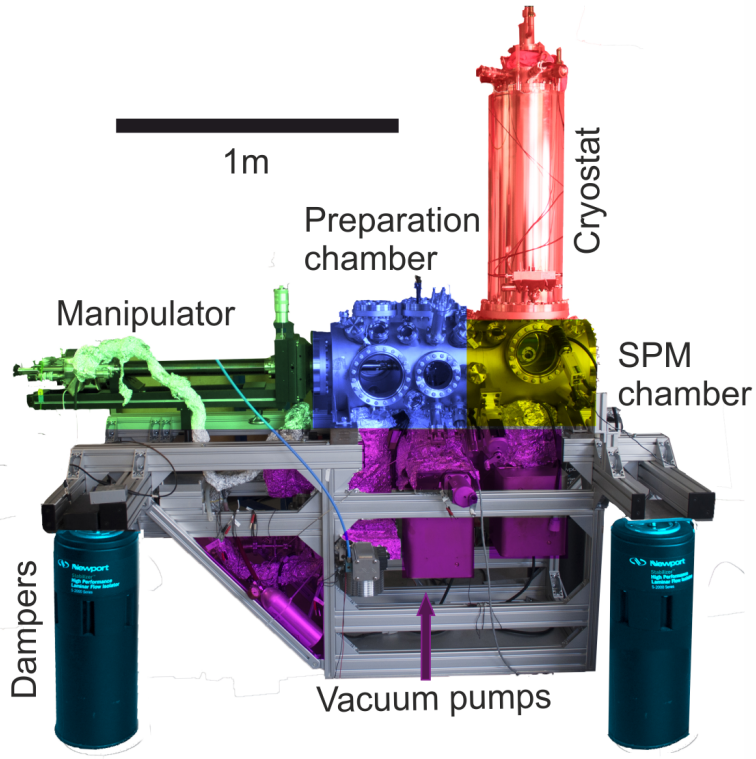

Figure 2.8: *STM/AFM microscope. The different parts are colored and are assigned as follows: green: manipulator, light blue: preparation chamber, red: cryostat filled with liquid nitrogen and liquid Helium, yellow: SPM chamber, blue: pneumatic dampers, and purple: vacuum pump system. The image was adapted from [100].*

in the SPM chamber when the gate valve between the chambers is closed. The gate valve is usually closed to protect the SPM chamber from relatively dirty sample preparation procedures. Furthermore, the preparation chamber holds several apparatuses to clean and prepare the investigated sample. For cleaning a sputter gun is installed, whereas to deposit metals or molecules on the sample several evaporators can be added. Some leak valves for gas dosage are connected to the chamber as e.g. Argon is used for the sputtering process.
Additionally a mass spectrometer is installed and a load-lock, which is used to exchange and transfer tips, samples, and sensors between chamber and ambient conditions without losing the established UVH. In the SPM chamber a leak valve with connected gas line is installed for CO dosage, which is needed to functionalize the AFM tips.
The cryostat colored in red in Figure 2.8 sits on top of the SPM chamber. The sample is transferred by the manipulator to the SPM chamber. Therefore the gate valve between preparation and SPM chamber and the transfer shutters depicted in Figure 2.9 has to be opened.

2.7.2 Cooling system

To freeze out thermally induced movements of the investigated samples and to reduce drift and creep within the measurement low and stable temperatures are needed. The cooling system sketched in Figure 2.9 keeps the SPM scanning stage at $\approx$ 5 K by thermal contact to the liquid Helium (LHe) reservoir holding 4 L LHe at $T = 4.2$ K. The LHe bath is surrounded by a larger liquid nitrogen (LN_2) reservoir with 15 L of (LN_2) at $T = 77$ K, to reduce the LHe consumption of the system. For low and constant temperatures the SPM head has to be additionally screened from radiation, which is realized by two layers of radiation shields at temperature hold at $T = 4.2$ K and $T = 77$ K. In normal operation the cryostat has to be refilled after around 72 hours. While the nitrogen is released into the room, the helium is fed into a helium recovery line and liquidized again.

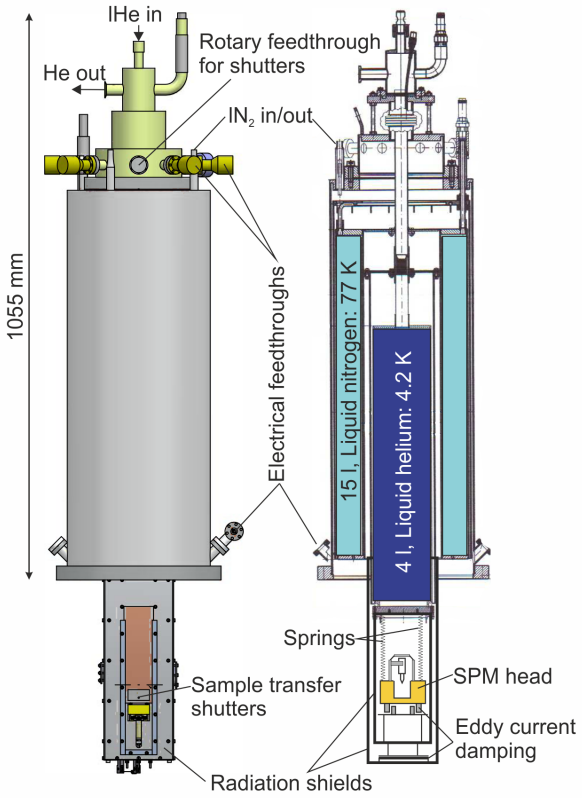

Figure 2.9: *Schematics of a cryostat with two reservoirs. A technical drawing is pictured on the left side. On the right side the cross section of the cryostat with the liquid Nitrogen (LN_2) and the liquid Helium (LHe) are shown. Two stages of radiation shields ensure a SPM scanner temperature of $T \approx 5$ K. The image was adapted from [101].*

2.7.3 Vibration damping system

The damping of external vibration, which can disturb the SPM operations comprises three stages. The whole instrument is placed on pneumatic dampers (blue colored in Figure 2.8), directly reducing vibrations of the chamber and which are also used to adjust the horizontal angle of the machine. The second damping stage employs an eddy current damping of the inner cryostat as depicted in Figure 2.9. Three springs hold the SPM scanner during the measurements and act in combination with a second eddy current damping as the third stage of the decoupling system from environmental vibrations. Electrical vibrations are minimized by the usage of screened cables and by the usage of filtered power supply and filtered grounds.

2.7.4 SPM scanner

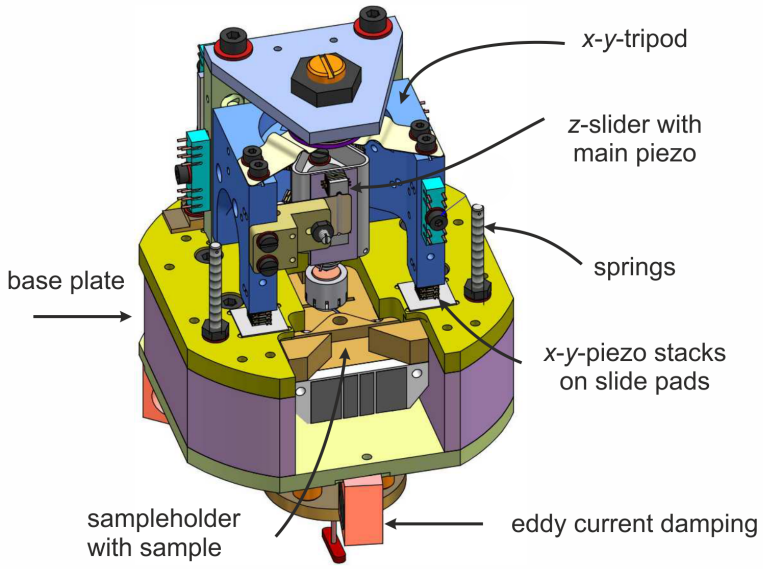

Figure 2.10: *SPM scanner. Schematic of the used SPM scanner with relevant labeling. Adapted from [102]*

The heart of the whole instrument, the SPM scanner is sketched in Figure 2.10 and is commercially available from Createc GmbH [103]. The base plate is colored in yellow and purple and hosts the sample holder. The sample holder is electrically contacted at its contact plate and can be pressed against the yellow part of the base plate to sit at a fixed position during the measurements. The whole SPM scanner can be pulled down, for sample transfer and increased thermal conductance and released for the measurements. In the released state the SPM scanner hangs from three springs and vibrations are reduced via an eddy current damping. While the sample is fixed at a certain position during the measurements the tip has to be move. The movement of the SPM sensor is realized by coarse piezo stacks with relatively large range, used to position the tip at the targeted sample position and a main tube piezo with higher

precision, which is used for the actual measurements.
The x-y-tripod sits on top of three shear piezo stacks carrying out the lateral coarse motion. To roughly position the tip, a voltage is slowly increased and the piezo stacks shear in one direction moving the x-y-tripod (Step 1 in Figure 2.11 (a)). In Step 2 the voltage is abruptly reduced and the shear piezo stacks slide over the ceramic slide pads on which they are located. Step 1 and Step 2 are referred to a stick and slip process. To obtain a significant displacement, this stick and slip process has to be repeatedly executed. The movement with shear piezo stacks is very sensitive on the magnitude and the frequency of the applied voltage. The x-y-tripod does not move in Step 2 due to its inertness.
The vertical coarse motion is also realized by shear piezo stacks, which move the main tube piezo sitting inside the triangular prism [104] shown in Figure 2.10. In contrast to the lateral movement with individual piezo stacks, two piezo stacks are used for the vertical movement of the sensor for safety reasons. A voltage is slowly increased to shear both piezo stacks in the same direction (Step 1 in Figure 2.11 (b)) similar to the lateral case. In the second step, the voltage at one piezo stack is switched off and the piezo is sliding along the surface. In the subsequent third step the voltage at the second piezo stack is also switched off and the piezo is also sliding over the surface. This way, one of the two piezo stacks is always in static contact with the moved surface inhibiting a slipping down of the sensor. For highly precise movements in vertical and lateral direction the main tube piezo depicted in Figure 2.11 (c) is used. The sensor is fixed magnetically to the bottom of the main tube piezo. By applying voltages at the outer electrode pairs (blue and red) the tube bends and causes lateral motion of the SPM tip. The inner contacts (black) are used to adjust the z-position of the sensor.

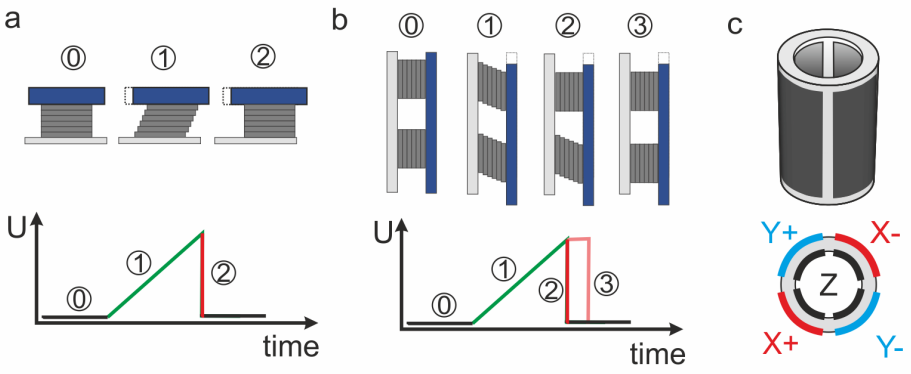

Figure 2.11: *Functionality of used piezos.* ***(a)*** *The shear piezo stacks are fixed at the blue legs of the x-y-tripod, which is moved upon the slow increase of the applied voltage (Step 1). The voltage is reduced fast and the inertness induced forces overcome the sticking friction of the piezo stacks on the ceramic plate and the piezo stacks move (Step 2).* ***(b)*** *Two piezo stacks are used for the vertical coarse movement to avoid falling down of the sensor. The voltage is increased slowly to move the sensor (Step 1), then the voltage at the first piezo stack is switched off (Step 2) followed by the second piezo stack (Step 3). Thus the piezo stacks move one after another and the sensor is secured by at least one piezo stack holding the sensor with sticking friction rather than with sliding friction.*

2.7.5 Electronics

The instrument is operated with a Nanonis control system and the corresponding Nanonis software [105].

2.7.6 Tip preparation

A sharp tip is essential for AFM operations as the geometry of the macroscopic tip is influencing the vdW background. The used qPlus sensor is bought from Createc GmbH [103] and shown in Figure 2.12 (a). Before bringing the sensor into the chamber the tip has to be shortened and sharpened, which is done by etching the end of the tip. In Figure 2.12 (b) the set up for the etching is sketched. The tip is hold into a NaOH solution with a concentration of 1 mol/L. A voltage of $V \approx 3.5$ V is applied between the tip and a stainless steel loop hold into the solution for several minutes until the lower part of the tip falls down. The hereby taking place reaction reads as:

$$W + 8OH^- \rightarrow WO_4^{2-} + 4H_2O + 6e^- \tag{2.25}$$

In Figure 2.12 (c) the apex of an etched tungsten tip is shown. A ideal shaped tip exhibits a tip peak length twice as long as the tip diameter. One crucial parameter for the resulting geometry of the tip is the immersion depth of the tip as it defines the force pulling down the tip apex. Directly after the etching the tip is cleaned with distilled water, acetone and isopropanol and transferred to the vacuum. A short tip is wanted as the mass of the tip influences Q-factor and resonance frequency of the qPlus sensor and a long tip can cause additional artifacts in the AFM measurements. Due to the limited field of vision into the SPM chamber a certain tip length is needed for an secure approach to the surface. Therefore the used tips should have a length ~ 1 mm. Consequently, there is usually only one try to obtain a nicely shaped tip at the targeted length for the bought qPlus sensors.

Another approach is to first etch the tip from a tungsten wire till a good geometry is achieved and subsequently glue it to the quartz tuning fork. Figure 2.12 (d) shows the tip from Figure 2.12 (c) glued to the sensor. Additionally the contact, a gold wire has to be glued to the sensor too. To grab and position the gold wire and the tip a Cu wire is used employing vdW interactions. A conducting two component glue Polytech EC 101 applied to fix tip and contact to the sensor [106]. The tuning fork can also be glued to the sensor holder with an insulating Loctite 608 epoxy glue [107].

During measurements modifications of the tip are done by poking the tip towards the surface and simultaneously apply higher voltages, so called tip formings (TF). Here tip and surface are heated locally and the tip is changed randomly. Therefore TFs are repeated until a decent tip is obtained. For strong TF we used $V = 10$ V and stung the tip into the surface up to 1 μm. If such strong TFs are not sufficient, field emission resonance (FER) stabilized heating was executed. For the FER tip preparation the tip is positioned with a small separation from the

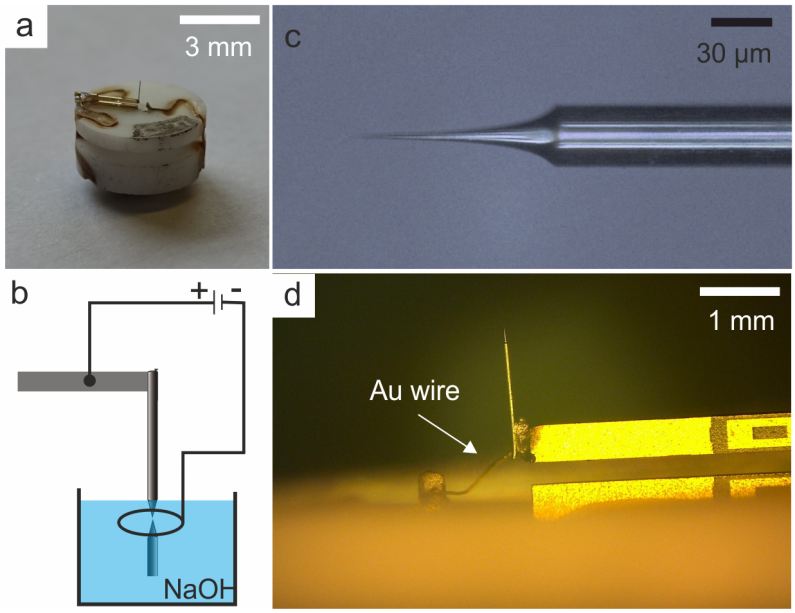

Figure 2.12: *Tip preparation.* ***(a)*** *qPlus sensor bought from Createc GmbH.* ***(b)*** *Sketch of set up for tip etching.* ***(c)*** *Etched tungsten tip.* ***(d)*** *Tungsten tip from (c) glued to a qPlus tuning fork.*

surface. A high voltage of about $V = 70 - 100$ V is applied between tip and surface. The flowing current is stabilized at around 0.5 mA for a while. Doing this a large heating power is applied to the tip and stronger tip modification is achieved. For safety reasons we used a resistance of 10000 Ω connected in series to limit the maximum current to 10 mA.

2.7.7 Sample holder design and preparation of samples

For our SPM experiments the sample holder shown in Figure 2.13 was used. The metal sample is assembled on the oven and fixed by a molybdenum star. Two of the four contact plates are used to heat the oven and two to read out the temperature of the sample via thermocouples. The thermocouples are connected to the molybdenum star. Furthermore the oven is isolated from the sample holder plate by insulating ceramics.

In this work we used Cu(111), Ag(111) and Au(111) as sample metal. To obtain a flat well defined metal surface, several sputter and annealing cycles were applied to the samples. For the sputtering the preparation chamber was filled with Argon at a pressure of $p = 2 * 10^{-5}$ mbar. The Argon atoms are ionized within the sputter gun and accelerated towards the sample with an energy of 1 keV. By hitting the metal surface the Argon ions remove the uppermost layers of the sample, resulting in a clean but corrugated metal surface. For the used parameter the sputter rate is $\approx$ 10ML/min [101, 109–111]. To subsequently flatten the surfaces the samples are heated to around 470 K for a short period of time and slowly cooled down ($1 - 2$ K per second) to avoid strain induced reconstructions.

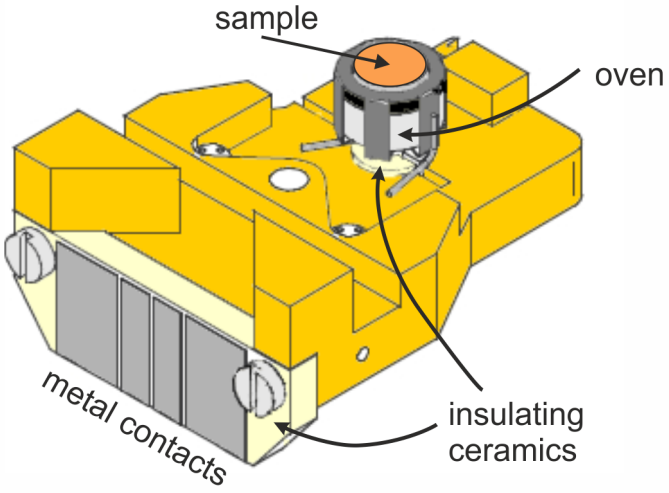

Figure 2.13: *Sample holder used for SPM experiments. The sample is fixed on the oven by a molybdenum star. Two of the electronic contacts are used to heat the oven and two for reading out the temperature via thermocouples connected to the molybdenum star. The oven is isolated from the sample holder plate by insulating ceramics. Sketch is taken from [108].*

2.8 Investigated materials

2.8.1 Porphyrins

Porphyrins are a class of functional molecules, which are used in nature for essential processes enabling life on earth. The most prominent representative of porphyrins is heme, the central part of the hemoglobin, which is responsible for the oxygen and CO_2 transport in the blood of animals. Furthermore, they take an important role in the photosynthesis of plants as pophyrins are part of chlorophyll and additionally the porphyrin-based vitamin B12 is important for metabolism in mammals.

Figure 2.14 shows the structural formula of a porphyrin molecule. Here the **R** is a place holder for different substituents. When all four **R** groups are replaced by hydrogen atoms the obtained molecule is the so-called porphine. The porphine consists of four pyrrole-like rings connected by four methine (=CH-) groups, which form a macrocyle and the chemical formula reads as $C_{20}H_{14}N_4$.

This porphine is the central parent compound, which all porphyrins have in common.

The properties of the porphyrins can be modified by attaching different ligands at the meta positions, where in Figure 2.14 the place holder **R** is depicted and by metalation of the central macrocycle. A comprehensive summary of porphyrins on surfaces is found in [30].

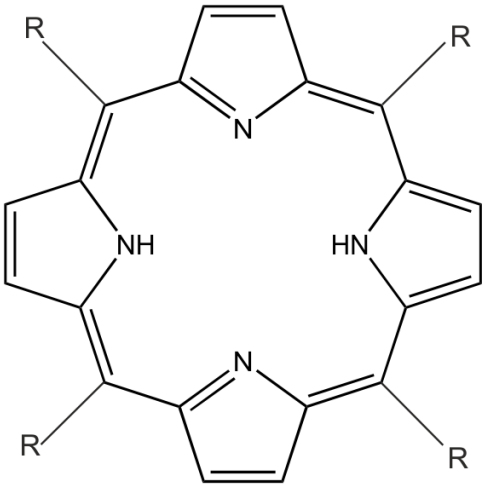

Figure 2.14: *Structural formula of a porphyrin molecule.* ***R*** *is place holder for different substituents, which can be modified for the particular usage of the molecules. In the case where all for* ***R*** *groups are replaced by a hydrogen atom the obtained molecule is a porphine.*

2.8.2 Metal supports

Cu(111), Ag(111), and Au(111) are metals with fcc structure, exhibiting a hexagonal symmetry on the (111) surface with a lattice constant of $a_{Cu} = 2.56$ Å, $a_{Ag} = 2.89$ Å, and $a_{Au} = 2.87$ Å. The monoatomic step height is $z_{Cu} = 2.36$ Å and $z_{Ag} = 2.08$ Å, and $z_{Au} = 2.35$ Å. While the Cu(111) and the Ag(111) surfaces appear rather flat, Au(111) reveals a so-called Heringbone reconstruction as theoretically described in [112].

2.8.3 Hexagonal boron nitride (*h*-BN)

Two dimensional hexagonal boron nitride exhibits exceptional properties such as chemical inertness, mechanical stability, and a rather large electronic band gap [39, 113]. Especially the electronic band gap opens up potential applications for *h*-BN as spacing or protective layer in van der Waals (vdW) heterostructures [114, 115]. The growth of single layer *h*-BN has been established for various metal supports (e.g. Cu(111) [116], Ag(111) [117], Rh(111) [118], Ni(111) [119], Ir(111) [120, 121], Pt(111) [122]) mainly via the chemical vapor deposition (CVD) method. In this work we used CVD grown *h*-BN on Cu(111) from the precursor molecule borazine following the recipe described in [116, 123]. The CVD growth of *h*-BN on copper, especially copper foils, is a promising way for scaling up the growth procedure for industrial purposes [124].

Moiré pattern From the lattice mismatch between two-dimensional layer and a underlying support, a so called Moiré pattern appears [125], as sketched in Figure 2.15. The periodic corrugations can be geometric and/or electronic. In [123] we present a comprehensive study of the *h*-BN/Cu(111) system, quantifying the geometric and the electronic corrugation of the

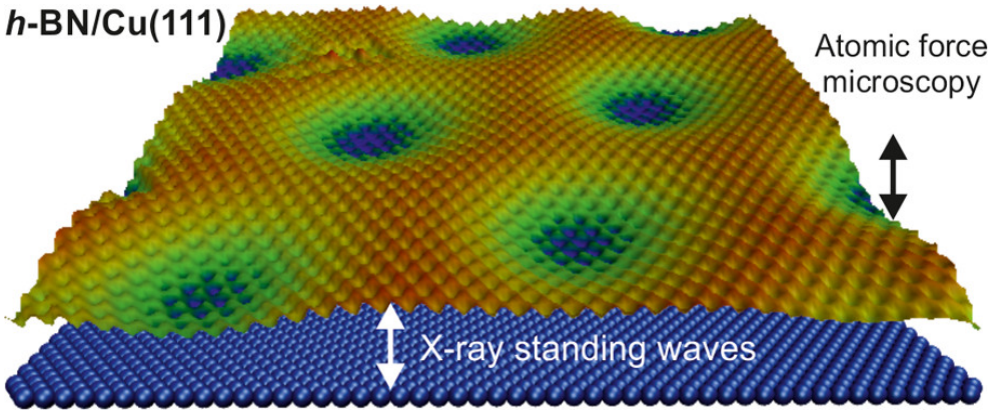

Figure 2.15: *Model of a two dimensional h-BN layer on Cu(111). A Moiré like superstructure, which arises from the lattice mismatch between Cu(111) and h-BN is clearly observable. Our comprehensive characterization of the h-BN/Cu(111) system is published in [123] using complementary methods such as STM, nc-AFM, DFT calculations, XPS, and XSW. The pore regions of the Moiré lattice exhibit the smallest adsorbtion height, while the wire regions are further separated from the metal support [123]. Picture taken from [123].*

Moiré like superstructure. As indicated in Figure 2.15 the pore regions of the Moiré exhibit the smallest adsorption height, while the wire regions are further separated from the Cu(111) [123]. So far superstructured h-BN/metal supports have been used to steer the adsorption positions of molecular adsorbates and to modify the orbital energy of molecules [27, 126–131].

2.9 Graphene growth

2.9.1 Growth of graphene on Cu(111) and Ag(111)

Graphene is an fascinating two dimensional material consisting of hexagonal packed carbon atoms [132–134], revealing unique properties [34, 135–142], which are opening up huge potentials for future nano technology [143–147].

Graphene can be grown on a large variety of metals such as Ni [148, 149], Ir [150], Ru [151], Pd [152], Cu [40, 153], etc [153, 154]. The most established method for large scale preparation of graphene layers on metals is the surface catalyzed growth of graphene from hydrocarbons such as methane and ethylene, via the so-called chemical vapor deposition (CVD) method [153]. Furthermore, a variety of other precursors can be used for the preparation of graphene, e.g. from cookies to legs of cockroaches [155, 156].

Copper surfaces have been shown to be suitable supports for the growth of graphene [153] and, in addition, the low cost of copper foils make them a very promising candidate for the growth of graphene for industrial purposes.

Due to the rather low affinity of copper and carbon [157–159] weakly bond copper carbon intermediates can be formed [160, 161], leading to an efficient catalytic growth of graphene. In

combination with the low carbon solubility of copper [157], a self-limiting growth of single layer graphene has been demonstrated [162–170].
However, for CVD grown graphene/Cu(111) a high density of domain boundaries, which can limit the carrier mobility was reported [163].
As the activation of the CVD growth process depends on the thermal energy and the catalytic properties of the metal surface, there is a limited pool of possible substrates for efficient CVD growth. However, for supports, which are initially not suitable for CVD growth of graphene, additional growth methods have been reported. (i) The disintegration of the precursor molecules can be enhanced by the accelaration of charged ethylene fragments via ion irradiation using a sputter gun [171]. Using ion irradiation, graphene can be grown on a Au(111) substrate with relatively low reactivity [171]. (ii) Another route for low temperature growth is based on the usage of atomic carbon, which is deposited onto the metal surface [172–175].
In this chapter, different methods for the high quality growth of graphene on Cu(111) and Ag(111) are described in detail. In the following, we refer to high quality graphene for graphene with high structural quality on a local scale.
For Ag(111) the low catalytic activity requires growth temperatures in conventional CVD approaches above the melting point of silver. Therefore we used two alternative methods: (i) An irradiation assisted CVD growth from C_2H_4 and (ii) the growth of graphene from an atomic carbon source. The atomic carbon was deposited from a purified carbon rod, which was heated by an electron beam.
For the high quality growth of graphene on Cu(111) at moderate temperatures we used the same atomic carbon source. Additionally, we grew graphene on Cu(111) from C_2H_4 precursor molecules without additional irradiation, at temperatures close to the melting temperature of copper [176].

2.9.2 Atomic carbon deposition by an electron beam (e-beam) evaporator

Design of e-beam evaporator During this thesis, we designed an e-beam evaporator with a maximum heating power of 600 W, sufficient to evaporate atomic carbon from a purified carbon rod. The commercially available e-beam evaporator with its heating power of 100 W was not capable of generating a sufficiently high atomic carbon flux. In Figure 2.16 the design of the home-built evaporator is presented. Figure 2.16 (a) shows the evaporator head, which is made of stainless steel. The evaporator head consists of a metallic cover with an circular opening that controls the direction and spread of the carbon flux. This opening can be closed and opened via a mechanical shutter. The interior of the evaporator head is depicted in Figure 2.16 (b). The head plate has a central circular opening where the carbon rod is fed through. It is crucial that the carbon does not touch the conducting plate as a contact would cause an electric shortcut. The filament holders sit on the head plate and are isolated from the plate by ceramics. The thoriated tungsten filament (tungsten/thorium = 99/1, diameter = 0.125 mm) is spot-welded to the filament holders and circles around the carbon rod. The diameter of the circle was usually

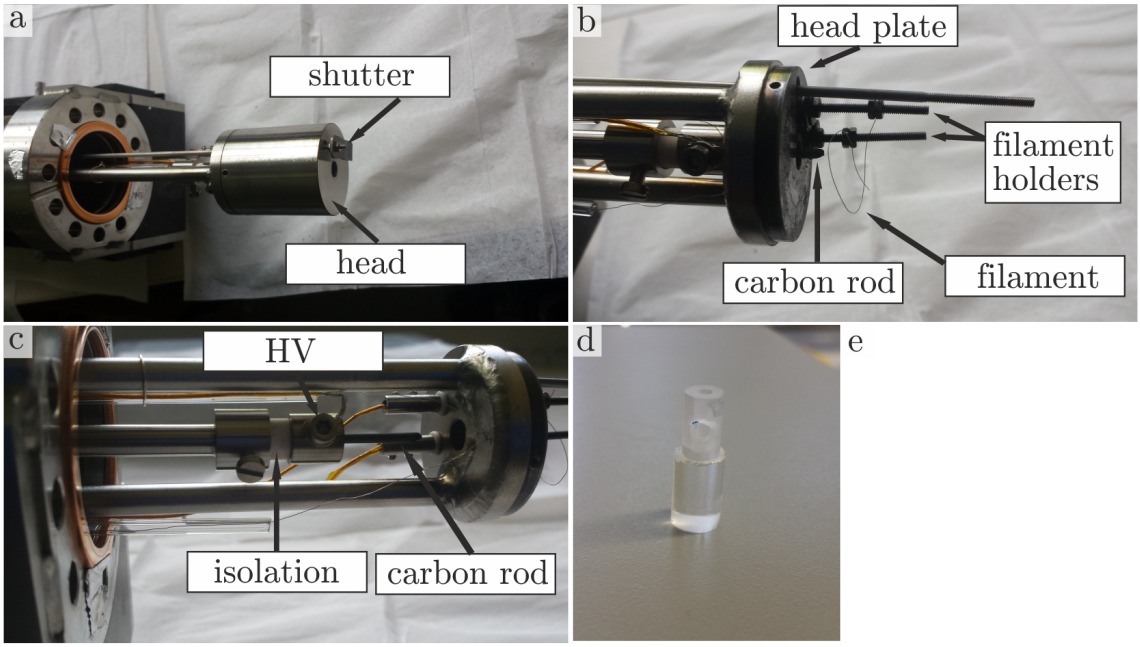

Figure 2.16: *Design of electron beam evaporator for atomic carbon deposition. (**a**) E-beam head protected by metallic cover to direct the carbon flux. The mechanical shutter is used for a defined duration of the carbon dosage. The flange is CF40 for scaling purposes. (**b**) Interior of e-beam head with two isolated filament holders, a circular bent thoriated tungsten filament, and a carbon rod. The carbon rod is fed through a circular opening in the head plate without contacting the plate. (**c**) High voltage (HV) contact to the carbon rod, isolation and filament contacts. (**d**) Enlarged image of electrical isolation of the HV.*

about 2 cm and the height difference of the two spot-welded positions on the filament holders was about 5 mm.

Cooling water is conducted through two stainless steel tubes and a milled channel at the bottom of the head plate. For the atomic carbon source we used a purified carbon rod with dimensions of 2 mm $\times$ 100 mm and an impurity density of $<$ 20 ppm ash residues, purchased from MaTecK GmbH [177]. A high voltage (HV) contact to the carbon rod is realized by a screw, which is pressed against the carbon rod as shown in Figure 2.16 (c).

The HV is isolated from the rest of the evaporator by insulating glass or bulk boron nitride. The isolation component is shown in Figure 2.16 (c) and enlarged in Figure 2.16 (d).

To generate a suitable carbon flux, a current of $I_{filament} = 1.5 - 2.0$ A and a voltage of $V_{filament} = 2 - 3$ V are applied to the filament and electrons are emitted, which are accelerated towards the carbon rod. The applied acceleration voltage was typically $V_{HV} = 1500$ V. The obtained emission current between filament and carbon rod was $I_{emission} = 100 - 130$ mA and the corresponding heating power around $150 - 180$ W. For reproducibility of the carbon flux we regulated $I_{emission}$ by adjusting $I_{filament}$, while keeping the applied HV constant. Doing that, $I_{emission}$ is directly related to the heating power. The emission current can be adjusted by increasing/decreasing the filament heating and the position of the carbon rod, which can be changed by a mechanical manipulator.

The relatively high heating power is needed as the solid carbon rod has to reach temperatures above 2270 K to generate a relevant carbon flux [175, 178]. The HV source provides a maximum voltage of $V_{HV} = 1500$ V, is limited to a power of $P_{HV} = 600$ W and was purchased from Matsusada [179].

Growth of graphene on Ag(111) and Cu(111) from e-beam carbon source For the growth of graphene on Ag(111) and Cu(111) we used the e-beam evaporator described above with comparable parameters. The sample is positioned at a distance of ~ 30 cm from the e-beam head, the carbon rod is heated with a power of $P = 150 - 180$ W, and the shutter is opened for $t = 180$ s. Longer carbon deposition times were avoided, as due to the high heating power the pressure in the preparation chamber was increasing with time, potentially contaminating the sample. During the deposition the sample is held at a constant temperature of $T_{Ag} = 900$ K for Ag(111) and $T_{Cu} = 1020$ K for Cu(111). Subsequent to the carbon deposition the samples are held at the growth temperature for additional five minutes.

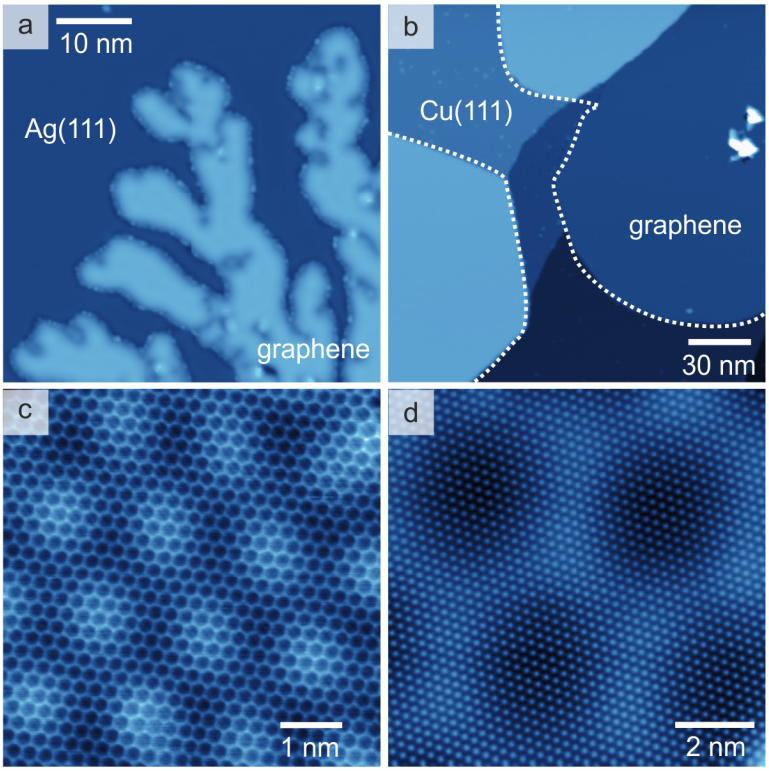

Figure 2.17: *Graphene grown from atomic carbon source (e-beam). (a) STM image of high quality graphene on Ag(111) exhibiting dendritic shaped islands ($V_S = 0.3$ V, $I = 300$ pA). (b) STM image of large islands with high quality graphene on Cu(111) ($V_S = 1$ V, $I = 100$ pA). The white dashed lines highlight the graphene islands. Protrusions are found within the islands. In both cases the graphene is limited to one layer. (c) Atomically resolved STM image of high quality graphene on Ag(111) ($V_S = 2.5$ V, $I = 50$ pA). (d) Constant height AFM image of atomically resolved graphene on Cu(111), proving the low defect density ($V_S = 0$ V).*

Scanning probe measurements of the graphene resulting from the solid carbon deposition growth are presented in Figure 2.17.
Figure 2.17 (a) depicts the graphene grown on Ag(111). The graphene islands exhibit a characteristic dendritic shape and the coverage of the graphene reaches around 70%. Bright dots are observed at the edges of the islands.
In comparison, graphene on Cu(111) (Figure 2.17 (b)) reveals more extended islands, exceeding 10000 nm^2 in size and exhibiting less ridged edges. In the Cu(111) case, we obtained graphene coverages up to 90 %. The graphene appears flat, with exception of some protrusions within the islands (see Figure 2.17 (b)).
In both cases, we grew high quality graphene, which was evidenced by atomic resolved STM and AFM measurements. Figure 2.17 (c), (d) depict atomically resolved graphene on Ag(111) and Cu(111) respectively, proving the low impurity density of graphene. From our measurements we conclude that the observed graphene islands on Ag(111) and Cu(111) are limited to one layer, as we observed uniform step heights for all graphene islands.

Growth of graphene on Ag(111) from a resistively heated carbon filament Another experimental approach to deposit atomic carbon is to use a resistively heated carbon source [175]. Compared to the e-beam case, for a resistively heated filament we could omit the HV, relaxing the safety constraints. Thus we designed the atomic carbon evaporator presented in Figure 2.18 (a). The evaporator consists of two copper bars where one of the bars is connected to the chamber ground and the second bar to a power supply. The carbon filament is fixed with screws and washers on top of the bars. For the atomic carbon deposition, the filament is heated by a power of ≈ 110 W ($I_{Filament} = 9.5$ A, $V_{Filament} = 11.7$ V) for 90 seconds and the sample is subsequently kept at the growth temperature of $T_{Ag} = 900$ K for additional five minutes.

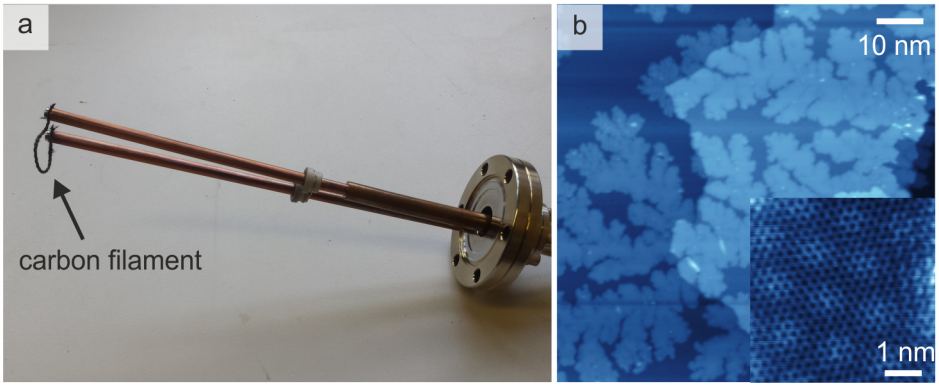

Figure 2.18: *Graphene grown from atomic carbon source (carbon filament). (a) Photograph of resistively heated atomic carbon source. A current is conducted through the carbon filament. At high temperature atomic carbon is evaporated from the filament. The depicted flange size is CF40. (b) STM image of graphene grown on Ag(111) with dendritic shaped islands ($V_S = 1$ V, $I = 200$ pA). The inset shows an atomically resolved STM image of the graphene, proving a low defect density of the obtained layer ($V_S = 0.2$ V, $I = 212$ pA).*

The resulting graphene structure is shown in the STM image displayed in Figure 2.18 (b), revealing dendritic shaped islands and a coverage exceeding 50%. Again the growth is limited to one layer and high quality graphene is obtained (see inset in Figure 2.18 (b)). However, we did not manage to control the carbon flux via the applied power in a reproducible way and consequently the filament frequently burned through. As a consequence a micro balance would be necessary to achieve better carbon flux control. Nevertheless, we obtained high quality graphene grown on a noble metal at low temperatures.

2.9.3 CVD growth of graphene on Cu(111) and Ag(111)

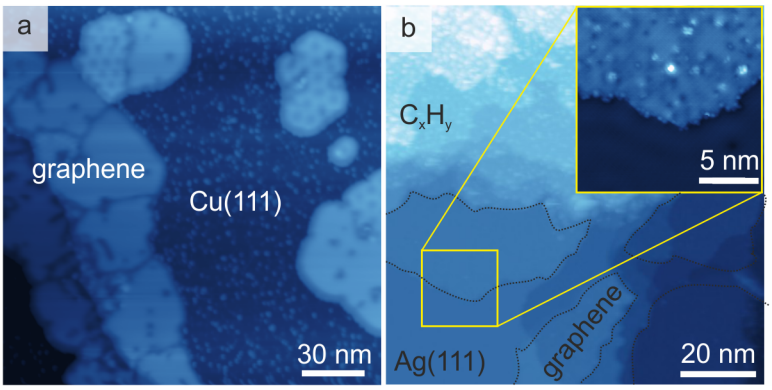

Figure 2.19: *Graphene grown from ethylene (C_2H_4) via CVD on Cu(111) and Ag(111). (a) STM image of graphene on Cu(111) shows several graphene islands merged to a coverage of ≈ 40% ($V_S = 4.0$ V, $I = 200$ pA). Islands with different Moiré periodicities and islands without resolved Moiré patterns are found. (b) STM image of sputter gun assisted CVD grown graphene on Ag(111). Large strongly corrugated region, which we assign to areas with not dissociated C_2H_4. Graphene areas are framed by black dashed lines as a guide to the eye ($V_S = 1.0$ V, $I = 200$ pA). The inset is an enlarged image of the graphene island marked in (b) ($V_S = 0.08$ V, $I = 200$ pA). The obtained graphene has a high density of defects. STM image is published in [117].*

Many studies report the growth of graphene from precursors like methane [40, 43, 180, 181] and ethylene [163, 182, 183] on a copper substrate. The typical temperatures for the graphene growth in these publications exceed 1250 K and therefore work fine for polycrystalline copper, but these growth temperatures are not accessible for crystalline Cu(111) or Ag(111). The transition from a highly crystalline metal to its amorphous counterpart occurs at roughly 75 % of its respective melting point and therefore sets an upper temperature limit of ∼ 1020 K for Cu(111) and ∼ 920 K for Ag(111) [184]. Consequently, we attempted a CVD growth at the highest accessible temperature for our Cu(111) sample and a sputter gun assisted approach for the Ag(111) sample. Gao et al. [163] achieved high coverage graphene grown by CVD on a crystalline Cu(111) surface by running several cycles of annealing and cooling down while keeping a constant supply of ethylene. They claim that only the ethylene adsorbed at low temperatures participates in the growth process. We followed the recipe given in [163] using a pressure of $p_{C_2H_4} = 1.5 \times 10^{-4}$ mbar during the growth process and a maximum sample temperature of $T_{Cu} = 1020$ K. The temperature is ramped up and kept at its maximum for 5 minutes. Sub-

sequently, the sample is cooled down to room temperature. This heating/cooling procedure is repeated 6 times and after the last cycle the sample is kept at $T_{Cu} = 1020$ K for additional five minutes after the ethylene supply is stopped. The ethylene adsorbed on the surface is thermally dissociated at high temperatures and graphene growth is induced. The Cu(111) surface activates the dissociation process and therefore the graphene growth is limited to one layer. Figure 2.19 (a) depicts an STM image of the resulting graphene on Cu(111). The graphene layer consists of many small patches merged together, where each patch does not exceed a size of 20 nm × 20 nm. Some islands appear flat, while others reveal different Moiré patterns with periodicities ranging from 2 nm to 7 nm. The obtained coverage is about 40%, and the residual Cu(111) surface is covered with impurities.
However, the applied recipe for graphene growth on Cu(111) is not transferable to an Ag(111) crystal. The lower melting point and the lower chemical activity of Ag(111) inhibit an efficient dissociation of the C_2H_4 precursor. Therefore we adopted the irradiation assisted method described in [171] for Au(111), for the growth of graphene on Ag(111). In this approach the sputter gun is activated and accelerates ionized precursor molecules towards the sample. The additional available kinetic energy of the ethylene increases the dissociation on the surface. For the growth we kept the sample temperature at $T_{Ag} = 900$ K and dosed C_2H_4 at a pressure of $p_{C_2H_4} = 10^{-4}$ mbar for 15 minutes. The sputter gun runs at an acceleration voltage of $V_{acc} = 300$ V and an emission current $I_{emission} = 4$ μA was collected at the sample. The ethylene supply and the sputter gun are stopped simultaneously and the sample is kept at $T_{Ag} = 910$ K for five more minutes. The resulting graphene/Ag(111) sample is shown in Figure 2.19 (b). We obtain three distinct regions: (i) A strongly corrugated region labeled with C_xH_y, which we assign to an area covered with not completely dissociated ethylene molecules. (ii) A region, revealing flat areas of Ag(111) (labeled Ag(111)), and (iii) a region of Ag(111) covered by a single layer of graphene (labeled graphene). The graphene regions are framed by dashed black lines as a guide to the eye. In the inset, the area marked in yellow in Figure 2.19 (b) is enlarged, depicting a graphene island edge. The observed graphene reveals a high defect density and thus appears corrugated. While the coverage of the single layer graphene is around 15%, the predominent area of the sample is the strongly corrugated region covered by fragments of ethylene.

Discussion We conducted different approaches for the growth of graphene on Cu(111) and Ag(111). The atomic carbon deposition method outperforms the CVD growth method, as we obtained higher graphene coverages and essentially larger islands with uniform orientation. Furthermore, by using atomic carbon we could reduce the activation temperature to enable the graphene growth even on Ag(111). Compared to the heated filament based method, the e-beam method reveals superior properties in terms of stability and reproducibility. Therefore, we conclude that the best results for our purposes are obtained by the e-beam heated solid carbon source.

3 Intercalation of porphines

Parts of this Chapter are taken from the following publication:

3.1 Introduction

A promising approach for the fabrication of tailored materials with well-defined physical and chemical properties at the nanoscale, is the synthesis of hybrid materials by combination of different materials classes, such as two-dimensional layered materials and organic molecular materials. Van der Waals (vdW) heterostructures have attracted much attention in materials science and engineering offering a wide scope of possible applications ranging from high temperature superconductors to highly efficient field effect tunneling transistors [115, 185]. *h*-BN is one of the prominent building blocks for such applications due to its insulating behavior, high thermal conductivity, chemical and thermal stability [186–188]. These properties afford application of *h*-BN as a dielectric spacing layer for transistors or as a protective capping layer [115, 186, 187]. Intercalation of atoms and small molecules has already been investigated for *h*-BN [189, 190] and other two-dimensional materials such as graphene [191, 192], as well as for layered materials [193, 194], very often in the context of electrochemical electrode reactions in batteries [195]. Intercalation is used to modify the properties of two-dimensional layers and to fabricate heterostructures that are not accessible via conventional delamination and transfer processes of two-dimensional materials [196–203]. Furthermore, reactions of small intercalated molecules (such as CO and ethylene) have been puplished [204–206]. To date, only very few studies exists that can image intercalated molecular entities (such as C60 underneath graphene [197, 198, 200]). However, none of these studies investigates the intercalation of functional molecules and their intrinsic properties. For such purposes, porphyrins are a particularly interesting class of organic molecules, which have attracted much attention due to their broad occurrence in biological systems [207] such as chlorophyll and hemoglobin and their potential application for solar energy harvesting and organic electronics [208, 209]. By the modification of their cores or their programmable substituents the physicochemical behavior of the porphyrins can be changed [30]. Here we show the fabrication of functional layered architectures through the intercalation of molecules. We used unsubstituted porphyrins (porphines), which we inter-

calated at the h-BN/Cu(111) interface. We investigated the modification of the collective (i.e. self-assembly) and intrinsic (i.e. tautomerization) properties of the porphines upon intercalation. The system was characterized in real space using scanning probe microscopy, exhibiting submolecular resolution. While nc-AFM gives access to the structural information of the capping h-BN layer, STM allows imaging and manipulating the intercalated molecules as the h-BN layer is electronically transparent. The intercalated molecules order in a close-packed arrangement upon intercalation under the capping h-BN layer. However, the tautomerization process of the intercalated molecules can be triggered electronically by the STM tip, showing that this intrinsic property is not diminished by the h-BN. Supported by density functional theory (DFT) calculations, our experiments elucidate the energetics of the intercalation process. As intercalation and self-assembly of intercalated molecules can be triggered at relatively low temperatures, this synthesis procedure is a promising route for large scale bottom-up fabrication of protected functional nano architectures and provides alternative synthesis protocols towards vertically stacked layered materials.

3.2 Scanning probe measurements of intercalated porphines

3.2.1 Intercalated islands

We deposited free-base porphines (2H-P, left structure in Figure 3.1 (a)) on a high coverage h-BN/Cu(111) sample, kept at $T_{sample} = 420$ K. We observe three different appearances of the obtained molecular assemblies as shown in Figure 3.1 (b) and (c). The brightest molecular units in Figure 3.1 (b) ($V_S = 0.56$ V) with apparent heights of 0.09 nm correspond to 2H-Ps adsorbed on the h-BN layer. These molecules accumulate at defects such as grain boundaries or wrinkles of the h-BN. Furthermore, in the vicinity of the triangular openings in the h-BN layer (marked by the red arrows in Figure 3.1 (b)) we observe extended molecular islands. We assign these islands (highlighted in yellow) to islands of intercalated molecules, which exhibit an apparent height of 0.04 nm. The intercalated molecules are sandwiched between the Cu(111) surface and the overlying h-BN, as is shown below. Such triangular holes give rise to exposed Cu(111) surfaces that are covered with molecules. Larger exposed Cu(111) areas can be seen for samples with lower h-BN coverage. For such low coverage samples, we observed three distinguishable regions (Figure 3.1 (c) ($V_S = 0.34$ V)): (i) A region with pristine h-BN on Cu(111) (labeled „h-BN on Cu(111)“). (ii) A region where the exposed Cu(111) surface is covered with molecules (labeled „Co-Ps on Cu(111)“). The molecules reveal an average neighbor distance of 1.27 ± 0.05 nm and are arranged in an irregular array. The molecules exhibit bright protrusions in their centers in contrast to the typical central depression reported for 2H-Ps [211]. As self-metalation of porphyrins typically occurs already for temperature beneath our preparation temperatures of 470 K, we assign these molecules to Cu-Ps (right structure in Figure 3.1 (a)) [212–214]. We observed additional bright species in this region, which are individual molecules adsorbed on the first

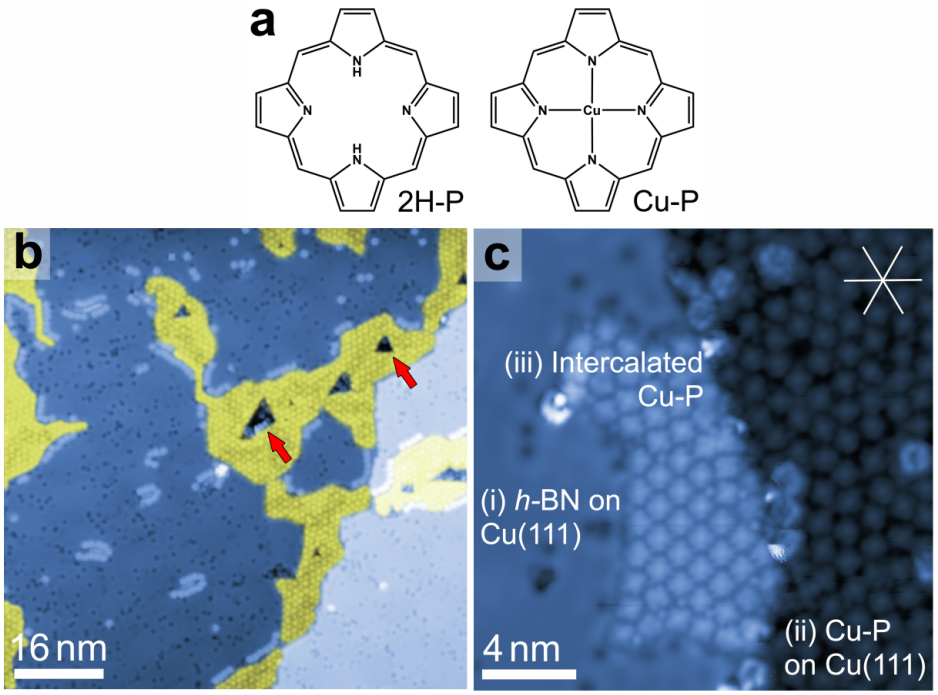

Figure 3.1: *STM measurements of intercalated porphines at the h-BN/Cu(111) interface. The samples were prepared by deposition of 2H-P onto h-BN/Cu(111) at 470 K.* ***(a)*** *Structural models of free-base porphine (2H-P) and copper porphine (Cu-P).* ***(b)*** *Overview STM image of high coverage h-BN on Cu(111). We identify intercalated prophines (highlighted in yellow), which appear in the vicinity of triangular openings in the h-BN layer (red arrows). Furthermore some molecules are adsorbed on the bare h-BN areas ($V_S = 0.56$ V, $I = 77$ pA).* ***(b)*** *STM topograph of intercalated molecules at sub-monolayer h-BN coverage exhibiting three distinct regions: (i) pristine h-BN/Cu(111), (ii) self-metalated porphines on the metal Cu(111) substrate, and (iii) intercalated Cu-Ps ($V_S = 0.34$ V, $I = 330$ pA). The Figure is reprinted from [210].*

Cu-P layer. (iii) A region where the molecular units self-assemble into a two-dimensional lattice (labeled „Intercalated Cu-Ps“) with a nearest neighbor (NN)-distance of 11.1 ± 0.05 nm. From our STM measurements we derive a superstructure of the intercalated molecule with respect to the Cu(111) support, described by the $\begin{pmatrix} 5 & 3 \\ 2 & -3 \end{pmatrix}$ matrix. The porphine axis along opposite nitrogen atoms in the molecular center is minutely aligned with the high symmetry direction of the metal support (compare calculated models in Figure 3.7). Within the intercalated islands we observe brighter and darker regions as illustrated in Figure 3.2. The brighter region in Figure 3.2 (a) exhibits a highly ordered arrangement with (NN)-distances of 1.11 ± 0.05 nm, whereas the molecules in the darker region reveal (NN)-distances of 1.28 ± 0.05 nm. The molecules with larger (NN)-distances are separated by additional adatoms and small molecules, which are highlighted by the white dashed circles. Small impurities can intercalated the *h*-BN without causing relevant geometric distortions [199], and might lower the delamination energy during the intercalation process. Such regions with higher impurity density are more frequently observed for samples with higher *h*-BN coverage. However the obtained apparent corrugation of the brighter

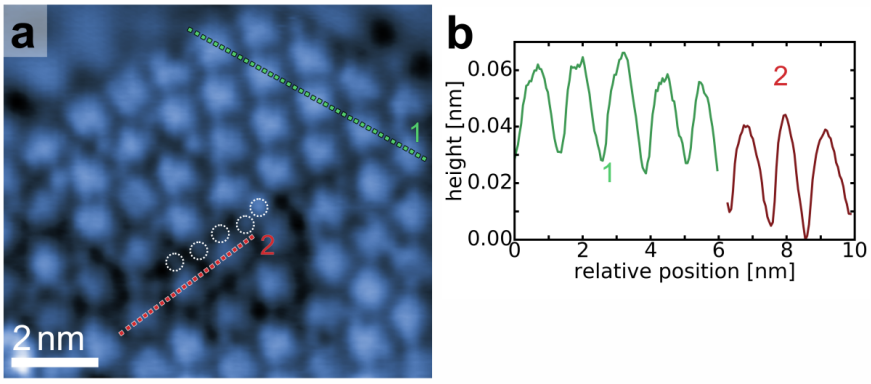

Figure 3.2: *STM image of intercalated Cu-Ps (V_S = 0.2 V, I = 800 pA).* ***(a)*** *Ordered molecules are imaged brighter and show nicely ordered arrangement with (NN)-distances of* 1.11 ± 0.05 nm. *Darker regions in (a) correspond to molecular islands, where the intercalated porphines are further separated due to impurities such as adatoms and small molecules (highlighted by the white dashed circles). Small impurities can intercalate the h-BN without causing relevant geometric distortions [199]. The (NN)-distance found for the darker region is* 1.28 ± 0.05 nm. *However the apparent corrugation within the darker and the brighter areas with* $\Delta h \sim 0.03$ nm *is very similar as shown by the height profiles in* ***(b)****. The green graph corresponds to the green dashed line in (a) in the brighter area, the red graph to the red dashed line. The Figure is reprinted from [210].*

and darker areas are very similar. The green graph in Figure 3.2 (b) shows a height profile along the green dashed line in Figure 3.2 (a) in the brighter area of the intercalated island. Similarly the red graph corresponds to the darker region in Figure 3.2 (a). The obtained apparent corrugation of 0.03 nm for both regions of the intercalated island are considerably smaller than the 0.08 nm found for Cu-Ps on Cu(111) and than 0.09 nm for 2H-Ps on pristine h-BN.

3.2.2 AFM experiment - direct proof of intercalated molecules

Combined STM/nc-AFM experiments reveal that the self-assembled molecular islands are intercalated between the Cu(111) surface and the h-BN capping layer. Figure 3.3 (a) presents a STM image of an intercalated island, located at the top left and an h-BN on Cu(111) region at the bottom right of the image. The circular feature in Figure 3.3 (a) correspond to ordered intercalated porphines. To transfer the exact molecule position from Figure 3.3 (a) to Figure 3.3 (b)-(d), we marked four Cu-P centers in Figure 3.3 (a) by the yellow dots. After a sample drift correction the molecular positions (i. e. local height maxima) are plotted in Figure 3.3 (b)-(d). In Figure 3.3 (b) a constant height AFM image of the same area is depicted, revealing atomic resolution with an lattice constant of $a_{h-BN} = 0.250$ nm [215] of the h-BN layer on the intercalated molecules in the Δf-signal. This observation gives direct proof that the molecules are located beneath the h-BN layer. We found an additional modification of the frequency shift at the nanometers length scale up to $\Delta f = 4$ Hz.
In contrast, we do not observe atomic contrast in the h-BN/Cu(111) region, as the tip-sample distance is substantially larger. The larger tip-sample separation causes an increase in Δf as the attractive vdW interaction is lowered, leading to the white imaged region in Figure 3.3 (b).

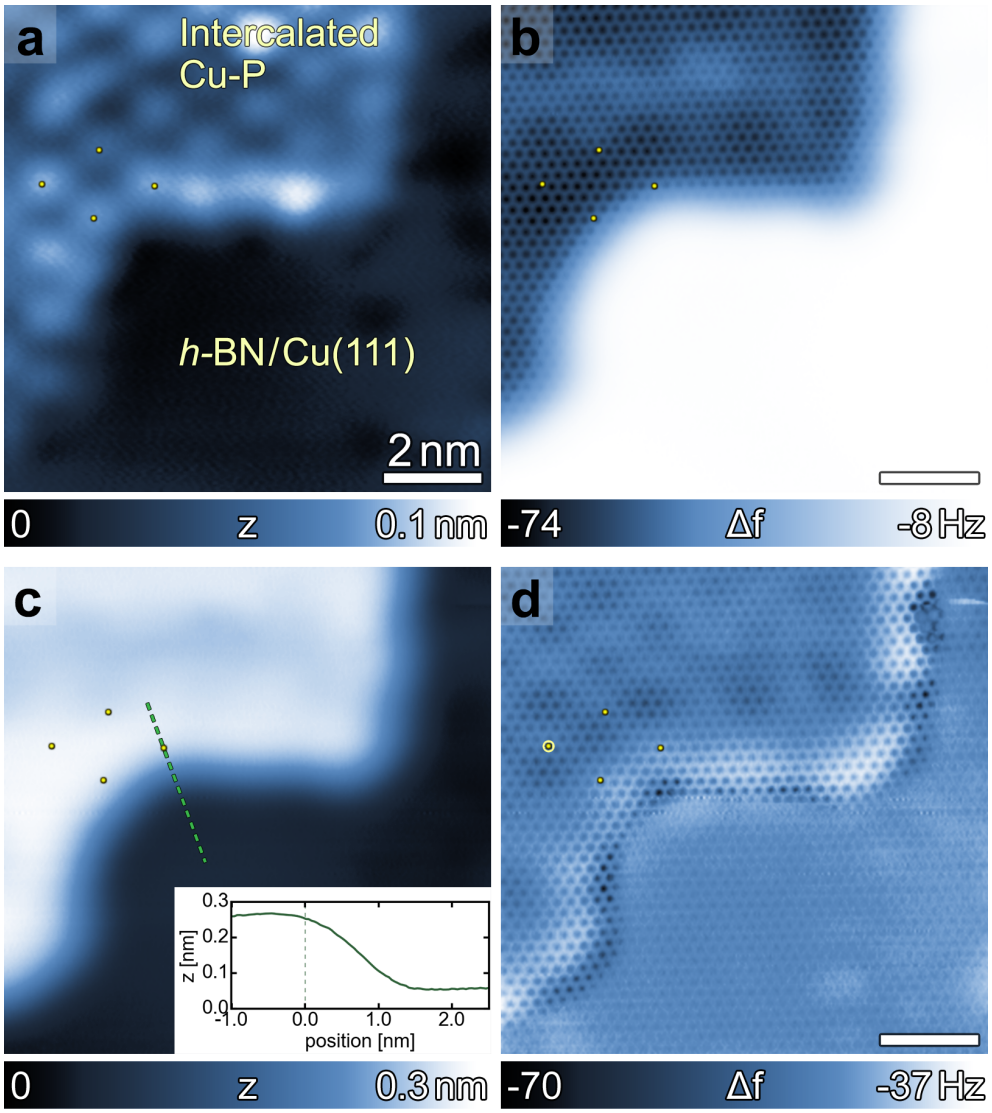

Figure 3.3: *High-resolution STM/nc-AFM experiments of intercalated molecules.* ***(a)*** *h-BN/Cu-P/Cu(111) system measured in constant-current STM mode ($V_S = 1$ V, $I = 15$ pA). The intercalated molecules order in a regular arrangement. The four yellow dots mark the position of molecular centers. Flat h-BN/Cu(111) is found in the bottom right.* ***(b)*** *Constant-height AFM measurement of the same region imaged in* ***(a)****, reveals atomic resolution of the h-BN lattice of the h-BN/Cu-P/Cu(111) system ($V_S = 0$ V).* ***(c)*** *Constant-Δf AFM measurement ($V_S = 0$ V, $\Delta f = 20$ Hz) of the same area. We observe an apparent height difference between h-BN/Cu-P/Cu(111) and h-BN/Cu(111) of $\Delta h_{h-BN} = 0.21$ nm. The inset depicts a height profile following the dashed green line in (c) where we define the position $x = 0$ nm to the center of the Cu-P.* ***(d)*** *Two-pass AFM image resolves the h-BN lattice in the h-BN/Cu(111) and the h-BN/Cu-P/Cu(111) region. The tip follows the height profile from (c) with an additional height offset of -0.090 nm towards the surface. The Figure is reprinted from [210].*

We executed a constant-Δf AFM measurement to determine the lifting up of the h-BN layer upon intercalation, as shown in Figure 3.3 (c). The Δf-feedback was set to $\Delta f = -20$ Hz while the applied voltage was $V_S = 0$ V. Additionally, we measured the height of an intercalated

island for different applied biases to confirm the negligible influence of the bias in the investigated voltage range as shown in Figure 3.5. The inset in Figure 3.3 (c) shows the height profile along the green dashed line in Figure 3.3 (c). Taking several islands into consideration, we obtain an average island height of $\Delta_{h-BN} = 0.21 \pm 0.02$ nm between h-BN/Cu(111)/Cu(111) and h-BN/Cu(111). Conducting a two-pass AFM measurement [90] we obtain an atomically resolved h-BN layer over the whole imaged area. In the two-pass experiment the tip follows the height trace measured in Figure 3.3 (c) while the tip is approached by -0.090 nm to the surface. The obtained Δf signal is imaged in Figure 3.3 (d). While the h-BN lattice is resolved across the whole range of the image, the Δf contrast is reduced on the lower terrace, i.e. the pristine h-BN/Cu(111). Also, a strong change of the Δf contrast is observed at the areas near the edges. This change is caused by tip convolution effects (as seen in the height profile inset in Figure 3.3 (c)), i.e. the tip-sample distance is already decreased on top of the molecular islands leading to higher contrast in the second-pass Δf image. Analogously, the lower terrace areas near the edge exhibit decreased contrast. A distortion of the h-BN lattice in Figure 3.3 (d) can be seen especially across the vertical edges: the h-BN lattice directions can deviate by a few degrees with respect to the directions on both terraces. This distortion results in a vertical translation shift of the h-BN lattice of up to half of a lattice constant. We did not observe a relevant modification in the lattice direction of h-BN/Cu-P/Cu(111) and h-BN/Cu(111) in the areas further away from the edges.

3.2.3 Additional investigation of the intercalated islands height

Figure 3.4 depicts eight height profile from the intercalated islands to the bare h-BN, crossing a molecular center. The tip lowers by $\Delta h_{h-BN}/2$ within a distance of $d = 0.7 \pm 0.015$ nm starting

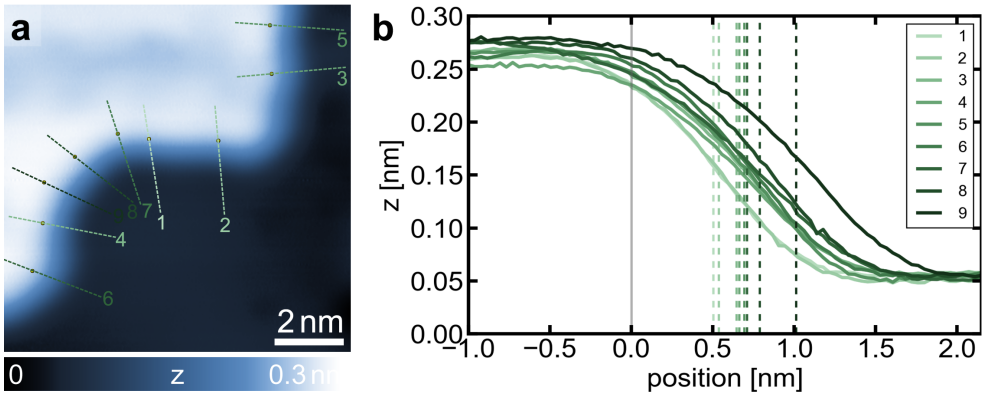

Figure 3.4: *Constant-Δf experiment of intercalated island ($\Delta f = -20$ Hz, $V_S = 0$ V). We evaluate a height difference between h-BN/Cu(111)/Cu(111) and h-BN/Cu(111) of $\Delta_{h-BN} = 0.21 \pm 0.02$ nm by averaging over the eight plotted lines in (a). The yellow dots define the location of the Cu-P center. (b) Height profiles along the dashed lines in (a). $x = 0$ on the x-axis defines the position of the Cu-P center. The vertical lines are set to the position where the tip is lowered by $\frac{\Delta_{h-BN}}{2}$. The Figure is reprinted from [210].*

from the Cu-Ps center of the molecules located closest to the island edge. However, as can be seen in the line scans a small decrease of the measured h-BN height was observed even directly above the centers of the edge molecules. This is caused by the finite radius of the tip apex, which leads to a smeared out line profile, i.e. the tip does not perfectly trace the height of the h-BN layer. Figure 3.5 presents bias dependent experiments to determine the height of the intercalated islands. Figure 3.5 (a)-(c) depict a intercalated island on the right top and pristine h-BN on the left bottom. In Figure 3.5 (d)-(f) height profiles along the yellow lines in Figure 3.5 (a)-(c) are presented. Three curves are shown for the diagonal (solid), horizontal (dashed), and vertical (dotted) direction in Figure 3.5 (a)-(c).

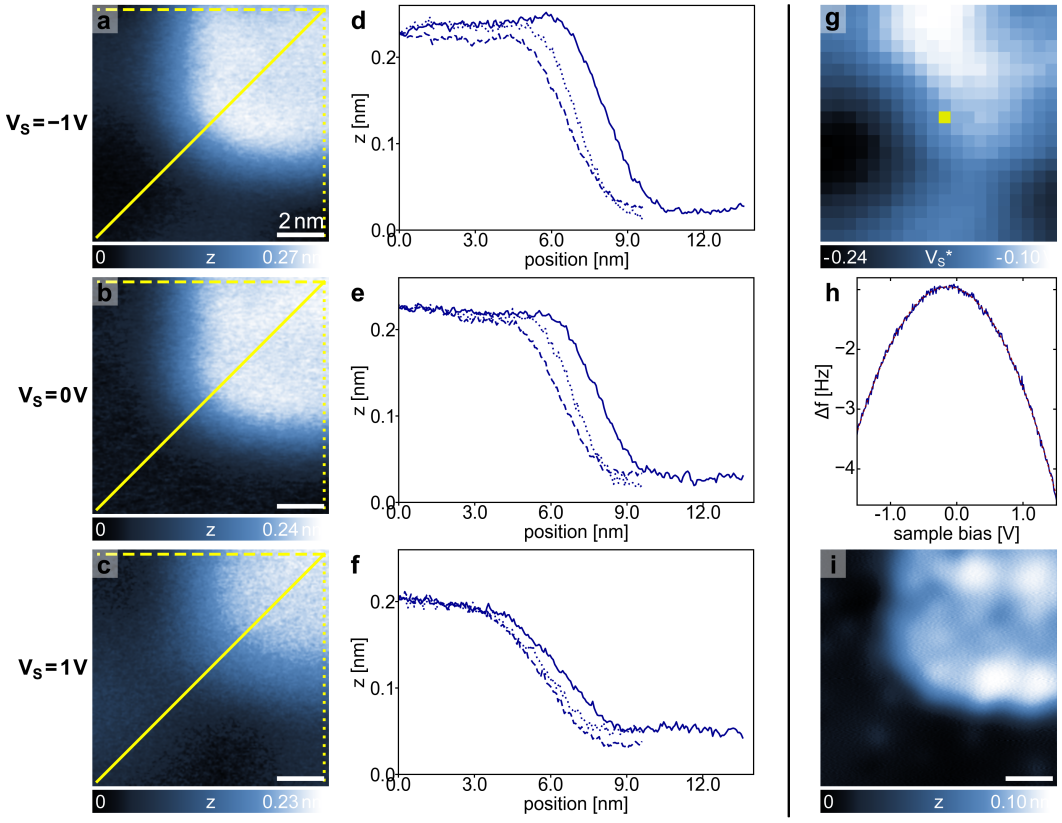

Figure 3.5: *Height determination of intercalated islands by constant-Δf measurements at different biases.* ***(a)*** *$\Delta f = -1.2$ Hz, $V_S = -1$ V,* ***(b)*** *$\Delta f = -0.4$ Hz, $V_S = 0$ V,* ***(c)*** *$\Delta f = -2$ Hz, $V_S = 1$ V.* ***(d)-(f)*** *Height profiles along the yellow plotted lines in (a)-(c). The dashed, solid and dotted curves correspond to the horizontal (dashed), the diagonal (solid), and the vertical (dotted) directions in the images (a)-(c). The curves in (d)-(f) evidence only small influence of the bias on the evaluated island height in the regarded voltage range.* ***(g)*** *Kelvin probe spectra maxima (V_S^*) map ($\Delta f = 1$ Hz, $V_S = 0.1$ V) [216–218]. We measured a 20×20 grid of Δf vs. V_S spectra over the region shown in (a)-(c). A typical spectrum taken at the yellow dot in (g) is depicted in (h). The blue line represents the measured data and the red dashed line corresponds to a parabolic fit. V_S^* is determined by the maxima of this parabolic fit for each pixel and imaged in (g). We can clearly observe the intercalated island in the V_S^* map. We identify an additional modification of V_S^* on the h-BN/Cu(111), which we assign to the Moiré corrugation of the h-BN.* ***(i)*** *STM topograph of same area measured at $V_S = 2.0$ V, $I = 15$ pA. The Figure is reprinted from [210].*

We observe only small deviations in the island height for different biases. Figure 3.5 (g) shows a Kelvin probe spectra maxima (V_S^*) map, where V_S^* is determined for each of the 20×20 pixels. V_S^* defines the contact potential difference between the tip and the sample. At an applied bias of V_S^* the electrostatic contributions in the Δf signal, arising from work function differences between tip and sample, are minimized. Therefore we measured Δf vs. V_S spectra, which exhibit a typical parabolic signature as shown in Figure 3.5 (g). This spectra was taken at the position of the yellow colored point in Figure 3.5 (g). The data is colored in blue and the red line is the corresponding parabolic fit. In the obtained V_S^* map we identify the intercalated island area and additional a corrugation of V_S^* in the pristine h-BN region. The maximum deviation of V_S^*, which corresponds to the work function differences $\Delta\Phi$ between different positions in Figure 3.5 (g) is $\Delta\Phi \sim 0.14$ V. The highest V_S^* is found at the region of the intercalated molecules. In the lower area of Figure 3.5 (g) the Moiré pattern of the h-BN is observable. Here, $\Delta\Phi$ between a Moiré pore and a wire regions is quantified to $\Delta\Phi \sim 0.08$ V. This value is evidently smaller than the $\Delta\Phi$ found on h-BN/Cu(111) via FER experiment with $\Delta\Phi \sim 0.25$ V [123]. We assign the smaller $\Delta\Phi$ deduced from the Kelvin probe experiments to a stronger spacial averaging in the AFM signal, compared to the FER measurements reported in [123].
As shown in Figure 3.5 (h) such small differences in the contact potential do not lead to relevant changes in the Δf signal. Therefore we conclude that our measurements of the intercalated island height give reasonable results for our specific investigated system and applied voltage range. In summary, this combination of nc-AFM and STM measurements give direct evidence for the intercalation of molecules.

3.2.4 Electronic structure of Co-porphines

We performed dI/dV spectroscopy to visualize the effect of the different adsorption positions on the electronic properties of the porphines. Therefore we used cobalt porphines (Co-P). The structure of Co-Ps is very similar to the structure of a Cu-Ps, except the central copper atom is exchanged by a cobalt atom. The Co associated resonances in the DOS accommodate information about the electronic coupling of the molecules to the metal surface [219, 220]. We deposited the Co-Ps on the h-BN/Cu(111) sample at 470 K following the same procedure used for the 2H-Ps. The inset in Figure 3.6 depicts an ordered island of intercalated molecules on the right side and a line of Co-Ps adsorbed on the h-BN/Cu(111) arranged along the island edge. We measured STS for three different Co-P positions. The spectrum of (i) Co-P on h-BN/Cu(111) (gray dotted line) was taken at the position of the gray dot in the STM image. We observe a pronounced resonance at $V_S \sim 1.1$ V, due to contributions of the Co states [126, 214]. The highest occupied molecular orbital of the porphine leads to a DOS resonance for biases lower than $V_S = -2.2$ V. The negative differential resistance (NDR) and the sharp DOS resonances point towards an efficient electronic decoupling of the porphines from the metal support [219]. (ii) STS of Co-P on Cu(111) (red dashed line). We do not image any sharp features in the STS, however we find a smooth ascent of the DOS for biases exceeding $V_S \sim 0.7$ V. Due to

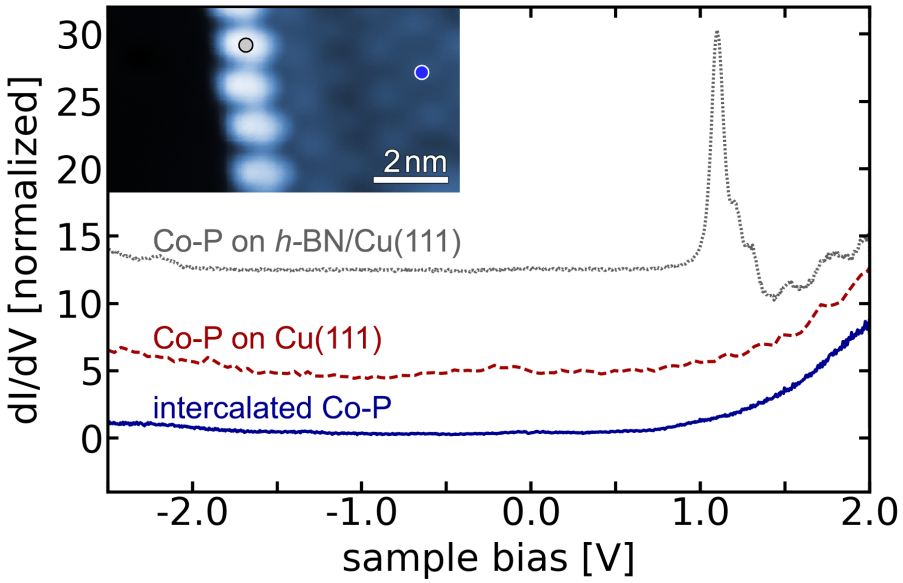

Figure 3.6: *Electronic structure of Co-Ps on different adsorption positions. (i) Co-P on h-BN/Cu(111) (gray dotted line). We observe a characteristic resonance at $V_S \sim 1.1$ V, which is attributed to the Co orbitals [126, 214]. (ii) Co-P on Cu(111) (red dashed line). No sharp features are found, but we observe a smooth increase of the DOS for biases exceeding $V_S \sim 0.7$ V. (iii) Intercalated Co-P (blue solid line). The STS shows similar signature as (ii) with no sharp resonances. The inset shows a STM topograph, where we marked the STS positions by a gray (Co-P/h-BN/Cu(111)) and a blue (intercalated Co-P) dot. The depicted spectra are normalized and vertically offset for presentation. The Figure is reprinted from [210].*

the electronic coupling of the molecule to the metal substrate, the intrinsic molecular DOS is broadened leading to the observed STS [221]. (iii) STS of intercalated Co-P (blue solid line), which was taken at the position of the blue dot in the STM image. The STS shows very similar signature as (ii) with no sharp resonances, leading to the assumption of a effective electronic coupling with the underlying metal.

3.2.5 Electronic switching of intercalated free-base porphines

As dI/dV spectroscopy indicates that the electronic structure of the porphines on Cu(111) is not significantly altered by the capping h-BN layer, the next step was to investigate electronically induced tautomerization reactions [15, 222, 223]. As outlined above, elevated temperatures that promote the intercalation process also lead to self-metalation of the molecules. Thus, in most of our experiments Cu-Ps are the predominant species. However, by reducing the time during which the sample temperature is kept above the metalation temperature, some 2H-Ps can be preserved and identified in STM scans of the intercalated islands. The dashed black circle in Figure 3.7 (a)-(c) marks such an intercalated 2H-P with its characteristic two-fold symmetry and a depression in the center (in contrast to the neighboring spherically symmetric Cu-Ps with bright centers) [214]. Applying a voltage pulse ($V_S = 1.6$ V, $t = 15$ s, $I = 2 - 5$ nA) with the STM tip positioned close to the center of the intercalated molecule induces an apparent

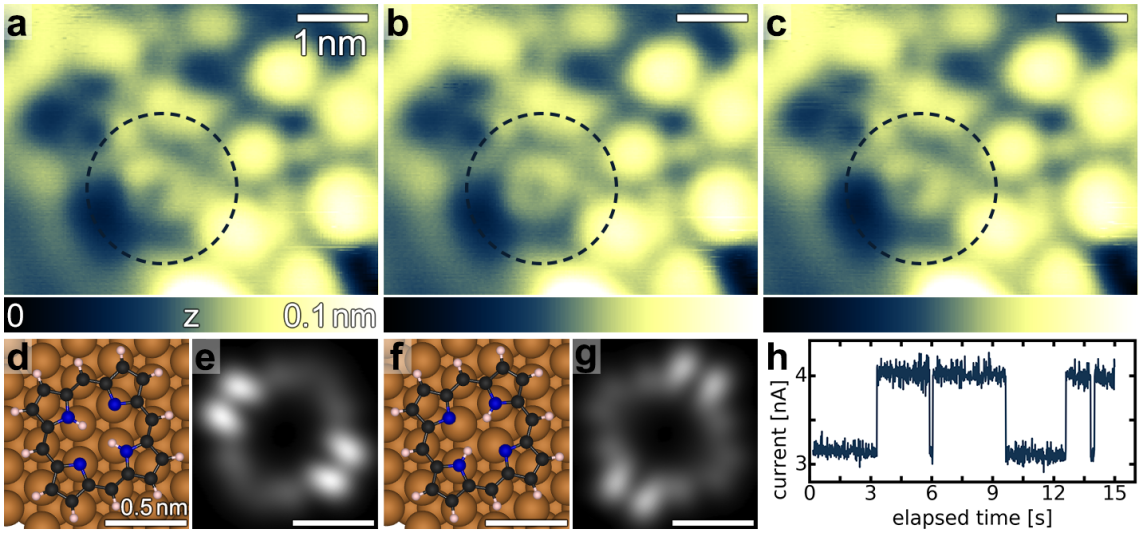

Figure 3.7: *Electronically triggered tautomerization of an intercalated free-base porphine.* ***(a)*** *The two-fold symmetry of the intercalated 2H-P (dashed black circle) can be resolved in STM measurements (V_S = 0.5 V, I = 200 pA for* ***(a)-(c)****).* ***(b)*** *STM image of the same area as in* ***(a)*** *reveals the other trans tautomer after applying a voltage pulse of* 1.6 V. *(c) A subsequent voltage pulse with the same parameter reverts the 2H-P configuration back to the initial state. White arrows in* ***(a)-(c)*** *indicate the orientation of the central hydrogen pair.* ***(d, f)*** *DFT-optimized structures of the two possible trans tautomers of 2H-P adsorbed on Cu(111) (Cu: brown, N: blue, C: black, H: white).* ***(e, g)*** *STM simulations (V_S = 0.5 V) for the two tautomers.* ***(h)*** *Current vs time trace recorded with the tip positioned above the molecule marked by the dashed black circle in* ***(a)-(c)*** *reveals switching between two distinct conductance levels (V_S = 1.6 V, t = 15 s). The Figure is reprinted from [210].*

rotation of the intramolecular features by 90° (compare Figure 3.7 (a) and (b)), indicating a transformation to the other trans tautomer of 2H-P. A subsequent voltage pulse with the same parameters can be used to restore the original orientation (Figure 3.7 (c)). A typical current vs time trace with the tip held at constant height above the intercalated molecule shows switching between two distinct conductance levels (Figure 3.7 (h)). Simulated STM images of the two trans tautomers of 2H-P on Cu(111) (Figure 3.7 (e) and (g)) resemble the experimental images that were obtained in the switching experiments (Figure 3.7 (a)-(c)). Both tautomers exhibit two-fold symmetry, but our experimental together with theoretical data show that one of the tautomers (Figure 3.7 (a),(c),(e)) exhibits brighter features along the N-H bond direction. This is likely caused by a different alignment of the amino hydrogen atoms with respect to the Cu surface: while the tautomer in Figure 3.7 (d) has the two amino N-H bonds aligned along the short bridge sites of the Cu(111) surface, [224] the amino bonds of the other tautomer are aligned along the long bridge sites (Figure 3.7 (f), the most stable adsorption mode of 2H-P on Cu(111), compare Figure 3.8) with the H atoms adsorbed on the hollow sites. According to our DFT calculations, both 2H-P tautomers are nearly isoenergetic with a small energy difference of 0.1 eV. Switching between the two forms can be triggered by tunneling-induced vibrational excitations of the molecule [15, 223] and corresponds to a change of the positions of the central

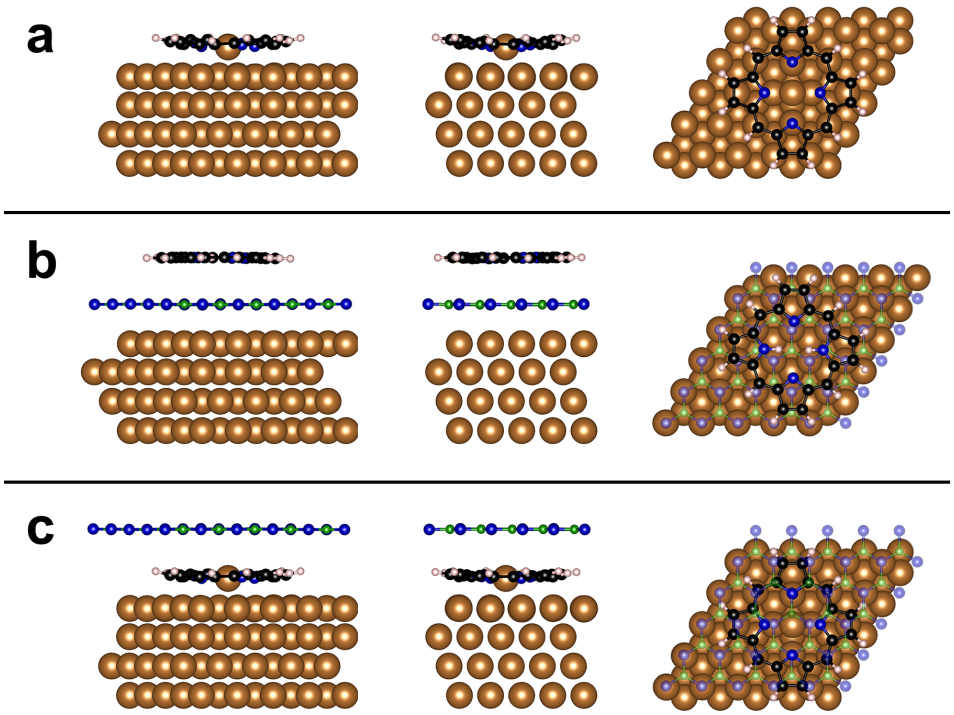

Figure 3.8: *DFT optimized structures of different adsorbtion positions of the porphines. Side and top views of the optimized geometries for* ***(a)*** *Cu-P on Cu(111),* ***(b)*** *2H-P on h-BN/Cu(111), and* ***(c)*** *Cu-P intercalated between Cu(111) and h-BN; Cu: brown, N: blue, B: green, C: black, H: white. In the top views in* ***(b)*** *and* ***(c)*** *the h-BN lattice is drawn semi-transparently for clarity. For the calculations a* $5 \times 5 \times 4$ *unit cell was used with the following lattice vectors (in nm):* $[1.2834, 0.0, 0.0], [0.6417, 0.1111, 0.0], [0.0, 0.0, 3.0]$. *The Figure is reprinted from [210].*

amino hydrogen atoms. A 90° rotation of the whole 2H-P could in principle yield similar results. However, such a rotation is unlikely, as neighboring molecules inhibit the rotation as presented in Figure 3.9. Figure 3.9 (a) and (b) depict a bias pulse induced tautomerization process similar to the one observed above, where the 2H-P rotates by 90°. In Figure 3.9 (c) structural models of the molecules overlay the molecular entities of the STM image. The molecules are in close proximity to each other, inhibiting a rotation of the whole molecule. Figure 3.9 (d) shows a AFM constant height image of the same area, proving that the tautomerized molecules are situated beneath the *h*-BN.

Furthermore, we have not observed tip-induced lateral movement of the intercalated molecules, suggesting a high barrier for translation and rotation of the intercalated molecules. Another change of the adsorption configuration of the 2H-P cannot be ruled out entirely, but the symmetry of the molecular appearance in STM (Figure 3.7 (a)-(c)) and the presence of two distinct conductance states (Figure 3.7 (h)) suggest that tunneling-facilitated hydrogen tautomerization takes place [225, 226]. We thus conclude that the intrinsic functionality of porphine switching is preserved upon intercalation, i.e., underneath a capping monolayer of *h*-BN.

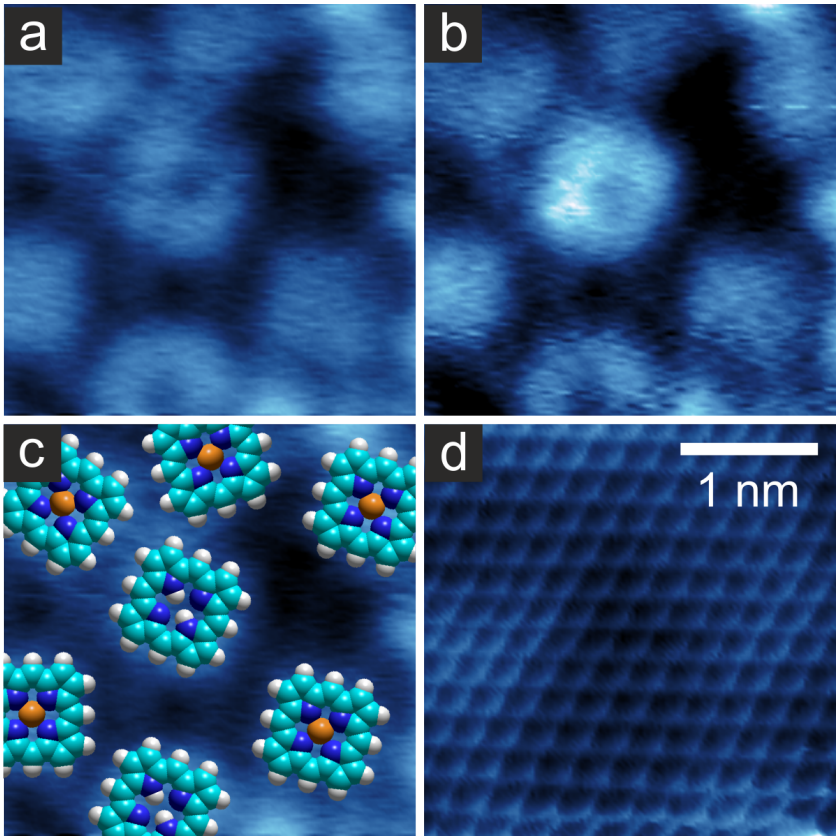

Figure 3.9: *Electronically triggered tautomerization of an intercalated free-base porphine.* ***(a)*** *STM image of free-base porphine exhibiting two-fold symmetry and a characteristic depression in the center ($V_S = 1.6$ V, $I = 10$ pA).* ***(b)*** *An apparent 90° rotation of the molecular configuration is observed after application of a bias pulse ($V_S > 2$ V) close to the center of the molecule ($V_S = 1.6$ V, $I = 10$ pA).* ***(c)*** *STM image of the same area as in* ***(a)*** *with overlaid molecular models illustrating steric hindrance between the central 2H-P and two adjacent Cu-P neighbors (top left) constraining molecular rotation. Tautomerization, i.e., a 90° rotation of the central hydrogen pair, is thus the most plausible explanation for the two distinct 2H-P configurations.* ***(d)*** *Constant-height AFM measurement ($V_S = 0$ V) of the same area shows an intact h-BN layer on top of the molecules. The Figure is reprinted from [210].*

3.2.6 Growth of graphene beneath *h*-BN using porphines as precursors

We annealed the sample to 560 K to covalently couple the intercalated porphines as shown in Figure 3.10 (a). Some molecules are still clearly separated from each other, while some molecules highlighted by the yellow circle exhibit pronounced LDOS at the contacts to the neighboring molecules.

Additionally, these molecules reveal a center-to-center separation of $d = 8.6 \pm 0.3$ Å, which matches the values reported for covalently coupled porphines on Ag(111) [227] and is evidently smaller than the molecule-molecule distance in the intercalated islands presented above. We assume that these molecules underwent a surface assisted dehydrogenative homocoupling as it has been shown for porphines on a metal support [227].

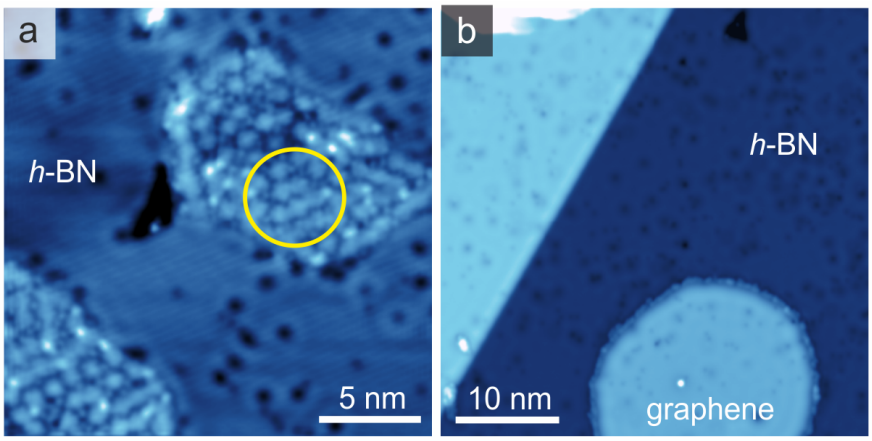

Figure 3.10: *Polymerization of and graphene growth from intercalated porphines.* ***(a)*** *After annealing the sample to* 560 K *we observe polymerized porphines. The yellow circle highlights examples of covalently coupled molecules* ($V_S = 0.5$ V, $I = 150$ pA)*.* ***(b)*** *We heated the sample to* 1070 K*, to disintegrate the intercalated porphines and thereby use them as precursor for the growth of graphene* ($V_S = -1.0$ V, $I = 350$ pA)*.*

In a next step we heated the sample to 1070 K to grow graphene from porphine precursors beneath the *h*-BN. While heating to these elevated temperatures, we expect the molecules to completely disintegrate and subsequently react. Figure 3.10 (b) shows a flat island at the bottom of the image, which we assign to a graphene island, which is situated under the *h*-BN. As we do not observe such islands, when heating an *h*-BN/Cu(111) sample without intercalated molecules to such temperature, we expect the island to origin from the porphine molecules. The energy of the surface state and the FER resonances are clearly shifted between the bare *h*-BN/Cu(111) regions and the region of the graphene island. Therefore, we can exclude that the island consists of migrated copper atoms.

Furthermore, we observe a triangular opening in the *h*-BN layer, which is localized relatively far away from the next graphene island. This points towards a desorption of molecules, which were situated beneath the *h*-BN. Another possible interpretation is that the whole intercalated islands have to move beneath the *h*-BN, what is unlikely due to the high activation energy for the movement of molecular clusters. In contrast single molecules might move to an opening in the *h*-BN layer and desorb from there.

As we expect the porphine molecules to disintegrate upon the growth process of the graphene, the molecules also supply nitrogen atoms. Therefore porphines might be suitable for the growth of n-doped graphene, which exhibits unique properties for nano electronic devices [162, 228–231].

3.3 Mechanism and energetics of the intercalation

For a deeper understanding of the intercalation process, we investigate the mechanism and the energetics in the following. The mechanism of the intercalation involves delamination of the *h*-BN starting at the edges of the weakly bonded layer from the Cu(111) substrate [123], such that intercalated islands can be formed through molecular diffusion. Thus, the intercalated molecular islands, consisting of 2H-P, Cu-P, or Co-P, are observed close to *h*-BN edges, which can occur at holes in the *h*-BN layer that are usually found at domain boundaries or which terminate submonolayer *h*-BN islands. No clear preference for intercalation at island edges, hole edges, or distinct *h*-BN domains was found as shown in Figure 3.11. Figure 3.11 (a) depicts intercalated islands at different *h*-BN orientations, whereas Figure 3.11 (b) shows intercalated islands at *h*-BN island edges (highlighted in red) and again within the *h*-BN islands (highlighted in yellow).

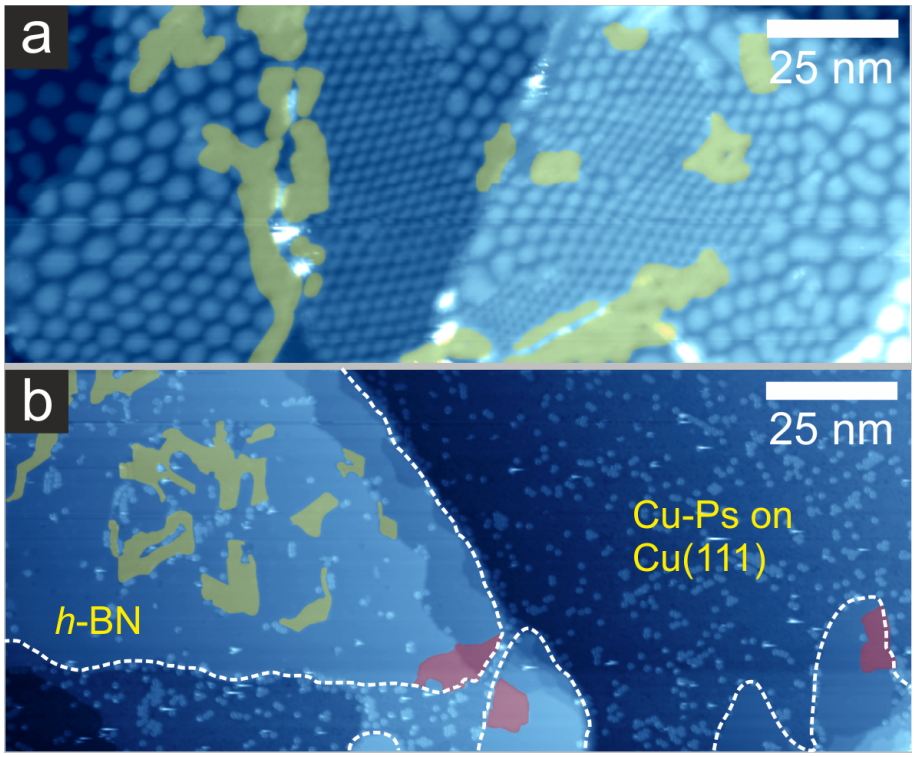

Figure 3.11: *Porphine intercalation at different defect types.* ***(a)*** *High-bias STM image of h-BN/Cu(111) after deposition of 2H-P onto a sample kept at* 470 K. *Intercalation of porphines (highlighted in yellow) at different Moiré domains is observed. No influence of the rotational direction of the h-BN overlayer on the intercalation was found* ($V_S = 4.0$ V, $I = 200$ pA). ***(b)*** *STM image showing intercalated molecular islands at h-BN island edges and domain boundaries. Dashed white lines mark edges of h-BN islands. Molecular assemblies that are intercalated at openings, which commonly appear at domain boundaries [232] of the h-BN layer are highlighted in yellow. Intercalated porphines close to h-BN island edges are highlighted in red* ($V_S = 1.5$ V, $I = 230$ pA). *The Figure is reprinted from [210].*

The size of most of the intercalated islands is significantly smaller than 1000 nm^2, which hints at a diffusion-limited process, as opposed to edge-delamination being the limiting step [191]. It is possible that the intercalation process is in some cases assisted with pre- or co-intercalation of small atomic or molecular species that can diffuse underneath the *h*-BN without inducing substantial geometric distortions [199] (see Figure 3.2). The activation energy associated with the delamination of the *h*-BN layer is reflected in the onset temperature of the intercalation process of about 420 K. Furthermore, our measurements show that efficient porphine intercalation is hampered at temperatures above 470 K, which can be explained by facile desorption of molecules at elevated temperatures. To investigate the energetics and driving forces of the intercalation process in detail, we performed DFT calculations including long-range van der Waals interactions [233]. The calculations where provided by the collaboration partners Alejandro Perez Paz and Angel Rubio.

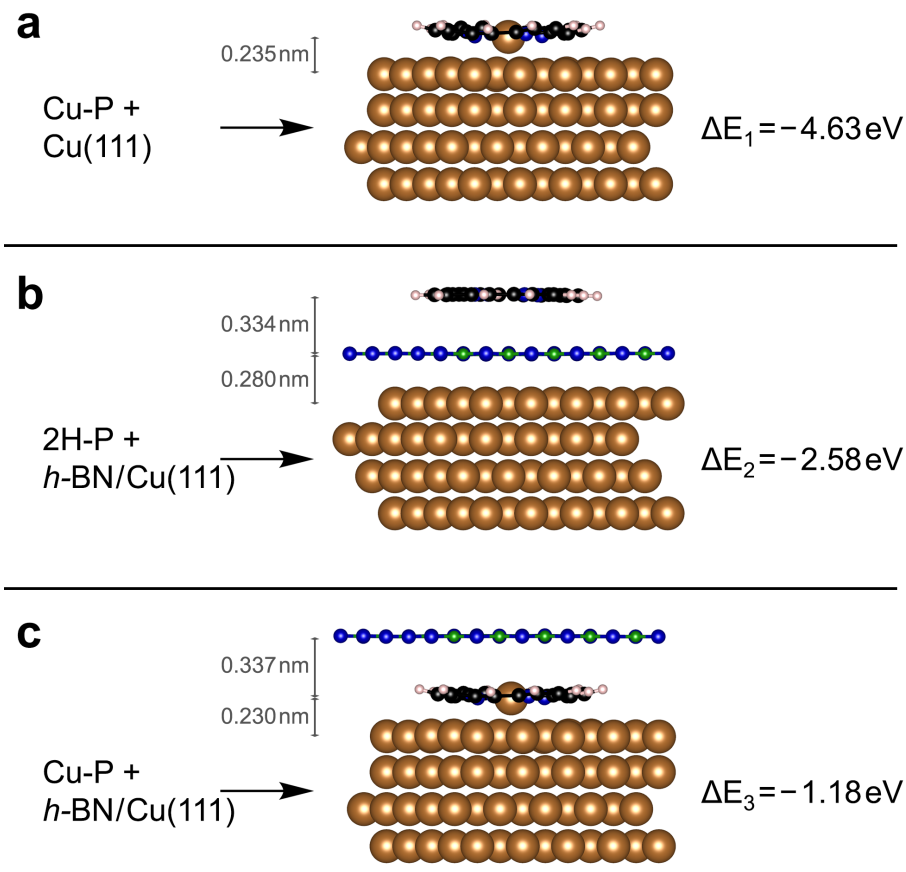

Figure 3.12: *DFT-optimized structures and respective adsorption energies for the experimentally observed porphine arrangements:* ***(a)*** *Cu-P on Cu(111),* ***(b)*** *2H-P on h-BN/Cu(111), and* ***(c)*** *intercalated Cu-P. The side views of calculated structures for* $5 \times 5 \times 4$ *Cu(111) slabs are shown (Cu: brown, N: blue, B: green, C: black, H: white). Calculated vertical heights of porphine center of mass with respect to the average of the Cu(111) top layer (or the h-BN layer, respectively) are given. The Figure is reprinted from [210].*

The optimized geometries for the three experimentally observed adsorption arrangements are shown in Figure 3.12 along with their corresponding calculated adsorption energies ΔE: (a) Cu-P on Cu(111) with $\Delta E_1 = -4.63$ eV, (b) 2H-P on h-BN/Cu(111) with $\Delta E_2 = -2.58$ eV, (c) intercalated Cu-P with $\Delta E_3 = -1.18$ eV. In the calculations we used a $5 \times 5 \times 4$ slab comprising four layers of copper atoms (25 atoms per layer), a total of 25 B and 25 N atoms in the h-BN layer, and one porphine. In this small supercell, the h-BN structure is rather flat. The separation between neighboring Cu-Ps is 1.28 nm, which is close to the experimentally observed (NN)-distance of $a = 1.11 \pm 0.05$ nm for intercalated molecules. In calculations, the vertical separation between h-BN and the top layer of Cu(111) without intercalated molecules, $h_{h-BN/Cu(111)} = 0.315$ nm, agrees quite well with references [116, 123, 234, 235]. Upon intercalation, the calculated vertical distance between h-BN and the top layer of Cu(111) increases to $h_{h-BN/Cu-P/Cu(111)} = 0.567$ nm. Therefore, the difference between these two heights is $\Delta h_{h-BN} = 0.252$ nm. This is slightly larger than the height difference that was determined from nc-AFM experiments averaged over different molecular islands ($\Delta h_{h-BN} = 0.21 \pm 0.02$ nm). This apparent discrepancy between theory and experiment can be caused by a variation in the long-range forces (such as electrostatic forces) on h-BN/Cu(111) and h-BN/Cu-P/Cu(111). This also explains the reduced atomic contrast of the h-BN/Cu(111) areas in Figure 3.3 (d) in which a larger tip-sample distance in this area leads to a reduced contrast. The adsorption height with respect to the molecular center of mass of intercalated Cu-P was calculated to be $h = 0.230$ nm, which is slightly reduced compared to $h = 0.235$ nm for Cu-P on Cu(111). Both systems show significant Bader charge transfer from the metal surface to the molecule: $1.45e^-$ for the intercalated Cu-P and $1.29e^-$ for the Cu-P on Cu(111), as calculated by DFT. The h-BN plays almost no role in the charge transfer but slightly reduces the vertical separation between the porphine molecule and the Cu(111) topmost layer (~ 0.005 nm). In contrast, for the 2H-P on h-BN/Cu(111) only a very small charge transfer of $0.06e^-$ is predicted (at the adsorption height of 0.334 nm above h-BN). The adsorption energies were calculated with respect to the separate constituents, consisting of an isolated porphine and the h-BN/Cu(111) or the Cu(111) surface, respectively:

$$\Delta E_1 = E(Cu-P/Cu(111)) - [E(Cu-P) + E(Cu(111))] \tag{3.1}$$

$$\Delta E_2 = E(2H-P/h-BN/Cu(111)) - [E(2H-P) + E(h-BN/Cu(111))] \tag{3.2}$$

$$\Delta E_3 = E(h-BN/Cu-P/Cu(111)) - [E(Cu-P) + E(h-BN/Cu(111))] \tag{3.3}$$

where E(x) is the calculated energy of the relaxed structure x. Please note that the metalation energy is not included in these calculations; that is, we assume that for the formation of intercalated Cu-Ps metalation precedes the intercalation. This is in line with temperature-dependent experiments indicating that the activation energy for metalation is lower than the activation energy for intercalation. However, the influence of the metalation energy is discussed below.

The intercalation is driven by the large adsorption energy of the molecules on Cu(111), $\Delta E_1 = -4.63$ eV. However, as the vdW interaction between *h*-BN and Cu(111) weakens when Cu-P intercalates, a smaller intercalation energy gain of $\Delta E_3 = -1.18$ eV results, with new vdW contacts formed between the intercalated Cu-Ps and *h*-BN. It should be noted that all three adsorption processes (Figure 3.12) are thermodynamically favorable. This is in agreement with our experiments, in which we observe all three adsorption arrangements.
Based on the calculated adsorption energies, the simulations predict that the porphines preferably adsorb on Cu(111), followed by adsorption on *h*-BN/Cu(111) and intercalation. The intercalated Cu-Ps are therefore predicted to exist in the smallest quantity. In fact, we observe in the experiments that intercalation takes place only when the exposed Cu(111) surface is completely covered by molecules. However, we typically observe a higher abundance of intercalated molecules compared to the number of molecules adsorbed on *h*-BN/Cu(111). For instance, Figure 3.1 (b) shows that only very few molecules are adsorbed on *h*-BN/Cu(111), most of which are located close to defect sites, such as wrinkles in the *h*-BN. This discrepancy between experiment and theory can be explained by several factors: (i) Overbinding between *h*-BN and Cu(111) can occur in the theoretical modeling caused by the overestimation of C6 coefficients in the vdW correction used [123, 236], which (ii) can be particularly relevant for the modeled *h*-BN/Cu(111) registry (N atoms on top of Cu atoms), representing the strongest interaction within the Moiré lattice [116].

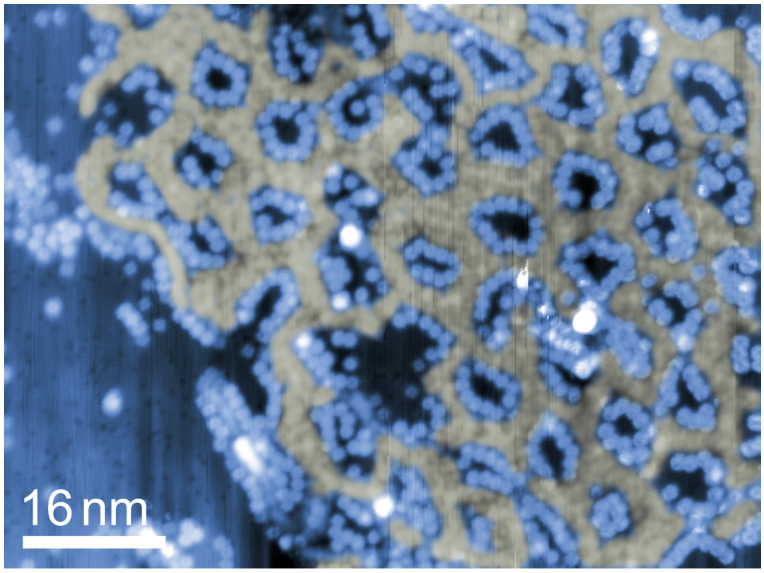

Figure 3.13: *STM image of a sample prepared at $T_{sample} \sim 420$ K evidences preferential intercalation of porphines at the weakly bonded wire areas of the h-BN/Cu(111) Moiré superlattice. The intercalated island (highlighted in yellow) shows voids that coincide with the pore regions, which exhibit the strongest interaction within the Moiré lattice (N atoms on-top of Cu atoms) leading to a higher energy cost for h-BN delamination. Additionally, porphines adsorbed on the h-BN layer can be observed, frequently occupying positions at the boundary of the voids in the intercalated island ($V_S = 1.6$ V, $I = 10$ pA). The Figure is reprinted from [210].*

This effect can clearly influence the intercalation process as can be seen in Figure 3.13, where the highlighted areas correspond to intercalated molecules. Upon annealing the porphines have enough energy to intercalate the wire regions of the Moiré, whereas the h-BN in the pore regions sticks still to the Cu(111) surface.
(iii) Also, the influence of different surface diffusion barriers might play a role in the experiments, i.e., porphine migration is readily possible from h-BN/Cu(111) toward Cu(111), but not in the opposite direction. (iv) Furthermore, porphine desorption from h-BN, which occurs at elevated temperatures during sample preparation, is hindered for the intercalated molecules. (v) The calculations clearly show the effect of the density of the intercalated porphines on the energy gain ΔE_3: The reduction of the (NN)-distance from $a = 2.05$ nm ($8 \times 8 \times 4$ slab) to $a = 1.28$ nm ($5 \times 5 \times 4$ slab) results in the intercalation energy changing its sign from a thermodynamically unfavorable situation with $+4.8$ eV to a favorable case with -1.18 eV. Higher densities (or smaller unit cells) thus yield a higher energy gain as the decrease of vdW interaction energy between h-BN and Cu(111) is smaller per intercalated molecule. According to this trend, the energy gain due to intercalation will further increase for the experimentally observed (NN)-distance of 1.11 ± 0.05 nm and thus explain the higher prevalence of intercalated species observed in experiment. This coverage effect is also likely the cause for the dense self-assembly of the intercalated molecules. (vi) Furthermore, energy gains or losses due to the metalation upon intercalation might be relevant for the energetics.

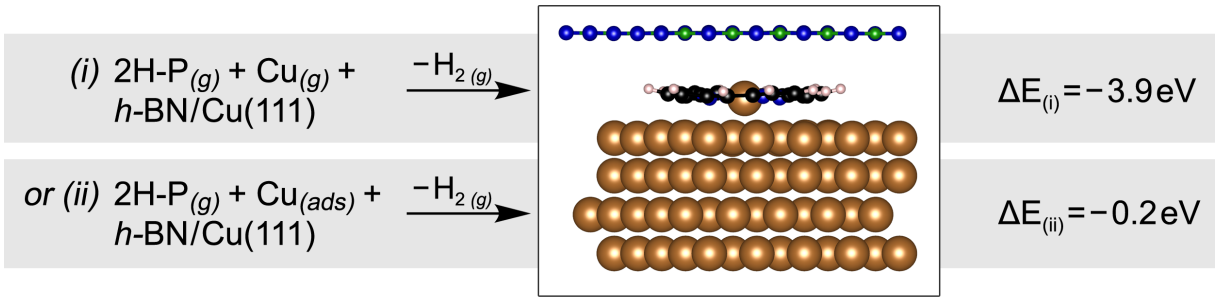

Figure 3.14: *Scheme of the limiting cases for the metalation/intercalation process. The process has been modeled in two ways, where the active Cu species can be either: (i) Cu-atoms in the gas phase, or (ii) Cu-adatoms on the Cu(111) surface. The Figure is reprinted from [210].*

Therefore we have modeled the possible combined metalation/intercalation process using two limiting cases as shown in Figure 3.14: starting from 2H-P, h-BN/Cu(111) and a Cu-atom (i) in the gas phase, or (ii) adsorbed as an adatom on the Cu(111) surface. In both cases, the final state consists of the intercalated Cu-P, i.e. h-BN/Cu-P/Cu(111), as well as H_2 in the gas phase. Regarding the energy release, the approximation in (i), i.e. using free Cu atoms to model the mobile Cu-species that mediate metalation [213, 214] is the most favorable case. In this case, the energy difference between the final and initial states is calculated to be $\Delta E_{(i)} = -3.9$ eV. The process is thus exothermic and thermodynamically favorable.

$$\begin{aligned}\Delta E_{(i)} = &[E(h-BN/Cu-P/Cu(111)) + E(H_{2,gas})] \\ &- [E(2H-P_{gas}) + E(Cu_{gas}) + E(h-BN/Cu(111))]\end{aligned} \tag{3.4}$$

On the other hand, the approximation in (ii), i.e. starting from a Cu-atom adsorbed on Cu(111) at the most stable site (3-fold fcc site, according to experimental and computational data [237]), is energetically less favorable but still exothermic:

$$\begin{aligned}\Delta E_{(ii)} = &[E(h-BN/Cu-P/Cu(111)) + E(Cu(111)) + E(H_{2,gas})] \\ &- [E(2H-P_{gas}) + E(Cu_{ads}/Cu(111)) + E(h-BN/Cu(111))]\end{aligned}$$

with $\Delta E_{(ii)} = -0.2$ eV. We believe that pathways (i) and (ii) constitute limiting cases of the true intercalation energy: the estimate given by path (i) is an upper bound whereas (ii) gives a lower bound of the intercalation energy. However, as the metalation most likely takes place before the intercalation and Co-Ps and 2H-Ps follow the same intercalation recipe, we assume that the metalation energy does not strongly influence the energetics of the whole process.

3.4 Conclusion

In conclusion, we have synthesized hybrid inorganic-organic heterostructures consisting of porphine molecules (2H-P, Cu-P, or Co-P) intercalated between Cu(111) and an h-BN layer at moderate temperatures. Furthermore we grew graphene covered by a h-BN layer from porphine precursors.

The intercalation process is driven by the high adsorption energy of the molecules on the metal surface and the formation of new vdW contacts between the porphines and h-BN. In a close-packed molecular assembly this energy gain can compensate the energy cost for delamination of h-BN (i.e., reduction of vdW interaction between h-BN and Cu(111)). The capping h-BN layer does not significantly alter the electronic properties of the molecules. Tautomerization can be triggered by injecting electrons through the h-BN layer.

This work opens up potential pathways toward the use of functional molecular architectures outside of ultra-high-vacuum environments. Furthermore, chemical reactions of intercalated molecules [206, 238] could be controlled by geometric confinement and/or the selectivity of the intercalation process to different reactants.

3.5 Methods

All experiments were performed in custom-designed ultra-high vacuum chambers housing a commercial STM/nc-AFM operated at $T = 5$ K (CreaTec). The base pressure during the experiments was below 2×10^{-10} mbar. Repeated cycles of argon sputtering and annealing up to 1070 K were used to prepare the Cu(111) single crystal. *h*-BN was grown from the precursor borazine at a pressure of 7×10^{-7} mbar and a sample temperature of 1070 K [116]. Subsequently, 2H-P molecules (Sigma-Aldrich, purity $\geq 99\%$) were evaporated from a thoroughly degassed quartz crucible held at 470 K. During deposition the sample temperature was kept at $420 - 470$ K. All STM images were recorded in constant-current mode using an electrochemically etched tungsten tip. nc-AFM measurements were performed using a qPlus sensor with a tungsten tip (resonance frequency ~ 25 kHz, oscillation amplitude 80 pm, Q value ~ 79000). dI/dV spectra were acquired at constant height (open feedback loop) with a lock-in amplifier using a modulation frequency of $470 - 770$ Hz and a modulation voltage of $14 - 35$ mV(rms). Current traces I(t) were recorded at constant height (open feedback loop). Slab calculations were performed using the projector augmented wave pseudopotential method [239] as implemented in the VASP code [240–243]. We used the PBE exchange-correlation functional in all calculations. [244] We included long-range vdW interactions via the Tkatchenko-Scheffler approach. [233] The convergence threshold of the electronic cycle was set to 10^{-5} eV. The Cu(111) surface was modeled with the coordinates derived from a typical PBE lattice constant of 0.363 nm [224, 235]. The low (high) coverage limit was modeled via $8 \times 8 \times 4 (5 \times 5 \times 4)$ slabs that feature lateral porphine separations of 2.053(1.283) nm. The adsorption mode of 2H-P on Cu(111) of Müller et al. [224], which places the two N-H amino (=N-imino) groups of 2H-P along the long (short) bridge position, agrees well with our experimental observations and was adopted for all porphine molecules on Cu(111). The B-N distance in *h*-BN (0.1482 nm) was stretched slightly ($< 3\%$) with respect to its experimental value (0.1446 nm) so as to achieve commensurate unit cells with the underlying Cu(111) surface [245]. The adsorption of *h*-BN on Cu(111) is dominated by vdW interactions, and we use a model that places the N atoms on top of Cu atoms and B over face-centered cubic (fcc) sites [116, 234, 235]. The optimal adsorption site of a single Cu adatom on the Cu(111) surface is the 3-fold fcc site according to STM experiments and DFT calculations [237]. The *h*-BN, adsorbate, adatoms, and the top Cu layer were relaxed until all ionic forces were below 2.5 eV/ nm. These geometry optimizations used a kinetic energy cutoff of 400 eV and $3 \times 3 \times 1 (1 \times 1 \times 1)$ k-point sampling for $5 \times 5 \times 4 (8 \times 8 \times 4)$ slabs. For accurate energetics, single-point energy calculations were performed at a 600 eV cutoff and $5 \times 5 \times 1 (3 \times 3 \times 1)$ k-point grid for $5 \times 5 \times 4 (8 \times 8 \times 4)$ slabs. Over 1.8 nm of vacuum and dipole corrections were used to decouple the periodic images along the normal z direction. We used spin-polarized calculations whenever necessary (Cu-P species). The charge transfers were computed via the Bader analysis code [246]. STM images were simulated under the Tersoff-Hamann approximation [70].

4 *h*-BN/Cu(111) after exposure to ambient conditions

h-BN reveals extraordinary properties in terms of thermal and chemical stability [247], which make this two-dimensional layer a promising candidate as a protective cover for all kind of nano devices [248, 249]. We have shown the intercalation of functional molecules at the *h*-BN/Cu(111) interface at moderate temperature and as a next step we wanted to investigate the protective properties of the covering *h*-BN layer against exposure to air.
As shown in the following, atmospheric oxygen can intercalate *h*-BN/Cu(111). The covering layer modifies the ordering behavior of the intercalated oxygen and several different adsorption geometries have been identified. By a subsequent thermal activation in vacuum we also achieved deintercalation of the oxygen. At even higher temperatures the *h*-BN starts to disintegrate.

4.1 Oxygen on Cu(111)

There is a large number of studies on oxygen on crystalline copper surfaces tracing back to the 70s [250–254]. Molecular oxygen adsorbs dissociatively [251, 253] and shows ordered arrangements on Cu(100) and Cu(110) [253, 255, 256], whereas the interpretation of the oxygen adsorption on Cu(111) is much more complex [257].
Many studies show no apparent ordering of oxygen on Cu(111) [250–252, 254, 255], however for thermally activated surfaces ordered arrangements were reported [256–262]. Two distinguishable structures, the so-called „29“-structure and the „44“-structure are found in several reports, identified with different complementary techniques such as STM and LEED [256, 258, 259].
The „29“-structure exhibits an unit cell of 0.91 nm $\times$ 1.8 nm with an opening angle of $\Phi = 76.7°$, whereas the basis cell of the „44“-structure is 2.2 nm $\times$ 1.18 nm with $\Phi = 84.3°$ [259].
The „44“-structure is the most commonly found regular structure on Cu(111) and is stable up to high temperatures of 1200 K [263]. Upon annealing to $\sim$ 723 K [259] the regular structures of the oxygen disappear in STM experiments due to dissolving oxygen in the copper bulk, but the LEED pattern of the annealed samples still show distinct spots corresponding to the „44“-structure [259]. By reducing the oxygen layer for example with CO, starting from the „44“-structure an oxygen deficient layer is formed, which exhibits an hexagonal lattice with lattice constant $a = 0.6$ nm. After further reduction separated chemisorbed oxygen is left, which appears as dark dots on the Cu(111) surface [264].
Furthermore, in some reports hexagonal lattices with only short range order exhibiting a periodicity of $\sim$ 0.6 nm were found [256, 258, 259, 261, 262, 264]. Two publications also report cubic symmetric oxygen structures on Cu(111) with periodicities of 0.51 nm [253] and 0.43 nm [251], respectively. However, the cubic structures were found in averaging experiments like LEED [251, 253] and high-resolution electron energy loss spectroscopy [251] and were so far not confirmed by real space experiments, e.g. STM.

4.2 Oxygen intercalated between copper and *h*-BN

h-BN on a copper support has been previously investigated after exposure to air [202, 265]. XPS experiments have shown that for *h*-BN on polycristalline copper [265] and Cu(100) [202] the intercalated element is mainly oxygen upon exposure to air. The elemental boron is oxidized and removed from the surface while some nitrogen-oxygen bonds are formed [265].
On Cu(100) the oxygen forms regular arrangements beneath the *h*-BN and for temperatures exceeding 870 K the oxygen etches away the *h*-BN.
On polycristalline copper a successful deintercalation of oxygen with intact *h*-BN has been reported. The deintercalation temperature depends on the exposure time of the system to air and for long term exposure *h*-BN disintegrates before oxygen is deintercalated:
For two days air exposure the deintercalation starts at 510 K, while the *h*-BN remains stable even above 920 K. After exposure of ten days no deintercalation has been detected up to 970 K. At these elevated temperatures *h*-BN starts to disintegrate and reacts, catalyzed by the copper surface, to N_2 and boron oxides [265].

4.3 Air exposure - experiment 1

To investigate the effect of exposure to air on *h*-BN/Cu(111) and on intercalated molecules, we prepared a sample with a submonolayer coverage ($\sim 90\%$) of *h*-BN on Cu(111). The *h*-BN was partly intercalated with 2H-Ps, while the Cu(111) areas were covered by porphines. The *h*-BN layer shows defects along grain boundaries as highlighted in Figure 4.1 (e). The sample was exposed to ambient conditions ($p_{air} \sim 1$ bar, $T_{sample} = RT$) for 10 minutes with subsequent annealing to 370 K for 60 minutes in UHV.
Figure 4.1 (a) shows an overview image of the exposed sample with three distinct regions. A strongly corrugated area, which we assign to the formerly *h*-BN free regions that were covered with porphines. Moreover, we observe two relatively flat areas, one brighter and the other one darker. As no Moiré pattern can be imaged, we assign these two areas to intercalated *h*-BN, most likely by oxygen. Figure 4.1 (b) shows different ordered arrangements beneath the *h*-BN, which are highlighted with colored frames. The area highlighted by a red rectangle exhibits a highly ordered structure with lattice constants $a_1 = a_2 = 0.65$ nm and $\varphi_{a_1 a_2} = 82°$ (see Figure 4.1 (c)). The yellow rectangle highlights an area exhibiting a structure with lattice vectors of $a_1 = 1.02$ nm and $a_2 = 2.2$ nm and $\varphi_{a_1 a_2} = 90°$ (see Figure 4.1 (d)). In the area framed by the green rectangle, we observe intercalated porphines, which are not ordered and well separated from each other. The porphyrins appear intact and show no indications of disintegration or

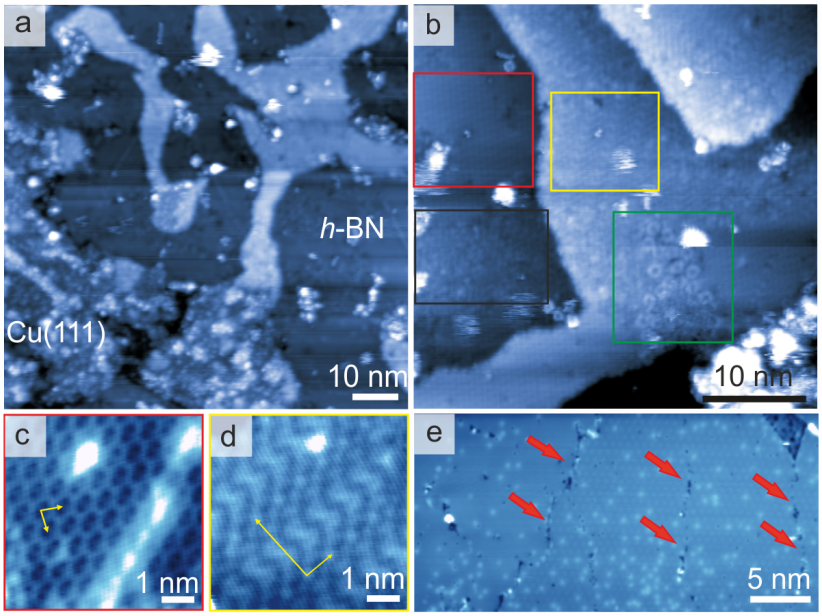

Figure 4.1: *Oxygen intercalated h-BN. h-BN on Cu(111) with regions of intercalated porphines after exposure to air for ten minutes and a subsequent annealing step to $T_{Sample} = 370$ K for 60 minutes. (**a**) Overview image with three distinct areas: (i) strongly corrugated areas, which corresponds to a porphine covered Cu(111) after oxygen exposure labeled with „Cu(111) “. (ii) A brighter and (iii) a darker flat area of the oxygen intercalated h-BN labeled „h-BN “($V_S = 1.13$ V, $I = 62$ pA). (**b**) Three different ordering regimes of the intercalated oxygen. Red rectangle: highly ordered symmetric area with lattice constant $a_1 = a_2 = 0.65$ nm and $\varphi_{a_1a_2} = 82°$ ($V_S = 1.5$ V, $I = 33$ pA) (Enlarged image in (**c**)($V_S = 1.5$ V, $I = 33$ pA)). Yellow rectangle: ordered area with lattice vectors of $a_1 = 1.02$ nm and $a_2 = 2.2$ nm and $\varphi_{a_1a_2} = 90°$ (Enlarged image in (**d**)($V_S = 1.0$ V, $I = 79$ pA)). Green rectangular: intercalated porphines showing no indications of disintegration. Black rectangle: no visible long range order. (**e**) h-BN before air exposure with defects at domain boundaries highlighted with red arrows ($V_S = 1.62$ V, $I = 720$ pA).*

polymerization. Additionally, we found regions with no apparent ordered structures, which are highlighted by the black rectangle in Figure 4.1 (b). In a subsequent annealing step the sample was heated to $T_{Sample} = 470$ K for 45 minutes. We find a predominant ordered structure with large extension, up to several tens of nanometers, which is depicted in Figure 4.2 (a). A close-up of the observed structure is imaged in Figure 4.2 (b) and Figure 4.2 (c). Figure 4.2 (c) depicts the atomically resolved *h*-BN lattice at the same position as (b) with a modified tip. Based on the lattice constant of the *h*-BN honeycombs, we find lattice vectors $a_1 = a_2 = 0.65$ nm with an opening angle $\varphi_{a_1a_2} = 82°$. The same structure was already identified before the second annealing step, however in much smaller patches (see Figure 4.1 (c)).

Increasing the annealing temperature further by 50 K to $T_{Sample} = 520$ K for 15 minutes leads to the formation of large areas exhibiting striped patterns as shown in Figure 4.2 (e). The zoom-in image in Figure 4.2 (d) reveals a $a_1 = 2.2$ nm, $a_2 = 1.03$ nm unit cell with $\varphi_{a_1a_2} = 90°$. However, the annealed sample additionally contains areas with no obvious long range periodicity as can be seen in Figure 4.2 (f).

The intercalated porphines presented in Figure 4.2 (g) exhibit deformations and polymerization

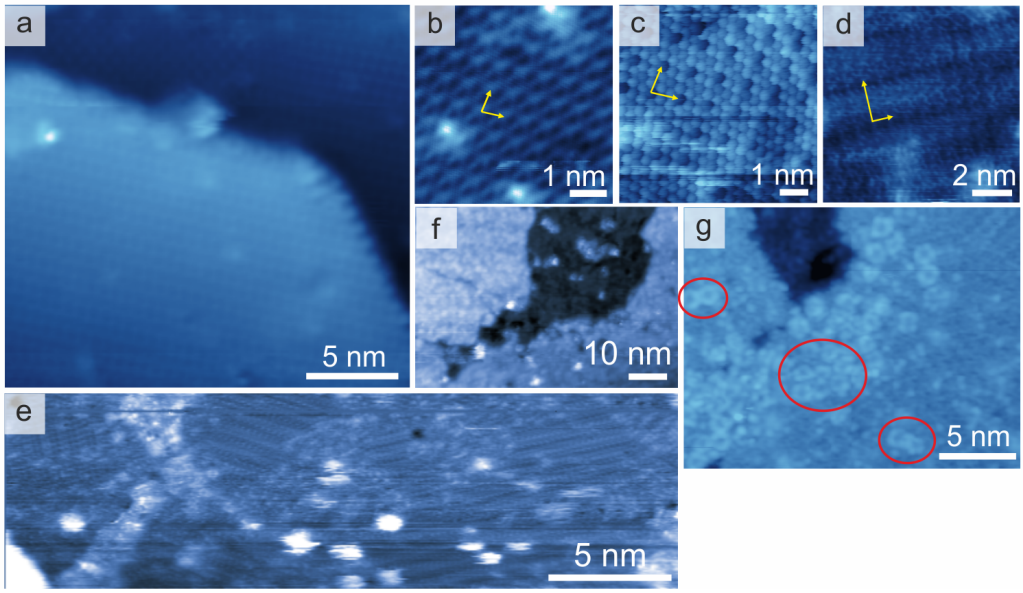

Figure 4.2: *Intercalated oxygen under h-BN after additional annealing steps at $T_{Sample} = 470$ K for 45 minutes ((**a**) - (**c**)) and $T_{Sample} = 520$ K for 15 minutes ((**d**) - (**g**)). (**a**) Extended ordered areas with $a_1 = a_2 = 0.65$ nm and $\varphi_{a_1a_2} = 82.4°$ ($V_S = 0.1$ V, $I = 71$ pA). (**b**) Zoom-in of (**a**) ($V_S = 0.1$ V, $I = 170$ pA) and (**c**) zoom-in with atomically resolved h-BN ($V_S = 0.01$ V, $I = 170$ pA). (**e**) Stripes with $a_1 = 2.2$ nm, $a_2 = 1.03$ nm as unit cell and $\varphi_{a_1a_2} = 90°$ ($V_S = 0.45$ V, $I = 200$ pA). (**d**) Zoom-in of stripe structure presented in (**e**) ($V_S = 0.89$ V, $I = 150$ pA). (**f**) areas with no long range periodicity ($V_S = 0.79$ V, $I = 94$ pA). (**g**) Intercalated molecules after annealing to $T_{Sample} = 520$ K showing deformation and polymerization (highlighted with red circles) ($V_S = 0.69$ V, $I = 1.5$ nA).*

as consequences to the high temperatures. Encircled in red are molecules, which underwent a polymerization process, as judged from the short center-to-center distance of ~ 8.5 Å.

After the sample was further annealed to 570 K most areas appeared unordered, similar to what was found in Figure 4.2 (f). The results after annealing the sample to 620 K for 15 minutes are shown in Figure 4.3. At low bias (Figure 4.3 (a) and (b)) most of the sample reveals an ordered structure on a small length scale. As one example, the yellow rectangle in Figure 4.3 (a) is enlarged in Figure 4.3 (b). The structure appears ordered with square symmetry and basis vectors $a_1 = a_2 = 0.6$ nm for a spatial extend of a few square nanometers. Figure 4.3 (c) is measured at the same position, atomically resolving the h-BN overlayer, showing that the ordered structure is situated beneath the h-BN. We assign the flat regions in Figure 4.3 (a) highlighted with the red arrows to deintercalated h-BN areas. These areas are flat and appear much brighter after increasing the bias voltage from $V_S = 3.50$ V (Figure 4.3 (d)) to $V_S = 4.09$ V (Figure 4.3 (e)) accessing the FER states of h-BN/Cu(111) [116]. We measured the atomically resolved h-BN lattice to ensure that there is still h-BN at the deintercalated areas.

Figure 4.3 (f) shows an additional ordered arrangement found on the sample. The protrusions have different brightnesses and are ordered in a hexagonal array with a nearest neighbor distance of $a = 0.78$ nm. On this sample, no intercalated porphines were detected. In the last annealing step the sample was heated to 720 K for 15 minutes. Figure 4.4 depicts a large area topograph

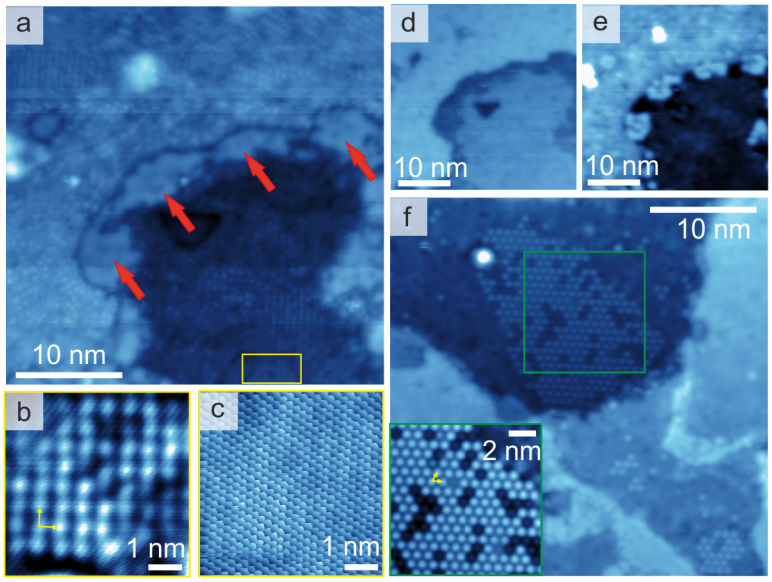

Figure 4.3: *Oxygen intercalated h-BN sample after annealing to $T_{Sample} = 620$ K. (**a**) Overview with ordered structures highlighted by a yellow rectangle and deintercalated areas highlighted by red arrows ($V_S = 0.38$ V, $I = 100$ pA). (**b**) Ordered structures with $a_1 = a_2 = 0.6$ nm and cubic symmetry ($V_S = 0.50$ V, $I = 1.5$ nA)). (**c**) Same area with atomically resolved h-BN overlayer ($V_S = 0.01$ V, $I = 3.5$ nA). (**d**) Same area as in (**a**), where deintercalated areas appear dark ($V_S = 3.50$ V, $I = 100$ pA). (**e**) Same area as (**a**) and (**d**) where deintercalated areas appear bright as the applied bias accesses the FER states of h-BN ($V_S = 4.09$ V, $I = 100$ pA)). (**f**) Hexagonal ordered structure with $a = 0.78$ nm exhibiting different brightnesses ($V_S = 1.80$ V, $I = 890$ pA)).*

of the *h*-BN (290 nm × 290 nm). The *h*-BN/Cu(111) Moiré pattern becomes visible at imaging conditions at high bias of $V_S = 4.09$ V. Some areas, for example in the top right corner appear like flat *h*-BN/Cu(111).

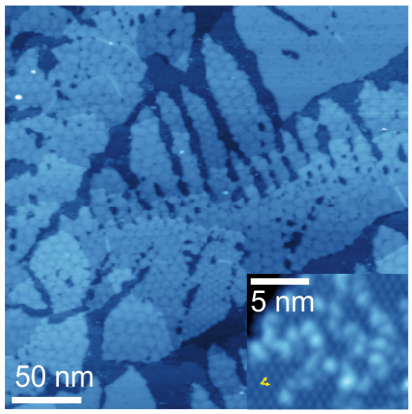

Figure 4.4: *Complete deintercalation and start of oxidation of h-BN at $T_{Sample} = 720$ K. 290 nm × 290 nm topograph of h-BN at $V_S = 4.09$ V. The h-BN is completely deintercalated and the Moiré pattern is visible. The h-BN sheet starts being etched away ($V_S = 4.09$ V, $I = 200$ pA). The inset shows an enlarged image of the h-BN free areas, which exhibit a hexagonal ordering with basis vector $a = 0.8$ nm and bright dots on top ($V_S = 0.50$ V, $I = 360$ pA).*

Consequently we assume that the h-BN/Cu(111) interface is essentially deintercalated. The h-BN also starts to be oxidized at these temperatures. The inset shows a zoom-in to an h-BN free area, where a hexagonal structure with basis vector $a = 0.8$ nm and additional bright dots are observed.

4.4 Air exposure - experiment 2

We performed a second experiment exposing a sample with intercalated porphines under h-BN on Cu(111) to air. The h-BN coverage was close to a monolayer. This time, the sample was exposed for about one hour to ambient conditions. Afterwards we annealed the sample in a first step to 470 K for 5 minutes in UHV. The sample in Figure 4.5 (a) reveals similar regions than in the previous experiment in Figure 4.1 (a). Again we observe brighter and darker rather flat areas. These flat areas have a different appearance as bare h-BN/Cu(111) (compare left side Figure 4.5 (b)) and therefore we assign them to intercalated h-BN, most likely by oxygen.

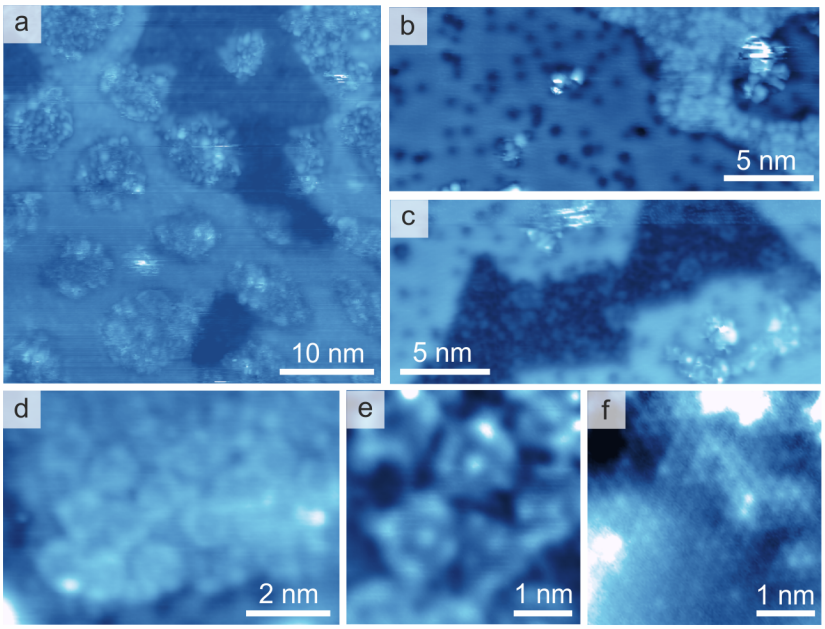

Figure 4.5: *Intercalated oxygen under h-BN on Cu(111).* ***(a)*** *STM image after exposure to air for 60 minutes and subsequent annealing to $T_{Sample} = 470$ K for five minutes. Overview topograph exhibiting three distinct regions. Brighter and darker relatively flat areas corresponding to oxygen intercalated h-BN and strongly corrugated regions ($V_S = 1.2$ V, $I = 50$ pA).* ***(b)*** *After a subsequent annealing step to $T_{Sample} = 570$ K for 15 minutes the h-BN is mostly deintercalated. Intercalated molecules are still found ($V_S = 1.50$ V, $I = 50$ pA).* ***(c)*** *h-BN free areas, which were completely covered with porphines before the exposure to air are almost porphine free after this annealing procedure ($V_S = 1.2$ V, $I = 50$ pA).* ***(d)*** *shows an island intercalated molecules measured at constant current STM ($V_S = 1.2$ V, $I = 50$ pA)).* ***(e)*** *is the current channel of a zoom-in image of* ***(d)*** *recorded at constant height ($V_S = 0.1$ V) showing the intercalated molecules.* ***(f)*** *is the simultaneously recorded Δf signal, which images the atomically resolved h-BN lattice on top of the molecules.*

The Moiré periodicity is still observed, pointing towards pores that might be not intercalated, similar to what is depicted in Section 3.3. At these pore regions we observe strong corrugations, which might come from clusters of adsorbates on the *h*-BN.
After annealing the sample to 570 K for 15 minutes we conclude that the *h*-BN is almost completely deintercalated from oxygen as the *h*-BN imaged in Figure 4.5 (b) exhibits typical *h*-BN/Cu(111) appearance. However, we found intercalated porphines in the brighter intercalated area. The molecules are clearly identifiable, but reveal deformations from their primarily symmetric appearance.
In contrast, Figure 4.4 (c) depicts an opening in the *h*-BN layer, which was completely covered with porphines before the exposure to air. Lacking the protection by *h*-BN most of the porphyrins in this area have disappeared. An area with intercalated porphines is imaged in Figure 4.5 (d) acquired in constant current mode in STM. Figure 4.4 (e) and (f) depict the same area measured in constant height mode. Figure 4.4 (e) images the current channel of a zoom-in of Figure 4.5 (d), whereas Figure 4.5 (f) shows the simultaneously recorded Δf signal. We obtain the atomically resolved *h*-BN layer in the Δf signal, giving evidence that the molecules imaged in the current signal are still intercalated under the *h*-BN.

4.5 Discussion

Structures Upon annealing the submonolayer *h*-BN/Cu(111) sample to 370 K we observed symmetric structures under the *h*-BN with $a_1 = a_2 = 0.65$ nm with an opening angle $\varphi_{a_1 a_2} = 82°$. This structure is most likely a phase of intercalated oxygen, which has so far not been identified on Cu(111). Two publications have reported cubic symmetric oxygen layers on Cu(111), but with much smaller periodicity of $a = 0.51$ nm [253] and $a = 0.43$ nm [251]. Many other studies showed hexagonal lattices with $a = 0.6$ nm [256, 258, 259, 261, 262, 264]. Both findings do not match our observations. Therefore, we conclude that this structure is induced by the *h*-BN cover.
Additionally, arrangements with periodicities $a_1 = 1.02$ nm and $a_2 = 2.2$ nm were found, which is too large for the „29“-structure ($a_1 = 0.91$ nm and $a_2 = 1.8$ nm), but agrees within the measured accuracy to the „44“-structure ($a_1 = 1.18$ nm and $a_2 = 2.2$ nm). Thus we address this stripe like structure to the „44“-structure.
After further annealing to 470 K the $a_1 = a_2 = 0.65$ nm structures extend to larger areas (Figure 4.2 (a)), whereas the „44“-structure becomes predominant as we increased the temperature to 520 K as shown in Figure 4.2 (e). Subsequent to this annealing step we observed also regions with no apparent order (see Figure 4.2 (f),(g)). Here we have to point out that it is likely that these different structures also coexist at the investigated temperatures. We speculate that this diffuse appearance might be caused by oxygen dissolved in the Cu(111) bulk [259]. These oxygen dissolved areas are the most abundant regions after annealing to 570 K. The sample annealed to

620 K reveals two distinct structures. (i) one shows a square symmetry with $a_1 = a_2 = 0.6$ nm, which we assign to a new oxygen phase on Cu(111). (ii) The second structure shows hexagonal ordering with different brightnesses and $a = 0.78$ nm and to our best knowledge has also been not reported so far. At 720 K the h-BN is completely deintercalated and a hexagonal ordered oxygen array with $a = 0.78$ nm is obtained in the h-BN free Cu(111) regions. This area might show an oxygen deficient copper oxide phase as has been reported in [264].

Deintercalation and disintegration We tried to deintercalate the oxygen from the h-BN by thermal activation. Here the two executed experiments described above reveal different behaviors. In experiment 1, no indications of deintercalation were found at 570 K and deintercalation only sets in at 620 K. For experiment 2, the sample was almost completely deintercalated after a short annealing process at $T_{Sample} = 570$ K for 5 minutes. From Kidambi et. al. [265] we know that the deintercalation temperature of oxygen under h-BN on polycristalline copper depends on the exposure time on air. They show that longer exposure times increases the temperature needed for the deintercalation. Our experiments show the opposite dependence, which we explain by the lower coverage of h-BN and furthermore by the lower growth temperature and quality of the h-BN sheet in experiment 1. In experiment 1 the h-BN was grown at $T_{Sample} = 1050$ K compared to $T_{Sample} = 1110$ K in experiment 2. Figure 4.1 (e) depicts the h-BN from experiment 1, where defects along the domain boundaries are highlighted by the red arrows. As we expect the oxygen to intercalate at such defects, the lower h-BN quality leads to an effective stronger air exposure of the sample and therefore increases the temperature of the deintercalation process.
In both cases, the temperature for the deintercalation lies above the temperature, which deforms and disintegrates the intercalated porphines. At 720 K the h-BN is etched away by oxidation, evidencing a limited thermal stability of h-BN on Cu(111) after exposure to ambient conditions.

4.6 Conclusion and outlook

In summary, we showed that we can intercalate and deintercalated oxygen between h-BN and Cu(111). We observed new ordered structures induced by the h-BN overlayer. The deintercalation process is strongly temperature dependent, but depends also on the coverage and quality of the h-BN overlayer and the corresponding effective air exposure.
By adjusting the parameter time and temperature during the deintercalation process, it should be possible to remove the oxygen sandwiched between h-BN and Cu(111), while the porphine molecules stay intercalated and intact. Furthermore, from our measurements we assume that even small defects such as grain boundaries are possible entrance channels for the oxygen intercalation. Therefore for future nano devices, which should be protected from the environment the quality of the CVD grown h-BN is of crucial importance.

5 Thermally induced chemical coupling on *h*-BN/Cu(111)

On-surface reactions are a powerful tool for the bottom-up synthesis of nano architectures [266–272]. Molecular products, which are not achievable by solution based chemistry have been reported [101, 273, 274]. On metal surfaces different reaction protocols have been explored, such as Ullmann coupling [275–280], Glaser coupling [281–288], various condensation reactions [289–295], and cycloaddition reactions [296–298]. However, while on-surface synthesis has essential advantages for bottom-up fabrication of nano architectures, the metal support limits the potential usage of the synthesized products as the metal strongly modifies the electronic properties of molecules.

Therefore it is essential to expand the bottom-up tool box by the implementation of on-surface reactions on insulating materials. The low catalytic activity of insulating materials, compared to metal catalysts, as well as the relatively weak coupling [299, 300] of molecules to the substrate are two main challenges of such reactions [274]. Consequently, so far only few studies address on-surface synthesis on insulating materials such as calcite [301–305], and boron nitride sheets [306–308]. Furthermore on-surface reactions have been shown on carbon based highly orientated pyrolitic graphite [276, 309–311].

Here, we report the reaction of polycyclic aromatic hydrocarbons, which are promising candidates for bottom-up synthesis of n-doped nano graphene [312, 313], on *h*-BN/Cu(111). The precursor molecule comprises highly reactive groups and aromatic carbon rings. The reaction leads to one-dimensional chains and was conducted on metal support and on *h*-BN/Cu(111).

5.1 Azomethine ylide coupling of polycyclic aromatic hydrocarbons: the concept

Cyano-substituted Dibenzo-9a-azaphenalene (DBAP) A structure of the used DBAP molecules is depicted in Figure 5.1 (b) and the corresponding synthesis is described in [312]. The used molecules were synthesized by the Müllen and the Feng groups. The molecules consists of several aromatic carbon rings, a dipolar azomethine group and a dipolarophile cyano group. We refer the cyano group as the head of the molecule and the four aromatic rings to the tail.

1,3 dipolar cycloaddition reaction of azomethine ylide (AMY) on a Au(111) support Azomethine ylides (AMY) are promising building blocks for atomically precise bottom-up synthesis of nano architectures. An AMY, a prototype 1,3-dipolar compound [314, 315] is depicted in Figure 5.1 (a). The positive charge is located at the central nitrogen atom, whereas the negative charge is equally distributed over the two carbon atoms connected to the nitrogen. The biradical [316–319] properties of the AMY cause a high reactivity [320, 321] and so far only few AMYs have been isolated [312, 322–328]. In a so-called 1,3 dipolar cycloaddition reaction or

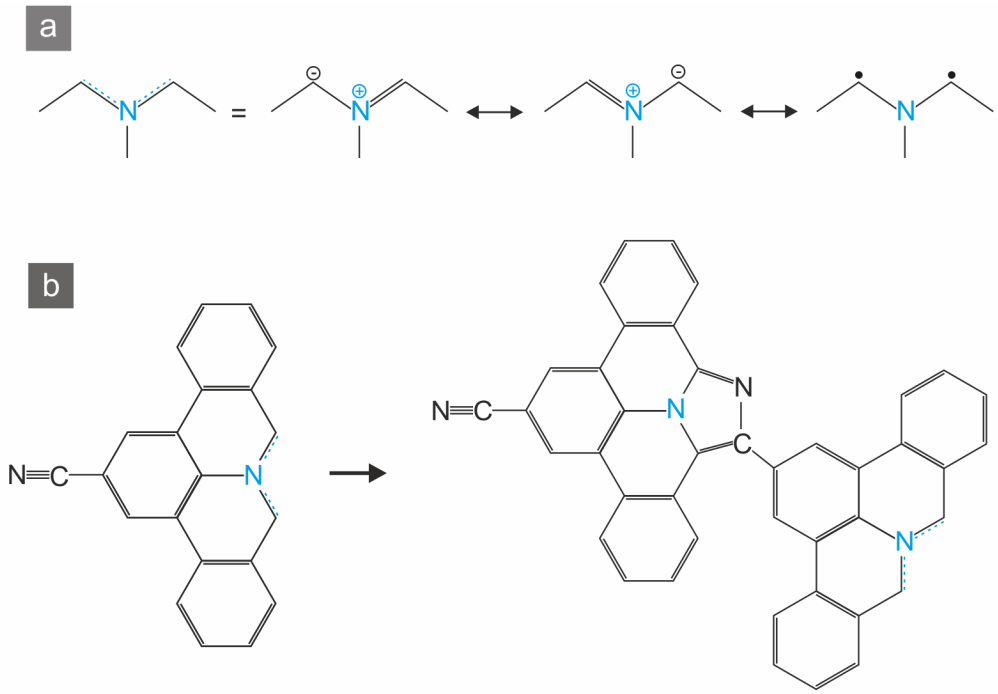

Figure 5.1: *Covalent coupling of polycyclic aromatic azomethine ylides.* ***(a)*** *Azomethine ylide with its different ionic and its biradical Lewis structure.* ***(b)*** *Cyano-substituted DBAP molecule consisting of aromatic carbon rings, a dipolar azomethine group and a dipolarophile cyano group. 1,3 dipolar cycloaddition reaction of two DBAP molecules. Image adapted from [312].*

click-reaction [312] the 1,3 dipolar AMY reacts with an additional dipolarophile group. Such a dipolar cycloaddition exhibits high selectivity [312, 329–332] and has already been demonstrated in solution [312]. Figure 5.1 (b) shows the molecule used in this study. The AMY group of one molecule reacts with the cyano group of a second molecule leading to a dimer, a molecular chain of two monomers, as depicted on the right side of Figure 5.1 (b).

5.2 Results

We deposited our DBAP molecules on a Au(111) surface held at 590 K by molecular beam evaporation at $T_{molecules}$ = 740 K from a $DBAP^{+}BF_4^{-}$ salt. For cyano group functionalized aromatic molecules on Au(111) different adsorption arrangements have been reported [333–335]: (i) Molecules can be stabilized via dipol-dipol interaction between the cyano groups and arrange in molecular pairs of two [333–335]. (ii) Furthermore, metal coordination, where the cyano groups of three molecules point towards a central gold atom have been shown [335]. (iii) Additionally to these findings, covalently bound molecules, which underwent the above described reaction can build molecular chains. We assign the covalently connected molecules to dimers (two covalently bond monomers), trimers (three monomers), etc.

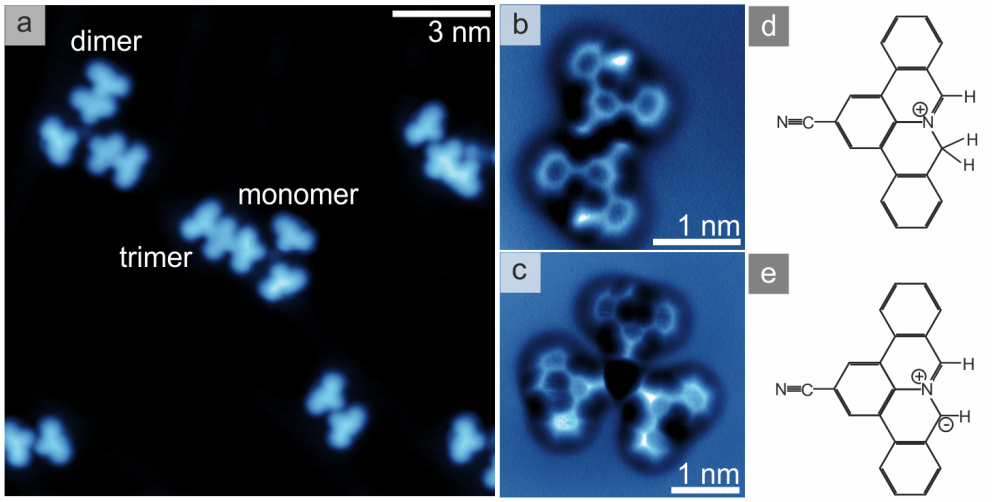

Figure 5.2: *DBAPs on Au(111).* ***(a)*** *Overview STM image, revealing different assemblies ($V_S = 50$ mV, $I = 20$ pA). We observe DBAP monomers, dimers and trimers. Some monomers arrange in pairs of two (enlarged AFM image in* ***(b)*** *($V_S = 0$ V)). In* ***(c)*** *three monomers arrange in a threefold symmetric structure ($V_S = 0$ V). These threefold symmetric arrangements are also found for combinations of monomers, dimers and trimers.* ***(d)*** *and* ***(e)*** *depict the molecular structure for the positively charged DBAP* ***(d)*** *and a neutral DBAP molecule* ***(e)****. While in STM the two different structures were not clearly distinguishable, in* ***(c)*** *the AFM topograph images two DBAPs with an asymmetric shape, which we attribute to a upwards pointing hydrogen atom. We assign the third DBAP molecule on the bottom right to the structure in* ***(e)*** *as it exhibits a rather symmetric appearance.*

Figure 5.2 (a) shows a STM topograph of the resulting sample. We identify monomers, dimers, and trimers, which are stabilized in different arrangements. The BF_4^- ions are not observed on the surface.

Threefold symmetric arrangements, where the cyano end groups of the molecules points towards each other are found. We observe such threefold symmetric systems comprising monomers, dimers, and trimers. The molecules' cyano groups are likely pointing towards a central metal atom as has already been reported for similar molecules [335–337].

Furthermore, monomers are found to stabilize in pairs as depicted in Figure 5.2 (a) and also in an enlarged AFM topograph in Figure 5.2 (b). The molecule pair is stabilized by intermolecular dipole-dipole interactions [333–335]. For similar molecules the dipole-dipole interaction energies have been calculated and exhibit comparable energies as hydrogen-bonding interactions [333]. The CN-CN coupling reveals an antiparallel orientation of the cyano groups of neighboring molecules [335]. The distance between the carbon atom of the CN-group and the nitrogen atom of the adjacent molecule's CN-group is about 4.2 Å, which is in good agreement with experimentally [333, 335] and theoretically [334, 338] obtained values in literature. The arrangement in pairs is additionally stabilized by the hydrogen bonding between the cyano nitrogen atom and the hydrogen of the molecule's phenyl ring.

In the AFM image the cyano group at the molecular head as well as three aromatic carbon rings are very well resolved. An additional feature is the protrusion imaged bright at the tail of the DBAPs, which can be assigned to a upwards pointing hydrogen atom as pictured in the

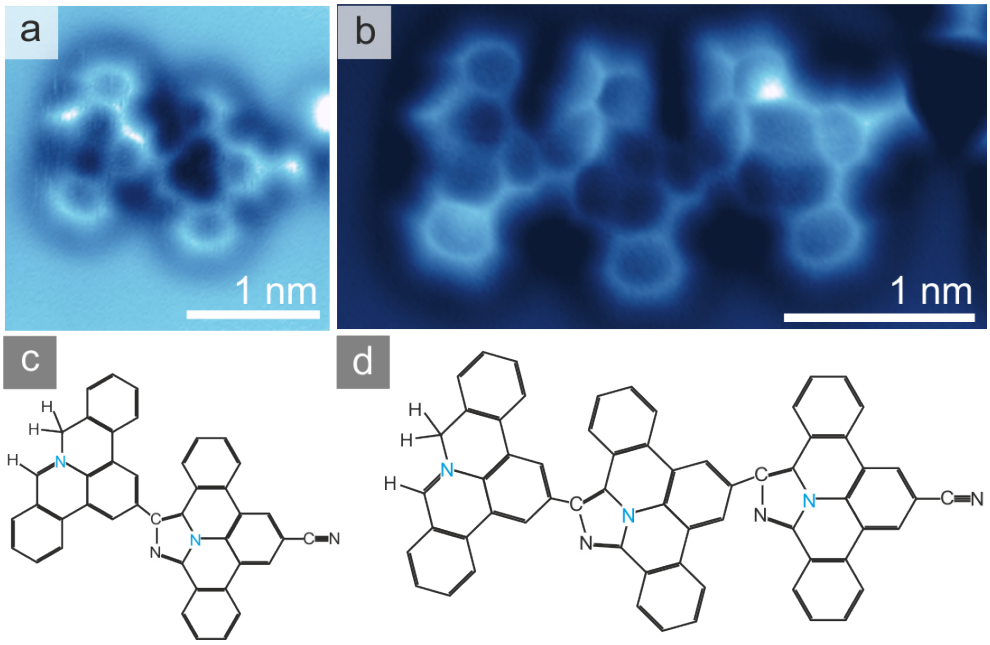

Figure 5.3: *On-surface synthesis of DBAP chains on Au(111).* ***(a)*** *DBAP dimer, where two monomers underwent an 1,3 dipolar cycloaddition reaction. The cyano group and the azomethine group from an aromatic diazole ring and covalently connect the two monomers at the predefined position ($V_S = 0$ V).* ***(b)*** *A chain of three DBAPs on Au(111) ($V_S = 0$ V). The corresponding structural formula are shown in* ***(c)*** *and* ***(d)****.*

molecular structure in Figure 5.2 (d). However the vicinity of the central nitrogen position of the DBAP is relatively dark and the bonds to the nitrogen are only hardly resolved. This observation can be caused by a geometric distortion of the molecule at this position or by the contribution of electrostatic forces caused by the charges located at the nitrogen atom. At the moment of writing, DFT calculations are performed by collaborative partners, to rationalize the origin of the obtained AFM contrast.

Furthermore, we found a minority species of molecules, where the bright hydrogen protrusion is missing as shown in Figure 5.2 (c). Two monomers in the exemplary threefold arrangement reveal the same shape as the DBAPs in Figure 5.2 (b). However the third molecule has a rather symmetric appearance, and consequently we assume that the upwards pointing hydrogen was cleaved off. The corresponding molecular structure is depicted in Figure 5.2 (e).

The oligomers in Figure 5.2 (a) were formed by a temperature induced chemical reaction. The obtained structures are imaged via AFM and agree with the structural formula in Figure 5.3. Already the STM topograph in Figure 5.2 (a) points towards covalently connected dimers and trimers as an increased LDOS is observed at the connection of the DBAPs. In contrast, the molecular pairs and the threefold arrangements reveal a clear separation of the molecules in the STM image. The periodicity of the molecular chains is determined by the average separation of the covalently coupled monomer centers and is quantified to $d \sim 8.5 \pm 0.3$ Å. The AFM measurements presented in Figure 5.3 reveal clearly the covalent character of the molecular bonding.

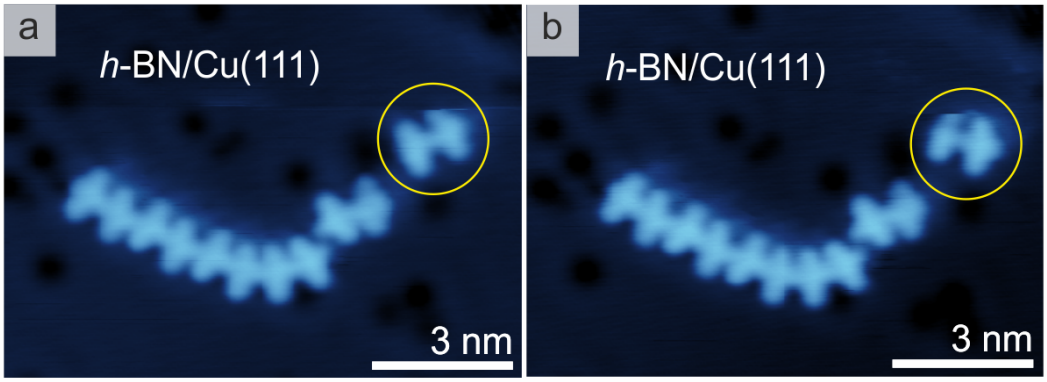

Figure 5.4: *On-surface synthesis of DBAP polymers on h-BN/Cu(111).* ***(a)*** *STM topograph after the deposition of DBAP molecules on an h-BN/Cu(111) surface held at T_{sample} = 520 K, depicting long molecular chains ($V_S = 660$ mV, $I = 60$ pA). The highlighted DBAP dimer can be laterally translated via the STM tip in* ***(a)*** *and* ***(b)*** *($V_S = 660$ mV, $I = 60$ pA) pointing towards covalently bound molecules. Therefore, the molecules very likely underwent an 1,3 dipolar cycloaddition reaction on an h-BN layer by thermal activation.*

Based on the observed bond structure, we conclude that the cyano head group reacts with the azomethine group, resulting in an aromatic diazol ring, consisting of three carbon and two nitrogen atoms. The used reactants and the observed products strongly point towards a 1,3 dipolar cycloaddition reaction on the Au(111) support. The covalent coupling of the molecules appears to be highly selective as less than 10% of different covalent coupling motifs were observed upon the applied thermal activation. Additionally to the dimers, we found one dimensional (1D) chains of three DBAPs as depicted in the AFM image in Figure 5.3 (b) and (d). However, we did not observe longer extended chains on Au(111) even though the reactive centers of the azomethine and the cyano group are still imaged in Figure 5.3 (a) and (b).

In the next step we expanded the polymerization reaction from a metal substrate to *h*-BN on Cu(111). To this end, we used CVD grown *h*-BN on Cu(111) [116] and deposited the DBAP molecules by molecular beam evaporation at $T_{molecules}$ = 670 K for two hours, on the sample held at T_{sample} = 520 K. As depicted in Figure 5.4 we find molecular chains with different lengths up to ten DBAP units. The periodicity of the chains is $d \sim 8.5 \pm 0.3$ Å. In Figure 5.4 two dimers and one chain of eight DBAP units are shown. The 1D chains exhibit a very similar appearance and a similar periodicity as on the Au(111) surface.

Furthermore the covalent structures can be laterally translated via the STM tip as depicted in Figure 5.4 (see dimer highlighted by a yellow circle). Both observation strongly point towards covalently bound DBAP units. Furthermore, we did not find individual molecules on *h*-BN as they desorb at the applied temperature.

In summary, these data demonstrate a reaction to covalently couple polyaromatic molecules on *h*-BN/Cu(111).

5.3 Discussion

The on-surface reaction of DBAPs to 1D dimensional chains has been demonstrated on a Au(111) and an *h*-BN/Cu(111) support. The reaction products have very similar appearance for both systems. The observed on-surface coupling mechanism is most likely the 1,3 dipolar cycloaddition reaction, similar to the reaction reported in solution [312]. While on *h*-BN long molecular chains up to 10 molecular units are observed, the chain length on Au(111) is limited to three DBAP molecules under the applied experimental conditions. We assign the limitation of the chain length growth to the influence of the Herringbone structure of Au(111) [339], which might exhibit position dependent catalytic activity. Indeed, for the less corrugated Ag(111) surface longer chains have been found [340].
We attribute the possibility to conduct the reaction also on rather *h*-BN/Cu(111) to the high reactivity of the azomethine group, leading to a relatively low reaction barrier. Therefore we can trigger the polymerization process by moderate thermal activation and even without direct contact to a metal support. Due to the higher desorption probability of DBAP units on the *h*-BN/Cu(111) compared to the Au(111) substrate, a lower yield of the chemical reaction is observed. After the thermal activation step no individual monomers can be found on the *h*-BN layer as they desorb at the applied elevated temperatures, while monomers still occur on Au(111). Therefore, to enhance the amount of the reaction products, we increased the deposition time of the molecules in the *h*-BN/Cu(111) preparation. As the on-surface reaction has to occur before the individual DBAP monomers desorb from the *h*-BN, the yield of the reaction could be further improved by increasing the molecular flux or the deposition of larger polyaromatic molecules with stronger vdW interaction with the underlying *h*-BN.

5.4 Summary and outlook

To summarize we have successfully introduced the 1,3 dipolar cycloaddition reaction between a cyano and an azomethine group to expand the on-surface tool box for the bottom-up synthesis of nano architectures. Therefore we demonstrate the covalent linking of polyaromatic molecules, which are very promising candidates for the engineering of atomically precise carbon based nano architectures such as n-doped graphene nanoribbons or graphene quantum dots. We showed that the surface assisted polymerization process can be performed on metal surfaces and furthermore on *h*-BN/Cu(111). Here the highly reactive azomethine group of our DBAP molecules causes a low activation barrier for the reaction to a point where the coupling occurs at moderate temperature and without direct contact to catalytic active metals. The selective 1,3 dipolar cycloaddition reaction in combination with polyaromatic molecules provides a large step towards well defined carbon based nano architectures on insulating materials, which is highly relevant for the bottom-up design of nano electronic devices.

6 Characterization of graphene on Ag(111) and Cu(111)

Results presented in this Chapter have partially been reported in following publication:

Reproduced with permission from
Garnica, M.; Schwarz, M.; Ducke, J.; He, Y.; Bischoff, F.; Barth, J. V.; Auwärter, W.; Stradi, D. Comparative study of the interfaces of graphene and hexagonal boron nitride with silver. *Phys. Rev. B* 2016, 94.

6.1 Introduction

Graphene exhibits remarkable intrinsic properties [34, 135–137] such as extremely high charge mobilities [138, 139] and extraordinary mechanical stability [140–142], which open up a huge amount of possible applications ranging from transistors [46, 341–345] to high performance supercapacitors [346–352] to the support for fuel cell catalysists [229, 353–357].
Upon graphene adsorption the electronic properties of the graphene/metal system are modified. In the following the electronic properties of graphene/Ag(111) and graphene/Cu(111) interfaces are investigated by mapping the dispersion of the Shockley-type surface state in combination with DFT calculations and by field emission resonance (FER) experiments.
The dispersion relations indicate that graphene is only weakly coupled to the Cu(111) and Ag(111) supports.
In the FER experiments of graphene/Cu(111), we observe a reduction of the work function upon graphene adsorption in accordance to literature [183, 358, 359]. Furthermore, we investigate the local variations of the work function Φ between different Moiré regions, with the pore regions exhibiting larger Φ than the wire regions. This electronic corrugation of graphene/Cu(111) is quantified by a difference $\Delta\Phi$ of some tens of milli-electron volts, between pore and wire region of the Moiré pattern.
Finally the quantification of the geometric corrugation of graphene/Cu(111) is described in this chapter. The geometry of graphene can strongly influence its electronic [360–363], magnetic [364] and thermal properties [365]. However, the determination of the local topography with scanning probe methods is challenging and a topic of current research [123]. Here, we apply a local Δf amplitude method [123] to evaluate the Moiré induced geometrical corrugation of graphene on Cu(111) with excellent vertical resolution to $\Delta z = 23.5 \pm 3$ pm. The pore regions reveal the highest position of the graphene, which coincides with the highest work function found at these areas via the FER experiments.

6.2 Electronic properties of graphene on Ag(111) and Cu(111)

In the following the electronic properties of the graphene/metal systems are presented. We examine how the Shockley-type surface state of the metal is influenced upon graphene growth. In accordance with calculations from our collaboration partner Daniele Stradi, we found weak coupling between the metal support and graphene for both systems.
Furthermore we quantify the work function modulation along the Moiré lattice for graphene on Cu(111) using field emission resonance (FER) experiments.

6.2.1 Electronic properties of graphene on Ag(111)

STM investigations of the Shockley-type surface state for graphene/Ag(111) Here we investigated the modifications of the Shockley-type surface state of Ag(111) upon graphene adsorption. The results are published in [117]. The graphene layer was grown by deposition of atomic carbon from an e-beam heated carbon rod. Figure 6.1 (a) shows an STM image of the graphene on Ag(111). We scanned over the same region at different sample biases and simultaneously recorded dI/dV-maps of the area as shown exemplarily in Figure 6.1 (b). In the dI/dV-maps we observe a standing wave pattern, which originates from the metal surface state. The corresponding wavelength is bias dependent and can by extracted from the STM images by a fast fourier transformation (FFT). By assuming a free electron gas model with

$$E = E_0 + \frac{\hbar k^2}{2m^*} \tag{6.1}$$

the bias dependence of the standing wave pattern gives information about the effective mass of the surface state electrons. Here, m^* is the effective mass, k the electron wave vector and E_0 the electron energy for $k = 0$. E_0 is determined by STS, as the onset energy of the surface state corresponds to E_0.
In Figure 6.1 (c) the STS spectra with the tip located at the bare Ag(111) (red) and at a graphene/Ag(111) region (green), respectively are shown. We detect an upwards shift of the surface state onset energy in the graphene/Ag(111) regions ($E_0 = 0.10$ eV) compared to $E_0 = -0.07$ eV [366] in the bare Ag(111) regions of $\Delta E_0 \sim 170$ meV. The effective mass is determined to $m^* = 0.35\ m_e$ for Ag(111) and $m^* = 0.32\ m_e$ for graphene/Ag(111).
As the weak bonding of the graphene does not greatly modify the metal surface, we expect that the effective mass is mostly defined by the metal properties. So far, an increase of the effective mass was found for insulating NaCl on Cu(111) [367]. However, for graphene an unchanged effective mass was observed on Au(111) [368] and a reduced effective mass on a Cu(111) substrate [183].

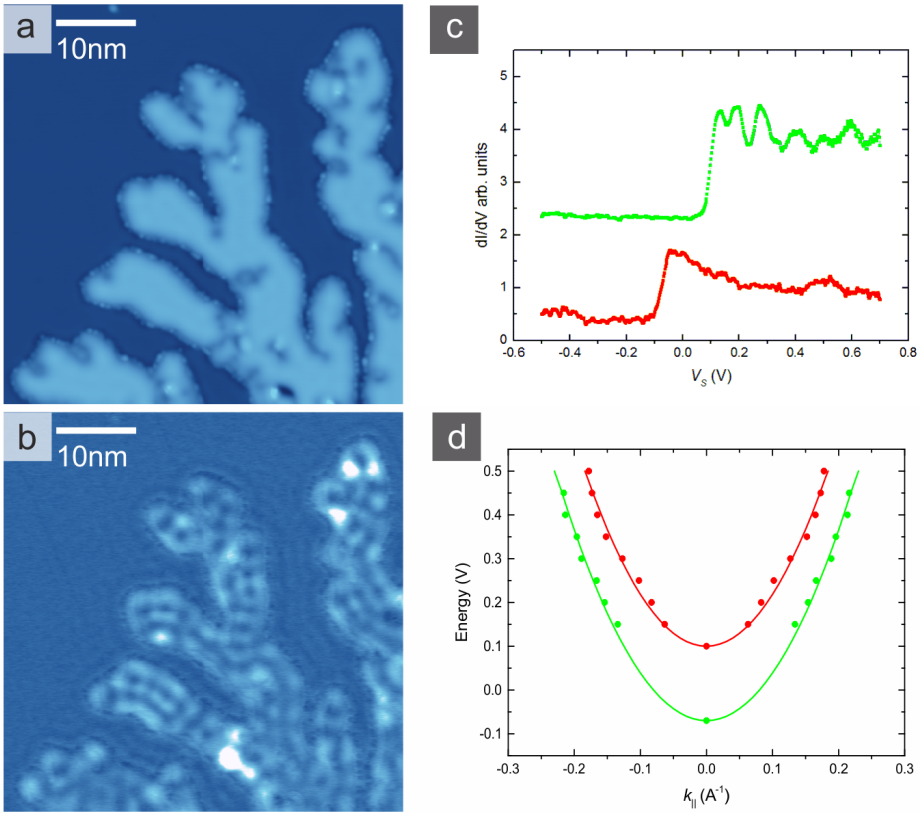

Figure 6.1: *Dispersion relation of Shockley-type surface state: (**a**) STM topograph of graphene on Ag(111) grown via atomic carbon deposition ($V_S = 0.3$ V, $I = 300$ pA). (**b**) dI/dV-maps of same area in (**a**) simultaneously recorded with the STM image. (**c**) STS measured on graphene (green) and on the Ag(111) surface (red), revealing the onset E_0 of the surface state. (**d**) Dispersion relation of the surface state of Ag(111) (red) and the graphene/Ag(111) areas (green).*

DFT calculations of graphene on Ag(111) For a comprehensive analysis of the graphene/Ag(111) interface DFT calculations were conducted by the collaboration partner, which are presented in Figure 6.2. Figure 6.2 (a) illustrates the band structure of graphene on Ag(111). The green line highlights the bands contributing to the Dirac cone of graphene. At the K point the Dirac cone is encircled in green. Additionally, the dispersion relation of the Shockley-type surface state for small energies is colored in red. Using a separation of $d_{G-Ag(111)} = 3.3$ Å between the graphene and the Ag(111) surface, in agreement with [369], we obtain an energy shift of 227.8 meV upon graphene adsorption. The corresponding adsorption energy per carbon atom is found to be $E_{ads} = 66.3$ meV, in good agreement with [369, 370]. Figure 6.2 (b) presents the dependence of the energy shift on the graphene Ag(111) separation $d_{G-Ag(111)}$. From our calculations presented in Figure 6.2 (b) and the experimentally determined energy shift, we estimate a separation of $d_{G-Ag(111)} \geq 3.3$ Å. This separation matches the experimentally determined adsorption heights for weakly interacting two-dimensional layers on metals such as h-BN on Cu(111) with $d_{h-BN/Cu(111)} = 3.38$ Å [123].

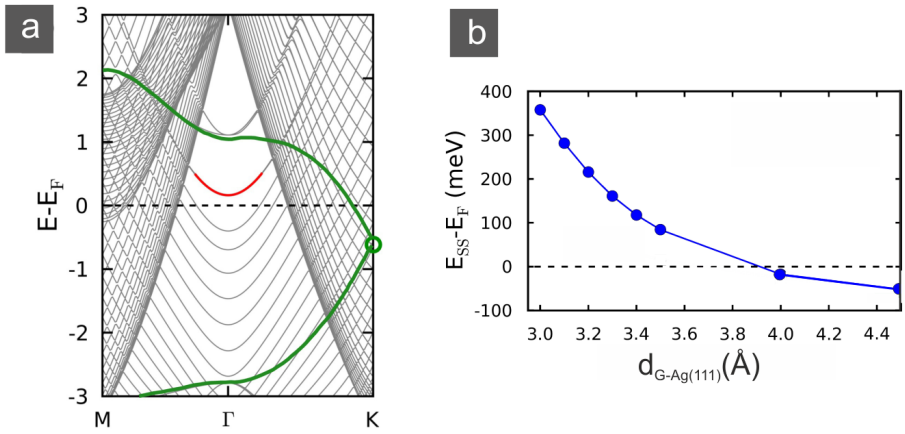

Figure 6.2: *DFT calculations of graphene on Ag(111). (**a**) Electronic band structure of graphene on Ag(111). The graphene bands contributing to the Dirac point (green cicle) at K are highlighted in green. The calculated Shockley surface state dispersion relation is colored in red. (**b**) The energy of the Shockley surface state E_{SS} of Ag(111) at the Γ-point is plotted against the distance between the graphene layer and the Ag(111) surface. The y-axis depicts the energy difference between E_{SS} and the Fermi energy $E_{SS} - E_F$. Images are adapted with permission from [117], calculations conducted by Daniele Stradi.*

Therefore we assume a weak interaction between the graphene layer and the substrate, leading to a confined silver surface state at the interface. In the contrary, publications of strongly interacting systems such as graphene on Ni(111) [371] and Ru(0001) [372] report a surface state evolving into an interface state.

Discussion By fitting bias dependent wave vectors of the surface state to Equation 6.1, as plotted in Figure 6.1 (d) we obtain $m^* = 0.35\ m_e$ for Ag(111) and $m^* = 0.32\ m_e$ for graphene/Ag(111). Our calculations show that the characteristic Dirac cone of graphene at the K point is preserved but shifted below the Fermi level by 0.57 eV, indicating a physisorbed n-doped graphene [117]. This down shift is caused by a charge transfer between graphene and the metal support, resulting in a depopulation of the surface state. The experimentally measured blueshift of the G band in Raman spectroscopy is in good agreement with our findings [174]. While the direction of the charge transfer points to an increase in the work function of the system, our calculations result in a decrease, which stands in line with calculations in [358, 373]. The decrease of the work function upon adsorption of the physisorbed layer is caused by a Pauli repulsion induced interfacial dipole. The contributions of this dipole dominate over the influence of the charge transfer on the work function.
As the graphene layer is only weakly interacting with the metal surface, we expect the effective mass to be mainly determined by the Ag(111). Here we observe a reduction of the effective mass by ~ 10 %, which is consistent with literature [183, 368].

6.2.2 Electronic properties of graphene/Cu(111)

To characterize the graphene/Cu(111) interface we again investigated the Shockley-type surface state by analyzing its dispersion and compare the results to the graphene/Ag(111). Furthermore, we quantify variations in local work function between graphene and Cu(111) regions and local work function modifications for different positions of the graphene/Cu(111) Moiré pattern and furthermore for different Moiré periodicities.

STM investigations of the Shockley-type surface state for graphene/Cu(111) We analyzed the dispersion relation of the Shockley-type surface state for graphene on Cu(111). Figure 6.3 (a) depicts the region where we measured the surface state standing wave pattern for different applied biases. Additionally, we determined the surface state onset energies for Cu(111) and graphene/Cu(111) from STS as shown in Figure 6.3 (b). The surface state energy E_0 on Cu(111) (red) is found at $E_{0,Cu(111)} = -0.44$ eV and an energetically upwards shifted surface state onset for the graphene/Cu(111) system (green) is observed at $E_{0,G} = -0.31$ eV. The upwards shift by $\Delta E_{Cu(111)} \sim 130$ meV is in the same order of magnitude as for graphene on Ag(111) ($\Delta E_{Ag(111)} \sim 170$ meV see above) and is in accordance with [183]. The dispersion relation is plotted in Figure 6.3 (c) and fitted according to Equation 6.1. From the parabolic fit we estimated the effective mass to $m^* = 0.384\ m_e$ close to values in literature of $m^* = 0.386\ m_e$ and considerable smaller than the effective mass on bare Cu(111) with $m^* = 0.420\ m_e$ [183].

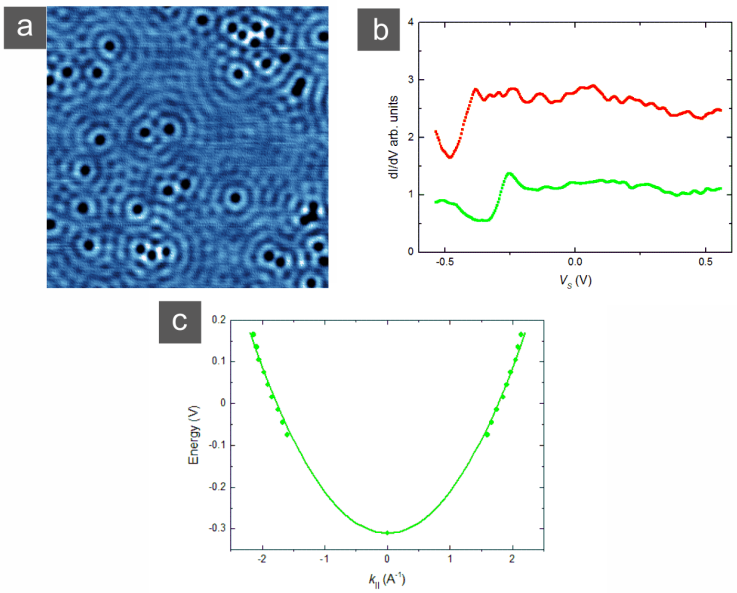

Figure 6.3: *Dispersion relation of Shockley-type surface state of graphene/Cu(111). (**a**) Graphene on Cu(111) revealing the standing wave pattern of the Cu(111) surface state. (**b**) STS of the surface state on Cu(111) (red) and on graphene/Cu(111) (green). (**c**) Dispersion relation of the surface state exhibits a reduced effective mass of $m^* = 0.386\ m_e$ on graphene/Cu(111) compared to $m^* = 0.420\ m_e$ on Cu(111).*

STM investigations of the work function of graphene/Cu(111) To investigate the local work function of graphene on Cu(111) we used CVD grown graphene islands with different Moiré patterns. Figure 6.4 (a) shows a graphene island with three distinct orientational domains. In region (i) we observe a Moiré pattern M1 with a periodicity of $a_1 = 5.0$ nm, in region (ii) a Moiré pattern M2 with periodicity of $a_2 = 2.7$ nm, and no apparent corrugation for region (iii). FER spectra can be used to estimate the local work function of surfaces and its spatial variation [374–380]. Figure 6.4 (b) shows two FER spectra of graphene/Cu(111) for the tip positioned on a wire (green) and on a pore (red) region. A shift of the FER peaks to higher energies for the pore region within the given energy resolution of 17 meV is observed.

We applied two different methods to evaluate the local work function variations along the Moiré patterns from our FER measurements. (i) A simple approach is shown in Figure 6.4 (c), where we plot the energy shift between pore and wire (compare Figure 6.4 (b)) for each of the eight measured FER resonances [183, 381]. The blue dots correspond to the M1 with large periodicity and the pink dots to the smaller Moiré pattern M1. For the large Moiré pattern we find FER energy shifts between pore and wire of $\Delta E_n \approx 50$ meV, which reduces for higher order resonances to $\Delta E_n \approx 35$ meV. This reduction for higher order resonances is due to an increased spatial averaging effect of the FER method, caused by the higher applied voltages [183, 381]. For the smaller Moiré pattern M1 we find a shift in the first two FER resonances of $\Delta E = 17$ meV, which reduces below the resolution limit of the measurement for higher orders. Therefore we estimate from this approach a work function difference between pore and wire of $\Delta\Phi_{M1} \approx 50$ meV for the large and $\Delta\Phi_{M2} \approx 17$ meV for the small Moiré.

Note that from the FER measurements it is not clear if the deviations between M1 and M2 are caused by the orientation dependent graphene-Cu(111) interaction or due to the higher impact of the averaging effect in the FER experiment for smaller Moirés.

(ii) A more accurate determination of local variations in the work function is accessible via the so-called Gundlach expression [374, 376]:

$$E_n = \Phi + \alpha(n - 1/4)^{\frac{2}{3}} \tag{6.2}$$

Here, E_n is the energy of the nth FER resonance, Φ is the local work function, n the number of the FER resonance and α a field and geometry dependent constant. In Figure 6.4 (d) the E_n on a graphene islands are plotted as green dots against $(n - \frac{1}{4})^{\frac{2}{3}}$. The red line is the corresponding fit according to Equation 6.2. For the fit we included all data with $n > 1$. The interception point of the red fit and the y-axis defines the local work function,

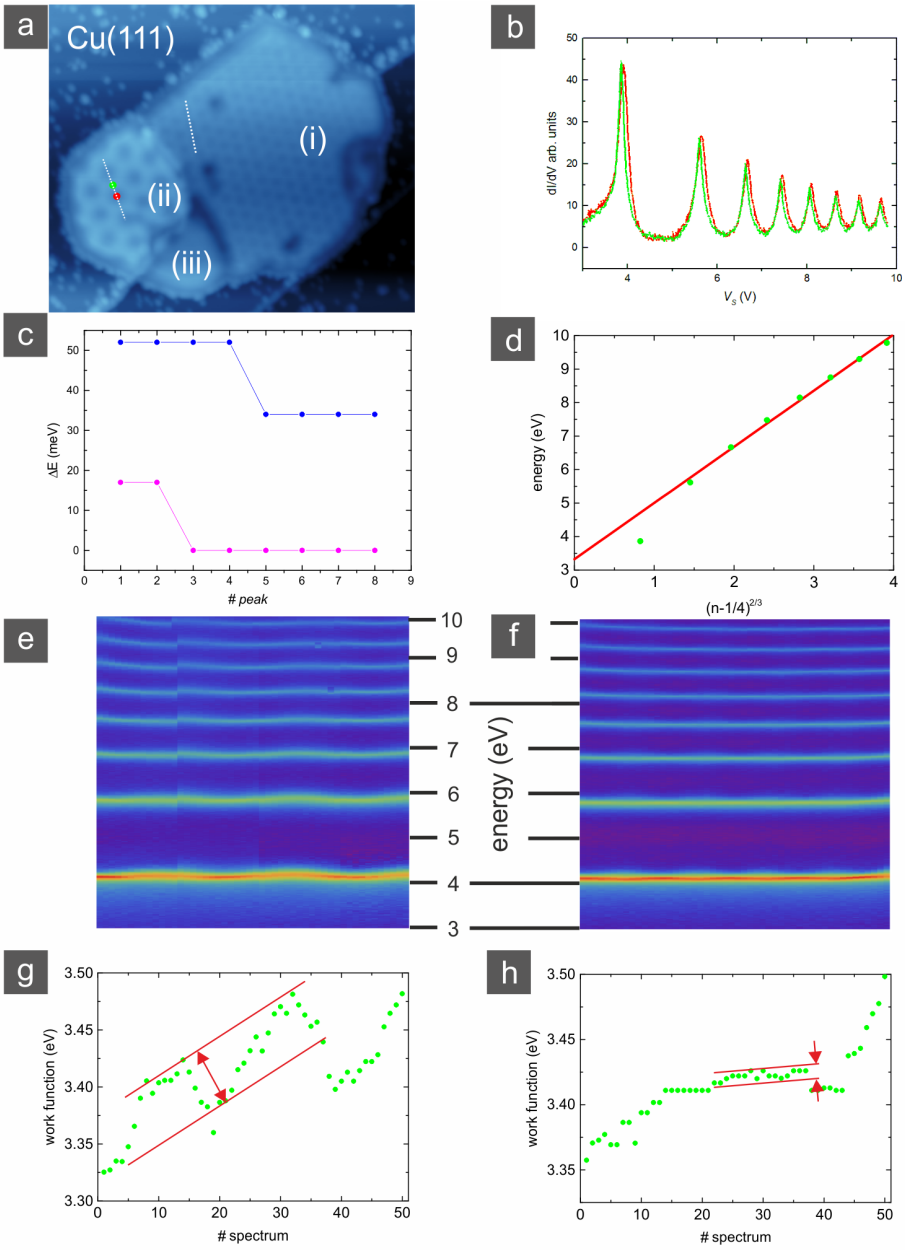

Figure 6.4: *Electronic properties of graphene/Cu(111): (**a**) CVD grown graphene on Cu(111) with two different Moiré patterns, exhibiting periodicities of $a_1 = 5.0$ nm and $a_2 = 2.7$ nm ($V_S = 3.9$ V, $I = 200$ pA). (**b**) FER taken at different Moiré positions as indicated with the green (wire) and the red (pore) dots in (**a**). A slight shift of the FER peak to higher energies is observed for the pore (red) compared to the wire (green) position. (**c**) Depicts the energy shift of the FER peaks between pore and wire region for the M1 (blue) and the M2 (pink) Moiré pattern for eight measured FER resonances. This shift can also be used for a local work function determination and reduces with higher order resonances due to a lateral averaging effect of the FER measurement. (**d**) The peak energies are fitted according to the Gundlach expression. The point of intersection of the fitted curve (red line) with the y-axis defines the local work function. (**e**) and (**f**) depict 50 STS spectra measured along the dashed lines in (**a**): (**e**) for Moiré M1 and (**f**) for M2. (**g**) and (**h**) show the corresponding work functions obtained from the Gundlach fit for the 50 STS spectra. The red parallel lines are used to determine the work function shifts between pore and wire regions.*

with $\Phi_{graphene/Cu(111)} = 3.41 \pm 0.3$ for graphene/Cu(111). For comparison, on the bare copper surface we found a $\Phi_{Cu(111)} = 4.22 \pm 0.1$, in accordance with literature [183]. The corresponding reduction of the local work function upon graphene adsorption of $\Delta\Phi \approx 800$ meV is in good agreement with [183, 358, 359]. To evaluate the work function modification along the Moiré patterns we measured FERs along the dashed white lines in Figure 6.4 (a). Figure 6.4 (e) ((f)) show 50 spectra each, taken across M1 (M2) starting from top to down. In both cases we clearly observe eight FER resonances, which show slight variations in intensity and energy as the tip is moved along the Moirés. The variations in intensity are due to the current defined starting point that was used for the STS measurements. For the work function determination, we fitted the peak energies for all of the spectra depicted in Figure 6.4 (e) and (f) to Equation 6.2 and extracted Φ from the corresponding fitting parameters. The obtained work functions are plotted in Figure 6.4 (g) (corresponds to M1 and Figure 6.4 (e)) and Figure 6.4 (h) (corresponds to M2 and Figure 6.4 (f)). Both graphs exhibit similar values for $\Phi \sim 3.4$ eV and an increase of the work function for higher spectra numbers on the x-axis. This increase in work function for subsequent spectra is most likely due to sample drift or creep. However, by introducing parallel lines as shown in Figure 6.4 (g) and (h) we can approximately compensate for drift/creep and obtain the variation of the local work function caused by the different Moiré positions. Doing this we acquire work function differences along M1 of $\Delta\Phi_{M1} \approx 50$ meV and $\Delta\Phi_{M2} \approx 10$ meV for M2, in excellent agreement with method (i) (see Figure 6.4 (c)).

Discussion Similar to graphene on Ag(111), we also observe a reduction of the effective mass of the surface state electrons and a reduction of the local work function upon graphene adsorption on Cu(111). From photoemission experiments we know that graphene on metal substrates exhibits n-doped behavior [172, 382]. However, similar to the Ag(111) case, the work function reduces upon graphene adsorption due to the formation of a dipole at the graphene Cu(111) interface [183]. We reproduced the work function modification upon graphene adsorption on Cu(111) [183, 359] in accordance with theory [358]. Furthermore, we investigated the subtle Moiré induced work function variations. These small variations between pore and wire regions are replicated for M1 with ~ 50 meV and M2 with $\sim 10 - 15$ meV by applying two different evaluation methods. As the FER experiments require relatively high voltages, the lateral resolution of the measurement is limited. In Figure 6.4 (c) we observe a reduction of ΔE at higher FER orders. Therefore, we conclude that due to the spatial resolution of the FER method, the values of the obtained work function variations along the Moiré are lower boundaries.
Such Moiré induced electronic corrugations of two-dimensional layers on metal supports can be used to guide the adsorption of molecules and to shift the energy levels of the molecular orbitals [27, 126–131]. In contrast to insulating h-BN, graphene exhibits a high electronic conductivity, which enables electronic contact with such molecular assemblies. In Chapter 7 the porphines on graphene/Ag(111) and graphene/Cu(111) are investigated.

6.3 Geometric corrugation of graphene/Cu(111)

Two-dimensional layers can reveal periodic geometric and electronic corrugations, caused by the lattice mismatch with the underlying substrate [360–363]. For graphene, additional local distortions such as wrinkles influence the thermal [365], electronic [383–386] and magnetic [364] properties of a graphene monolayer. In order to correlate the geometry of graphene with its intrinsic properties, it is crucial to quantitatively determine the geometric topography.
However, STM fails to quantify the geometric corrugation of a corrugated Moiré pattern. In several studies, combined surface sensitive experiments such as STM, nc-AFM and complementary DFT calculations were applied to investigate the Moiré lattice of different systems. Most reports concentrate on graphene/metal systems with supports such as Rh(111) [387], Ir(111) [388, 389], and Ru(0001) [390]. Furthermore, different two-dimensional materials such as h-BN on Rh(111) [391] and silicene on Ag(111) [392, 393] are of current interest for the scientific community [394]. The most comprehensive investigated system so far is graphene on Ir(111), where the Moiré induced corrugation was characterized in exquisite detail. Amongst others, complimentary methods such as STM, nc-AFM [389, 395, 396], low-energy electron diffraction (LEED) [396], x-ray standing wave (XSW) [397], surface x-ray diffraction (SXRD) [398], extended x-ray reflectivity (EXRR) [398], and DTF calculations [394, 396–398] were applied. The pore regions are found to be further separated from the Ir(111) surface than the wire regions and the quantitative results for the geometric corrugation range from $\Delta z \sim 35$ pm to $\Delta z \sim 97$ pm.
Hamalainen et al. achieved good agreement with DFT calculations using nc-AFM. They extracted the geometric corrugation from constant frequency shift Δf scans with a CO terminated tip [396]. They claim that for an chemically inert tip and the scanning being executed in the repulsive regime the real topography is obtained, as local variations in chemical reactivity or local density of states do not influence the measurement [396]. However they do not consider the following effects:

- Electrostatic forces differ between different positions of the Moiré.
- In a constant Δf experiment, convolution effects of the tip smear out geometric features.
- The vdW background caused by the tip-metal interaction influences the Δf signal depending on the Moiré position as explained in [395]. At Moiré positions, where the two-dimensional layer has a smaller separation from the metal support a increased vdW background between tip and metal is observed.
- Tip induced distortions of the graphene layer [390, 399].

In the following we present the local Δf amplitude method [123], for a more accurate determination of the Moiré corrugation on graphene/Cu(111). We compare the obtained height distribution to estimated height differences from $\mathrm{d}\Delta f/\mathrm{dz}$ spectroscopy as described in [91].

Therefore we took dΔf/dz spectra at both, pore and wire positions, in order to determine the geometric corrugation by the comparison of particular points in the dΔf/dz spectra.

Δf amplitude method [123] For our measurements we did not functionalize the tip on purpose. Metal tips can easily image the atomic contrast of carbon based systems like graphite and graphene [400–407]. We obtained the geometric corrugation of the graphene layer by establishing a correlation between the atomic contrast measured in the Δf signal in constant height mode and the tip-surface separation. To this end, a series of small size constant height images of 1×1 nm^2 at different tip heights are measured.
In Figure 6.5 such series are presented for the pore and the wire regions . To reduce the influence of noise and background contributions we processed the images using a Gaussian low-pass ($\sigma = 0.03$ nm) and a Gaussian high-pass filter ($\sigma = 0.15$ nm). As a next step the local Δf amplitude ($A_{\Delta f}$) was estimated, which we define as $\Delta f_{max} - \Delta f_{min}$ within a defined area. $A_{\Delta f}$ is determined at each pixel of the small-size images by calculating $\Delta f_{max} - \Delta f_{min}$ within a surrounding square box with side lengths of 0.275 nm, slightly exceeding a graphene unit cell. The $A_{\Delta f}$ values are then averaged over the whole small-size image and assigned to a relative tip height as shown in Figure 6.6 (b). These calibration curves are measured for increasing tip sample distances and also for the opposite direction to demonstrate the small influence of drift and creep. For pore and wire regions such calibration scans are performed as shown in Figure 6.5.

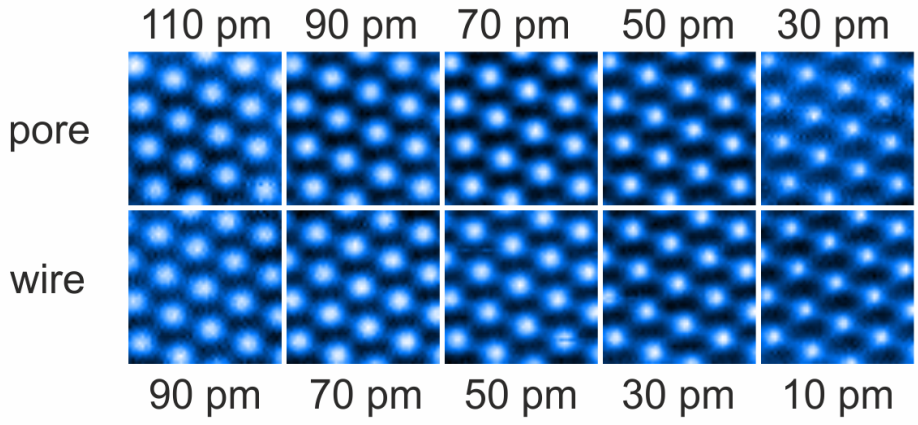

Figure 6.5: *Geometric corrugation of graphene/Cu(111). Small-size* 1×1 nm^2 *constant height AFM images used for the calibration curve shown in Figure 6.6 (b). The pore images (upper row) are shifted by* 20 pm *compared to the lower row wire images. The appearances of the pore and wire images in the same column show high resemblance.*

For a certain range of $A_{\Delta f}$ the calibration curves in Figure 6.6 (b) can be fitted with a linear slope. Thus the local tip-sample separation $d_{tip-sample}$ can be estimated from the $A_{\Delta f}$ using

the $A_{\Delta f} \propto d_{tip-sample}$ relation. Large scale constant height images, as exemplarily shown in Figure 6.6 (a) are transformed in a calculated height image pixel by pixel, leading to a geometric topograph of the graphene layer as shown in Figure 6.6 (c).

Results of Δf amplitude experiments In Figure 6.6 (a) a constant height AFM image of a graphene layer on Cu(111) is depicted. The graphene lattice is resolved and we clearly observe a Moiré pattern with periodicity of 5 nm. The contrast of the Moiré lattice does not directly correspond to the geometric height of the region as it can be inverted due to the tip termination [123].
The measured calibration curves for pore (green) and wire (red) regions are depicted in Figure 6.6 (b).

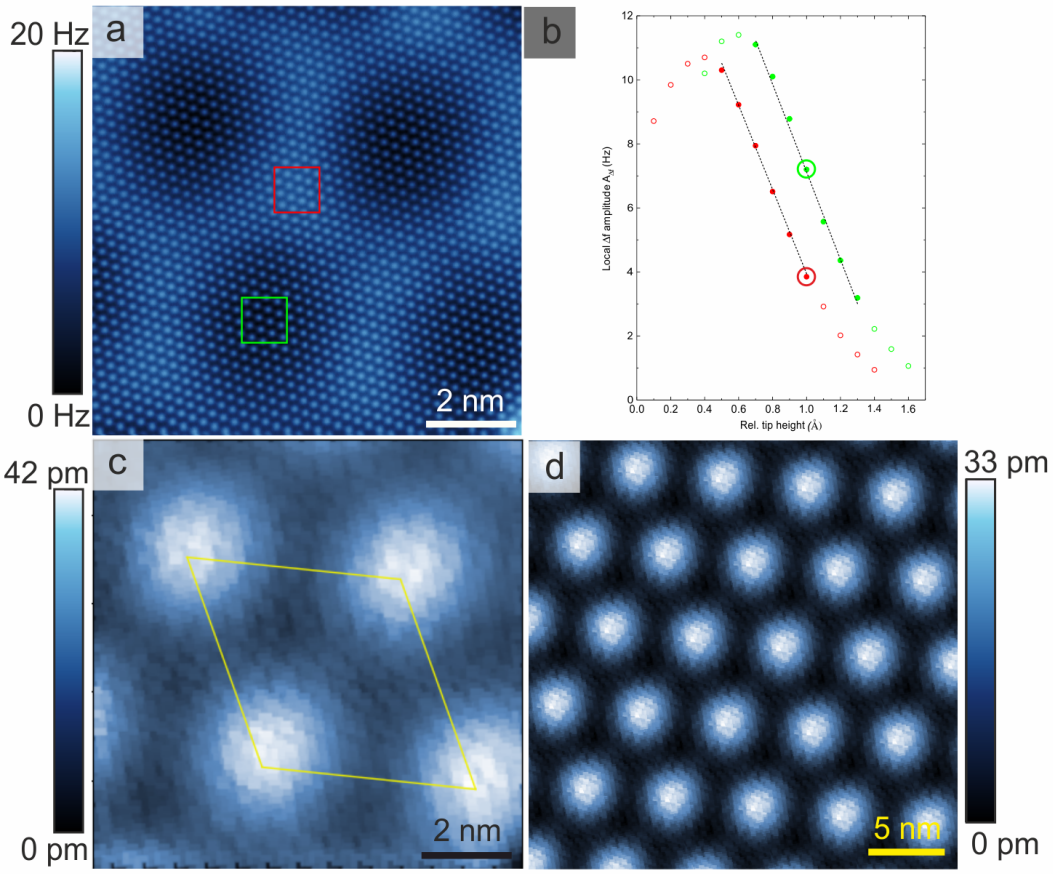

Figure 6.6: *Geometric corrugation of graphene/Cu(111).* ***(a)*** *Δf channel of constant height AFM image, revealing atomically resolved graphene on Cu(111) ($V_{sample} = 0$ V).* ***(b)*** *$A_{\Delta f}$ vs. relative tip height calibration curves for pore (green) and wire (red). The dashed lines are a linear fit to the solid dotted data points. The two encircled points represent the atomic contrast of the highlighted rectangle in* ***(a)*** *at a relative tip height of 1.0 Å.* ***(c)*** *Calculated geometric height map of the graphene with drawn unit cell.* ***(d)*** *An array of the obtained unit cell reveals a regular Moiré pattern.*

The calibration curves exhibit very similar signature for the pore and the wire regions except that they are shifted in the relative tip height. Three regions of the calibration curves are found: (i) For large tip sample distances the local Δf amplitude ($A_{\Delta f}$) is increasing super linear while the tip approaches the surface. The obtained $A_{\Delta f}$ in this region is relatively small and the noise level has a relevant impact. (ii) By further reducing the relative tip height (r.t.h.) the local $A_{\Delta f}$ reveals a linear increase. The dashed lines are fits to the experimental data (solid dots) in the calibration curves with $A_{\Delta f} \propto$ r.t.h., exhibiting good accordance with the measured data sets. The larger red and green circles in the linear region correspond to the $A_{\Delta f}$ of the 1×1 nm^2 squares highlighted in Figure 6.6 (a). The two data points are located at the same r.t.h. as the image in Figure 6.6 (a) was recorded in constant height mode. (iii) For even smaller tip sample separations a maximum is reached, before $A_{\Delta f}$ starts to decrease again. Consequently we have to keep in mind that for small tip sample distances the $A_{\Delta f}$ is not unambiguously correlated with the r.t.h. However all the presented height measurements were recorded in the linear regime of the calibration curves.

We now used the obtained slope of the calibration to transform the local $A_{\Delta f}$ in Figure 6.6 (a) to a calculated geometric height. The result is shown in Figure 6.6 (c). The pore regions are further separated from the Cu(111) substrate than the wire regions. The obtained height distribution has a maximum width of 42 pm within one unit cell. To evaluate the geometric corrugation, we assign the minimum width including 95% ($\sim 2\sigma$ of a Gaussian distribution) of a height histogram to the maximum height difference between pore and wire regions.

The Moiré unit cell with its periodicity of 5.0 nm is drawn in Figure 6.6 (c). In Figure 6.6 (d) a superlattice of the Moiré is shown proving that the determined unit cell has the correct dimensions.

In Figure 6.6 (a)-(c) we determined a geometric Moiré corrugation of 22 pm.

To increase the validity of our Δf amplitude method, we performed several geometric corrugation experiments with different tip terminations, absolute tip heights z, oscillation amplitudes, and Moiré sizes as shown in Table 1. We obtain an average geometric corrugation of 23.5 pm $\pm$ 3 pm for graphene on Cu(111). We do not observe an increase or decrease in the measured corrugation upon decreasing tip-sample separation. Furthermore the oscillation amplitude of the qPlus sensor does not affect the measurement in a relevant way.

Experiment	corrugation (pm)	Δz (pm)	Amplitude (pm)	Moiré periodicity (nm)
1	25 22 23 27 29 26 24	0 -10 -20 -50 -70 -80 -90	80	5
2	23 17 19 24	0 -10 -20 -80	80	6.1
3	24 28	0 0	60	6.1
4	20 22	0 0	80	3.7

Table 1: *Overview geometric corrugation experiments. Experiment: Experiment 1, 2, and 4 were measured at different positions with different tips. In experiment 2 and 3 we used the same position and same tip, but different oscillation amplitude. Corrugation: Minimum value where 95% of the height distribution of an unit cell are covered. Δz: negative values correspond to an approach of the tip towards the sample. Amplitude: Oscillation amplitude of the cantilever. Moiré periodicity: Size of the Moiré unit cell.*

Complementary methods to determine geometric corrugation. We performed two complementary experiments to determine the geometric corrugation of graphene/Cu(111) and to compare the results to the Δf amplitude method:

- Constant Δf scans
- dΔf/dz spectroscopy

In Figure 6.7 (a) a constant Δf image of the graphene/Cu(111) system is depicted. In Figure 6.7 (b) a typical dΔf/dz spectra of the graphene/Cu(111) is shown. The red dot corresponds to $\Delta f = 37$ Hz, which is used as set point in the constant Δf measurement in Figure 6.7 (a). The determined corrugation from Figure 6.7 (a) is 17 pm. Depending on the Δf set point and the tip apex we observe corrugations ranging from $2 - 17$ pm.
The dΔf/dz method is presented in Figure 6.7 (b)-(d). To get information about the height differences between pore and wire regions we compare the respective dΔf/dz curves [91]. Figure 6.7 (b) depicts a typical spectrum exhibiting a lower turning point and a strong increase of Δf for further decreasing tip-sample distances. A zoom-in to the turning point in the dΔf/dz curves is presented in Figure 6.7 (c). The red graph belongs to the wire regions, whereas the green graph was measured at a pore region in Figure 6.7 (a). Depending on the tip location

on the atomic scale (center of carbon atom or center of honeycomb or above C-C bonds) shifts in the position of the Δz turning point are observed [388]. Therefore, the spectra shown in Figure 6.7 (c) are averaged over 64 spectra taken with small lateral shifts. We identify a shift in Δz between pore and wire of roughly 2 Hz and a difference in relative tip height of 22 pm. The downshift in Δf for the wire region might be caused by additional vdW contribution due to the increased tip-Cu(111) interaction as modeled in [395] or by electrostatic contributions. In Figure 6.5 (d) we overlay the spectra of pore and wire and obtain a good accordance in shape.

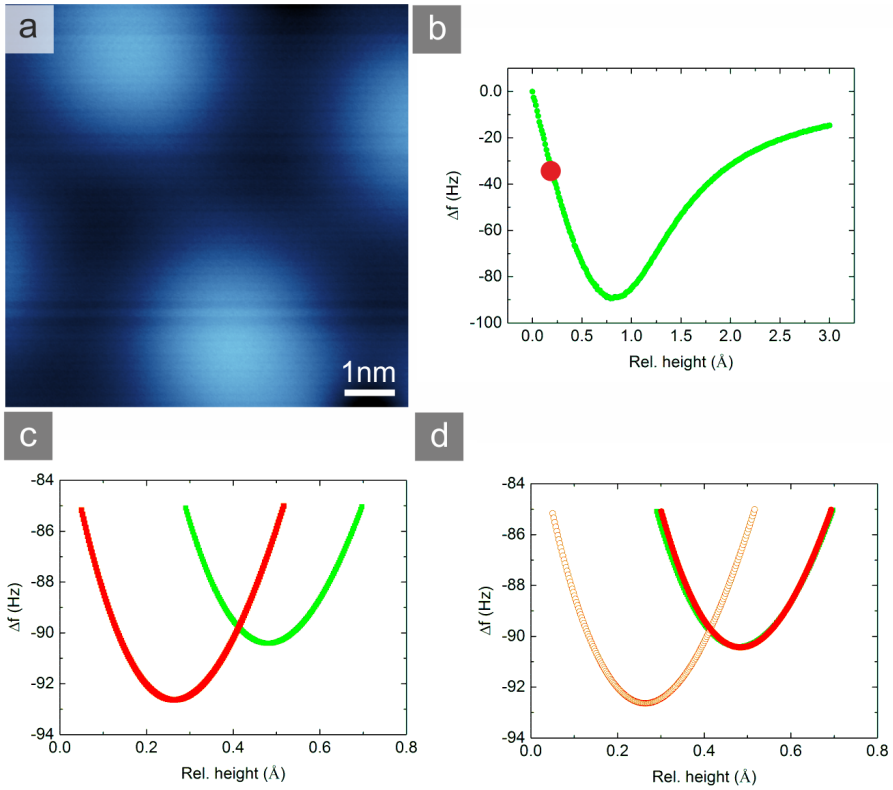

Figure 6.7: *Complementary determination of graphene/Cu(111) corrugation.* ***(a)*** *Constant Δf image of graphene/Cu(111) Moiré with periodicity of* 6.1 nm. *Δf is set to* 37 Hz *in the repulsive regime as highlighted by the red dot in* ***(b)****.* ***(b)*** *Typical long range $d\Delta f/dz$ spectra revealing the specific turning point.* ***(c)*** *Zoom-in to the turning points for the pore (green) and the wire (red) region. The turning points are shifted by $\Delta f = 2$ Hz and $\Delta z = 22$ pm.* ***(d)*** *Illustrates the high accordance in shape of the two different spectra.*

Discussion of the geometric corrugation of graphene/Cu(111) We obtained a geometric corrugation of 23.5 pm $\pm$ 3 pm for graphene on Cu(111) applying the Δf amplitude method. Our method exhibits extraordinary accuracy as explained in the following.

Compared to the range of values obtained for the constant frequency shift measurements of $2 - 17$ pm, our results from the Δf amplitude method exhibit much higher reproducibility. We overcome the above described issues of the constant Δf method, namely the electrostatic and

additional vdW contributions. In our method we determine the local variations of Δf only on the atomic scale. Within such small lateral displacements the long range vdW background and the electrostatic contributions effecting the tip can be assumed to be constant. Therefore the influence of the background vdW and the electrostatic on the local Δf amplitude are diminished. Furthermore, as our method images the sample in constant height mode, we reduce the smearing out of features on the surface, which appears for the constant Δf method due to enhanced convolution effects of the tip apex.
The smearing out of features in the Δf method as well as the vdW background contributions lead to a decrease in the measured geometric corrugation [395]. Consequently, the obtained maximum value of 17 pm in our constant Δf experiments is smaller than the value of 23.5 pm obtained by analyzing the Δf amplitude.
The $\mathrm{d}\Delta f/\mathrm{dz}$ method overcomes the smearing out effects but is still influenced by the vdW background and the electrostatic contributions. Furthermore, for this method an accurate plane correction is more crucial compared to our Δf amplitude method. However the obtained geometric corrugation of 22 pm is in good agreement with our Δf amplitude method.
Our method allows to determine the geometric topography spatially resolved over large areas as long as the surface can be imaged with atomic contrast. This is outperforming the $\mathrm{d}\Delta f/\mathrm{dz}$ method, which is applied very locally. Furthermore, in case of stronger corrugated systems the Δf amplitude method might be applicable with an additional two-pass correction [90].
Nevertheless, all three presented methods do not take into account possible tip induced deformations of the graphene. However, we have several arguments showing that the influence of the different deformation behavior of pore and wire has no large impact in our experiments.

- If graphene is deformed differently for different positions, we would expect variations in the slope of the calibrations curves in Figure 6.6 (b).
- If we compare the small-size calibration images taken at pore and wire with an offset of 20 pm as depicted in Figure 6.5, the images reveal high resemblance. This points to similar tip-sample interaction.
- Assuming a less strongly bound graphene at the pore regions, which leads to an easier deformation of the graphene layer, we would expect a decrease in the geometric corrugation upon decreasing the tip-sample distance in the repulsive regime.
- We do not observe a relevant signature in the dissipation channel, which is associated to strong graphene deformations [408].

All of these four observations point to a negligible influence of the variations in the deformation behavior of the graphene on the Cu(111) support.

Comparison geometric and electronic corrugation For the investigated graphene/Cu(111) system we obtain a geometric corrugation of 23.5 pm ± 3 pm by averaging over different Moiré patterns. The corresponding work function variations range from 10 to 50 meV, while it is not clear if the determined small $\Delta\Phi$ values are caused by an increased spatial averaging of the applied experimental method.

For h-BN/Cu(111) we found a geometric corrugation of 50 pm, while $\Delta\Phi$ goes up to $\sim$ 250 meV. Even though both two-dimensional layers are only weakly coupled to the Cu(111) support, we identify a five times higher electronic corrugation in h-BN/Cu(111) compared to graphene/Cu(111). In contrast, the geometric corrugation of h-BN/Cu(111) is only twice as high. The weaker electronic corrugation of graphene/Cu(111) might be explained with the intrinsic metallic properties of graphene.

For both systems we found a correlation between the adsorption height of the two-dimensional materials and the local work function. For smaller layer-metal separation a smaller work function is found. This observation stands in line with the work function reduction upon graphene and h-BN adsorption on bare Cu(111): The work function is the stronger reduced the stronger the two-dimensional layer is adsorbed.

In summary we developed a highly precise method to determine the geometric corrugation of two-dimensional layers on metals and revealed a qualitative correlation to the electronic variations across the Moiré patterns.

7 Porphyrins on graphene/Cu(111) and graphene/Ag(111)

Functional molecules open up possibilities for the ultimative down scaling of nano size electronics [7, 14, 23, 51, 409–415]. However, in order to produce molecular nano devices for industrial purposes, fundamental understanding of the molecule-surface interactions has to be acquired. Information on the driving forces for the molecular self-assembly as well as the electronic coupling of molecules to different supports are crucial for the design of devices.
For nano electronics, graphene exhibits extraordinary properties as described in Section 6. The Moiré pattern formed by the two-dimensional layers on metal substrates can be used to steer self-assembly positions of molecules, while the two-dimensional materials decouple molecules from the underlying metal [27].
For highly corrugated graphene on Ir(111) [416–419], Ru(0001) [420, 421] and Rh(111) [422] Moiré-directed adsorption has been reported. For example, metal clusters accumulate in the wire regions of graphene [417, 419, 422]. Also in these systems the local work function in the pore regions exhibits higher values compared to the wires regions [389, 416]. On Ru(0001) the Moiré corrugation was used to form Kagome lattices of iron phthalocyanine and the obtained porous Kagome network [423] was used to host tert-butyl zinc phthalocyanine in their centers [424]. Again the molecules start to preferentially adsorb along the wire regions of the graphene. However, reports of lanthanides on graphene claim a preferential adsorption on the pore regions of graphene/Ir(111) [425, 426].
In the following, low and high coverages of porphines on graphene/Cu(111) and graphene/Ag(111) are presented, investigating the self-assemblies and the electronic structures of the molecules. The porphines exhibit a rather low vdW interaction with the graphene/metal systems. Interestingly, the porphine adsorption positions on graphene/Cu(111) and on graphene/Ag(111) are not influenced by the electronically corrugated Moiré lattice, which stands in contrast to molecules adsorbed, for example on graphene/Ru(0001) [423, 424]. We assign this observation to the relatively small electronic and geometric corrugation of the investigated graphene/metal systems as shown in Section 6.
We show that graphene electronically decouples the molecules from the underlying support similar to insulating two-dimensional layers, such as *h*-BN [27]. Furthermore, for high molecular coverage, we observed a strong electronic screening between neighboring molecular entities, causing an additional energetic shift of the molecular orbitals.
These findings give important insights for design of molecular devices based on graphene.

7.1 Co-P on graphene/Cu(111)

7.1.1 Assembly and electronic structure of Co-Ps on graphene/Cu(111) - low molecular coverage

We deposited Co-Ps on graphene/Cu(111), where the graphene coverage was around 70 %. The graphene was grown via carbon from the e-beam heated carbon rod as described in Section 2. We intended to investigate the self-assembly and the electronic structure of the Co-Ps. Especially the DOS resonances associated with the Co centers contain information about the coupling of the molecule to the support [219].

Assembly of Co-Ps on graphene/Cu(111) For typical molecule deposition rates, and the sample kept at room temperature, we obtained completely covered metal surfaces while the graphene/Cu(111) regions remain empty. Consequently in order to inhibit molecular desorption, we had to decrease the sample temperature to $T_{sample} = 140$ K, resulting in molecular agglomerates on graphene as depicted in Figure 7.1 (a). In contrast, on the bare Cu(111) surface the molecules are randomly distributed.

At $T_{sample} = 140$ K the molecules on graphene are immobilized and they consequently stay on the graphene rather than diffusing to the Cu(111) surface. However the molecules are still mobile enough to accumulate on the graphene to clusters. We found nicely arranged porphines at preparation sample temperatures down to $T_{sample} = 50$ K, evidencing a high mobility of the molecules on graphene/Cu(111).

Furthermore, we did not manage to stably image individual molecules on graphene/Cu(111) at the measurement temperature of $T = 5$ K, what strongly points towards very weak graphene-molecule interaction.

In Figure 7.1 (d), no significant influence of the Moiré pattern on the molecular assembly of the Co-Ps on graphene/Cu(111) is identified. The molecules are mainly attached to defects such as island edges, wrinkles, and impurities. Due to the low preparation temperatures a high impurity density on the surface is observed. Such impurities on the graphene are highlighted with red arrows in Figure 7.1 (b), which is an enlarged topograph of the region framed yellow in Figure 7.1 (a).

The bright species correspond to Co-Ps, which accumulate in the proximity of the highlighted impurities. In the imaged cluster also one 2H-P is found as labeled in Figure 7.1 (b). The green dot defines the position where the STS presented in Figure 7.1 (c) was taken.

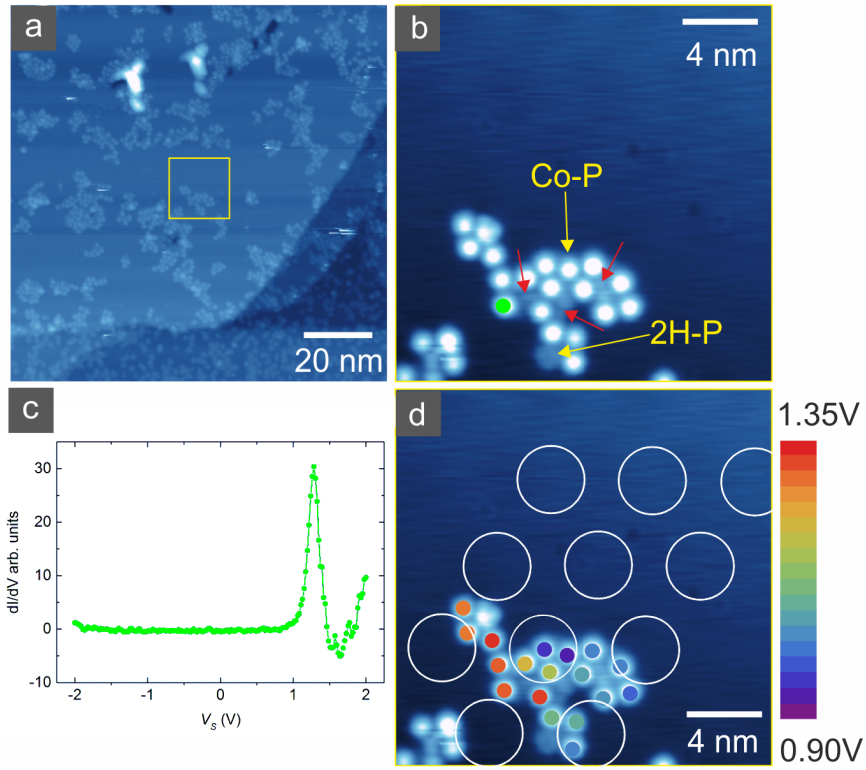

Figure 7.1: *Assembly and electronic structure of Co-Ps on graphene/Cu(111) at low molecular coverage. (**a**) Co-P deposited on a sample kept at 140 K with molecules accumulating in small clusters close to defects such as graphene edges, wrinkles and impurities ($V_S = 1.4$ V, $I = 3$ pA). (**b**) Enlarged molecular cluster, which is framed in (**a**) ($V_S = 1.4$ V, $I = 6$ pA). Bright protrusions correspond to Co-Ps, whereas one 2H-P is observed. The red arrows highlight impurities on the graphene layer. (**c**) Typical STS measurement taken at the center position of the molecule marked in (**b**) by the green dot. (**d**) Same area as depicted in (**b**) ($V_S = 1.4$ V, $I = 6$ pA), where the white circles correspond to the pores of the Moiré pattern. The colored dots correspond to the STS positions and the color code is used to visualize the Co resonance energies for each molecule in the Co-P cluster. The Co resonance energies ranging from $V \sim 0.90$ V (violet) to $V \sim 1.35$ V (red), revealing much larger variation as expected from the local work function variations of graphene/Cu(111). Furthermore, the energy shift of the Co peaks does not directly correlate with the Moiré corrugation or the number of neighboring molecules.*

STS of Co-Ps/graphene/Cu(111) The Co related resonances in STS carry information about the strength of coupling of molecular adsorbates with metal substrates [219]. The spectrum of Co-P on graphene/Cu(111) reveals a pronounced peak at $V_{sample} = 1.2$ V, which is attributed to the Co DOS [126, 214]. The relatively sharp Co-peak, as well as the NDR for higher sample biases, point towards an efficient decoupling of the Co-P from the underlying metal [219]. For higher energies the DOS increases again due to the lowest unoccupied molecular orbital (LUMO) of the Co-P molecule. The HOMO orbitals appear for energies below ~ -2.0 eV.

The STS reveals an apparent band gap between HOMO and LUMO of $\Delta Egap \sim 3.7$ eV, in good accordance with decoupled porphines on h-BN/Cu(111) [27] and substantially smaller than $\Delta Egap \sim 5.0$ eV for porphines in the gas phase [427, 428].

In comparison, STS of Co-P on Cu(111) reveals no sharp features, as shown in Figure 7.5.

Figure 7.1 (d) presents the same region as Figure 7.1 (b), with an overlay of white circles, which highlight the pore positions of the graphene Moiré pattern with periodicity of 5.0 nm. The colored dots are the positions where we measured STS and the energy of the Co resonance is color-coded.
We obtain a large shift of the Co resonance energies up to $\Delta E_{Co} = 400$ meV, which substantially exceeds the work function differences of $\Delta\Phi \sim 50$ meV for different Moiré positions (see Section 6.2.2). Additionally the variations ΔE_{Co} are not directly correlated with the Moiré corrugation. We also do not observe a clear correlation between the peak energy and the number of neighboring molecules, which can influence the screening of the molecular electronic states. Therefore we conclude that the adsorbed impurities on the graphene might influence the electronic structure of the porphines.

7.1.2 Assembly and electronic structure of Co-Ps on graphene/Cu(111) - high molecular coverage

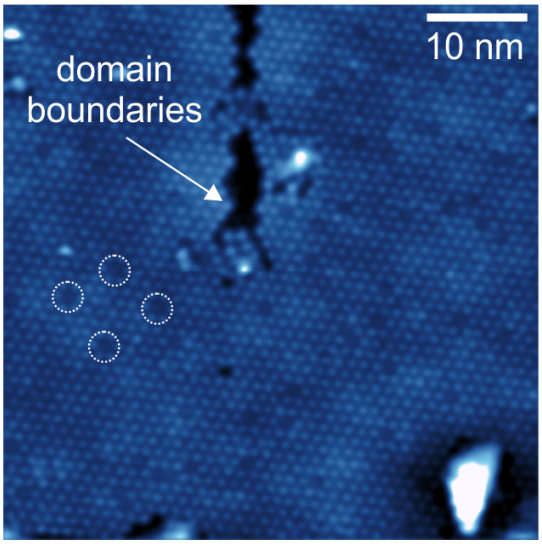

Figure 7.2: *STM topograph of Co-Ps completely covering a graphene layer on Cu(111) ($V_S = 2.6$ V, $I = 5$ pA). Spatially extended molecular arrangements are observed, which reveal hexagonal ordering with NN-distances of 12 Å. The slightly dimmer molecules highlighted by the dashed white circles correspond to free base porphines. Furthermore we can identify domain boundaries of the graphene.*

Assembly of Co-Ps on graphene/Cu(111) A different approach to improve the adsorption yield of molecules on the graphene/Cu(111) is to increase the deposition rate of the porphines. For higher flux, individual Co-Ps interact with each other before leaving the surface and thereby their desorption is diminished.
Figure 7.2 presents a sample, where the molecules were deposited at a higher rate, while the sample was kept at room temperature. The higher molecule flux was realized by a higher

evaporation temperature. Note that the Co-P flux at a certain evaporation temperature is decreasing with time, which impedes the quantitative determination of the molecular flux. The resulting surface exhibits a highly ordered arrangement of molecules on graphene, extended over a large area. The Co-Ps reveal a hexagonal packing with a NN-distance of 12 Å. The white dashed circles in Figure 7.2 highlight free base species. Furthermore we assign the region, which is not covered with molecules to domain boundaries of the graphene.

STS of Co-Ps/graphene/Cu(111) - Grid experiment 1

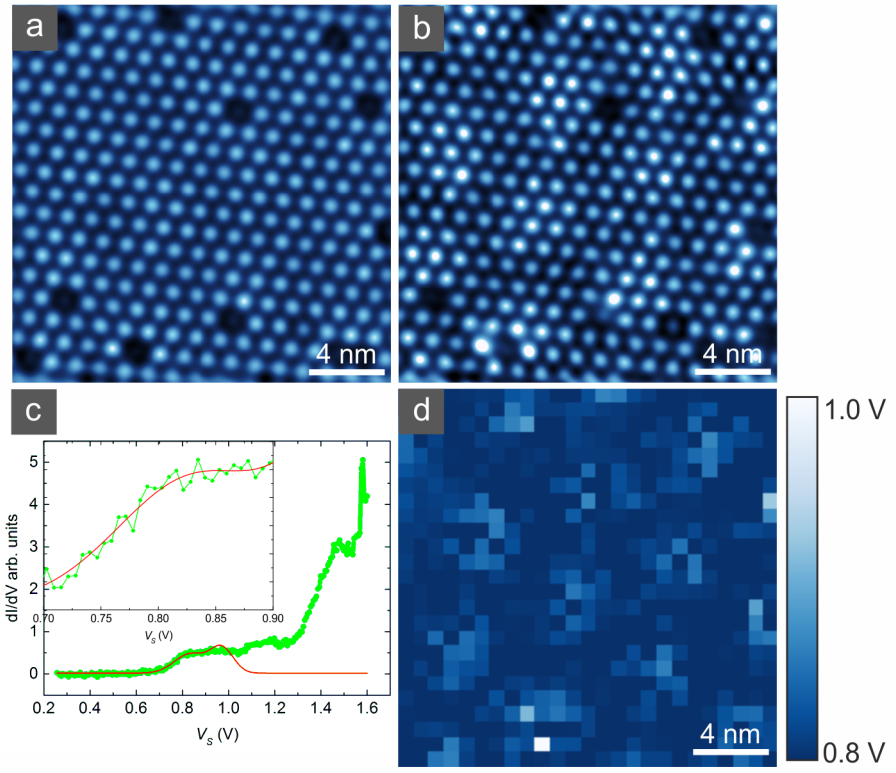

Figure 7.3: *Grid experiment of Co-P on graphene/Cu(111). (**a**) STM image of closed packed Co-Ps (bright dots), including dimmer 2H-Ps ($V_S = 1.5$ V, $I = 5$ pA). (**b**) Topograph of same area as shown in (**a**) at different bias revealing the underlying Moiré pattern ($V_S = 2.0$ V, $I = 5$ pA). (**c**) Typical STS (green points) exhibiting strongly broadened features, which are superimposed with a featureless increase in the DOS for higher biases. The red line is a fit to the data in the range of $V = 0.8 - 1.3$ V. The inset in (**c**) depicts a zoom-in to the fit revealing good agreement with the measured data points. (**d**) For each point of the grid we extracted the position of the first peak from our fits. The plot in (**d**) shows the same region as (**a**) and (**b**) where the color code corresponds to the peak positions.*

For a comprehensive investigation of the electronic modifications of the molecules caused by the Moiré superstructure, we conducted STS grid experiments as presented in Figure 7.3 and Figure 7.4. Figure 7.3 (a) depicts an island of Co-Ps (bright dots), which includes few darker imaged free base porphines. At an applied bias of $V = 2.0$ V in Figure 7.3 (b) we observe a Moiré periodicity of 6.4 nm. In the STS grid experiment we measured dI/dV spectra at

25×25 positions in the area presented in Figure 7.3 (a) and (b). A typical spectrum is shown in Figure 7.3 (c), where the green points correspond to the measured data. The red line is a fit to the data set applying two Gaussian peaks and a constant offset in the voltage range of $V = 0.8 - 1.3$ V. The fit nicely matches the data as highlighted in the inset in Figure 7.3 (c). Figure 7.3 (d) depicts the same region as Figure 7.3 (a) and (b), where each pixel carries the information of the first peak position of the STS taken at the respective location. The first peak energy, which is color coded, varies from ~ 0.8 V to ~ 1.1 V. We roughly estimate the Moiré induced corrugation of the peak energy to ~ 50 meV, which is slightly exceeding the value found for a line scan experiment with a different tip (compare Appendix A).
Interestingly, even though we can extract the local variations of the peak energies along the Moiré lattice, we do not resolve obvious variations in peak energy and amplitude between 2H-Ps and Co-Ps in the measurements shown in Figure 7.3. Blunt tips and/or tip positions, which are spatially offset from the molecular center might cause this observation.

STS of Co-Ps/graphene/Cu(111) - Grid experiment 2

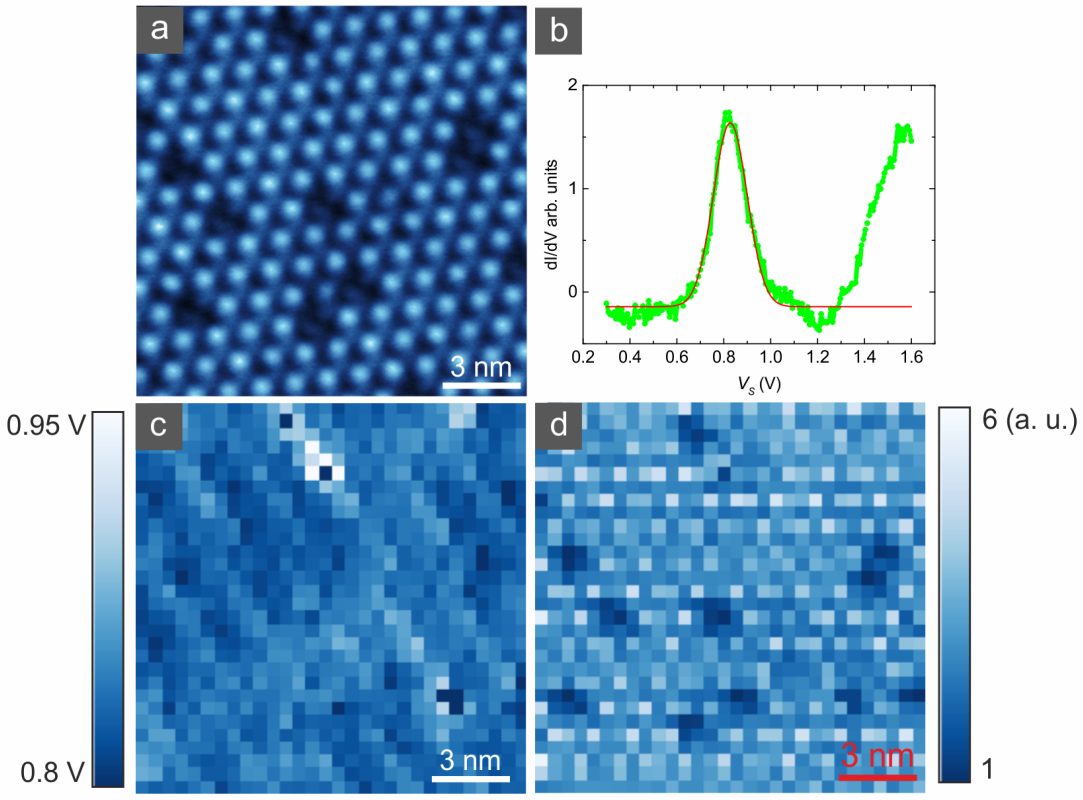

Figure 7.4: *Grid experiment with Co-P on graphene/Cu(111). (**a**) STM image of highly structured Co-Ps (bright dots), interspersed with dimmer 2H-Ps ($V_S = 0.6$ V, $I = 5$ pA). (**b**) Typical grid STS revealing peak around $V = 0.8$ V. (**c**) Corresponding peak position plot with peak energies ranging from $\sim 0.8 - 0.95$ V. (**d**) Amplitude of the fitted STS peaks. Here we can easily identify the 2H-P positions.*

In Figure 7.4 an additional grid experiment is presented. Figure 7.4 (a) shows an STM image of the investigated sample area, which consists of Co-Ps (bright dots) and 2H-Ps (darker dots). The region shown in Figure 7.4 (a) is examined in a 30×30 grid experiment. A typical spectrum is pictured in Figure 7.4 (b). In contrast to the STS in Figure 7.3 (c) we observe a sharp LDOS resonance at $V \sim 0.8$ V, followed by a region with a NDR for higher biases and a strong increase for biases above $V \sim 1.3$ V. We fit the sharp resonance at $V \sim 0.8$ V to a Gaussian peak and a constant offset. The obtained peak position is depicted in Figure 7.4 (c). We do not observe any corrugation in the peak position correlating with a Moiré pattern. The potential reason, that the Moiré lattice periodicity is larger than the investigated region can be excluded as for graphene/Cu(111) the observed Moiré periodicities range from $a = 1.5 - 7.0$ nm [163, 181, 183, 429]. Again we do not identify the free base species in the peak position plot. However, in Figure 7.4 (d) the amplitude of the resonance peak is imaged for each pixel. In the peak amplitude we can clearly distinguish between 2H-Ps and Co-Ps. Therefore we assign the DOS resonance at $V \sim 0.8$ V to originate from the Co center of the porphines.

7.1.3 Comparison between Co-Ps on Cu(111), *h*-BN/Cu(111), and graphene/Cu(111)

Co-Ps on Cu(111) Figure 7.5 (a) shows a Cu(111) surface with Co-Ps deposited at a low coverage of molecules. The Co-Ps are separated from each other due to their charge induced repulsive interaction [211].

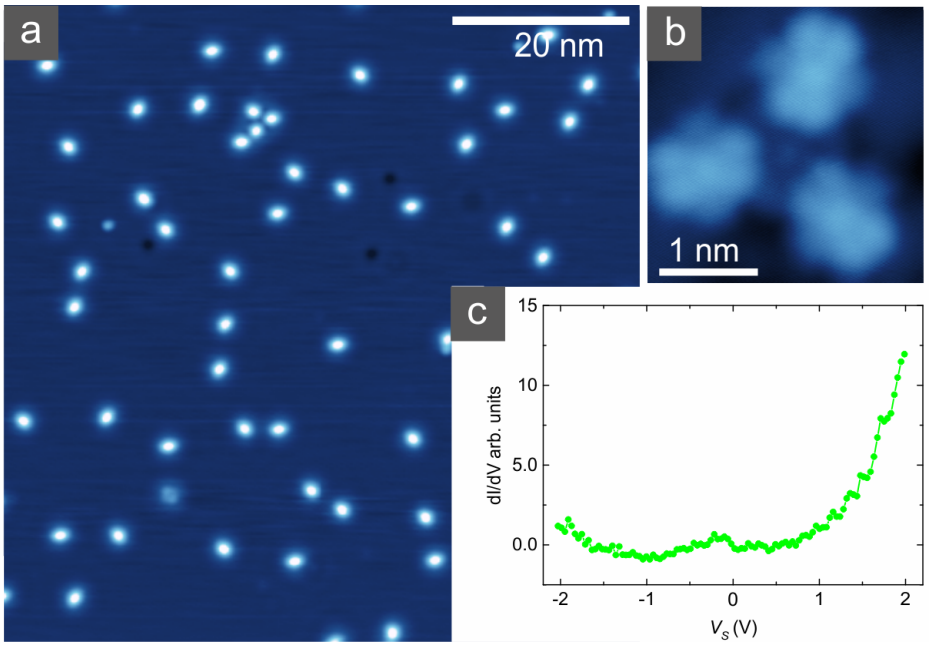

Figure 7.5: *Co-Ps on Cu(111): (**a**) Co-P distributed on Cu(111) at a low molecular coverage ($V_S = -0.65$ V, $I =$ 100 pA). (**b**) Three Co-Ps grouped together in a three fold symmetric arrangement. The molecules reveal a two fold symmetry ($V_S = 60$ mV, $I = 40$ pA). (**c**) Typical STS of a Co-P on Cu(111), exhibiting no sharp features.*

However, in contrast to free base porphine on a metal substrate [211], the molecules exhibit a two fold symmetry [220]. The bright axis of the Co-Ps is aligned perpendicular to the high symmetry axis of the Cu(111) substrate, occupying bridge sites [220]. Furthermore, we obtain groups of molecules arranged in a threefold geometry as depicted in Figure 7.5 (b).
Figure 7.5 (c) depicts a STS of a Co-P on Cu(111). We do not observe sharp features in the STS, however we find a smooth increase of the LDOS for voltages exceeding $V_S \sim 1$ V. The electronic coupling of the molecule to the metal substrate causes the intrinsic molecular electronic states to be broadened, which leads to the measured STS signal [210, 221].

Co-Ps on *h*-BN/Cu(111) Figure 7.6 (a) depicts Co-Ps deposited on *h*-BN/Cu(111) held at room temperature. The image reveals a Moiré periodicity of 6.6 nm. The work function differences between pore and wire of *h*-BN/Cu(111) are quantified to $\Delta E \sim 250$ meV [123],

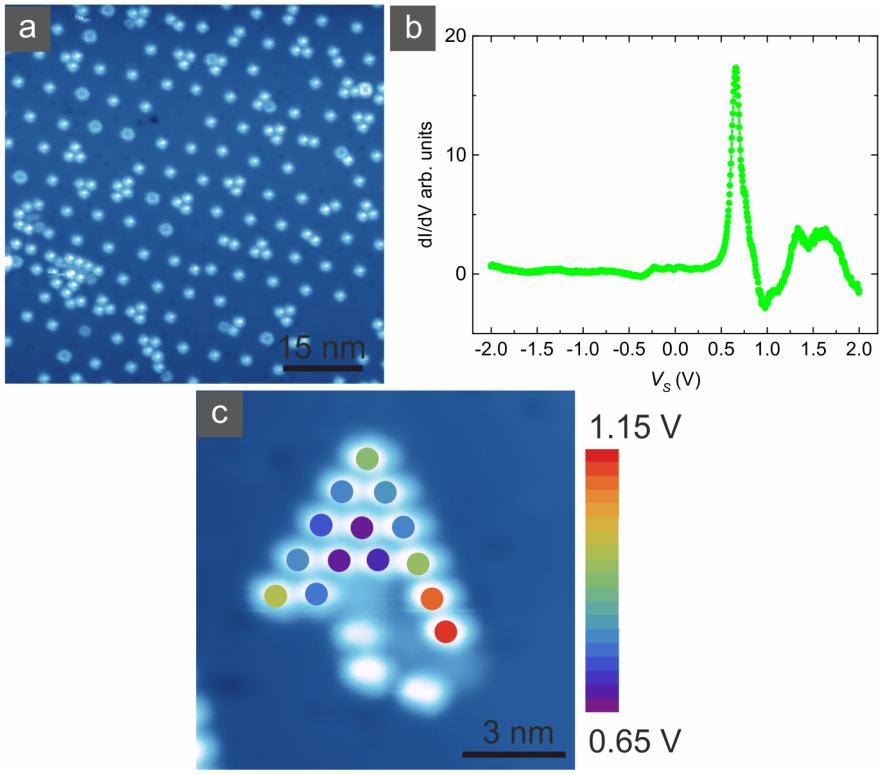

Figure 7.6: *Co-Ps on h-BN/Cu(111). (**a**) STM topograph of Co-Ps (bright dots) and 2H-Ps (molecular species with apparent depression in the center) are distributed on h-BN/Cu(111) ($V_S = 1.25$ V, $I = 40$ pA). Molecules arrange with the Moiré lattice exhibiting a periodicity of* 6.6 nm. *(**b**) Typical STS taken at the center of a Co-P on h-BN/Cu(111). The Co associated resonances are strongly pronounced and a NDR for higher biases is observed. The STS points towards an efficient decoupling of the Co-Ps from the metal support. (**c**) Co-P island trapped in a Moiré pore ($V_S = 1.25$ V, $I = 300$ pA). The colored points visualize the position of the STS and the color code corresponds to the peak position of the Co resonances. The peak energy is reduced in the center of the molecular island.*

which is much larger than for the graphene/Cu(111) with $\Delta E \sim 50$ meV. Furthermore, for h-BN/Cu(111) the pores reveal a lower work function as the wire region, opposite to the graphene/Cu(111) system [27, 116, 123, 235].
In contrast to the porphines on graphene/Cu(111), the molecular adsorption on h-BN/Cu(111) is influenced by the Moiré lattice. The molecules adsorb on the h-BN even at room temperature and are trapped at the Moiré pores [27, 49, 430–432]. On h-BN/Cu(111), the porphines desorb at temperatures exceeding 450 K.
In Figure 7.6 (b) a typical STS of Co-P on h-BN/Cu(111) is depicted, which indicates effective decoupling of the molecules from the metal substrate. We obtain a sharp Co resonance at ~ 0.8 V, which is followed by a NDR region at larger bias. A subsequent increased DOS for higher biases is observed as additional unoccupied molecular orbitals contribute to the STS signal.
The measured STS reveal a very similar signature as the spectra taken on graphene/Cu(111) (see Figure 7.1 (c)). In Figure 7.6 (c) the Co-peak positions are marked by colored dots. Here, the energy of the Co-peaks is reduced for the molecules situated in the center of the molecular island. The observed shift in energy goes up to 0.5 eV within a lateral distance of ~ 1 nm. This large shift can be partly explained with the molecule's position on the Moiré lattice [27], but is mainly influenced by the neighboring molecules [408, 433].

7.2 2H-Ps on graphene/Ag(111)

Complementary to the different Cu(111)-based systems, we investigated the molecular adsorption of porphines on graphene/Ag(111). The graphene was grown from the e-beam heated carbon rod at $T_{sample} = 900$ K. Here we additionally focused on the covalent functionalization of graphene by the molecules.

Assembly Figure 7.7 (a) shows a graphene/Ag(111) sample covered by 2H-Ps. The molecules were deposited while the sample was kept at room temperature.
We observe three distinct regions in Figure 7.7 (a): (i) monolayer 2H-Ps and (ii) bilayer 2H-Ps on Ag(111). The assembly of porphines on Ag(111) is mainly determined by their repulsive interaction and the formation of first and second layer porphine assemblies is described in [211]. The third region (iii) correspond to 2H-Ps on graphene/Ag(111). In the center of the graphene islands the molecules are highly ordered. We found a basis cell with basis vectors $a_1 = 1.3$ nm and $a_2 = 1.2$ nm and an opening angle $\Phi_{a_1 a_2} = 52°$ as depicted in Figure 7.7 (b). The porphines on graphene/Ag(111) and in the first layer on Ag(111) exhibit a square like appearance.

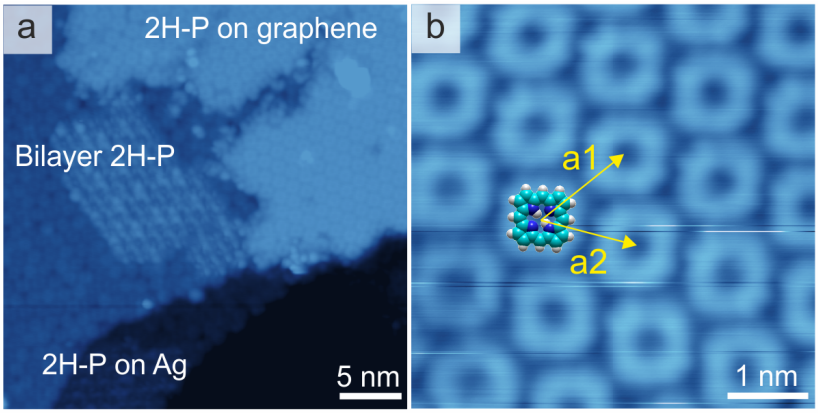

Figure 7.7: *High coverage 2H-Ps on graphene/Ag(111).* ***(a)*** *Three regions are identified: (i) 2H-Ps on Ag(111) and (ii) bilayer 2H-Ps on Ag(111). (iii) 2H-Ps on graphene/Ag(111), which exhibit a highly ordered structure in the center of the graphene layer ($V_S = 1$ V, $I = 50$ pA).* ***(b)*** *Zoom-in of ordered 2H-Ps on graphene/Ag(111) with basis vectors $a_1 = 1.3$ nm and $a_2 = 1.2$ nm and an opening angle $\Phi_{a_1 a_2} = 52°$ ($V_S = 0.8$ V, $I = 60$ pA).*

Figure 7.8 (a) shows a graphene/Ag(111) sample at lower porphines coverage, where the sample was kept at room temperature during porphine deposition. The 2H-Ps were only observed on the graphene, when the Ag(111) surface was completely covered by molecules.
The molecules on the graphene/Ag(111) accumulate at graphene edges, grain boundaries, impurities on the graphene, and defects in the graphene layer. We observe small molecular clusters but also individual molecules, which we can image in a stable way upon applying typical scanning parameters.
While porphines typically exhibit a four-fold symmetry on graphene/Ag(111) the individual im-

aged porphines reveal a depression at one corner as shown in Figure 7.8 (b) for three molecules. However, by laterally manipulating such molecules we can restore the four-fold symmetry as depicted in Figure 7.8 (c) and Figure 7.8 (d). The encircled molecule in Figure 7.8 (c) has an apparent depression at one corner and is manipulated by a bias pulse. Figure 7.8 (d) shows the subsequent STM image, where the square like shape of the porphine encircled in white is restored.

Therefore we assume that the molecule is intact and we assign the previously observed depression to a defect in the underlying graphene layer, which interacts with the porphine.

Indeed, the inset in Figure 7.8 (d) shows an image of the atomically resolved defect.

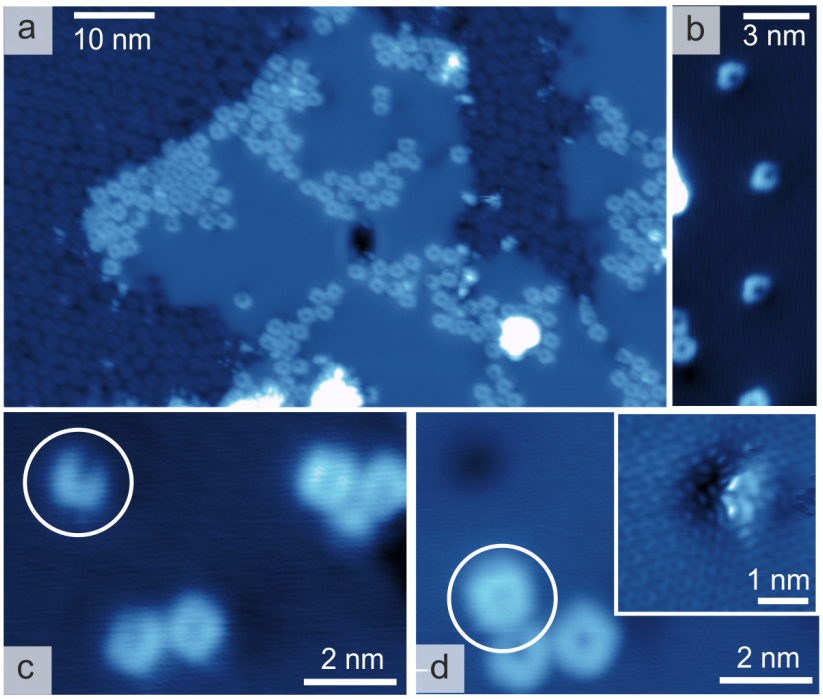

Figure 7.8: *2H-Ps on graphene/Ag(111) at low coverage.* ***(a)*** *STM image shows low molecule density on graphene, while the Ag(111) is completely covered. The 2H-Ps accumulate at graphene edges, grain boundaries, impurities on the graphene, and defects in the graphene layer. Small molecular clusters, but also individual 2H-Ps can be imaged on the graphene ($V_S = 1.3$ V, $I = 10$ pA).* ***(b)*** *Three individual molecules trapped at a defect in the graphene layer, revealing a depression at one corner of the molecule ($V_S = 1.3$ V, $I = 10$ pA).* ***(c)*** *Molecule with characteristic depression on the top left of the image encircled in white ($V_S = 1.3$ V, $I = 10$ pA). This molecule is manipulated by a bias pulse and imaged in* ***(d)****. In* ***(d)*** *the moved molecule exhibits a square like shape pointing to an intact molecule ($V_S = 1.3$ V, $I = 10$ pA). The inset in* ***(d)*** *shows an atomically resolved image of the defect, which caused the depression of the 2H-P in* ***(c)*** *($V_S = 17$ mV, $I = 500$ pA).*

STS We conducted STS of 2H-Ps on graphene/Ag(111) to obtain information about their electronic properties. Figure 7.9 (a) - (c) depict the same molecule for three different applied biases: Figure 7.9 (a) at $V_S = 1.0$ V, Figure 7.9 (b) at $V_S = 1.5$ V, and Figure 7.9 (c) at $V_S = 2.0$ V. The molecule reveals a square like shape for small bias ($V_S \leq 1.5$ V), while the LUMO appears clearly at $V_S = 2.0$ V (compare LUMO in [211]).

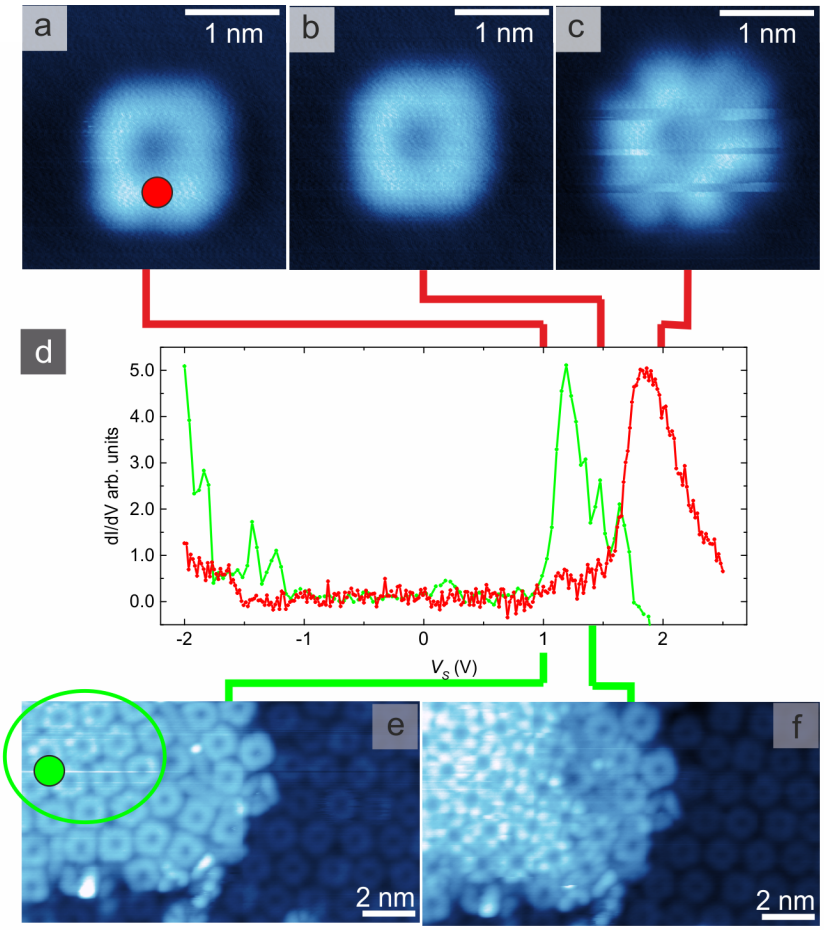

Figure 7.9: *Electronic properties of 2H-P on graphene/Ag(111).* ***(a)-(c)*** *Individual molecule imaged at different biases, $V_S = 1.0$ V* ***(a)****, $V_S = 1.5$ V* ***(b)*** *and $V_S = 2.0$ V* ***(c)*** *($I = 5$ pA). The 2H-Ps reveal a square like shape for $V_S \leq 1.5$ V and for higher voltages the LUMO appears. The red graph in* ***(d)*** *shows the STS taken at the positions marked by the red dot in* ***(a)****. The red curve reveals a DOS resonance at $V_S = 1.9$ V, which we assign to the LUMO. A broader increase in the DOS due to the HOMO for $V_S < -1.5$ V is observed. The red solid lines on top of the STS graphs visualize the bias at which the images* ***(a)-(c)*** *were acquired.* ***(e)*** *and* ***(f)*** *depict the same region imaged at $V_S = 1.0$ V* ***(e)*** *and $V_S = 1.4$ V* ***(f)*** *($I = 10$ pA). The green graph in* ***(d)*** *corresponds to a STS taken at the position marked in* ***(e)****. The green curve exhibits similar signature as the red graph but is shifted to lower voltages. The LUMO shifts roughly by $\Delta E_{LUMO} = 0.7$ eV, whereas the HOMO is shifted by $\Delta E_{HOMO} \sim 0.3$ eV. In* ***(e)*** *the molecules reveal square like shape, while the encircled molecules show some additional intramolecular features. In* ***(f)*** *all molecules on the graphene exhibit the intramolecular features, which we assign to the LUMO.*

The red dot in Figure 7.9 (a) defines the position where the red spectrum presented in Figure 7.9 (d) was taken. The STS shows a clear resonance at $V_S = 1.9$ V, which we assign to the LUMO and a broader resonance for $V_S < -1.5$ V, which we assign to the onset of the HOMO of the 2H-P.
The relatively sharp resonances reveal an effective decoupling of the molecules from the metal support [27].
The red lines on top of the STS graphs visualize the voltage at which the images in Figure 7.9 (a) - (c) were acquired. Figure 7.9 (a) and (b) were measured at $V_S < V_{LUMO}$ and the applied bias for Figure 7.9 (c) lies at the LUMO resonance.
Figure 7.9 (e) and (f) show a sample at higher molecular coverage. The left side depicts molecules on graphene/Ag(111), while the molecules on the right are adsorbed on Ag(111). In Figure 7.9 (e) ($V_S = 1.0$ V) the porphines on the graphene/Ag(111) reveal a square like shape, similar to the appearance on the metal support. The green dot shows the STS location of the green spectrum presented in Figure 7.9 (d). The green circle in Figure 7.9 (e) highlights molecules, which exhibit additional intramolecular features. In Figure 7.9 (f) ($V_S = 1.4$ V) such intramolecular features, which we assign to the LUMO, are identified for all molecules on graphene. In contrast, the 2H-Ps on Ag(111) do not change their appearance for higher biases.
The green trace in Figure 7.9 (d) of the high molecular coverage system reveals a very similar signature than in the low coverage case, but is shifted to lower energies. The LUMO shifts by about $\Delta E_{LUMO} = 0.7$ eV, while the HOMO is only shifted by $\Delta E_{HOMO} = 0.3$ eV. This shift of the orbital energies is assigned to a screening of the neighboring molecules and additionally the Moiré pattern might have an influence.

7.2.1 Chemical functionalization of graphene/Ag(111) by porphines

Functionalization of graphene/Ag(111) To modify the electronic properties of graphene, chemical functionalization is an actively researched topic [434–439]. E.g., Lattelais et al. [440] propose that metal porphines can covalently bind to metal supported graphene.
By pulsing the individual molecules as described in [441], we did not observe a covalent coupling to the graphene layer, which was also proposed in [440]. However we laterally moved the molecules on the surface.
While we did not succeed to chemically bind porphines on the graphene layer, we functionalized the edges of the graphene with free base porphines, as briefly discussed in the following.

Edge functionalization

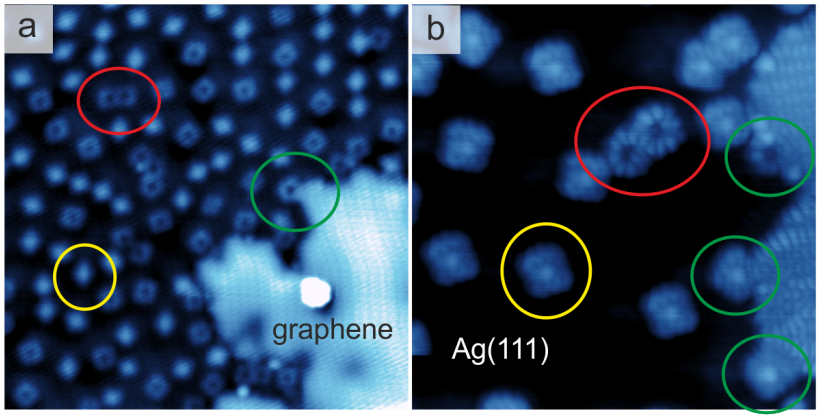

Figure 7.10: *Porphines covalently bound to graphene edges. Red circles highlight covalently coupled and yellow circles silver metalated porphines in* ***(a)*** *($V_S = 1.0$ V, $I = 30$ pA) and* ***(b)*** *($V_S = -1.0$ V, $I = 300$ pA). The green circles present porphines, which are chemically connected to the edge of the graphene islands.*

We coupled porphines covalently to the edges of graphene/Ag(111) by thermal activation. In Figure 7.10 (a), the very same sample presented in Figure 7.7 after an additional annealing step to $T_{sample} = 570$ K for ten minutes, is shown. After annealing, the graphene surface is almost completely empty. Interestingly, the molecular coverage on the metal is strongly reduced, even though 2H-P desorption from the metal does typically not occur at the applied temperatures [227]. The observed desorption might be enhanced by a two step process involving the graphene layer.
The red circles in Figure 7.10 (a) and (b) highlight dehydrogenative homocoupled porphines (compare [101, 227]), while the yellow circles highlight metalated silver porphines [227]. The green circles highlight porphines (free base and metalated), which are covalently connected to the graphene sheet. A more comprehensive study of the graphene edge functionalization triggered by these preliminary experiments is published in [273].

7.2.2 Discussion and outlook - porphines on graphene on Cu(111) and Ag(111)

Our experiments point towards a high mobility and low adsorption energy of porphines on graphene/Cu(111). Individual molecules desorb from the graphene surface already at room temperature. We showed that even at sample temperatures of $T_{sample} = 50$ K the porphines are mobile enough to form ordered arrays. Furthermore, at $T = 5$ K the individual molecules are still too mobile to be stably imaged with STM. Both observations points towards small vdW interaction between porphines and graphene/Cu(111).
On Ag(111), we observe a slightly stronger interaction between molecules and graphene, as we can image individual porphines with our STM tip.
For both systems, the molecules do not preferentially adsorb on specific Moiré positions. However, they rather accumulate at defects in the graphene layer or impurities on the graphene. We identify the following possible explanations for the negligible influence of the Moiré pattern in the self-assembly of the porphines.
(i) The work function differences of different positions on the graphene/metal system can cause differences in the adsorption energy of the molecules [27]. For similar two-dimensional layer/metal systems the energetically preferred adsorption positions on the Moiré correlate with the positions revealing the lowest work functions [27, 416–419]. As the work function differences between pore and wire for the graphene/Cu(111) are significantly smaller than for example for *h*-BN/Cu(111) (compare Section 6), this might be the reason for the small influence of the Moiré pattern on the molecular self-assembly.
(ii) Furthermore lateral electric fields can play an important role in the ordering mechanism of molecules [27, 430, 442]. Again the smaller electrical corrugation of graphene/Cu(111) and graphene/Ag(111) compared to *h*-BN/Cu(111) leads to smaller electric fields and therefore to a weaker site-specific bonding.
(iii) In additional to the electronic consideration of the adsorption energetics, the geometric corrugation might be important for the self-assembly of the porphines. From our geometric determination of the Moiré corrugation of *h*-BN/Cu(111) [123] and graphene/Cu(111) (compare Section 6), we conclude that the Moiré positions with the lowest work function coincide with the smallest adsorption height. As a consequence the position dependent adsorption energy of molecules on the Moiré might be influenced by the molecule metal interaction, which is strongly distance dependence.

With regards to the electronic structure of the molecules we observed varying behaviors for the high and low molecular coverage experiments.
For the low molecular coverage on graphene/Cu(111), we observed an efficient electronic decoupling of the molecules from the underlying metal support. The efficient decoupling was evidenced by pronounced resonances and NDR regions in the STS of the Co-Ps. The signature of the Co-P spectra on graphene/Cu(111) reveals very similar appearance as the Co-P spectra on *h*-BN/Cu(111). The shape, the resonance energies, the NDR as well as the apparent band

gap show high similarities between molecules on h-BN/Cu(111) and graphene/Cu(111). Thus, we assume that graphene decouples molecules with similar efficiency from the metal support as h-BN.

Furthermore, in the high coverage case, we identified two different STS signatures.

In the first experiment we obtained strongly broadened features in the STS and we could not identify the Co attributed resonances. This broadening might be caused by contributions to the STS signal of molecular orbitals from neighboring molecules. These orbitals can exhibit different energies due to the Moiré induced level alignment [27]. Furthermore, the geometry of the tip can cause a broadening of the STS features. However, from the energy of the molecular orbitals we could identify the Moiré periodicity and we found an electronic corrugation of ~ 50 meV, which is in good agreement with the work function shifts found for graphene/Cu(111) (see Section 6).

We found different electronic properties for a high coverage molecular island on graphene/Cu(111) without apparent Moiré corrugation. Here, we assign the sharp resonance to the Co orbitals as they are not observable for free base species. The Co orbital energy is shifted down to $E_{Co} = 0.8$ eV compared to the low coverage case, which we attribute to a screening by surrounding molecules.

It is not obvious why for one system the DOS features are severely broadened, while we observed sharp peaks in the other case. Interestingly, we could clearly determine the Moiré periodicity from the strongly broadened STS data, while the energy of the sharply resolved Co resonance did not follow an obvious Moiré lattice.

A blunt tip might explain the strong broadening, but since we observed the broad resonances for many different tips, the STS modifications might also come from different adsorption configuration of the graphene layer on the underlying support.

We observed graphene with pronounced Moiré pattern in one case, while the other graphene island appears flat. The flat graphene island might exhibit different coupling to the Cu(111), which has already been reported for h-BN on Ni(111) [205].

To summarize, even though the graphene sheet is a conducting material, it efficiently decouples molecules from an underlying metal substrate. Furthermore, the adsorption sites of porphines on graphene/Cu(111) and graphene/Ag(111) is not dictated by the Moiré pattern.

8 Neural networks

The work presented in this Chapter was done during a research stay at the National Institute for Materials Science in Tuskuba (Japan), in collaboration with the Nano Functionality Integration Group of Tomonobu Nakayama.

Artificial Intelligence (AI) is outplaying human minds in more and more fields. Giving first significant attention to a broader audience in 1997, when a computer beat Garri Kasparow (at that time chess world champion) in chess [443], computer based AI [444] is now omnipresent. While the self-learning program AlphaGo defeats the worlds best Go player, which was said to be the *holy grail* of AI [445], AI starts to get access to daily life. Autonomous cars [446] and image recognition [447–449] are just two examples, where AI is already giving huge impact to society. Face recognition algorithms are in a stage where AI is used to survey and track down individual persons [450] and can even provide information about the sexual orientation just from the shape of someone's face [451].
However, to manage these tasks software based AI consumes huge amounts of energy whereas the human brain completes all it's challenges with tens of Watts [452]. The hardware approach to neural networks tries to overcome the energy issue of the software based AI.
In the following we present metal-insulator-metal (MIM) [453] nanowire systems, which are used for an artificial neural network in this work. We executed multi-probe SPM experiments on MIM junctions. From the two-probe experiment we conclude that the Power Spectral Density (PSD) of the measured current through the MIM junction, gives clear information about the activation and deactivation of the junction. Furthermore, we assembled a macroscopic neural network device, which manages to memorize five different input patterns successfully.

8.1 Preparation of silver nanowires (Ag NWs) and switching principle

8.1.1 Ag NW synthesis

The Ag NWs are synthesized following the procedure presented by Bi et. al. [454] performing a pyrrolidone (PVP) mediated polyol process [455–457]. We used the following recipe:

- Heat oil bath to 400 K
- Dissolve Polyvinylpyrrolidone K90 (PVP) (0.085 g) with an average molecular weight of 630 kg/ mol in 5 ml 1,2-propylene glycol to obtain a concentration of 0.027 mmol/L by stirring it for 1 hour with a magnetic stirrer.
- Heat PVP to 400 K in oil bath for 30 minutes.

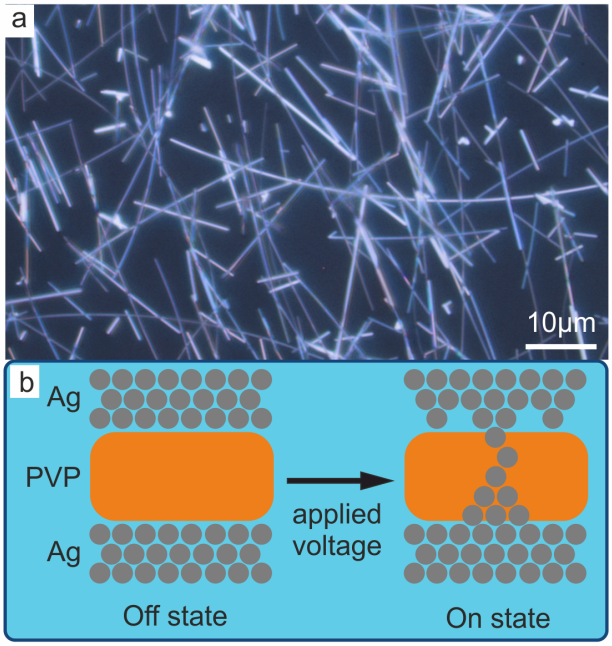

Figure 8.1: *MIM junctions and principle of activation. (**a**) Optical microscope image of synthesized Ag NWs, which act as MIMs. The Ag NWs are covered by an insulating PVP layer and reveal a length up to 100 µm. (**b**) Sketch of a MIM junction consisting of two Ag NWs separated by an insulating PVP layer. Silver atoms are depicted in gray the PVP in orange. When a bias is applied Ag^+ ions migrate to the cathode and open a conducting channel within the insulating layer.*

- Dissolve $AgNO_3$ (0.085 g) in 5 ml 1,2-propylene glycol to obtain a concentration of 0.15 mmol/ L
- Add 100 ml of NaCl solution (5 mmol/ L) to the PVP.
- Keep solution at 400 K for 4 minutes
- Add all of the $AgNO_3$ solution to the PVP and keep it at 400 K for 1 hour, with the bottle being closed.

After the synthesis the Ag NW solution has to be purified. Therefore the solution is diluted with isopropanol and centrifuged at 4000 rpm for 1 minute. The solvent is removed and the residual Ag NWs are dissolved in isopropanol again. This purification step is repeated three times. In Figure 8.1 (a) the obtained Ag NWs are imaged with an optical microscope. With this image the purity is checked and if too many residuals from the syntheses are distributed on the sample surface, the purification procedure has to be repeated. The imaged Ag NWs are clean and have diameters ranging from a few tens to a few hundreds of nanometers and a length up to hundreds of microns. The obtained Ag NWs are covered by an insulating layer of PVP.

8.1.2 Switching principle of Ag NW junctions

Figure 8.1 (b) sketches the switching of a metal-insulator-metal (MIM) junction from the non conducting off state to a conducting on state. The Ag atoms of two Ag NWs are drawn in gray, which are separated by the insulating PVP layer. When a voltage is applied between the Ag NWs, Ag^+ ions migrate to the cathode and thereby open a conducting Ag channel within the insulating layer [453, 458–461]. This channel is illustrated on the right side in Figure 8.1 (b).

8.2 Multiprobe measurements on individual Ag NW and Ag NW junctions

Multi-probe AFM/STM gives access to the electrical properties of nanomaterials in the nanometer regime [462, 463]. Whereas two-probe experiments struggle with the influence of the probe-sample contacts, four probes are needed to overcome this issue [462, 463]. Multi-probe measurements have been reported on various nanoscale materials [462, 464–467]. Here we present a study of multi-probe measurements on metal-insulator-metal junctions.
In the following we measure conductance (G) and resistance (R) of single Ag-NWs and of Ag-NWs junctions. Therefore we record the conductance at constant voltage for several different voltages. For a more comprehensive analysis we additionally analyze the power spectral density (PSD) of the measured currents. Demis et al. [468] have shown that they can state if a macroscopic nanowire network is activated or deactivated from the shape of the PSD. We obtain the PSD by fast fourier transform (FFT) of the measured current signal. To describe the shape of the PSD we fit the data to a power law behavior of $\propto 1/f^{\beta}$ and use the β value to compare the different measurements. The shape of the PSD is determined by three superimposed processes [469]:

- 1/f noise with $PSD \propto 1/f^{\beta}$
- Johnson-Nyquist noise with $PSD \propto R$ [470, 471]
- Shot noise with $PSD \propto I$ [472, 473]

In the following we show measurements at Ag-NWs and Ag-NWs junctions at different applied biases, different currents, and different conductances and compare them to the corresponding β values of the PSD.

8.2.1 Four-probe AFM

The used four-probe AFM was developed and built by Yoshitaka Shingaya. In Figure 8.2 (a) the vacuum chamber providing a pressure in the order of 10^{-5} mbar is shown. All measurements presented in this work are performed at this particular pressure and at room temperature. Above the vacuum chamber an optical microscope is placed, which can be moved with micrometer

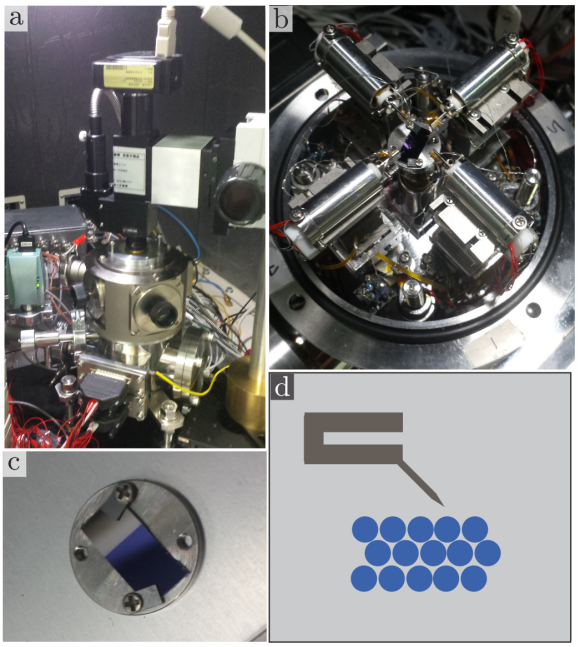

Figure 8.2: *Experimental approach of four-probe microscope. (**a**) Four-probe microscope chamber holding a vacuum of* $\sim 10^{-5}$ mbar. *Optical camera above the chamber to locate the four individual probes on the sample. (**b**) Opened chamber revealing the four tip holders. (**c**) Investigated sample, which is mechanically fixed on the sample holder with two clamps. The top left part of the sample is covered by a metallic layer (metallic color). The bottom right part is the support for the investigated materials (dark blue color). (**d**) qPlus tuning fork with tilted glued tip.*

.

screws and is used to locate the four tips and to find the area one wants to measure via AFM. In Figure 8.2 (b) the inside of the vacuum chamber is pictured, showing four independently movable tip holders. Each of these tip holders can be positioned via coarse piezos in x-y-z directions with a movement range up to 6 mm. For scanning and for precise positioning, each probe can be moved with a tube piezo with a maximum range of 9 μm. An additional tube piezo is used to translate the sample. All four tungsten tips are glued to a qPlus sensor each with a resonance frequency of about $f_{res} = 25$ kHz. The excitation amplitude of the qPlus sensor was set to $a = 2$ nm for the measurements.

In contrast to tips used in one-probe AFMs, the tip is not pointing straight down to the sample, but is tilted as sketched in Figure 8.2 (d) [474]. The tip length is around 2 mm and the resolution of each probe is ~ 2 nm. The smallest distance between the tips is limited by their thickness, causing a minimum separation between opposite tips of ~ 100 nm and for neighboring tips of ~ 1 μm. All measurements are done in constant Δf-mode.

Figure 8.2 (c) shows a sample holder with a sample sitting in the center of it, which is fixed mechanically with two clamps. One part of the sample is covered with a metallic layer, where the conductivity of the four tips can be tested. The investigated material is put on the other side of the sample. For the AFM measurements the tips are approached till a threshold $\Delta f_{threshold} =$

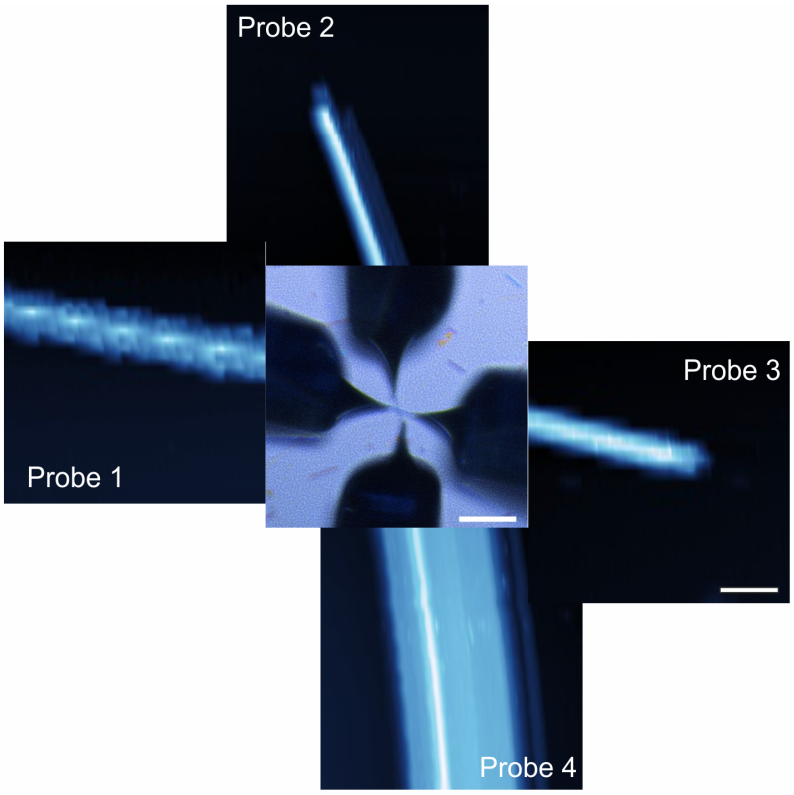

Figure 8.3: *Imaging MIM junction via a four-probe AFM. Optical microscope picture in the center, showing four tips and two crossing Ag NW contacted by the four tips (Scale bar = 50 μm). Four AFM images measured simultaneously with the four individual probes (Scale bar = 1 μm).*

-2 Hz is reached. Then all actual Δf values are set to zero as an offset-correction and the $\Delta f_{measure}$ are set to measure AFM in Δf-mode. These $\Delta f_{measure}$ values are usually between -2 to -4 Hz.

The electrical measurements can be done after some hours of AFM scanning, when the drift is reduced. For the electrical measurements the tips are placed at the position where the sample should be measured, the AFM feedback is switched off and the tips are moved towards the surface by $\Delta z = 20$ nm. The maximum useable Δz range is 40 nm.

8.2.2 Electrical measurements with multi-probe AFM

Imaging Ag NW junctions via AFM In the center of Figure 8.3 an optical microscope image of the measured sample is shown. The sample is a SiO_2 crystal, where one part is covered by an Pt/Au layer and on the SiO_2 part a strongly diluted Ag NW solution has been drop casted. We observe a density of a few Ag NWs per 100 μm^2. The whole sample mounted on the holder is presented in Figure 8.2 (c). The four tips in Figure 8.3 are positioned via the coarse piezos above two crossing Ag NWs with a length of ~ 30 μm each.

The four AFM images (labeled Probe 1 - 4) are measured simultaneously. Probe 2 and 3 image

the two different Ag NWs with a height of $h \sim 250$ nm and a width of $w \sim 500$ nm. We neglect the observations for h and w of Probe 1 and 4 as they give too high values due to blunt tips. For the following electrical measurements on this Ag NW system the four tips are positioned above the Ag NWs, the AFM feedback is switched off and the tips are approached towards the surface by 20 to 40 nm.

Activation of junctions Figure 8.4 depicts an exemplary activation of a metal-insulator-metal junction between Probe 1 and Probe 3. In such a two-probe experiment the voltage is applied between Probe 1 and Probe 3. Therefore the measured resistance is a combination of the single Ag NW resistance and the contact resistances of the tip-Ag NW contacts. We do not expect an activation inside one single Ag NW but the tip-Ag NW contacts can be activated. The blue (orange) lines corresponds to the current measured at Probe 1 (Probe 3) and are plotted against the applied voltage. For the first voltage sweep no current is detected as the junctions are not activated (Figure 8.4 (a)). After several voltage sweeps with applied voltages up to 10 V relevant currents are measured as the MIM junctions are activated (Figure 8.4 (b)). For $V \gtrsim 2$ V the current reaches overload, which is set to 1 μA. The curves exhibit hystereses when the voltage is swept in opposite directions. These hystereses are caused by activation/deactivation of the tip-Ag NW contacts.

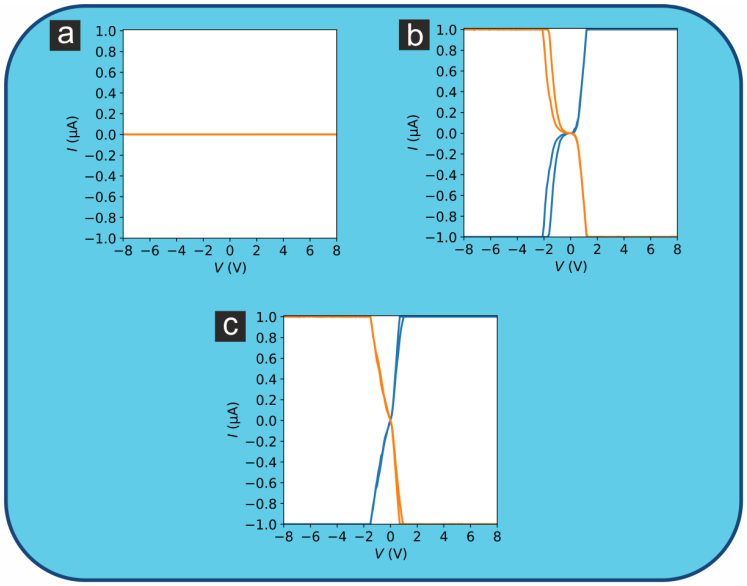

Figure 8.4: *Activation of junctions between Probe 1 and Probe 3 where the blue (orange) lines corresponds to the current measured at Probe 1 (Probe 3): (**a**) I vs V curve shows no conductivity for inactive channel. (**b**) After several voltage sweeps the channel becomes activated. In this intermediate state we observe a hystereses in the I vs V curve. (**c**) An almost ohmic behavior for a small voltage range is found after more sweeps. Depending on the contact between tips and Ag NWs this ohmic region can be much further extended. At a current of $I = 1$ μA the measured current reaches its limitation. The system is deactivated after some time and goes back to the situation demonstrated in (**a**).*

After additional voltage sweeps the measured channel becomes more conductive, the hystereses diminish and ohmic behavior is achieved for a small voltage range as can be seen in Figure 8.4 (c). Depending on the contacts the ohmic behavior can be much further extended.
In Figure 8.5 we consider the time scales of the activation process of the junctions. Figure 8.5 (a) depicts the measured current between Probe 1 and Probe 4 at an applied voltage of $V = 100$ mV. The channel is slightly activated and deactivated for the first ~ 0.2 s. The conductance does not show a clear tendency over time, but increases and decreases on the millisecond and also on longer time scales. The black arrow highlights a distinct jump in the current. This strong increase in conductance, by at least one order of magnitude occurs within 1 ms, which is the time resolution of the measurement.
Additionally to the constant voltage experiment we performed constant current measurements. In the constant current experiment shown in Figure 8.5 (b), the current was set to $I = 1$ nA and the resulting voltage was measured between Probe 1 and Probe 4. We identify a slow increase of the voltage from close to zero Volts to values exceeding 2 V within a few seconds. We assign this process to the deactivation of the junctions. The subsequent activation reveals a sharp reduction in voltage, which occurs again faster then the time resolution of the experiment (in this case 42 ms).
The PID control of the feedback can be ruled out to be responsible for the differences of the slow deactivation and the fast activation process as a PID control reacts symmetric on deviations from the given set point. From these activation experiments we conclude that the activation of the metal-insulator-metal junctions can occur within 1 ms.

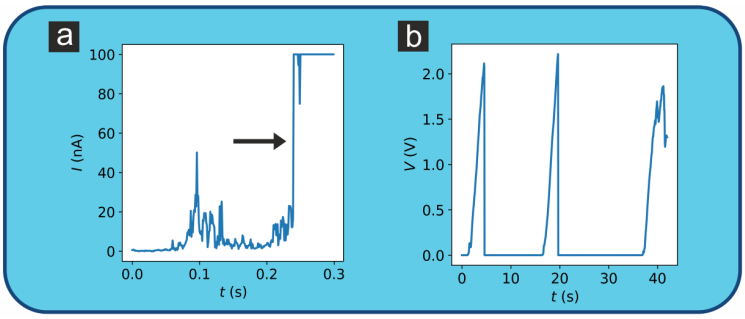

Figure 8.5: *Timescales for activations/deactivations of MIM junctions. (**a**) Current measured at a constant applied voltage of* 100 mV *between Probe 1 and Probe 4. The distinct jump in the current from only few* nA *to over* 100 nA *(highlighted with a black arrow) occurs within* 1 ms*, which was the time resolution of the measurement. (**b**) Voltage measured when the constant current was set to* 1 nA *between Probe 1 and Probe 4. The deactivation of the channel (increasing voltage) occurs within a few seconds, whereas the activation (voltage drops to almost* 0 V*) occurs within one measuring interval of* 42 ms.

.

Two-probe constant voltage We measured the conductance between Probe 1 and Probe 3 in constant voltage mode for a range of different applied voltages. Probe 1 to Probe 3 means that we have two tip-Ag NW contacts, which can be activated but no MIM junction between different Ag NWs. Figure 8.6 (a) depicts the evolution of the conductance of the channel for 33 subsequent measurements. All measurements where the currents exceeded the current limitation were removed from the data. The different applied voltages are shown in Figure 8.6 (c) for each measurement. The orange colored data points correspond to measurements with specific β values as explained below. For the first data points ($0-8$ in Figure 8.6 (a)) the conductance is small and almost constant.

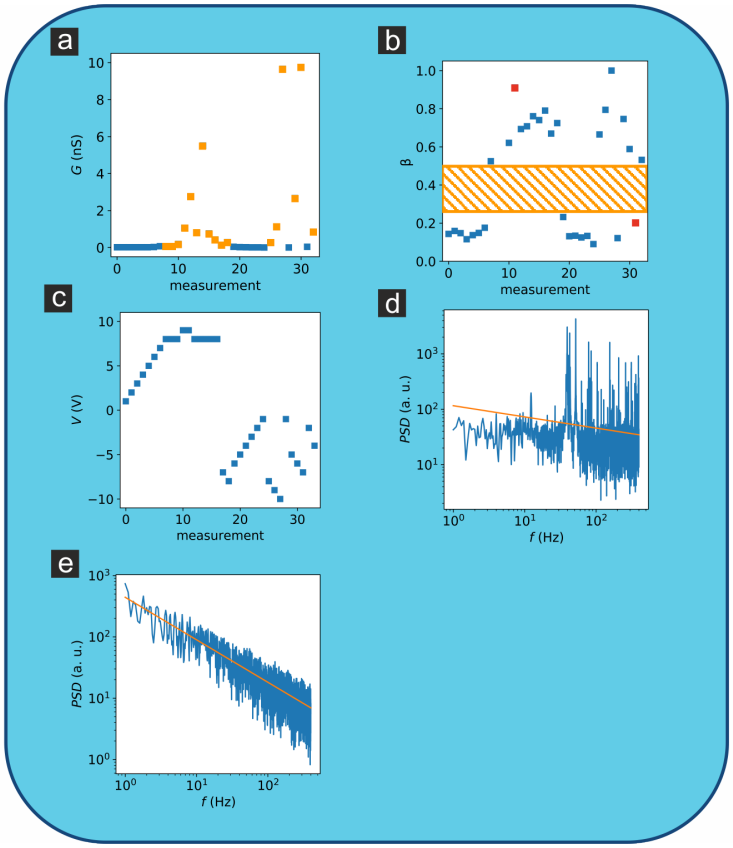

Figure 8.6: *Conductance and power spectral density (PSD) analysis of two-probe measurements between Probe 1 and Probe 3 in constant voltage mode.* (**a**) *Measured conductance for 33 measurements. Low conductance at the first measurements* ($0-8$) *are followed by higher conducting* ($9-18$), *then by low conducting* ($19-25$) *and subsequent higher conducting measurements* ($26-32$). *All data points are highlighted in orange if the corresponding* β *value in* (**b**) *lies above* $\beta \sim 0.47$. (**b**) *Shows fitting* β *parameter of the PSD of the measured currents for each measurement. The PSD spectra are fitted to a power law behavior of* $\propto 1/f^{\beta}$. *The corresponding fits to the red squares highlighted in* (**b**) *are presented in* (**d**) *and* (**e**). *The* β *values are distributed from* $\beta \sim 0.1$ *to* $\beta \sim 1$. *However no* β *values are found for the region* $\beta \sim 0.25$ *to* ~ 0.47, *which is highlighted in orange. The* β *values does not scale with the measured conductance.* (**c**) *presents the applied voltage for each measurement.* (**d**) *and* (**e**) *show PSD measurements with corresponding power law fit with low* β (**d**) *and with large* β (**e**).

Data points $9-18$ show increased conductance, which drops to the initial conductance again for data points $19-25$ and reveals higher values for data points $26-32$. Figure 8.6 (b) shows the corresponding fitting parameters β for each measurement. To obtain β the PSD of the measured current is fitted to the power law behavior of $\propto 1/f^{\beta}$.
Two examples of the PSD and the corresponding fits are shown in Figure 8.6 (d) and (e). Figure 8.6 (d) (measurement 9) and (e) (measurement 31) correspond to the data points highlighted by the red squares in Figure 8.6 (b). The fit range is set from 1 to 400 Hz. The β values in Figure 8.6 (b) are distributed between 0.1 and $\sim$ 1. Noticeably, we do not find any values for β in between 0.25 and 0.47. This region is marked with the orange striped rectangle in Figure 8.6 (b). For all βs lying above the orange rectangle the corresponding conductance points in Figure 8.6 (a) are colored in orange.

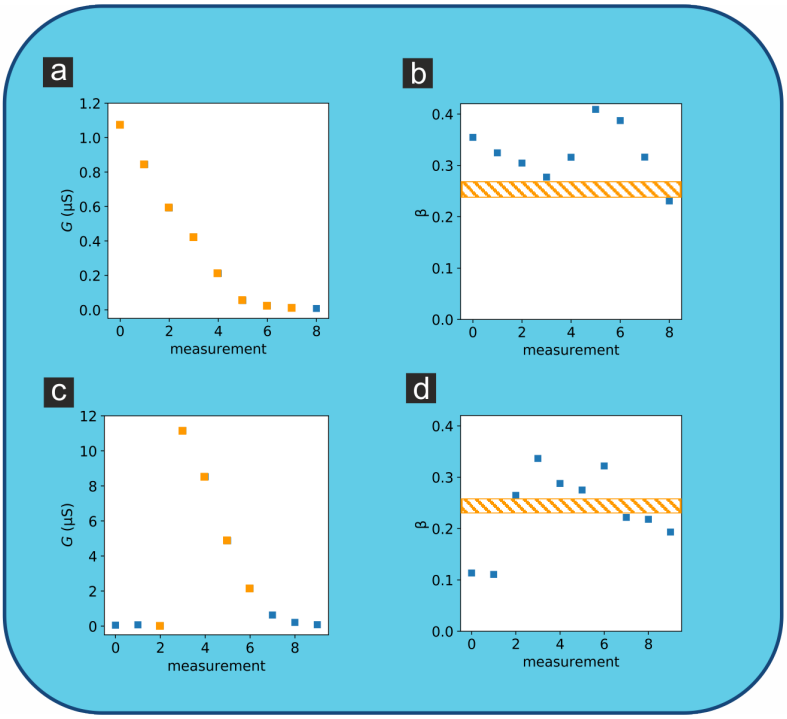

Figure 8.7: *Conductance and power spectral density (PSD) analysis of two-probe measurements between Probe 1 and Probe 4 including a Ag NW-Ag NW junction, in constant voltage mode. (**a**) Conductance for 9 measurements. Initial conductance decreases with each conducted measurement. Data points with corresponding $\beta > 0.28$ in (**b**) are colored in orange. (**b**) Corresponding β values from the PSD fitting. All β values stay in the corridor of $0.28 \gtrsim \beta \gtrsim 0.42$ except the last measured data point with $\beta \sim 0.2$. A region between this data point and the β values in the corridor is marked in oranges (also in (**d**)). (**c**) Additional conductance measurements between Probe 1 and Probe 4 where data points with $\beta > 0.27$ are colored orange. (**d**) Corresponding β values. The first two data points exhibit low β. Data points 3 - 7 accumulate in the corridor $0.27 \gtrsim \beta \gtrsim 0.35$, whereas the corresponding conductance values first strongly increase and then continuously decrease. The last three data points are close to $\beta = 0.2$.*

In the following we performed two-probe experiments between Probe 1 and Probe 4 including also a Ag NW-Ag NW junction. Such Ag NW-Ag NW junctions are the essential elements for trainable neural networks. Figure 8.7 (a) shows the conductance of the system, which starts at $G \sim 1.1$ μS and is continuously reduced below $G = 0.01$ μS. The applied voltage was set to $V = 0.1$ V. The corresponding β values, which are fitted the same way as explained above, are presented in Figure 8.7 (b). All β values lie in a corridor of $0.28 \gtrsim \beta \gtrsim 0.42$ except the last data point with $\beta \sim 0.2$. Similar to the orange striped rectangle in Figure 8.6 (b) we mark the region without measured β values. Noticeably, we do not have any β values below $\beta = 0.2$ in Figure 8.7 (b). The reduction of the conductance in Figure 8.7 (a) is likely due to the drifting of the probes away from the surface. Also here we do not observe a scaling of the β values with the conductance. A second set of measurements between Probe 1 and Probe 4 is shown in Figure 8.7 (c) and (d). Two data points (between points 2 and 3) were removed as the current exceeded the current limitations of the measurement. The applied voltage was set to $V = 0.01$ V except for data point 0 (0.1 V), 1 (-0.1 V) and 2 (1 V). After the first three low conducting measurements the conductance increased above $G \sim 11$ μS and subsequently reduced below $G = 0.01$ μS within six subsequent measurement. The corresponding β values are shown in Figure 8.7 (d). For the first two data points β is close to 0.1. For data points 3 to 6 the β values lie at $0.27 \gtrsim \beta \gtrsim 0.35$ and the last three data points are close to $\beta \sim 0.2$. Again we find a corridor without β values, in this case the corridor lies between $0.22 \gtrsim \beta \gtrsim 0.27$.

Two-probe constant current To get a more comprehensive picture of the system we performed additional experiments in constant current mode, which are shown in Figure 8.8. Figure 8.8 (a) - (c) show the results for the measurements between Probe 1 and Probe 4 consisting of a Ag NW-Ag NW and two Probe-Ag NW junctions. Figure 8.8 (a) presents the obtained conductance values for each measurement. The conductance stays relatively small and has a peak around measurement 12. Figure 8.8 (b) depicts the corresponding β values, which are scattered between 0.35 and 1.2. The β values are not directly compareable to the βs in the constant current experiments above as they are fitted to a data range of 1 to 119 Hz due to the available data set. Figure 8.8 (c) shows the applied current set points. The current set points are adjusted by a PID feedback. Similarly, Figure 8.8 (d) - (f) show the conductance (d), the β values (e) and the current set points (f) for measurements between Probe 2 and Probe 4 consisting only of two Probe-Ag NW junctions. The conductance stays small and has a peak at data point 3 whereas the β values stick close to 1.02 with only small deviations up to 0.2. For both constant current experiments the evaluated β values do not correlate with the conductance nor with the current set point of the system. Furthermore, in comparison to the constant voltage experiments we do not find two levels for the β values, which we could assign to activated or deactivated paths.

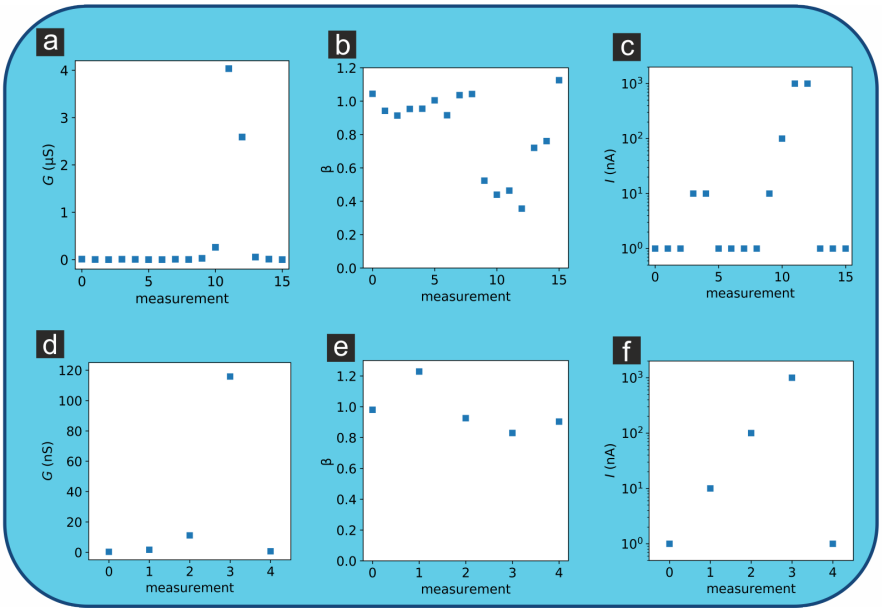

Figure 8.8: *Conductance and power spectral density (PSD) analysis of two probe measurements in constant current mode.* ***(a)*** *-* ***(c)*** *Experiment with Probe 1 and Probe 4 including a Ag NW-Ag NW junction in the investigated system.* ***(a)*** *Conductance between Probe 1 and Probe 4 stays realtively low and has a peak for measurements 10 to 12.* ***(b)*** *Corresponding β values, which are distributed between 0.4 and 1.2.* ***(c)*** *Current set points for each measurement reaching from 1 to* 1000 nA. *β values do not show a clear correlation with current or conductance.* ***(d)*** *-* ***(f)*** *Experiment with Probe 2 and Probe 4 including only two Probe-Ag NW junctions in the investigated system.* ***(d)*** *Conductance with peak at measurement 3.* ***(e)*** *Corresponding β values, which are distributed between $\sim$ 0.8 and $\sim$ 1.2.* ***(f)*** *Current set points for each measurement reaching from 1 to* 1000 nA. *Again, β values do not show a clear correlation with current or conductance.*

Four-probe constant current We performed four-probe experiments to circumvent the influence of the probe contacts. Figure 8.9 (a) displays the positions of Probe 1 - 4. The *I vs V* graphs are presented in Figure 8.9 (b) - (d). Probe 1 - Probe 2 is shown in Figure 8.9 (b), Probe 1 - Probe 4 in Figure 8.9 (c), and Probe 1 - Probe 3 in Figure 8.9 (d). The electrical paths between Probe 1 - Probe 2 and Probe 1 - Probe 4 exhibit high conductance and ohmic behavior, whereas Probe 1 - Probe 3 has lower conductance and a non-ohmic signature. Consequently, the Ag NW is decently contacted to Probe 1, 2, and 4, whereas the contact to Probe 3 reveals also non ohmic contributions. For the four-probe conductance measurement of the Ag NW we set a constant current between Probe 1 and Probe 3, which is adjusted by a PID feedback on the applied voltage. As the current is flowing, we measure the potential at Probe 2 and Probe 4. By calculating the difference between the potentials at Probe 2 and Probe 4 $\Delta\Phi_{2-4}$, we obtain the conductance of the Ag NW between the positions of Probe 2 and Probe 4 without the influence of the contact resistances. Assuming the current as constant we can fast fourier transform $\Delta\Phi_{2-4}$ to obtain the *PSD* of the measured signal.

Figure 8.10 shows two *PSD* of subsequent measurements of $\Delta\Phi_{2-4}$. The constant current was set to $I = 1$ μA and the conductance was very similar for both experiments with $G_1 = 5.1$ mS and $G_2 = 4.9$ mS. For experiments with low currents of $I = 0.1$ μA the obtained conductance

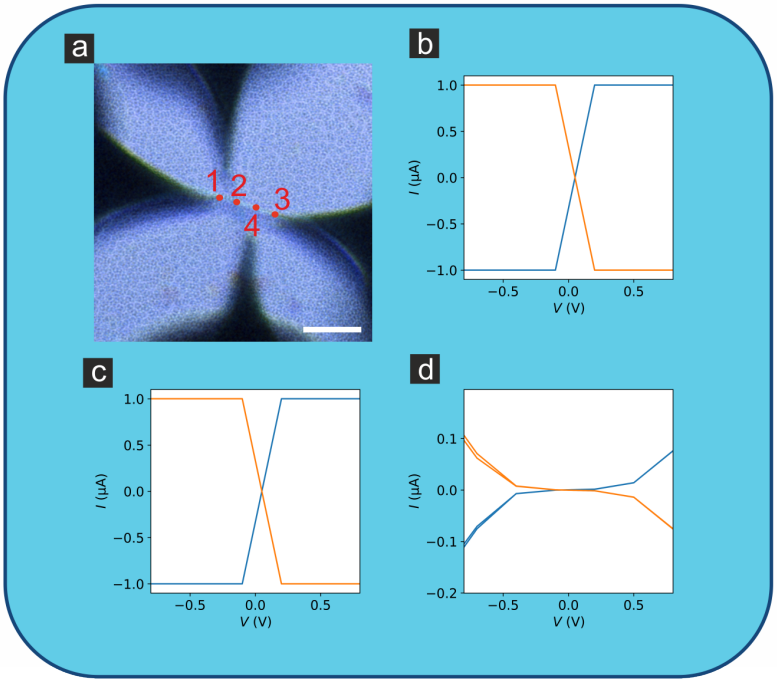

Figure 8.9: *Four probe experiment. (**a**) Positions of probes on measured Ag NW are marked by the red dots. (**b**) $I vs V$-curve between Probe 1 and Probe 2 exhibiting high ohmic conductance. (**c**) I vs V-curve between Probe 1 and Probe 4 exhibiting high ohmic conductance. (**d**) I vs V-curve between Probe 1 and Probe 3 exhibiting relatively low and not ohmic conductance.*

was negative, most likely due to a relevant noise level. For both PSD we find $\beta_{1/2}$ clearly deviating from 0 with $\beta_1 = 0.81$ (**a**) and $\beta_2 = 0.36$ (**b**).
Also in the case of our four probe measurements we obtain a power law behavior of the PSD of our measured $\Delta\Phi_{2-4}$. We observe a strong deviation between β_1 and β_2 by more then a factor of two for the same current and the same conductance.

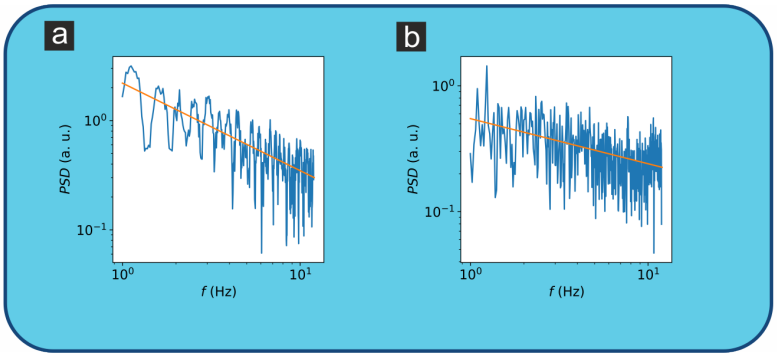

Figure 8.10: *PSD analysis of four probe experiment. A constant current of $I = 1$ μA is applied between Probe 1 and Probe 3. The voltage differences Δ V between Probe 2 and Probe 3 are fast fourier transformed and plotted in (**a**) and (**b**) for two subsequent measurements. Both PSD graphs show a power law behavior (see section above) with $\beta_1 = 0.81$ (**a**) and $\beta_2 = 0.36$ (**b**).*

Discussion of multi-probe measurements From the presented multi-probe experiments we identified several conclusions. The analyzed β value in our constant voltage experiments can be used to define whether a metal-insulator-metal junction is activated or deactivated. The measured current I reveals the following issues that make it difficult to use I for the distinction of activated and deactivated junctions. The current and the corresponding conductance of a system result always from a combination of different conducting paths. In our system small currents can flow through the impurity incorporated PVP layer or the SiO_2 surface. These currents are additionally strongly voltage dependent. Therefore, depending on the particular system it is almost impossible to define a threshold current $I_{threshold}$ or threshold conductance $G_{threshold}$ from which we can determine that our junction is activated (in case $I_{threshold}$ or $G_{threshold}$ are exceeded). In contrast the β value has at least two different levels, which are separated by a region with no β values. We assign these two, separated β levels to activated and deactivated junctions:

Activated junction ($\beta > 0.27 \rightarrow \beta_{activated1}$ in Figure 8.7 (d), $\beta > 0.28 \rightarrow \beta_{activated2}$ in Figure 8.7 (b), $\beta > 0.47 \rightarrow \beta_{activated3}$ in Figure 8.6 (b)) We assign the measurements with $\beta > \beta_{activated}$ to systems with activated junctions. In the three experiments shown in Figure 8.6 and Figure 8.7 the conductance data points, which correspond to $\beta > \beta_{activated}$ are colored in orange. The conductance of the activated junctions can vary by orders of magnitude and can also approach the deactivated values. In contrast, the β values reveal digital behavior between $\beta > \beta_{activated} \rightarrow$ *junction activated* and $\beta < \beta_{activated} \rightarrow$ *junction deactivated*. In Figure 8.6 (b) the β values of the activated junctions are further distributed than for Figure 8.7 (b) and Figure 8.7 (d). Furthermore, the β region without measured values is extended more than for Figure 8.7 (b) and Figure 8.7 (d). For Figure 8.7 (b) and Figure 8.7 (d) the βs of the activated junctions are scattered within a compact region of ± 0.08. The differences in extension and position of the orange rectangles in Figure 8.6 (b), Figure 8.7 (b), and Figure 8.7 (d) might be affected by the magnitude of the measured current, the applied voltage, the number of junctions, and/or differences in the metal-Ag NW contacts. From our measurements we find that the current and the applied voltage play no critical role for the β value. We would expect a decreasing β value for higher currents (shot noise $\propto I$) and increased resistance (Johnson-Nyquist noise $\propto R$) as shot and Johnson-Nyquist noise are overlaid with the $1/f^{\beta}$ signature. However, from our measurements we do not observe a clear tendency for increasing current, increasing resistance or increasing voltage on our obtained β. Furthermore, the number of junctions, changing from two to three seems to have no strong influence on the measurements. The number of junctions in Figure 8.6 is two (two Probe-Ag NW junctions) and for Figure 8.7 we investigated a three junction (two Probe-Ag NW junctions and one Ag NW-Ag NW junction) system. Therefore we would expect a larger scattering of the β value for the three junction system than for the two junction system, which stands in contrast to our results. The experiments showed very similar behavior between the two and the three junction system. Especially both systems (two and three junctions) could be activated and deactivated. Thus we expect the Probe-Ag NW contacts to

influence the position of the orange rectangles in Figure 8.6 and Figure 8.7. This assumption is supported as Figure 8.7 (b) shows similar signatures as Figure 8.7 (d) even though different voltages are applied and a range of currents and conductances were measured.
Deactivated junction ($\beta < 0.24 \rightarrow \beta_{deactivated1}$ in Figure 8.6 (b), $\beta < 0.23 \rightarrow \beta_{deactivated2}$ in Figure 8.7 (b), $\beta < 0.22 \rightarrow \beta_{deactivated3}$ in Figure 8.7 (d)). In Figure 8.6 (b) the β values occupy the whole range from $\beta = 0.1$ to $\beta = 0.24$, in contrast to Figure 8.7 (d), where the first two data points are close to $\beta \sim 0.1$ and the last three points exhibit values close to $\beta \sim 0.2$. These differences in β could be due to combinations of activated and deactivated junctions. For example, $\beta \sim 0.1 \rightarrow$ *no junction activated* and $\beta \sim 0.2 \rightarrow$ *one/two junction activated*. For all junctions activated we then would observe βs exceeding $\beta_{activated}$ again. For the constant current experiments we did not observe such an obvious correlation between β values and activation state of the junctions.

8.3 Neural network device consisting of Ag NWs

In Figure 8.11 (a) a nine channel Ag NW network device is shown. The device consists of nine metal contacts on both sides, which are separated by $\sim$ 1 mm from the neighboring contacts. We assign the 9 contacts on the left side of Figure 8.11 (a) to input 1 to input 9 (counting from bottom to top). Similarly, the contacts on the right are named output 1 to output 9 from bottom to top.
The gold/palladium contacts are sputtered on a glass plate and have a thickness of $\sim$ 80 nm. Subsequently, the region in the center between the contacts is sputtered with air, leading to a more hydrophilic surface and hereby to a better distribution of the Ag NW isopropanol solution when the solution is drop casted on the glass plate.

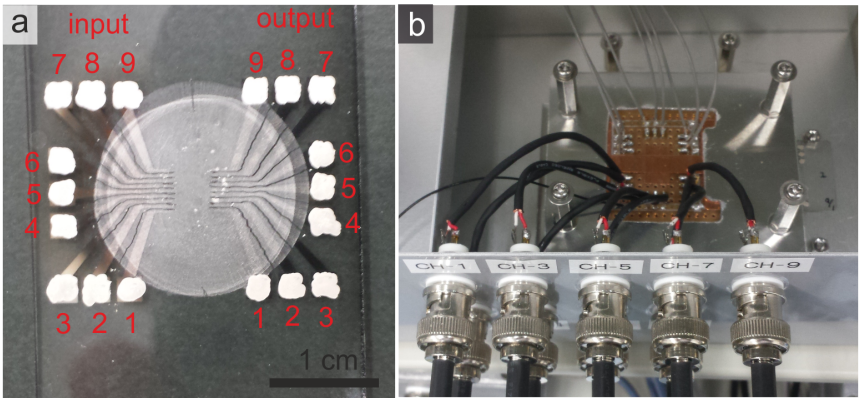

Figure 8.11: *Neural network device consisting of Ag NWs. (**a**) Glass plate hosting a Ag NW network in the center of the nine channel device. The nine input and nine output metallic contacts are numerated. The white squares at one end of the contacts consists of conductive silver paste, added for better contacting. The white round disc in the center are the Ag NW. (**b**) Training box where the network is trained and tested.*

The contact ends pointing away from the center (outside contacts) are larger and further separated than the contact ends pointing to the center (center contacts). The outside contacts are additionally painted with conducting silver paste to make them easier to contact. The Ag NWs are drop-casted (2 μL) onto the center of the device and the density is probed by an optical microscope (see Figure 8.1 (a)). Then additional drops are added until the targeted density is reached. The droplet size determines the extension of the network, consequently several smaller droplets help to position the network in the center of the device. As a next step the region in between the neighboring contacts is scratched free with a toothpick to avoid shortcuts between them. The glass plate hosting the Ag NW network is then placed in the training box shown in Figure 8.11 (b) and the 18 contacts (9 on each side) are mechanically contacted by tightening the four skrews in Figure 8.11 (b).

8.3.1 Experimental approach of the network training

The Ag NW network uses the activation of MIM junctions to change the conductance macroscopically between different metals contacts. By applying a potential difference between two contacts, many Ag NW-Ag NW junctions are activated and the conductance between the two contacts is increased.

Hardware A photograph of the training box, which is used for training and testing the Ag NW network is shown in Figure 8.11 (b). Figure 8.12 illustrates the experimental set up of the training box. Each of the 18 metal contacts is connected to an electrical amplifier, which is used to apply a defined voltage in the range of -10 V to $+10$ V. The current flowing through the output contact is additionally amplified by a factor of 10^7, then converted from analog to digital and fed into the computer.

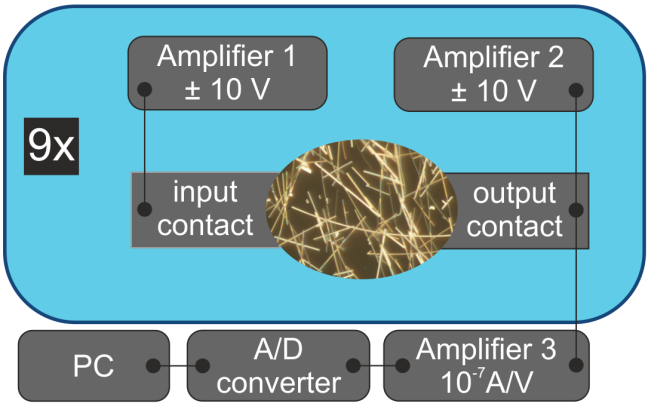

Figure 8.12: *Schematics of experimental setup. Amplifiers are used to apply a voltage in the range of -10 V and $+10$ V to the input and output contacts. The current flowing through the output contact is then again amplified and fed to a computer after being converted from an analog to a digital signal.*

Training and testing

Connectivity check Before starting the neural network training we check if all contacts are connected to the macroscopic Ag NW network. Therefore, we apply a voltage pulse to all 9 inputs one after another and measure the current at all 9 output contacts. Each input voltage pulse should cause a measurable current at each output. In case all contacts are connected to the neural network we continue with the training and testing processes.

Training and test The principle of the training process is explained in Figure 8.13 with a single example pattern shown in Figure 8.13 (a). In the following the understanding of a trained pattern is exemplarily presented. In the two channel pattern (Figure 8.13 (a)) channel 1 and channel 5 should be trained as one connected pattern. The numeration of the channels is shown in Figure 8.13 (b). In the subsequent Figures, we use the same color code as used in the presented patterns. Gray squares correspond to trained channels, blue squares to applied biases to input and output contacts, and green squares to measured currents at the output contacts. Figure 8.13 (c) shows the target behavior of a network, which memorizes the trained pattern from Figure 8.13 (a). When a bias is applied to input 1, or to input 5, or to input $1+5$ the highest currents are measured at output contacts 1 and 5. The highest currents at output 1 and

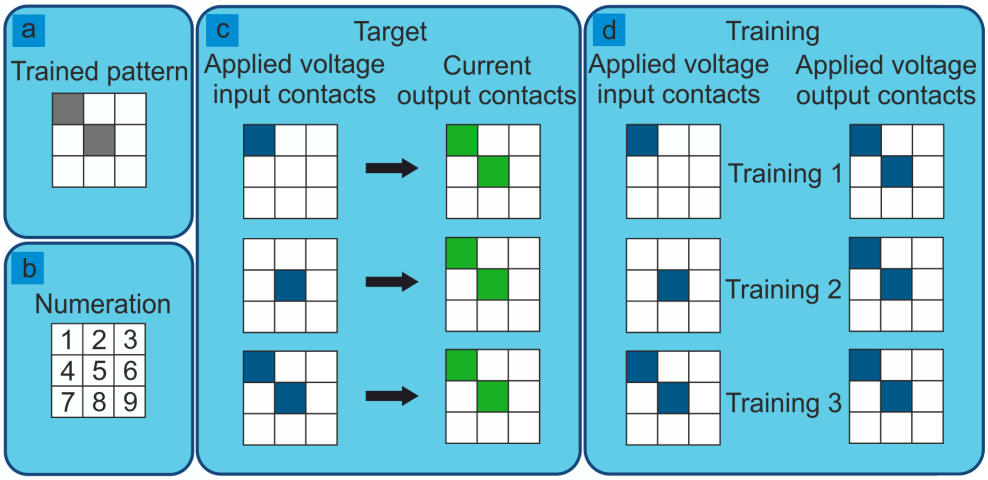

Figure 8.13: *Principle of the pattern recognition and the training process of the neural network. Blue squares always correspond to applied voltages, green to measured currents at the output and gray for trained patterns. (**a**) Pattern which is trained to the neural network. In this pattern we want to connect channel 1 and channel 5. The numeration of the nine channels is displayed in the nine part square in (**b**). We use the same numeration for input and output contacts. (**c**) Target for a neural network, which memorizes the pattern shown in (**a**) successfully. The blue colored squares define to which input contacts a voltage is applied, whereas the green squares correspond to the measured currents at the output contacts. If the network remembers the pattern shown in (**a**), a voltage input at contact 1, 5, and $1+5$ result in the same measured output pattern of output $1+5$. **(d)** Sketches the three training steps to teach the neural network. By applying a potential difference between input 1 and output $1+5$ (training 1), input 5 and output $1+5$ (training 2), and input $1+5$ and output $1+5$ (training 3) we activate the conducting paths between input $1+5$ and output $1+5$.*

5 show that the electrical path between input 1 and output 1 and 5 and between input 5 and output 1 and 5 are activated and therefore channels 1 and 5 are connected with each other. The training process to achieve a memorized network is sketched in Figure 8.13 (d). One training cycle consists of three subsequent training steps. In training step 1 a constant voltage is applied to input 1 with $V_{input1} = constant$, and a variable voltage to output 1 and 5 $V_{output1,5} = variable$. Both voltages are set against ground and have opposite signs to induce currents between input 1 and output $1 + 5$. All the other inputs and outputs are set to floating. During the training the output voltage $V_{output1}$ and $V_{output5}$ are ramped up starting at zero until a threshold current $I_{threshold}$ is reached at output 1 and output 5, respective. The threshold current has to be set and determines the strength of the training. When the current has reached $I_{threshold}$, the applied voltage is reduced to zero and the training step is completed. The measured current increases upon increasing applied biases at the outputs due to two adding up effects. The increased applied voltage causes directly an increase in current according to Ohm's Law. Additionally a decrease in the resistance of the electronic paths increases the current, which is caused by the activation of many Ag NW-Ag NW junctions. The MIM junctions are activated due to the additionally applied voltage. The speed of the ramping up of the voltages is steered by a PID feedback loop and is independent for both output channels. In the first training cycle V_{input1} has to be set. In the subsequent cycles V_{input1} is adjusted using following approach to obtain similar values for V_{input} and V_{output}. By applying similar V_{input} and V_{output} the wanted channels are trained in a more efficient way than the remaining channels. In the limiting case where a voltage is only applied to one output, all channels between each input and this particular output would be trained with a similar strength. V_{input1} is therefore changed after each cycle to $V_{input1} = (V'_{input1} + V'_{output})/2$ where V'_{input1} is the applied input voltage in the previous cycle and V'_{output} is the lower value of the two maximum applied voltages $V'_{max,output1}$ and $V'_{max,output5}$ in the previous cycle. Consequently in the subsequent cycle, V_{input1} has a similar value as $V_{max,output}$ when $I_{threshold}$ is reached as $I_{threshold}$ is obtained when V_{input1} and the ramped up V_{output} add up to $V'_{threshold} \sim V'_{input1} + V'_{output}$ of the previous cycle. The second and third training step shown in Figure 8.13 (d) are executed subsequently to training step 1 following the same procedure. After completing one training cycle (training 1-3), the network is tested to determine if the wanted pattern is memorized.

Therefore, we prove that the target behavior shown in Figure 8.13 (c) is obtained. The three voltage patterns on the left side in Figure 8.13 (c) are tested at the network and the output currents are compared to the wanted output pattern shown on the right side in Figure 8.13 (c). The input voltage is typically set to $V_{test} \sim 0.1$ V and the pulse duration is in the order of seconds. Evidently larger integration times t_{int} would reduce the noise but are not accessible as the network tends to forget the trained pattern in the timescale of a few seconds up to a few minutes. The current is measured at all nine outputs after a delay time of $t_{delay} = 0.1$ s to reduce the influence of capacitive effects. If the output pattern are correct (highest currents at output $1 + 5$), the network was trained successfully and remembers the wanted pattern in

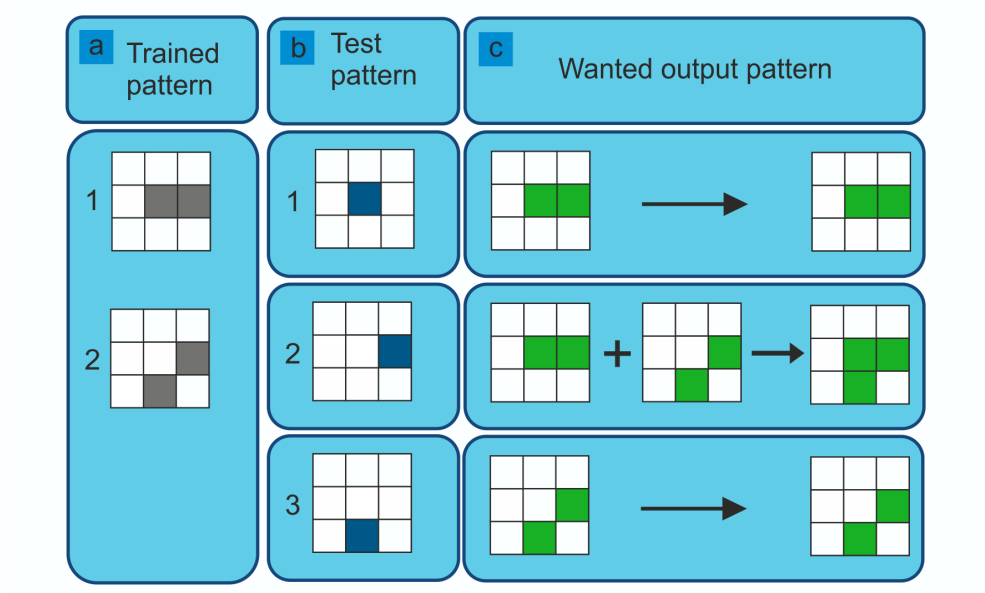

Figure 8.14: *Principle of the combination of overlapping patterns: (**a**) Two trained patterns which overlap in the activation of channel 6. (**b**) Three test pattern where single inputs are tested. (**c**) Wanted output patterns: For an applied voltage at input 5 (input 8) pattern 1 (pattern 2) are activated and the resulting wanted outputs are shown here. For an applied voltage at input 6, pattern 1 and 2 are activated and the resulting wanted output now consists of three high current outputs, namely output 5, 6, and 8.*

Figure 8.13 (a). As long as the tests are not successful the training cycle is repeated and the network is tested again. When more than one different pattern is trained to the network, the individual patterns are trained one after another and independently of each other. After all patterns are trained, all tests are executed subsequently and the next training/test cycle starts until all patterns are tested successfully.

If multiple patterns are trained to the network, the wanted output is modified in case the different trained patterns overlap. An example of a trained network with overlapping patterns is shown in Figure 8.14. The two trained patterns (see Figure 8.14 (a)) are overlapping at channel 6. In Figure 8.14 (b) the three different single input test pattern are shown. When test pattern 1 (Figure 8.14 (b)) is tested a voltage is applied to input 5 and therefore output 5 and 6 should be activated. Similar behavior is obtained by applying a voltage to input 8 (test pattern 3), which gives highest currents at output 6 and 8. When a voltage is applied to input 6 both pattern 1 and 2 are activated and the resulting wanted output consists of three highest current outputs, namely output 5, 6, and 8. Depending on the number of trained patterns and the number of overlapping channels the wanted output can vary in the number of different output patterns and in the number of highest current outputs. In the following one measured example is shown with five trained patterns, leading to three different output patterns.

8.3.2 Neural network memorizes five patterns

In Figure 8.15 the training of a nine channel neural network device is illustrated with overlapping patterns. Figure 8.15 (a) shows five different patterns, which were trained to the network with the above described method. All five patterns are trained subsequently in the training cycle and after finishing the training all five patterns are tested. As the patterns are overlapping, we obtain three different successful output patterns (Figure 8.15 (b) 1-3). All tested pattern (1-3) during the testing cycles are shown in Figure 8.15 (c) and assigned to the successful output patterns in Figure 8.15 (b). A bias applied to input 6 and to input 7 gives unique wanted output patterns with three highest current outputs. For example input 6 is connected to trained patterns 1 and 2 and therefore the wanted output is given by highest currents at outputs 5, 6, and 8. All other tested inputs result in the same four highest current output pattern. For example input 5 activates the trained patterns 1, 3, and 5 and consequently the highest currents should be measured at outputs 5, 6, 7, and 8. Figure 8.16 shows the evolution of the executed training on the neural network device. In the left column Figure 8.16 (a) the input test patterns are shown and in (b) the corresponding highest current output patterns. Figure 8.16 (c) presents the obtained currents at the outputs, which were measured before the network was trained. The applied test voltage was set to 0.15 V and the measured current is color coded with a scale shown at the bottom of Figure 8.16 ranging from 0 A to 10^{-8} A.

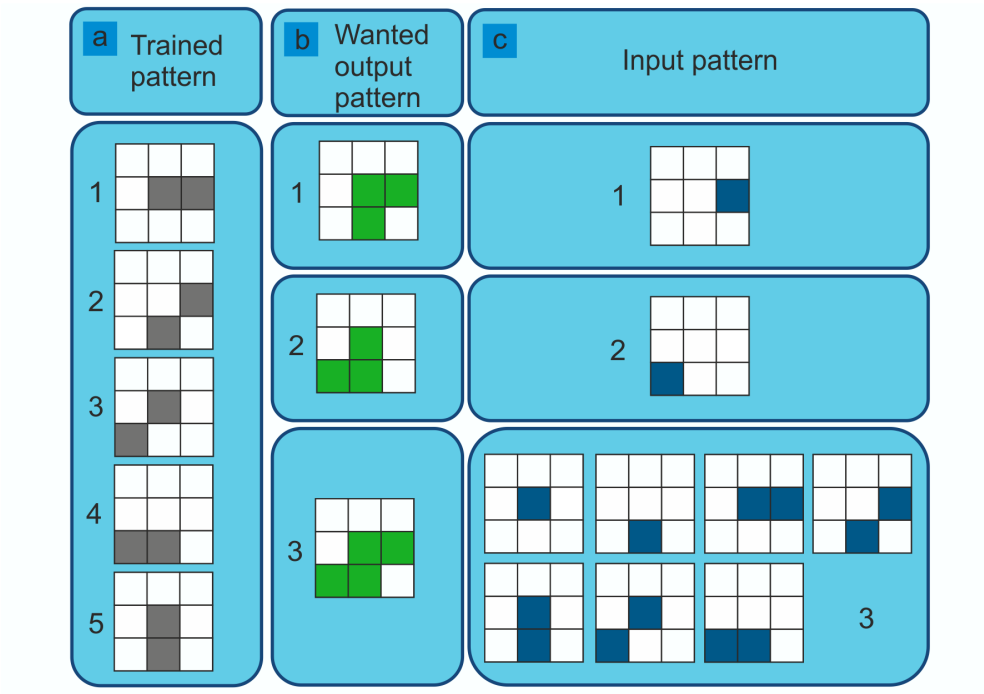

Figure 8.15: *Neural network device, which memorizes five different patterns. (**a**) Five different patterns, which are trained to the neural network device. (**b**) Three different correct output patterns for the trained patterns in (**a**). (**c**) All different tested input patterns dedicated to the corresponding output patterns in (**b**).*

Figure 8.16: *Evolution of training of the neural network device, which memorizes five different patterns. (**a**) 15 tested patterns where a voltage of* 0.15 V *is applied to the blue colored squares. (**b**) The wanted output patterns for each test pattern in (**a**), where the green squares correspond to the outputs with the highest currents. (**c**) Color coded measured output currents before training was started and evaluation if the output patterns are correct (green check) or incorrect (red cross). Already five input patterns out of 15 lead to correct output patterns, whereas ten inputs result in wrong output patterns. (**d**) Color coded measured output currents after more than 20 cycles of training and evaluation if the output patterns are correct (green check) or incorrect (red cross). Now after several training cycles, all 15 tests result in correct output patterns.*

In the right part of column (c) the output pattern is evaluated and if the output is correct or (incorrect) it is marked by a green check (red cross). In Figure 8.16 (d) the measured output patterns after more than 20 trainings cycles with $I_{threshold} = 10^{-7}$ A and the corresponding evaluations whether the tests are correct or incorrect are shown.
Before the training was started the network gave correct outputs for 5 of 15 tested patterns. The five correct outputs gave the right result just by chance. However 10 measured output patterns showed incorrect current distributions. As the trained patterns are overlapping some of the single channel input patterns are tested and trained several times per cycle. It is noteworthy that the same input pattern can give different results because of a relevant noise level reaching up to several 10^{-10} A. For example the second test pattern with an applied voltage at input 5 results in the correct output pattern whereas test patterns 8 and 14 (input 5) exhibit incorrect output patterns in the first test cycle. After the network was trained for more than 20 cycles the success rate has reached its maximum of 15 correct patterns out of 15 tests. All 15 tested input pattern led to the wanted output, giving evidence that the network has memorized 5 different input and 3 different outputs due to the specific training described above.

8.3.3 Visualizing the evolution of the training

For a better understanding of the training effect we applied a modified training and testing method. For the following measurements, channels 1-9 (e.g. channel 1 = input 1 to output 1) are trained during the training cycle. In Figure 8.17 the conductance, obtained from the current measurements at the output, between input 1 and the nine output channels is plotted against the test cycle number. The graph Channel 1-1 belongs to the conductance between input 1 and output 1, whereas Channel 1-2 belongs to the conductance between input 1 and output 2, etc. The conductance was calculated by I/V and still carries the information of the direction of the current. In Figure 8.17 input 1 is exemplarily shown and the same analysis is done for input 2-9. Several properties of the neural network device are noticeable:

- From input 1 only the electrical path to output 1 was intended to be trained. However, also channel 2-9 show relevant modifications when a voltage is applied to input 1.
- The graph of channel 1-1 shows only slight increase of conductance over time.
- The graph of channel 1-4 shows current in opposite directions than the graphs of channel 1-3 and 1-5.
- The graphs of channel 1-4 and 1-5 show that the electric paths can switch from low conducting to high conducting and the other way around within one training cycle.
- The graph of channel 1-9 reveals that the path can be activated/deactivated continuously but also stepwise.

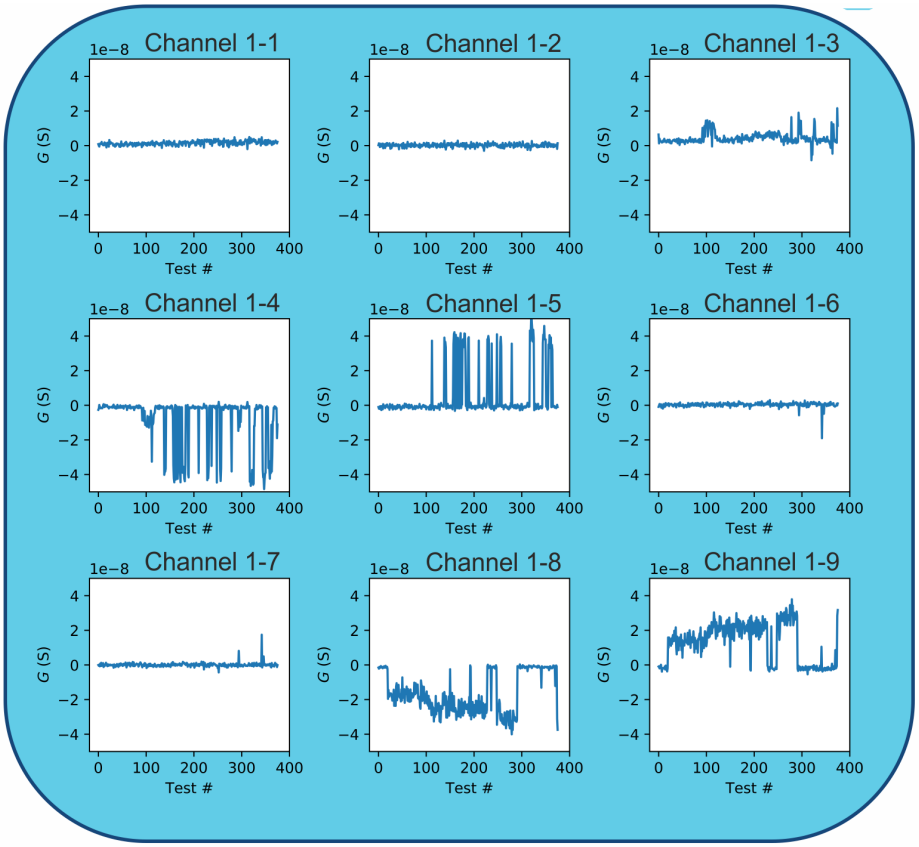

Figure 8.17: *Evolution of conductance between the nine different outputs and input 1. Channel 1-1 shows the conductance between input 1 and output 1, whereas Channel 1-2 shows the conductance between input 1 and output 2, etc. Each point in a graph represents one conductance measurement.*

- For most test cycles the conductance of channel 1-1 does not show the highest conductance of all nine channels. This means that in this case it was not possible to teach the network to memorize the pattern with input 1 and output 1.

Figure 8.18 shows the same data set as used for Figure 8.17 but presented as explained in the following.
The graphs show the measured conductances at output 1 for applied voltages at different inputs. Channel 1-1 shows the conductance between input 1 and output 1, whereas Channel 2-1 shows the conductance between input 2 and output 1, etc.. In Figure 8.18, we obtain a slight increase of the conductance for channel 1-1, whereas the conductance of the remaining 8 channels stays almost constant with increasing number of training/test cycles. In the presentation of Figure 8.18 we see that the current at output 1 could be increased upon training of channel 1, whereas channel 2-1, 3-1, etc. weren't trained.

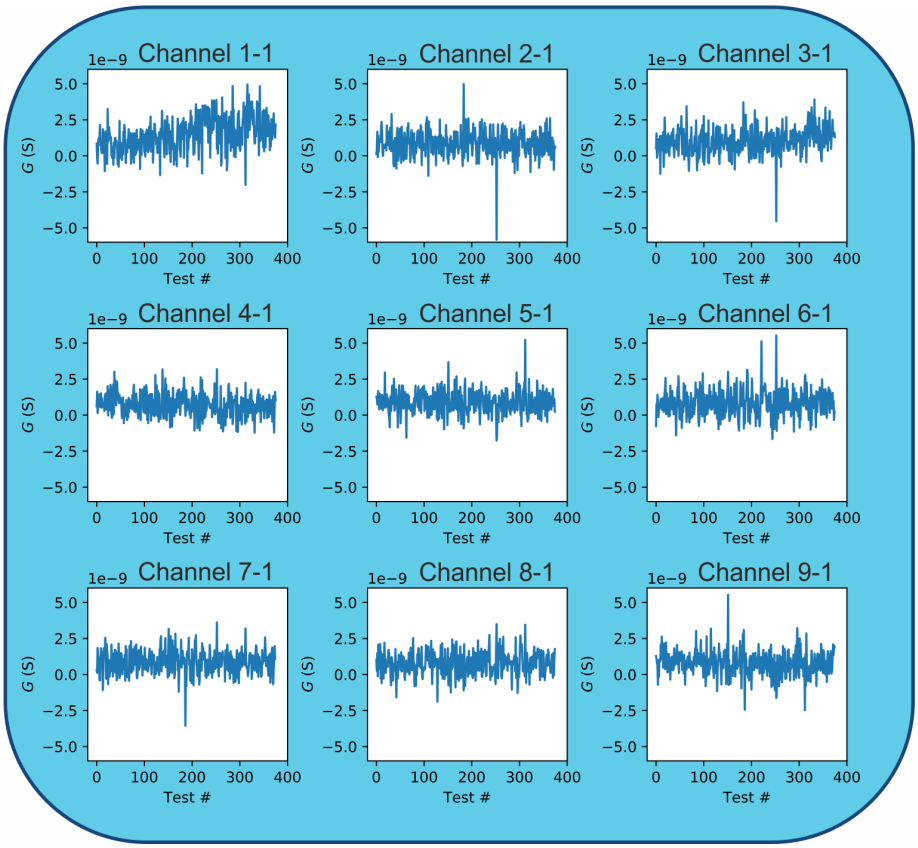

Figure 8.18: *Evolution of conductance between the nine different inputs and output 1. Channel 1-1 shows the conductance between input 1 and output 1, whereas Channel 2-1 shows the conductance between input 2 and output 1, etc.. Each point in a graph represents one conductance measurement.*

8.4 Power spectrum density

For the nine channel neural network device shown above, which memorized five different patterns we used the measured current at the outputs to define which channels are activated. In this approach instantly one major problem appears: to state if the measured output patterns are correct one has to know initially how many activated channels the wanted output patterns has. This substantially limits the use of an unknown but already trained neural network device. A different or expanded approach to distinguish between activated and deactivated channels is the examination of the characteristic power spectral density (PSD) of the measured current. Demis et. al. [468] showed in a similar system that the slope of the PSD against the frequency f is different for activated and deactivated conducting paths. Figure 8.19 shows several PSDs of the current measured at the outputs 1-9 during an applied voltage at input 1. A fast fourier transformation (FFT) and a subsequent Gaussian filter is applied to convert the current signal into the PSD graphs pictured in Figure 8.19. The blue lines correspond to the PSDs before the training of the network was started. All outputs except output 3 show a almost constant PSD

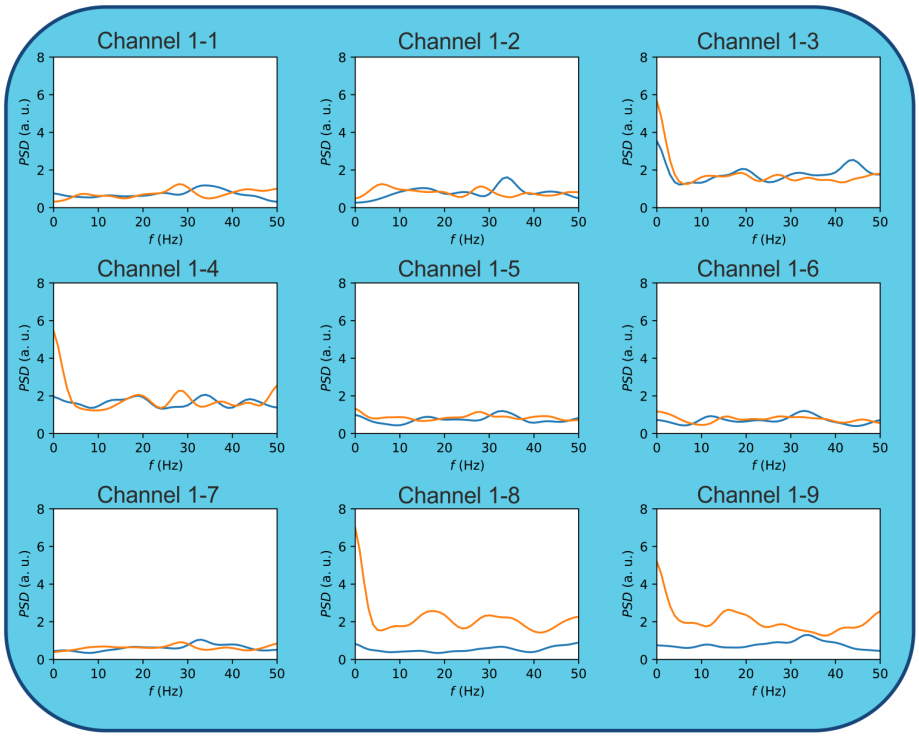

Figure 8.19: *Power spectral density (PSD) analysis. PSD of output currents 1-9 when voltage applied to input 1. The blue graphs show the PSD spectra before the network was trained. The orange lines present the PSD spectra after the network was trained for 100 cycles. Before training only channel 3 shows a signature of high PSD for small frequencies, which we assign to be characteristic for activated channels. After 100 cycles of training channel 3,4,8, and 9 reveal this specific activated PSD behavior.*

for the whole frequency range. Output 3 exhibits a strong increase in its PSD for frequencies $f \longrightarrow 0$ Hz. The orange lines correspond to the PSD after the network was trained for 100 cycles. Now, outputs 3, 4, 8, and 9 show the characteristic increase in PSD for small frequencies. After 120 cycles outputs 8 and 9 and after 180 cycles outputs 4,5,8, and 9 reveal similar PSD behavior. We assign these channels with high PSD for low frequencies to our activated channels. By comparing the results from Figure 8.19 with the conductance evolution graphs in Figure 8.17 a correlation between conductance and PSD signature is observable. At the first test cycle only output 3 shows the activated channel signature in its PSD and a slightly enhanced conductance at channel 3 is also found in Figure 8.17. After 100 cycles we find an increased conductance for channels 3,4,8, and 9, which matches again the observations in the PSD graphs. The same observations are made for the measurements after 120 and 180 cycles. Interestingly, the PSD of the activated channels appear to have similar signature, even though the conductance differs by more than one order of magnitude. To quantify our PSD spectra we fitted the graphs to a power law behavior of $\propto 1/f^{\beta}$ with a fitting range from 1 to 6 Hz. For the orange PSD spectra in Figure 8.19 after 100 cycles we obtain β-values for the not activated channels of $\beta \sim 0.1$ and $\beta = 0.83 \pm 0.05$ for the activated channels.

8.5 Summary and outlook

We have shown in our multi-probe measurements that the PSD characteristics of the MIM junctions can be used to state if the junction is activated or deactivated. In contrast to a continuous transition from not conducting to conducting in the current or conductance values, the β value obtained from fitting a power law behavior $\propto 1/f^{\beta}$ to the PSD shows digital behavior. Furthermore we showed that the activation process takes place within the time period of 1 ms. By scaling up from a single MIM junction to a network of thousands of Ag NWs we created a macroscopic nine channel neural network device. Starting from memorizing 5 out of 15 tested patterns we achieved a complete set of all 15 tested patterns memorized by the neural network device after > 20 training cycles. To introduce the new findings from our multi-probe measurements we analyzed the PSD from our macroscopic network. These promising results show that the PSD signature is suitable to state which channels are activated in a significantly better way than the measured current, especially with regards to trained but unknown neural networks.

9 Summary and outlook

The bottom-up approach for the production of nano electronic devices is picking up momentum within the last years. Massive research efforts focus on the self-assembly of molecules and the on-surface synthesis of atomically precise nanostructures, leading to a huge number of accessible bottom-up fabrication protocols.
In this work, we succeeded in expanding the tool box for bottom-up assembly.

1. We introduced the intercalation of functional molecules in a sp^2-hybridized boron nitride/metal system, opening up the possibility to protect molecules below an h-BN layer. The presented intercalation process can be triggered by moderate temperatures, and is consequently suitable for organic materials. While the molecules self-assemble in a highly ordered arrangement, the intrinsic functionality of the electronically triggered switching of the molecules is preserved.
   The largest potential of the intercalation lies in the creation of nano electronic devices based on vdW heterostructures comprising different two-dimensional materials and molecules. With a deeper understanding of the intercalation process it should be possible to develop protocols to selectively intercalate specific molecules in such stacked heterostructures.
   However, so far devices based on organic materials such as photovoltaics often struggle with their long term stability on air. Therefore, we characterized the h-BN/molecule/Cu(111) system after exposure to ambient conditions and showed that the interfaces are modified. Accordingly, the quality of the h-BN monolayer was not high enough to provide perfect protection from the ambient environment. Most likely, oxygen percolates the h-BN layer at the very same defects that act as entrance channels for the (metal-)organic molecules. Consequently, a method to subsequently close such defects has to be found. By positioning the read-out electrodes of the device at such defect locations the intercalation of oxygen might be inhibited.

2. On-surface synthesis opens up ways to structure covalently bound nano architectures with atomic precision. However, so far such reactions have been mostly reported on a catalytic active metal support. Here a molecule was introduced with a highly reactive azomethine group, which exhibits a low reaction barrier in a way that we successfully achieved the on-surface synthesis of long polyaromatic chains on h-BN/Cu(111).
   We showed that the coupling of azomethine with a cyano group is a promising reaction to create carbon based nano architectures on non-metallic supports. The implementation of on-surface reactions on insulating materials will be crucial for the realization of bottom-up produced nano devices with molecular functionalities.

3. Graphene is one of the most promising materials for high performance nano technology. Geometric distortions in the two-dimensional graphene alter its electronic properties. We revealed a correlation between adsorption height of graphene and the local work function of the graphene/Cu(111) system. For the challenging determination of the geometric corrugation we introduced a method providing outstanding vertical precision.
   Furthermore, functional porphine molecules on graphene reveal an efficient decoupling from an underlying metal surface. We showed that the porphines' self-assembly on graphene/Cu(111) and graphene/Ag(111) is undisturbed by the Moiré induced electronic corrugation. Furthermore, on graphene the intrinsic electronic properties of porphines are only slightly influenced, in contrast to the adsorption on metal surfaces. Therefore, graphene, which exhibits outstanding electronic conductance, can be used as a read-out electrode for functional molecules outperforming bulk metals as the molecular electronic structure is essentially less disturbed.

4. An artificial neural network device was investigated in the macroscopic and the microscopic regime. We conducted electronic measurements on the microscopic level with a four-probe AFM. We showed that the findings on single nano wires can be transferred to the electronic analysis of the macroscopic nano wire arrangement of the neural network device. Such microscopic electrical measurements will be necessary to prove the functionality of bottom-up developed electronic devices. In nano electronic devices the read-out of the molecular states will be challenging and the understanding of the electronic transport on the microscopic scale is crucial. Therefore, multi-probe experiments, enabling conductance measurements in the nano scale, will become increasingly relevant. Furthermore, electrical measurement of molecular architectures on insulating materials can profit from multi-probe experiments.

List of publications

Garnica, M.; Schwarz, M.; Ducke, J.; He, Y.; Bischoff, F.; Barth, J. V.; Auwärter, W.; Stradi, D. Comparative study of the interfaces of graphene and hexagonal boron nitride with silver. *Phys. Rev. B* 2016, 94.

He, Y.; Garnica, M.; Bischoff, F.; Ducke, J.; Bocquet, M.-L.; Batzill, M.; Auwärter, W.; Barth, J. V. Fusing tetrapyrroles to graphene edges by surface-assisted covalent coupling. *Nature Chem* 2016, 9, 33-38.

Ducke, J.; Riss, A.; Pérez Paz, A.; Seufert, K.; Schwarz, M.; Garnica, M.; Rubio, A.; Auwärter, W. Layered Insulator/Molecule/Metal Heterostructures with Molecular Functionality through Porphyrin Intercalation.*ACS Nano* 2018.

Schwarz, M.; Riss, A.; Garnica, M.; Ducke, J.; Deimel, P. S.; Duncan, D. A.; Thakur, P. K.; Lee, T.-L.; Seitsonen, A. P.; Barth, J. V.; Allegretti, F.; Auwärter, W. Corrugation in the Weakly Interacting Hexagonal-BN/Cu(111) System: Structure Determination by Combining Noncontact Atomic Force Microscopy and X-ray Standing Waves. *ACS Nano* 2017, 11, 9151-9161.

Schwarz, M.; Garnica, M.; Duncan, D. A.; Pérez Paz, A.; Ducke, J.; Deimel, P. S.; Thakur, P. K.; Lee, T.-L.; Rubio, A.; Barth, J. V.; Allegretti, F.; Auwärter, W. Adsorption Conformation and Lateral Registry of Cobalt Porphine on Cu(111). *J. Phys. Chem. C* 2018.

Schwarz, M.; Garnica, M.; Duncan, D. A.; Ducke, J.; Deimel, P. S.; Thakur, P. K.; Lee, T.-L.; Rubio, A.; Barth, J. V.; Allegretti, F.; Auwärter, Adsorption Geometry of Cobalt Porphine on Two-Dimensional Hexagonal Boron Nitride. *in preparation*

Bischoff, F.; Riss, A.; Ducke, J; Barth J. V.; Auwärter. Surface-catalyzed ring-opening reaction and porphyrin deconstruction via conformational design. *in preparation*

Ducke, J.; Riss, A.; Pérez Paz, A.; Feng, X.; Auwärter, W.; Palma, C.A..; Müllen, K.; N-doped polyaromatic oligomers through selective AB azomethine ylide cycloadditions on metals and insulating layers. *in preparation*

A Appendix

STS of Co-Ps/graphene/Cu(111) - Linescan In Figure A.1 (a) a Co-P island on graphene/Cu(111) is depicted, where the dark disks correspond to the centers of the molecules. We can visualize the Moiré periodicity of 7 nm by applying a Gaussian filter (Figure A.1 (a)). The corresponding Moiré pores are encircled in white, whereas the red dots mark positions where dI/dV spectra were taken.

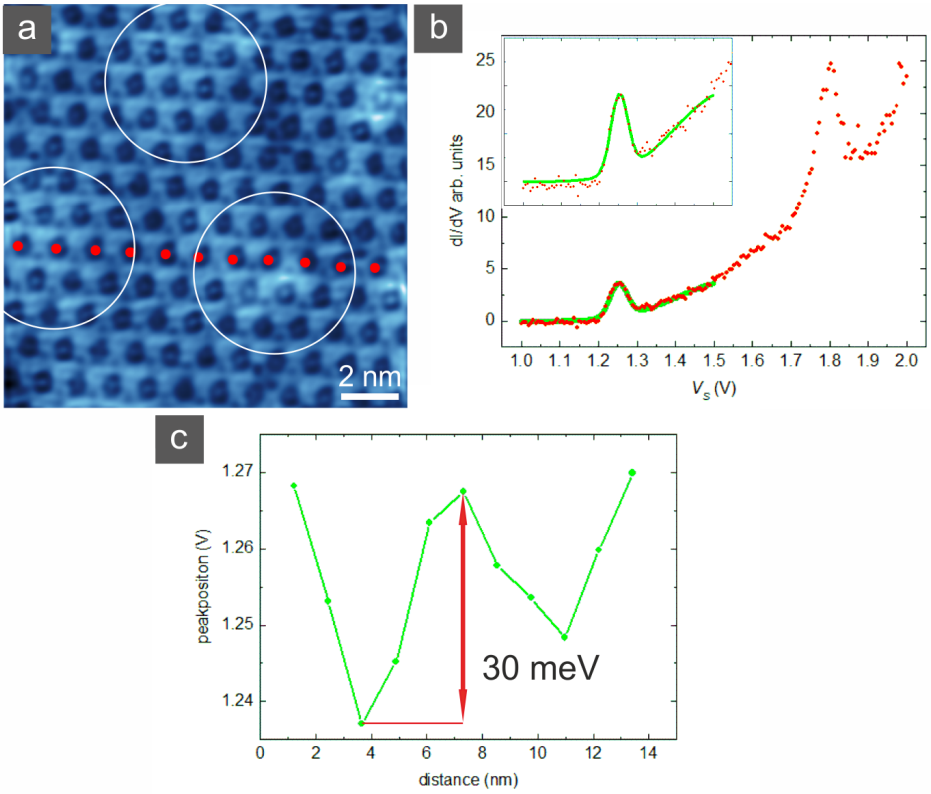

Figure A.1: *STS linescan of Co-P on graphene/Cu(111) at high coverage. (**a**) Hexagonally ordered Co-Ps with NN-distance of $a = 12$ Å. White circles mark the pores of the Moiré lattice and red dots are the locations where STS were taken. (**b**) Typical STS spectrum taken at the center of a Co-P as marked in (**a**). Red points present the measured data and in green the corresponding fit is depicted. The inset shows an enlarged graph of the STS and the corresponding fit. The measured STS shows distinct resonances at $V_S \sim 1.25$ V and $V_S \sim 1.8$ V and an increase of the DOS for higher voltages. The inset, a zoom-in to the fitted data, exhibits good consistency between data and fit. (**c**) The position of the peaks in the fits are used to visualize the energy variations of the DOS peak in (**b**). The peak positions are plotted against the distance along the line of the marked Co-Ps in (**a**). We quantify the energy shift between pore and wire region to $\Delta E \sim 30$ meV.*

A typical STS spectrum is plotted in Figure A.1 (b), where the red dots represent the measured data points and the green solid line is a fit to the data set, using two Gaussian peaks and a constant offset. For the high coverage Co-P system the STS spectra are strongly

modified compared to the low coverage system described above. We observe distinct resonances, at $V_S \sim 1.25$ V and $V_S \sim 1.8$ V, which are less pronounced than for small agglomerates and superimposed by a strong featureless increase in the DOS for higher voltages.
The measured data are fitted to two Gaussian peaks and a constant offset. The fit region is enlarged in the inset of Figure A.1 (b) and reveals very good agreement with the measured dI/dV curves.
In Figure A.1 (c) the fitted peak positions are used to visualize the shifts of the peak energy across the Moiré. We clearly see a correlation of the peak energy with the corresponding lateral position on the Moiré lattice. We quantify the energy shift between pore and wire region to $\Delta E \sim 30$ meV as shown in Figure A.1 (c).

References

[1] J. Bardeen and W. H. Brattain. "The Transistor, a Semi-Conductor Triode". In: *Physical Review* 74.2 (1948), pp. 230–231. DOI: 10.1103/PhysRev.74.230.

[2] Gordon E. Moore. *Cramming more components onto integrated circuits*. New York: McGraw-Hill, 1965.

[3] R. R. Schaller. "Moore's law: Past, Present and Future". In: *IEEE Spectrum* 34.6 (1997), pp. 52–59. DOI: 10.1109/6.591665.

[4] Laszlo B. Kish. "End of Moore's Law: Thermal (Noise) Death of Integration in Micro and Nano Electronics". In: *Physics Letters A* 305.3-4 (2002), pp. 144–149. DOI: 10.1016/S0375-9601(02)01365-8.

[5] M. Mitchell Waldrop. "The Chips are Down for Moore's Law". In: *Nature* 530.7589 (2016), pp. 144–147. DOI: 10.1038/530144a.

[6] J. L. Brédas and R. R. Chance. *Conjugated Polymeric Materials: Opportunities in Electronics, Optoelectronics, and Molecular Electronics*. Vol. 182. NATO ASI Series, Series E: Applied Sciences. Dordrecht: Springer Netherlands, 1990. ISBN: 9789400920415.

[7] J. Chen. "Large On-Off Ratios and Negative Differential Resistance in a Molecular Electronic Device". In: *Science* 286.5444 (1999), pp. 1550–1552. DOI: 10.1126/science.286.5444.1550.

[8] James M. Tour. "Molecular Electronics. Synthesis and Testing of Components". In: *Accounts of Chemical Research* 33.11 (2000), pp. 791–804. DOI: 10.1021/ar0000612.

[9] R. Lloyd Carroll and Christopher B. Gorman. "The Genesis of Molecular Electronics". In: *Angewandte Chemie International Edition* 41.23 (2002), pp. 4378–4400. DOI: 10.1002/1521-3773(20021202).

[10] James R. Heath and Mark A. Ratner. "Molecular Electronics". In: *Physics Today* 56.5 (2003), pp. 43–49. DOI: 10.1063/1.1583533.

[11] Gianaurelio Cuniberti, Giorgos Fagas, and Klaus Richter. *Introducing Molecular Electronics*. Vol. 680. Lecture Notes in Physics. Berlin, Heidelberg: Springer, 2006. ISBN: 978-3-540-31514-8.

[12] Ben L. Feringa, ed. *Molecular Switches*. 1. Nachdruck. Weinheim: Wiley-VCH, 2003. ISBN: 3527299653. DOI: 10.1002/3527600329.

[13] N. J. Tao. "Electron Transport in Molecular Junctions". In: *Nature nanotechnology* 1.3 (2006), pp. 173–181. DOI: 10.1038/nnano.2006.130.

[14] Jonathan E. Green, Jang Wook Choi, Akram Boukai, Yuri Bunimovich, Ezekiel Johnston-Halperin, Erica DeIonno, Yi Luo, Bonnie A. Sheriff, Ke Xu, Young Shik Shin, Hsian-Rong Tseng, J. Fraser Stoddart, and James R. Heath. "A 160-Kilobit Molecular Electronic Memory Patterned at 10(11) Bits per Square Centimetre". In: *Nature* 445.7126 (2007), pp. 414–417. DOI: 10.1038/nature05462.

[15] Willi Auwärter, Knud Seufert, Felix Bischoff, David Ecija, Saranyan Vijayaraghavan, Sushobhan Joshi, Florian Klappenberger, Niveditha Samudrala, and Johannes V. Barth. "A Surface-Anchored Molecular Four-Level Conductance Switch Based on Single Proton Transfer". In: *Nature. Nanotech.* 7.1 (2011), pp. 41–46. DOI: 10.1038/nnano.2011.211.

[16] L. Schmidt-Mende, A. Fechtenkötter, K. Müllen, E. Moons, R. H. Friend, and J. D. MacKenzie. "Self-Organized Discotic Liquid Crystals for High-Efficiency Organic Photovoltaics". In: *Science* 293.5532 (2001), pp. 1119–1122. DOI: 10.1126/science.293.5532.1119.

[17] Christoph J. Brabec. "Organic Photovoltaics: Technology and Market". In: *Solar Energy Materials and Solar Cells* 83.2-3 (2004), pp. 273–292. DOI: 10.1016/j.solmat.2004.02.030.

[18] E. Bundgaard and F. KREBS. "Low Band Gap Polymers for Organic Photovoltaics". In: *Solar Energy Materials and Solar Cells* 91.11 (2007), pp. 954–985. DOI: 10.1016/j.solmat.2007.01.015.

[19] Bernard Kippelen and Jean-Luc Brédas. "Organic Photovoltaics". In: *Energy & Environmental Science* 2.3 (2009), p. 251. DOI: 10.1039/b812502n.

[20] G. Whitesides, J. Mathias, and C. Seto. "Molecular self-assembly and nanochemistry: A Chemical Strategy for the Synthesis of Nanostructures". In: *Science* 254.5036 (1991), pp. 1312–1319. DOI: 10.1126/science.1962191.

[21] C. Joachim, J. K. Gimzewski, and A. Aviram. "Electronics Using Hybrid-Molecular and Mono-Molecular Devices". In: *Nature* 408.6812 (2000), pp. 541–548. DOI: 10.1038/35046000.

[22] Shuguang Zhang. "Fabrication of Novel Biomaterials Through Molecular Self-Assembly". In: *Nature Biotechnology* 21.10 (2003), pp. 1171–1178. DOI: 10.1038/nbt874.

[23] J. Christopher Love, Lara A. Estroff, Jennah K. Kriebel, Ralph G. Nuzzo, and George M. Whitesides. "Self-Assembled Monolayers of Thiolates on Metals as a Form of Nanotechnology". In: *Chemical reviews* 105.4 (2005), pp. 1103–1169. DOI: 10.1021/cr0300789.

[24] Abraham Ulman. *An Introduction to Ultrathin Organic Films: From Langmuir–Blodgett to Self–Assembly*. Burlington: Elsevier Science, 2013. ISBN: 0080926312.

[25] Bin Li, Liduo Wang, Bonan Kang, Peng Wang, and Yong Qiu. "Review of Recent Progress in Solid-State Dye-Sensitized Solar Cells". In: *Solar Energy Materials and Solar Cells* 90.5 (2006), pp. 549–573. DOI: 10.1016/j.solmat.2005.04.039.

[26] Riccardo Po, Chiara Carbonera, Andrea Bernardi, Francesca Tinti, and Nadia Camaioni. "Polymer- and Carbon-Based Electrodes for Polymer Solar Cells: Toward Low-Cost, Continuous Fabrication over Large Area". In: *Solar Energy Materials and Solar Cells* 100 (2012), pp. 97–114. DOI: 10.1016/j.solmat.2011.12.022.

[27] Sushobhan Joshi, Felix Bischoff, Ralph Koitz, David Ecija, Knud Seufert, Ari Paavo Seitsonen, Jürg Hutter, Katharina Diller, José. I. Urgel, Hermann Sachdev, Johannes V. Barth, and Willi Auwärter. "Control of Molecular Organization and Energy Level Alignment by an Electronically Nanopatterned Boron Nitride Template". In: *ACS Nano* 8.1 (2014), pp. 430–442. DOI: 10.1021/nn406024m.

[28] John T. Groves. "The Bioinorganic Chemistry of Iron in Oxygenases and Supramolecular Assemblies". In: *Proceedings of the National Academy of Sciences* 100.7 (2003), pp. 3569–3574. DOI: 10.1073/pnas.0830019100.

[29] W. Kühlbrandt, D. N. Wang, and Y. Fujiyoshi. "Atomic Model of Plant Light-Harvesting Complex by Electron Crystallography". In: *Nature* 367.6464 (1994), pp. 614–621. DOI: 10.1038/367614a0.

[30] Willi Auwärter, David Écija, Florian Klappenberger, and Johannes V. Barth. "Porphyrins at Interfaces". In: *Nat. Chem.* 7.2 (2015), pp. 105–120. DOI: 10.1038/NCHEM.2159.

[31] K. S. Novoselov, A. K. Geim, S. V. Morozov, D. Jiang, M. I. Katsnelson, I. V. Grigorieva, S. V. Dubonos, and A. A. Firsov. "Two-Dimensional Gas of Massless Dirac Fermions in Graphene". In: *Nature* 438.7065 (2005), pp. 197–200. DOI: 10.1038/nature04233.

[32] Yuanbo Zhang, Yan-Wen Tan, Horst L. Stormer, and Philip Kim. "Experimental Observation of the Quantum Hall Effect and Berry's Phase in Graphene". In: *Nature* 438.7065 (2005), pp. 201–204. DOI: 10.1038/nature04235.

[33] Sasha Stankovich, Dmitriy A. Dikin, Geoffrey H. B. Dommett, Kevin M. Kohlhaas, Eric J. Zimney, Eric A. Stach, Richard D. Piner, SonBinh T. Nguyen, and Rodney S. Ruoff. "Graphene-based Composite Materials". In: *Nature* 442.7100 (2006), pp. 282–286. DOI: 10.1038/nature04969.

[34] C. Lee, X. Wei, J. W. Kysar, and J. Hone. "Measurement of the Elastic Properties and Intrinsic Strength of Monolayer Graphene". In: *Science* 321.5887 (2008), pp. 385–388. DOI: 10.1126/science.1157996.

[35] R. R. Nair, P. Blake, A. N. Grigorenko, K. S. Novoselov, T. J. Booth, T. Stauber, Peres, N. M. R., and A. K. Geim. "Fine Structure Constant Defines Visual Transparency of Graphene". In: *Science* 320.5881 (2008), p. 1308. DOI: 10.1126/science.1156965.

[36] C. R. Dean, A. F. Young, I. Meric, C. Lee, L. Wang, S. Sorgenfrei, K. Watanabe, T. Taniguchi, P. Kim, K. L. Shepard, and J. Hone. "Boron Nitride Substrates for High-Quality Graphene Electronics". In: *Nature nanotechnology* 5.10 (2010), pp. 722–726. DOI: 10.1038/nnano.2010.172.

[37] Haibo Wang, Thandavarayan Maiyalagan, and Xin Wang. "Review on Recent Progress in Nitrogen-Doped Graphene: Synthesis, Characterization, and Its Potential Applications". In: *ACS Catalysis* 2.5 (2012), pp. 781–794. DOI: 10.1021/cs200652y.

[38] Gianluca Giovannetti, Petr A. Khomyakov, Geert Brocks, Paul J. Kelly, and Jeroen van den Brink. "Substrate-Induced Band Gap in Graphene on Hexagonal Boron Nitride: Ab Initio Density Functional Calculations". In: *Physical Review B* 76.7 (2007). DOI: 10.1103/PhysRevB.76.073103.

[39] Kenji Watanabe, Takashi Taniguchi, and Hisao Kanda. "Direct-Bandgap Properties and Evidence for Ultraviolet Lasing of Hexagonal Boron Nitride Single Crystal". In: *Nature Materials* 3.6 (2004), pp. 404–409. DOI: 10.1038/nmat1134.

[40] X. Li, W. Cai, J. An, S. Kim, J. Nah, D. Yang, R. Piner, A. Velamakanni, I. Jung, E. Tutuc, S. K. Banerjee, L. Colombo, and R. S. Ruoff. "Large-Area Synthesis of High-Quality and Uniform Graphene Films on Copper Foils". In: *Science* 324.5932 (2009), pp. 1312–1314. DOI: 10.1126/science.1171245.

[41] Phaedon Avouris and Christos Dimitrakopoulos. "Graphene: Synthesis and Applications". In: *Materials Today* 15.3 (2012), pp. 86–97. DOI: 10.1016/S1369-7021(12)70044-5.

[42] Li Song, Lijie Ci, Hao Lu, Pavel B. Sorokin, Chuanhong Jin, Jie Ni, Alexander G. Kvashnin, Dmitry G. Kvashnin, Jun Lou, Boris I. Yakobson, and Pulickel M. Ajayan. "Large Scale Growth and Characterization of Atomic Hexagonal Boron Nitride Layers". In: *Nano letters* 10.8 (2010), pp. 3209–3215. DOI: 10.1021/nl1022139.

[43] Hokwon Kim, Cecilia Mattevi, M. Reyes Calvo, Jenny C. Oberg, Luca Artiglia, Stefano Agnoli, Cyrus F. Hirjibehedin, Manish Chhowalla, and Eduardo Saiz. "Activation Energy Paths for Graphene Nucleation and Growth on Cu". In: *ACS Nano* 6.4 (2012), pp. 3614–3623. DOI: 10.1021/nn3008965.

[44] Kang Hyuck Lee, Hyeon-Jin Shin, Jinyeong Lee, In-yeal Lee, Gil-Ho Kim, Jae-Young Choi, and Sang-Woo Kim. "Large-Scale Synthesis of High-Quality Hexagonal Boron Nitride Nanosheets for Large-Area Graphene Electronics". In: *Nano letters* 12.2 (2012), pp. 714–718. DOI: 10.1021/nl203635v.

[45] L. Britnell, R. V. Gorbachev, R. Jalil, B. D. Belle, F. Schedin, A. Mishchenko, T. Georgiou, M. I. Katsnelson, L. Eaves, S. V. Morozov, Peres, N. M. R., J. Leist, A. K. Geim, K. S. Novoselov, and L. A. Ponomarenko. "Field-Effect Tunneling Transistor Based on Vertical Graphene Heterostructures". In: *Science* 335.6071 (2012), pp. 947–950. DOI: 10.1126/science.1218461.

[46] Gwan-Hyoung Lee, Young-Jun Yu, Xu Cui, Nicholas Petrone, Chul-Ho Lee, Min Sup Choi, Dae-Yeong Lee, Changgu Lee, Won Jong Yoo, Kenji Watanabe, Takashi Taniguchi, Colin Nuckolls, Philip Kim, and James Hone. "Flexible and Transparent MoS2 Field-Effect Transistors on Hexagonal Boron Nitride-Graphene Heterostructures". In: *ACS Nano* 7.9 (2013), pp. 7931–7936. DOI: 10.1021/nn402954e.

[47] Meric, Inanc, et al. "Graphene Field-Effect Transistors Based on Boron Nitride Gate Dielectrics." In: *arXiv preprint arXiv:1101.4712 (2011)* ().

[48] Achim Woessner, Mark B. Lundeberg, Yuanda Gao, Alessandro Principi, Pablo Alonso-González, Matteo Carrega, Kenji Watanabe, Takashi Taniguchi, Giovanni Vignale, Marco Polini, James Hone, Rainer Hillenbrand, and Frank H. L. Koppens. "Highly Confined Low-Loss Plasmons in Graphene-Boron Nitride Heterostructures". In: *Nature Materials* 14.4 (2015), pp. 421–425. DOI: 10.1038/nmat4169.

[49] Simon Berner, Martina Corso, Roland Widmer, Oliver Groening, Robert Laskowski, Peter Blaha, Karlheinz Schwarz, Andrii Goriachko, Herbert Over, Stefan Gsell, Matthias Schreck, Hermann Sachdev, Thomas Greber, and Jürg Osterwalder. "Boron Nitride Nanomesh: Functionality from a Corrugated Monolayer". In: *Angewandte Chemie* 119.27 (2007), pp. 5207–5211. ISSN: 00448249. DOI: 10.1002/ange.200700234.

[50] May Ling Ng, A. B. Preobrajenski, A. A. Zakharov, A. S. Vinogradov, S. A. Krasnikov, A. A. Cafolla, and N. Mårtensson. "Effect of Substrate Nanopatterning on the Growth and Structure of Pentacene Films". In: *Physical Review B* 81.11 (2010). DOI: 10.1103/PhysRevB.81.115449.

[51] Bin Wang and Marie-Laure Bocquet. "Monolayer Graphene and h-BN on Metal Substrates as Versatile Templates for Metallic Nanoclusters". In: *The Journal of Physical Chemistry Letters* 2.18 (2011), pp. 2341–2345. DOI: 10.1021/jz201047c.

[52] Fabian Donat Natterer, François Patthey, and Harald Brune. "Ring State for Single Transition Metal Atoms on Boron Nitride on Rh(111)". In: *Physical Review Letters* 109.6 (2012). DOI: 10.1103/PhysRevLett.109.066101.

[53] Steffen Kahle, Zhitao Deng, Nikola Malinowski, Charlène Tonnoir, Alicia Forment-Aliaga, Nicha Thontasen, Gordon Rinke, Duy Le, Volodymyr Turkowski, Talat S. Rahman, Stephan Rauschenbach, Markus Ternes, and Klaus Kern. "The Quantum Magnetism of Individual Manganese-12-Acetate Molecular Magnets Anchored at Surfaces". In: *Nano letters* 12.1 (2012), pp. 518–521. DOI: 10.1021/nl204141z.

[54] S. Koch, M. Langer, S. Kawai, E. Meyer, and Th Glatzel. "Contrast Inversion of the h-BN Nanomesh Investigated by nc-AFM and Kelvin Probe Force Microscopy". In: *Journal of physics. Condensed matter : an Institute of Physics journal* 24.31 (2012), p. 314212. DOI: 10.1088/0953-8984/24/31/314212.

[55] R. H. Fowler and L. Nordheim. "Electron Emission in Intense Electric Fields". In: *Proceedings of the Royal Society A: Mathematical, Physical and Engineering Sciences* 119.781 (1928), pp. 173–181. DOI: 10.1098/rspa.1928.0091.

[56] J. Frenkel. "On the Electrical Resistance of Contacts between Solid Conductors". In: *Physical Review* 36.11 (1930), pp. 1604–1618. DOI: 10.1103/PhysRev.36.1604.

[57] G. Binnig, H. Rohrer, Ch. Gerber, and E. Weibel. "Surface Studies by Scanning Tunneling Microscopy". In: *Physical review letters* 49.1 (1982), pp. 57–61. DOI: 10.1103/PhysRevLett.49.57.

[58] G. Binnig and H. Rohrer. "Scanning Tunneling Microscopy". In: *Surface Science* 126.1-3 (1983), pp. 236–244. DOI: 10.1016/0039-6028(83)90716-1.

[59] Gerd Binnig and Heinrich Rohrer. "Scanning Tunneling Microscopy—From Birth to Adolescence". In: *Reviews of Modern Physics* 59.3 (1987), pp. 615–625. DOI: 10.1103/RevModPhys.59.615.

[60] Binnig, Quate, and Gerber. "Atomic Force Microscope". In: *Physical review letters* 56.9 (1986), pp. 930–933. DOI: 10.1103/PhysRevLett.56.930.

[61] Gerd K. Binnig. "Atomic Force Microscope and Method for Imaging Surfaces with Atomic Resolution". Pat. 4,724,318. 1986.

[62] Franz J. Giessibl. "AFM's Path to Atomic Resolution". In: *Materials Today* 8.5 (2005), pp. 32–41. DOI: 10.1016/S1369-7021(05)00844-8.

[63] T. R. Albrecht, P. Grütter, D. Horne, and D. Rugar. "Frequency Modulation Detection Using High– Q Cantilevers for Enhanced Force Microscope Sensitivity". In: *Journal of Applied Physics* 69.2 (1991), pp. 668–673. DOI: 10.1063/1.347347.

[64] F. J. Giessibl. "Atomic Resolution of the Silicon (111)-(7x7) Surface by Atomic Force Microscopy". In: *Science* 267.5194 (1995), pp. 68–71. DOI: 10.1126/science.267.5194.68.

[65] F. J. Giessibl. "Vorrichtung Zum Berührungslosen Abtasten einer Oberfläche und Verfahren dafür". Pat. 1996.

[66] Franz J. Giessibl. "High-Speed Force Sensor for Force Microscopy and Profilometry Utilizing a Quartz Tuning Fork". In: *Applied Physics Letters* 73.26 (1998), pp. 3956–3958. DOI: 10.1063/1.122948.

[67] Franz J. Giessibl. "Atomic resolution on Si(111)-(7×7) by noncontact atomic force microscopy with a force sensor based on a quartz tuning fork". In: *Applied Physics Letters* 76.11 (2000), pp. 1470–1472. DOI: 10.1063/1.126067.

[68] Matthias Emmrich, Ferdinand Huber, Florian Pielmeier, Joachim Welker, Thomas Hofmann, Maximilian Schneiderbauer, Daniel Meuer, Svitlana Polesya, Sergiy Mankovsky, Diemo Ködderitzsch, Hubert Ebert, and Franz J. Giessibl. "Surface Structure. Subatomic Resolution Force Microscopy Reveals Internal Structure and Adsorption Sites of Small Iron Clusters". In: *Science* 348.6232 (2015), pp. 308–311. DOI: 10.1126/science.aaa5329.

[69] L. Gross, F. Mohn, N. Moll, P. Liljeroth, and G. Meyer. "The Chemical Structure of a Molecule Resolved by Atomic Force Microscopy". In: *Science* 325.5944 (2009), pp. 1110–1114. DOI: 10.1126/science.1176210.

[70] J. Tersoff and D. R. Hamann. "Theory of the Scanning Tunneling Microscope". In: *Physical Review B* 31.2 (1985), pp. 805–813. DOI: 10.1103/PhysRevB.31.805.

[71] C. Julian Chen. *Introduction to Scanning Tunneling Microscopy*. 2. Aufl. Vol. 64. Monographs on the physics and chemistry of materials. Oxford: Oxford University Press, 2015. ISBN: 9780198754756.

[72] J. Bardeen. "Tunnelling from a Many-Particle Point of View". In: *Physical Review Letters* 6.2 (1961), pp. 57–59. DOI: 10.1103/PhysRevLett.6.57.

[73] R. J. Hamers. "Atomic-Resolution Surface Spectroscopy with the Scanning Tunneling Microscope". In: *Annual Review of Physical Chemistry* 40.1 (1989), pp. 531–559. DOI: 10.1146/annurev.pc.40.100189.002531.

[74] R. García. "Dynamic Atomic Force Microscopy Methods". In: *Surface Science Reports* 47.6-8 (2002), pp. 197–301. DOI: 10.1016/S0167-5729(02)00077-8.

[75] Franz J. Giessibl. "Forces and Frequency Shifts in Atomic-Resolution Dynamic-Force Microscopy". In: *Physical Review B* 56.24 (1997), pp. 16010–16015. DOI: 10.1103/PhysRevB.56.16010.

[76] Franz J. Giessibl. "Advances in Atomic Force Microscopy". In: *Reviews of Modern Physics* 75.3 (2003), pp. 949–983. DOI: 10.1103/RevModPhys.75.949.

[77] S. Morita, Franz J. Giessibl, E. Meyer, and R. Wiesendanger. *Noncontact Atomic Force Microscopy*. Nanoscience and technology. Cham: Springer, 2015. ISBN: 978-3-319-15587-6.

[78] Neil W. Ashcroft and N. David Mermin. *Solid State Physics*. India ed. New Delhi: Cengage Learning, 2011. ISBN: 9788131500521.

[79] Rudolf Gross and Achim Marx. *Festkörperphysik*. 2. Auflage. De Gruyter Studium. München: Oldenbourg, 2014. ISBN: 3110358700.

[80] Gordon Baym. *Lectures on Quantum Mechanics*. [Repr.] Lecture notes and supplements in physics. Boulder, Colo. u.a.]: Westview Press, 2010. ISBN: 0805306676.

[81] H. C. Hamaker. "The London—Van Der Waals Attraction between Spherical Particles". In: *Physica* 4.10 (1937), pp. 1058–1072. DOI: 10.1016/S0031-8914(37)80203-7.

[82] Jacob N. Israelachvili. *Intermolecular and Surface Forces: Revised Third Edition*. San Diego, CA, USA: Elsevier Science & Technology Books, 2011. ISBN: 978-0-080-92363-5.

[83] H. Krupp and G. Sperling. "Theory of Adhesion of Small Particles". In: *Journal of Applied Physics* 37.11 (1966), pp. 4176–4180. DOI: 10.1063/1.1707996.

[84] Roger H. French. "Origins and Applications of London Dispersion Forces and Hamaker Constants in Ceramics". In: *Journal of the American Ceramic Society* 83.9 (2000), pp. 2117–2146. ISSN: 00027820. DOI: 10.1111/j.1151-2916.2000.tb01527.x.

[85] U. Hartmann. "Theory of Van Der Waals Microscopy". In: *Journal of Vacuum Science & Technology B: Microelectronics and Nanometer Structures* 9.2 (1991), p. 465. DOI: 10.1116/1.585590.

[86] L. Olsson, N. Lin, V. Yakimov, and R. Erlandsson. "A Method for in Situ Characterization of Tip Shape in AC-Mode Atomic Force Microscopy using Electrostatic Interaction". In: *Journal of Applied Physics* 84.8 (1998), pp. 4060–4064. DOI: 10.1063/1.368618.

[87] B. M. Law and F. Rieutord. "Electrostatic Forces in Atomic Force Microscopy". In: *Physical Review B* 66.3 (2002), p. 476. DOI: 10.1103/PhysRevB.66.035402.

[88] Shin-ichi Kitamura and Masashi Iwatsuki. "Observation of 7x 7 Reconstructed Structure on the Silicon (111) Surface using Ultrahigh Vacuum Noncontact Atomic Force Microscopy". In: *Japanese Journal of Applied Physics* 34.Part 2, No. 1B (1995), pp. L145–L148. DOI: 10.1143/JJAP.34.L145.

[89] U. Dürig, H. R. Steinauer, and N. Blanc. "Dynamic Force Microscopy by Means of the Phase-Controlled Oscillator Method". In: *Journal of Applied Physics* 82.8 (1997), pp. 3641–3651. DOI: 10.1063/1.365726.

[90] César Moreno, Oleksandr Stetsovych, Tomoko K. Shimizu, and Oscar Custance. "Imaging Three-Dimensional Surface Objects with Submolecular Resolution by Atomic Force Microscopy". In: *Nano Letters* 15.4 (2015), pp. 2257–2262. ISSN: 1530-6984. DOI: 10.1021/nl504182w.

[91] Bruno Schuler, Wei Liu, Alexandre Tkatchenko, Nikolaj Moll, Gerhard Meyer, Anish Mistry, David Fox, and Leo Gross. "Adsorption Geometry Determination of Single Molecules by Atomic Force Microscopy". In: *Physical review letters* 111.10 (2013), p. 106103. DOI: 10.1103/PhysRevLett.111.106103.

[92] S. Akamine, R. C. Barrett, and C. F. Quate. "Improved Atomic Force Microscope Images using Microcantilevers with Sharp Tips". In: *Applied Physics Letters* 57.3 (1990), pp. 316–318. DOI: 10.1063/1.103677.

[93] T. R. Albrecht, S. Akamine, T. E. Carver, and C. F. Quate. "Microfabrication of Cantilever Styli for the Atomic Force Microscope". In: *Journal of Vacuum Science & Technology A: Vacuum, Surfaces, and Films* 8.4 (1990), pp. 3386–3396. DOI: 10.1116/1.576520.

[94] O. Wolter. "Micromachined Silicon Sensors for Scanning Force Microscopy". In: *Journal of Vacuum Science & Technology B: Microelectronics and Nanometer Structures* 9.2 (1991), p. 1353. DOI: 10.1116/1.585195.

[95] M. Tortonese, R. C. Barrett, and C. F. Quate. "Atomic Resolution with an Atomic Force Microscope using Piezoresistive Detection". In: *Applied Physics Letters* 62.8 (1993), pp. 834–836. DOI: 10.1063/1.108593.

[96] J. Rychen, T. Ihn, P. Studerus, A. Herrmann, and K. Ensslin. "A Low-Temperature Dynamic Mode Scanning Force Microscope Operating in High Magnetic Fields". In: *Review of Scientific Instruments* 70.6 (1999), pp. 2765–2768. DOI: 10.1063/1.1149842.

[97] S. Hembacher, F. J. Giessibl, and J. Mannhart. "Evaluation of a Force Sensor Based on a Quartz Tuning Fork for Operation at Low Temperatures and Ultrahigh Vacuum". In: *Applied Surface Science* 188.3-4 (2002), pp. 445–449. DOI: 10.1016/S0169-4332(01)00976-X.

[98] E. Momosaki, ed. *Proceedings of International Frequency Control Symposium*. Vol. 552–565. 552–565. IEEE, 1997. ISBN: 0-7803-3728-X.

[99] Franz J. Giessibl, Hartmut Bielefeldt, Stefan Hembacher, and Jochen Mannhart. "Calculation of the Optimal Imaging Parameters for Frequency Modulation Atomic Force Microscopy". In: *Applied Surface Science* 140.3-4 (1999), pp. 352–357. DOI: 10.1016/S0169-4332(98)00553-4.

[100] Yuanqin He. "Installation of a Low-temperature Scanning Probe Microscope and Investigations of Low-dimensional Metal-organic Networks". In: *MA Thesis* (2013).

[101] Felix Bischoff. "Scanning probe microscopy studies of surface conned molecules and (metal-organic) nanostructures: PhD Thesis". In: *Technische Universität München* (2018).

[102] Createc GmbH. *How to install the LT-STM head*. 2013.

[103] *Createc Fischer & Co. GmbH, Industriestr. 9, 74391 Erligheim, Germany.*

[104] S. H. Pan, E. W. Hudson, and J. C. Davis. "3He Refrigerator Based Very Low Temperature Scanning Tunneling Microscope". In: *Review of Scientific Instruments* 70.2 (1999), pp. 1459–1463. DOI: 10.1063/1.1149605.

[105] *SPECS Zurich GmbH, Technoparkstrasse 1, 8005 Zurich, Switzerland.*

[106] *Henkel AG & Co. KGaA Standort München*. 2018. URL: http://www.loctite.de.

[107] *Polytech GmbH Schwarzschildstraße 1, Germany*. 2018. URL: www.polytec.com.

[108] Createc GmbH. *How to Assemble a Metal Sample Holder*. 2018.

[109] Y. Yamamura and Hio Tawara. "Energy Dependence of Ion-Induced Sputtering yields from Monatomic Solids at Normal Incidence". In: *Atomic Data and Nuclear Data Tables* 62.2 (1996), pp. 149–253. DOI: 10.1006/adnd.1996.0005.

[110] SPECS GmbH. *Useful Information and Facts about the Practice of Sputtering*. 2018.

[111] Schmid M. *Simple Sputter Yield Calculator*. 2018. URL: https://www.iap.tuwien.ac.at/www/surface/sputteryield.

[112] Felix Hanke and Jonas Björk. "Structure and Local Reactivity of the Au(111) Surface Reconstruction". In: *Physical Review B* 87.23 (2013). DOI: 10.1103/PhysRevB.87.235422.

[113] Yumeng Shi, Christoph Hamsen, Xiaoting Jia, Ki Kang Kim, Alfonso Reina, Mario Hofmann, Allen Long Hsu, Kai Zhang, Henan Li, Zhen-Yu Juang, Mildred S. Dresselhaus, Lain-Jong Li, and Jing Kong. "Synthesis of Few-Layer Hexagonal Boron Nitride Thin Film by Chemical Vapor Deposition". In: *Nano letters* 10.10 (2010), pp. 4134–4139. DOI: 10.1021/nl1023707.

[114] Régis Decker, Yang Wang, Victor W. Brar, William Regan, Hsin-Zon Tsai, Qiong Wu, William Gannett, Alex Zettl, and Michael F. Crommie. "Local Electronic Properties of Graphene on a BN Substrate via Scanning Tunneling Microscopy". In: *Nano letters* 11.6 (2011), pp. 2291–2295. DOI: 10.1021/nl2005115.

[115] A. K. Geim and I. V. Grigorieva. "Van der Waals Heterostructures". In: *Nature* 499.7459 (2013), pp. 419–425. DOI: 10.1038/nature12385.

[116] Sushobhan Joshi, David Ecija, Ralph Koitz, Marcella Iannuzzi, Ari P. Seitsonen, Jürg Hutter, Hermann Sachdev, Saranyan Vijayaraghavan, Felix Bischoff, Knud Seufert, Johannes V. Barth, and Willi Auwärter. "Boron Nitride on Cu(111): An Electronically Corrugated Monolayer". In: *Nano Letters* 12.11 (2012), pp. 5821–5828. ISSN: 1530-6984. DOI: 10.1021/nl303170m.

[117] Manuela Garnica, Martin Schwarz, Jacob Ducke, Yuanqin He, Felix Bischoff, Johannes V. Barth, Willi Auwärter, and Daniele Stradi. "Comparative Study of the Interfaces of Graphene and Hexagonal Boron Nitride with Silver". In: *Physical Review B* 94.15 (2016). DOI: 10.1103/PhysRevB.94.155431.

[118] M. Corso. "Boron Nitride Nanomesh". In: *Science* 303.5655 (2004), pp. 217–220. DOI: 10.1126/science.1091979.

[119] W. Auwärter, T. J. Kreutz, T. Greber, and J. Osterwalder. "XPD and STM Investigation of Hexagonal Boron Nitride on Ni(111)". In: *Surface Science* 429.1-3 (1999), pp. 229–236. DOI: 10.1016/S0039-6028(99)00381-7.

[120] Fabian Schulz, Robert Drost, Sampsa K. Hämäläinen, Thomas Demonchaux, Ari P. Seitsonen, and Peter Liljeroth. "Epitaxial Hexagonal Boron Nitride on Ir(111): A Work Function Template". In: *Physical Review B* 89.23 (2014). DOI: 10.1103/PhysRevB.89.235429.

[121] Ferdinand H. Zum Farwick Hagen, Domenik M. Zimmermann, Caio C. Silva, Christoph Schlueter, Nicolae Atodiresei, Wouter Jolie, Antonio J. Martínez-Galera, Daniela Dombrowski, Ulrike A. Schröder, Moritz Will, Predrag Lazić, Vasile Caciuc, Stefan Blügel, Tien-Lin Lee, Thomas Michely, and Carsten Busse. "Structure and Growth of Hexagonal Boron Nitride on Ir(111)". In: *ACS Nano* 10.12 (2016), pp. 11012–11026. DOI: 10.1021/acsnano.6b05819.

[122] A. B. Preobrajenski, A. S. Vinogradov, May Ling Ng, E. Ćavar, R. Westerström, A. Mikkelsen, E. Lundgren, and N. Mårtensson. "Influence of Chemical Interaction at the Lattice-Mismatched h-BN/Rh(111) and h-BN/Pt(111) Interfaces on the Overlayer Morphology". In: *Physical Review B* 75.24 (2007), p. 146. DOI: 10.1103/PhysRevB.75.245412.

[123] Martin Schwarz, Alexander Riss, Manuela Garnica, Jacob Ducke, Peter S. Deimel, David A. Duncan, Pardeep Kumar Thakur, Tien-Lin Lee, Ari Paavo Seitsonen, Johannes V. Barth, Francesco Allegretti, and Willi Auwärter. "Corrugation in the Weakly Interacting Hexagonal-BN/Cu(111) System: Structure Determination by Combining Noncontact Atomic Force Microscopy and X-ray Standing Waves". In: *ACS Nano* 11.9 (2017), pp. 9151–9161. DOI: 10.1021/acsnano.7b04022.

[124] Farzaneh Mahvash, Etienne Paradis, Dominique Drouin, Thomas Szkopek, and Mohamed Siaj. "Space-Charge Limited Transport in Large-Area Monolayer Hexagonal Boron Nitride". In: *Nano letters* 15.4 (2015), pp. 2263–2268. DOI: 10.1021/nl504197c.

[125] Gerald Oster, Mark Wasserman, and Craig Zwerling. "Theoretical Interpretation of Moire Patterns". In: *Journal of the Optical Society of America* 54.2 (1964), p. 169. ISSN: 0030-3941. DOI: 10.1364/JOSA.54.000169.

[126] José I. Urgel, Martin Schwarz, Manuela Garnica, Daphné Stassen, Davide Bonifazi, David Ecija, Johannes V. Barth, and Willi Auwärter. "Controlling Coordination Reactions and Assembly on a Cu(111) Supported Boron Nitride Monolayer". In: *Journal of the American Chemical Society* 137.7 (2015), pp. 2420–2423. DOI: 10.1021/ja511611r.

[127] Fabian Schulz, Mari Ijäs, Robert Drost, Sampsa K. Hämäläinen, Ari Harju, Ari P. Seitsonen, and Peter Liljeroth. "Many-Body Transitions in a Single Molecule Visualized by Scanning Tunnelling Microscopy". In: *Nature Physics* 11.3 (2015), pp. 229–234. ISSN: 1745-2473. DOI: 10.1038/nphys3212.

[128] Peter Jacobson, Tobias Herden, Matthias Muenks, Gennadii Laskin, Oleg Brovko, Valeri Stepanyuk, Markus Ternes, and Klaus Kern. "Quantum Engineering of Spin and Anisotropy in Magnetic Molecular Junctions". In: *Nature communications* 6 (2015), p. 8536. DOI: 10.1038/ncomms9536.

[129] Avijit Kumar, Kaustuv Banerjee, and Peter Liljeroth. "Molecular Assembly on Two-Dimensional Materials". In: *Nanotechnology* 28.8 (2017), p. 082001. ISSN: 0957-4484. DOI: 10.1088/1361-6528/aa564f.

[130] Peter Jacobson, Matthias Muenks, Gennadii Laskin, Oleg Brovko, Valeri Stepanyuk, Markus Ternes, and Klaus Kern. "Potential Energy-Driven Spin Manipulation via a Controllable Hydrogen Ligand". In: *Science advances* 3.4 (2017), e1602060. DOI: 10.1126/sciadv.1602060.

[131] Tae Hoon Lee, Kwanpyo Kim, Gwangwoo Kim, Hyo Ju Park, Declan Scullion, Leo Shaw, Myung-Gil Kim, Xiaodan Gu, Won-Gyu Bae, Elton J. G. Santos, Zonghoon Lee, Hyeon Suk Shin, Yoshio Nishi, and Zhenan Bao. "Chemical Vapor-Deposited Hexagonal Boron Nitride as a Scalable Template for High-Performance Organic Field-Effect Transistors". In: *Chemistry of Materials* 29.5 (2017), pp. 2341–2347. ISSN: 0897-4756. DOI: 10.1021/acs.chemmater.6b05517.

[132] A. K. Geim and K. S. Novoselov. "The Rise of Graphene". In: *Nature materials* 6.3 (2007), pp. 183–191. ISSN: 1476-1122. DOI: 10.1038/nmat1849.

[133] Phillip N. First, Walt A. de Heer, Thomas Seyller, Claire Berger, Joseph A. Stroscio, and Jeong-Sun Moon. "Epitaxial Graphenes on Silicon Carbide". In: *MRS Bulletin* 35.04 (2010), pp. 296–305. ISSN: 0883-7694. DOI: 10.1557/mrs2010.552.

[134] Michael S. Fuhrer, Chun Ning Lau, and Allan H. MacDonald. "Graphene: Materially Better Carbon". In: *MRS Bulletin* 35.04 (2010), pp. 289–295. ISSN: 0883-7694. DOI: 10.1557/mrs2010.551.

[135] A. H. Castro Neto, F. Guinea, Peres, N. M. R., K. S. Novoselov, and A. K. Geim. "The Electronic Properties of Graphene". In: *Reviews of Modern Physics* 81.1 (2009), pp. 109–162. DOI: 10.1103/RevModPhys.81.109.

[136] Yanwu Zhu, Shanthi Murali, Weiwei Cai, Xuesong Li, Ji Won Suk, Jeffrey R. Potts, and Rodney S. Ruoff. "Graphene and Graphene Oxide: Synthesis, Properties, and Applications". In: *Advanced materials (Deerfield Beach, Fla.)* 22.35 (2010), pp. 3906–3924. DOI: 10.1002/adma.201001068.

[137] Alexander A. Balandin. "Thermal Properties of Graphene and Nanostructured Carbon Materials". In: *Nature Materials* 10.8 (2011), pp. 569–581. DOI: 10.1038/nmat3064.

[138] K. I. Bolotin, K. J. Sikes, Z. Jiang, M. Klima, G. Fudenberg, J. Hone, P. Kim, and H. L. Stormer. "Ultrahigh Electron Mobility in Suspended Graphene". In: *Solid State Communications* 146.9-10 (2008), pp. 351–355. ISSN: 00381098. DOI: 10.1016/j.ssc.2008.02.024.

[139] Xu Du, Ivan Skachko, Anthony Barker, and Eva Y. Andrei. "Approaching Ballistic Transport in Suspended Graphene". In: *Nature nanotechnology* 3.8 (2008), pp. 491–495. DOI: 10.1038/nnano.2008.199.

[140] I. W. Frank, D. M. Tanenbaum, A. M. van der Zande, and P. L. McEuen. "Mechanical Properties of Suspended Graphene Sheets". In: *Journal of Vacuum Science & Technology B: Microelectronics and Nanometer Structures* 25.6 (2007), p. 2558. DOI: 10.1116/1.2789446.

[141] Mohammad A. Rafiee, Javad Rafiee, Zhou Wang, Huaihe Song, Zhong-Zhen Yu, and Nikhil Koratkar. "Enhanced Mechanical Properties of Nanocomposites at Low Graphene Content". In: *ACS Nano* 3.12 (2009), pp. 3884–3890. DOI: 10.1021/nn9010472.

[142] F. Scarpa, S. Adhikari, and A. Srikantha Phani. "Effective Elastic Mechanical Properties of Single Layer Graphene Sheets". In: *Nanotechnology* 20.6 (2009), p. 065709. ISSN: 0957-4484. DOI: 10.1088/0957-4484/20/6/065709.

[143] Edward P. Randviir, Dale A.C. Brownson, and Craig E. Banks. "A Decade of Graphene Research: Production, Applications and Outlook". In: *Materials Today* 17.9 (2014), pp. 426–432. DOI: 10.1016/j.mattod.2014.06.001.

[144] Amaia Zurutuza and Claudio Marinelli. "Challenges and Opportunities in Graphene Commercialization". In: *Nature nanotechnology* 9.10 (2014), pp. 730–734. DOI: 10.1038/nnano.2014.225.

[145] Xin Ting Zheng, Arundithi Ananthanarayanan, Kathy Qian Luo, and Peng Chen. "Glowing Graphene Quantum Dots and Carbon Dots: Properties, Syntheses, and Biological Applications". In: *Small (Weinheim an der Bergstrasse, Germany)* 11.14 (2015), pp. 1620–1636. DOI: 10.1002/smll.201402648.

[146] François Perreault, Andreia Fonseca de Faria, and Menachem Elimelech. "Environmental Applications of Graphene-Based Nanomaterials". In: *Chemical Society reviews* 44.16 (2015), pp. 5861–5896. ISSN: 1460-4744. DOI: 10.1039/c5cs00021a.

[147] Prasanna Chandrasekhar. *Conducting Polymers, Fundamentals and Applications Including Carbon Nanotubes and Graphene*. Second edition. Cham: Springer, 2018. ISBN: 331969376X.

[148] Keun Soo Kim, Yue Zhao, Houk Jang, Sang Yoon Lee, Jong Min Kim, Kwang S. Kim, Jong-Hyun Ahn, Philip Kim, Jae-Young Choi, and Byung Hee Hong. "Large-Scale Pattern Growth of Graphene Films for Stretchable Transparent Electrodes". In: *Nature* 457.7230 (2009), pp. 706–710. DOI: 10.1038/nature07719.

[149] Alfonso Reina, Xiaoting Jia, John Ho, Daniel Nezich, Hyungbin Son, Vladimir Bulovic, Mildred S. Dresselhaus, and Jing Kong. "Large Area, Few-Layer Graphene Films on Arbitrary Substrates by Chemical Vapor Deposition". In: *Nano Letters* 9.1 (2009), pp. 30–35. ISSN: 1530-6984. DOI: 10.1021/nl801827v.

[150] Johann Coraux, Alpha T. N'Diaye, Carsten Busse, and Thomas Michely. "Structural Coherency of Graphene on Ir(111)". In: *Nano Letters* 8.2 (2008), pp. 565–570. ISSN: 1530-6984. DOI: 10.1021/nl0728874.

[151] Peter W. Sutter, Jan-Ingo Flege, and Eli A. Sutter. "Epitaxial Graphene on Ruthenium". In: *Nature Materials* 7.5 (2008), pp. 406–411. DOI: 10.1038/nmat2166.

[152] Soon-Yong Kwon, Cristian V. Ciobanu, Vania Petrova, Vivek B. Shenoy, Javier Bareño, Vincent Gambin, Ivan Petrov, and Suneel Kodambaka. "Growth of Semiconducting Graphene on Palladium". In: *Nano letters* 9.12 (2009), pp. 3985–3990. DOI: 10.1021/nl902140j.

[153] Cecilia Mattevi, Hokwon Kim, and Manish Chhowalla. "A Review of Chemical Vapour Deposition of Graphene on Copper". In: *Journal of Materials Chemistry* 21.10 (2011), p. 3324. ISSN: 0959-9428. DOI: 10.1039/C0JM02126A.

[154] Matthias Batzill. "The Surface Science of Graphene: Metal Interfaces, CVD Synthesis, Nanoribbons, Chemical Modifications, and Defects". In: *Surface Science Reports* 67.3-4 (2012), pp. 83–115. DOI: 10.1016/j.surfrep.2011.12.001.

[155] Zhengzong Sun, Zheng Yan, Jun Yao, Elvira Beitler, Yu Zhu, and James M. Tour. "Growth of Graphene from Solid Carbon Sources". In: *Nature* 468.7323 (2010), pp. 549–552. DOI: 10.1038/nature09579.

[156] Gedeng Ruan, Zhengzong Sun, Zhiwei Peng, and James M. Tour. "Growth of Graphene from Food, Insects, and Waste". In: *ACS Nano* 5.9 (2011), pp. 7601–7607. DOI: 10.1021/nn202625c.

[157] Rex B. McLellan. "The Solubility of Carbon in Solid Gold, Copper, and Silver". In: *Scripta Metallurgica* 3.6 (1969), pp. 389–391. ISSN: 00369748. DOI: 10.1016/0036-9748(69)90262-2.

[158] Chuhei Oshima and Ayato Nagashima. "Ultra-Thin Epitaxial Films of Graphite and Hexagonal Boron Nitride on Solid Surfaces". In: *Journal of Physics: Condensed Matter* 9.1 (1997), pp. 1–20. DOI: 10.1088/0953-8984/9/1/004.

[159] G. A. López and E. J. Mittemeijer. "The Solubility of C in Solid Cu". In: *Scripta Materialia* 51.1 (2004), pp. 1–5. ISSN: 13596462. DOI: 10.1016/j.scriptamat.2004.03.028.

[160] A. Earnshaw and Thomas John Harrington. *The Chemistry of the Transition Elements*. Vol. no. 13. Oxford chemistry series. Oxford: Clarendon Press, 1973. ISBN: 9780198554257.

[161] P. Sutter, M. S. Hybertsen, J. T. Sadowski, and E. Sutter. "Electronic Structure of Few-Layer Epitaxial Graphene on Ru(0001)". In: *Nano letters* 9.7 (2009), pp. 2654–2660. DOI: 10.1021/nl901040v.

[162] Dacheng Wei, Yunqi Liu, Yu Wang, Hongliang Zhang, Liping Huang, and Gui Yu. "Synthesis of N-Doped Graphene by Chemical Vapor Deposition and Its Electrical Properties". In: *Nano letters* 9.5 (2009), pp. 1752–1758. DOI: 10.1021/nl803279t.

[163] Li Gao, Jeffrey R. Guest, and Nathan P. Guisinger. "Epitaxial Graphene on Cu(111)". In: *Nano Letters* 10.9 (2010), pp. 3512–3516. ISSN: 1530-6984. DOI: 10.1021/nl1016706.

[164] Yun-Hi Lee, and Jong-Hee Lee. "Scalable Growth of Free-Standing Graphene Wafers with Copper(Cu) Catalyst on SiO2/Si Substrate: Thermal Conductivity of the Wafers". In: *Applied Physics Letters* 96.8 (2010), p. 083101. DOI: 10.1063/1.3324698.

[165] Ved Prakash Verma, Santanu Das, Indranil Lahiri, and Wonbong Choi. "Large-Area Graphene on Polymer Film for Flexible and Transparent Anode in Field Emission Device". In: *Applied Physics Letters* 96.20 (2010), p. 203108. DOI: 10.1063/1.3431630.

[166] Anchal Srivastava, Charudatta Galande, Lijie Ci, Li Song, Chaitra Rai, Deep Jariwala, Kevin F. Kelly, and Pulickel M. Ajayan. "Novel Liquid Precursor-Based Facile Synthesis of Large-Area Continuous, Single, and Few-Layer Graphene Films". In: *Chemistry of Materials* 22.11 (2010), pp. 3457–3461. ISSN: 0897-4756. DOI: 10.1021/cm101027c.

[167] Youngbin Lee, Sukang Bae, Houk Jang, Sukjae Jang, Shou-En Zhu, Sung Hyun Sim, Young Il Song, Byung Hee Hong, and Jong-Hyun Ahn. "Wafer-Scale Synthesis and Transfer of Graphene Films". In: *Nano letters* 10.2 (2010), pp. 490–493. DOI: 10.1021/nl903272n.

[168] Sukang Bae, Hyeongkeun Kim, Youngbin Lee, Xiangfan Xu, Jae-Sung Park, Yi Zheng, Jayakumar Balakrishnan, Tian Lei, Hye Ri Kim, Young Il Song, Young-Jin Kim, Kwang S. Kim, Barbaros Ozyilmaz, Jong-Hyun Ahn, Byung Hee Hong, and Sumio Iijima. "Roll-to-Roll Production of 30-Inch Graphene Films for Transparent Electrodes". In: *Nature nanotechnology* 5.8 (2010), pp. 574–578. DOI: 10.1038/nnano.2010.132.

[169] Helin Cao, Qingkai Yu, L. A. Jauregui, J. Tian, W. Wu, Z. Liu, R. Jalilian, D. K. Benjamin, Z. Jiang, J. Bao, S. S. Pei, and Yong P. Chen. "Electronic Transport in Chemical Vapor Deposited Graphene Synthesized on Cu: Quantum Hall Effect and Weak Localization". In: *Applied Physics Letters* 96.12 (2010), p. 122106. DOI: 10.1063/1.3371684.

[170] Ariel Ismach, Clara Druzgalski, Samuel Penwell, Adam Schwartzberg, Maxwell Zheng, Ali Javey, Jeffrey Bokor, and Yuegang Zhang. "Direct Chemical Vapor Deposition of Graphene on Dielectric Surfaces". In: *Nano letters* 10.5 (2010), pp. 1542–1548. DOI: 10.1021/nl9037714.

[171] Antonio J. Martínez-Galera, Iván Brihuega, and José M. Gómez-Rodríguez. "Ethylene Irradiation: A New Route to Grow Graphene on Low Reactivity Metals". In: *Nano Letters* 11.9 (2011), pp. 3576–3580. ISSN: 1530-6984. DOI: 10.1021/nl201281m.

[172] Andrew L. Walter, Shu Nie, Aaron Bostwick, Keun Su Kim, Luca Moreschini, Young Jun Chang, Davide Innocenti, Karsten Horn, Kevin F. McCarty, and Eli Rotenberg. "Electronic Structure of Graphene on Single-Crystal Copper Substrates". In: *Physical Review B* 84.19 (2011). DOI: 10.1103/PhysRevB.84.195443.

[173] Shu Nie, Norman C. Bartelt, Joseph M. Wofford, Oscar D. Dubon, Kevin F. McCarty, and Konrad Thürmer. "Scanning Tunneling Microscopy Study of Graphene on Au(111): Growth Mechanisms and Substrate Interactions". In: *Physical Review B* 85.20 (2012). DOI: 10.1103/PhysRevB.85.205406.

[174] Brian Kiraly, Erin V. Iski, Andrew J. Mannix, Brandon L. Fisher, Mark C. Hersam, and Nathan P. Guisinger. "Solid-Source Growth and Atomic-Scale Characterization of Graphene on Ag(111)". In: *Nature Communications* 4 (2013). ISSN: 2041-1723. DOI: 10.1038/ncomms3804.

[175] Irene Hernández-Rodríguez, Jorge M. García, José A. Martín-Gago, de Andrés, Pedro L., and Javier Méndez. "Graphene Growth on Pt(111) and Au(111) Using a MBE Carbon Solid-Source". In: *Diamond and Related Materials* 57 (2015), pp. 58–62. DOI: 10.1016/j.diamond.2015.03.004.

[176] Zachary R. Robinson, Parul Tyagi, Tyler R. Mowll, Carl A. Ventrice, and James B. Hannon. "Argon-Assisted Growth of Epitaxial Graphene on Cu(111)". In: *Physical Review B* 86.23 (2012). DOI: 10.1103/PhysRevB.86.235413.

[177] MaTeck GmbH. *Im Langenbroich 20, 52428 Juelich, Germany.* 2018. URL: www.mateck.com.

[178] D. Reuter, A. D. Wieck, and A. Fischer. "A Compact Electron Beam Evaporator for Carbon Doping in Solid Source Molecular Beam Epitaxy". In: *Review of Scientific Instruments* 70.8 (1999), p. 3435. DOI: 10.1063/1.1149933.

[179] Matsusada. *745 Aojicho Kusatsu-shi, Shiga-ken, 525-0041, Japan.* 2018. URL: http://www.matsusada.com/.

[180] Ivan Vlassiouk, Sergei Smirnov, Murari Regmi, Sumedh P. Surwade, Nishtha Srivastava, Randall Feenstra, Gyula Eres, Chad Parish, Nick Lavrik, Panos Datskos, Sheng Dai, and Pasquale Fulvio. "Graphene Nucleation Density on Copper: Fundamental Role of Background Pressure". In: *The Journal of Physical Chemistry C* 117.37 (2013), pp. 18919–18926. DOI: 10.1021/jp4047648.

[181] P. Süle, M. Szendro, C. Hwang, and L. Tapasztó. "Rotation Misorientated Graphene Moiré Superlattices on Cu (111): Classical Molecular Dynamics Simulations and Scanning Tunneling Microscopy studies". In: *Carbon* 77 (2014), pp. 1082–1089. DOI: 10.1016/j.carbon.2014.06.024.

[182] L. Zhao, K. T. Rim, H. Zhou, R. He, T. F. Heinz, A. Pinczuk, G. W. Flynn, and A. N. Pasupathy. "Influence of Copper Crystal Surface on the CVD Growth of Large Area Monolayer Graphene". In: *Solid State Communications* 151.7 (2011), pp. 509–513. ISSN: 00381098. DOI: 10.1016/j.ssc.2011.01.014.

[183] S. M. Hollen, G. A. Gambrel, S. J. Tjung, N. M. Santagata, E. Johnston-Halperin, and J. A. Gupta. "Modification of Electronic Surface States by Graphene Islands on Cu(111)". In: *Physical Review B* 91.19 (2015). DOI: 10.1103/PhysRevB.91.195425.

[184] D. Stull , G. Sinke. *Thermodynamic Properties of the Elements*. 2012. ISBN: 125838194X.

[185] Yuan Liu, Nathan O. Weiss, Xidong Duan, Hung-Chieh Cheng, Yu Huang, and Xiangfeng Duan. "Van der Waals Heterostructures and Devices". In: *Nature Reviews Materials* 1.9 (2016), p. 16042. DOI: 10.1038/natrevmats.2016.42.

[186] Roland Widmer, Simon Berner, Oliver Gröning, Thomas Brugger, Jürg Osterwalder, and Thomas Greber. "Electrolytic in Situ STM Investigation of h-BN-Nanomesh". In: *Electrochem. Commun.* 9.10 (2007), pp. 2484–2488. DOI: 10.1016/j.elecom.2007.07.019.

[187] S. J. Haigh, A. Gholinia, R. Jalil, S. Romani, L. Britnell, D. C. Elias, K. S. Novoselov, L. A. Ponomarenko, A. K. Geim, and R. Gorbachev. "Cross-Sectional Imaging of Individual Layers and Buried Interfaces of Graphene-Based Heterostructures and superlattices". In: *Nat. Mater.* 11.9 (2012), pp. 764–767. DOI: 10.1038/nmat3386.

[188] Amir Pakdel, Yoshio Bando, and Dmitri Golberg. "Nano Boron Nitride Flatland". In: *Chem. Soc. Rev.* 43.3 (2014), pp. 934–959. DOI: 10.1039/C3CS60260E.

[189] A. Fedorov, C. S. Praveen, N. I. Verbitskiy, D. Haberer, D. Usachov, D. V. Vyalikh, A. Nefedov, C. Wöll, L. Petaccia, S. Piccinin, H. Sachdev, M. Knupfer, B. Büchner, S. Fabris, and A. Grüneis. "Efficient Gating of Epitaxial Boron Nitride Monolayers by Substrate Functionalization". In: *Physical Review B* 92.12 (2015), p. 125440. DOI: 10.1103/PhysRevB.92.125440.

[190] Stijn F. L. Mertens, Adrian Hemmi, Stefan Muff, Oliver Groning, Steven de Feyter, Jurg Osterwalder, and Thomas Greber. "Switching Stiction and Adhesion of a Liquid on a Solid". In: *Nature* 534.7609 (2016), pp. 676–679. DOI: 10.1038/nature18275.

[191] Elin Grånäs, Jan Knudsen, Ulrike A. Schröder, Timm Gerber, Carsten Busse, Mohammad A. Arman, Karina Schulte, Jesper N. Andersen, and Thomas Michely. "Oxygen Intercalation under Graphene on Ir(111): Energetics, Kinetics, and the Role of Graphene Edges". In: *ACS Nano* 6.11 (2012), pp. 9951–9963. DOI: 10.1021/nn303548z.

[192] Al Balushi, Zakaria Y., Ke Wang, Ram Krishna Ghosh, Rafael A. Vilá, Sarah M. Eichfeld, Joshua D. Caldwell, Xiaoye Qin, Yu-Chuan Lin, Paul A. DeSario, Greg Stone, Shruti Subramanian, Dennis F. Paul, Robert M. Wallace, Suman Datta, Joan M. Redwing, and Joshua A. Robinson. "Two-Dimensional Gallium Nitride Realized via Graphene Encapsulation". In: *Nat. Mater.* 15.11 (2016), pp. 1166–1171. DOI: 10.1038/nmat4742.

[193] Nina I. Kovtyukhova, Yuanxi Wang, Ruitao Lv, Mauricio Terrones, Vincent H. Crespi, and Thomas E. Mallouk. "Reversible Intercalation of Hexagonal Boron Nitride with Brønsted Acids". In: *Journal of the American Chemical Society* 135.22 (2013), pp. 8372–8381. DOI: 10.1021/ja403197h.

[194] Robert P. Smith, Thomas E. Weller, Christopher A. Howard, Mark P.M. Dean, Kaveh C. Rahnejat, Siddharth S. Saxena, and Mark Ellerby. "Superconductivity in Graphite Intercalation Compounds". In: *Physica C: Superconductivity and its Applications* 514 (2015), pp. 50–58. DOI: 10.1016/j.physc.2015.02.029.

[195] Subrahmanyam Goriparti, Ermanno Miele, Francesco de Angelis, Enzo Di Fabrizio, Remo Proietti Zaccaria, and Claudio Capiglia. "Review on Recent Progress of Nanostructured Anode Materials for Li-Ion Batteries". In: *J. Power Sources* 257 (2014), pp. 421–443. DOI: 10.1016/j.jpowsour.2013.11.103.

[196] D. Usachov, V. K. Adamchuk, D. Haberer, A. Grüneis, H. Sachdev, A. B. Preobrajenski, C. Laubschat, and D. V. Vyalikh. "Quasifreestanding Single-Layer Hexagonal Boron Nitride as a Substrate for Graphene Synthesis". In: *Physical Review B* 82.7 (2010), p. 075415. DOI: 10.1103/PhysRevB.82.075415.

[197] Andrei Varykhalov, Wolfgang Gudat, and Oliver Rader. "Imaging Buried Molecules: Fullerenes under Graphene". In: *Advanced Materials* 22.30 (2010), pp. 3307–3310. DOI: 10.1002/adma.201000695.

[198] Jiong Lu, Yi Zheng, Anastassia Sorkin, and Kian Ping Loh. "Growing Suspended Graphene on C60 Molecules". In: *Small* 8.24 (2012), pp. 3728–3732. DOI: 10.1002/smll.201201113.

[199] M. Petrović, I. Šrut Rakić, S. Runte, C. Busse, J. T. Sadowski, P. Lazić, I. Pletikosić, Z.-H. Pan, M. Milun, P. Pervan, N. Atodiresei, R. Brako, D. Šokčević, T. Valla, T. Michely, and M. Kralj. "The Mechanism of Caesium Intercalation of Graphene". In: *Nat. Commun.* 4 (2013), p. 2772. DOI: 10.1038/ncomms3772.

[200] E. Monazami, L. Bignardi, P. Rudolf, and P. Reinke. "Strain Lattice Imprinting in Graphene by C60 Intercalation at the Graphene/Cu Interface". In: *Nano Letters* 15.11 (2015), pp. 7421–7430. ISSN: 1530-6984. DOI: 10.1021/acs.nanolett.5b02851.

[201] Manabu Ohtomo, Yoshiaki Sekine, Shengnan Wang, Hiroki Hibino, and Hideki Yamamoto. "Etchant-Free Graphene Transfer Using Facile Intercalation of Alkanethiol Self-Assembled Molecules at graphene/metal interfaces". In: *Nanoscale* 8.22 (2016), pp. 11503–11510. DOI: 10.1039/C6NR01366J.

[202] Chuanxu Ma, Jewook Park, Lei Liu, Yong-Sung Kim, Mina Yoon, Arthur P. Baddorf, Gong Gu, and An-Ping Li. "Interplay Between Intercalated Oxygen Superstructures and Monolayer h -BN on Cu(100)". In: *Physical Review B* 94.6 (2016), p. 064106. DOI: 10.1103/PhysRevB.94.064106.

[203] A. J. Martínez-Galera, U. A. Schröder, F. Huttmann, W. Jolie, F. Craes, C. Busse, V. Caciuc, N. Atodiresei, S. Blügel, and T. Michely. "Oxygen Orders Differently under Graphene: New Superstructures on Ir(111)". In: *Nanoscale* 8.4 (2016), pp. 1932–1943. DOI: 10.1039/C5NR04976H.

[204] Yanhong Zhang, Xuefei Weng, Huan Li, Haobo Li, Mingming Wei, Jianping Xiao, Zhi Liu, Mingshu Chen, Qiang Fu, and Xinhe Bao. "Hexagonal Boron Nitride Cover on Pt(111): A New Route to Tune Molecule–Metal Interaction and Metal-Catalyzed Reactions". In: *Nano Letters* 15.5 (2015), pp. 3616–3623. ISSN: 1530-6984. DOI: 10.1021/acs.nanolett.5b01205.

[205] Yang Yang, Qiang Fu, Haobo Li, Mingming Wei, Jianping Xiao, Wei Wei, and Xinhe Bao. "Creating a Nanospace under an h-BN Cover for Adlayer Growth on Nickel(111)". In: *ACS Nano* 9.12 (2015), pp. 11589–11598. DOI: 10.1021/acsnano.5b05509.

[206] Qiang Fu and Xinhe Bao. "Surface Chemistry and Catalysis Confined under Two-Dimensional Materials". In: *Chem. Soc. Rev.* 46 (2017), pp. 1842–1874. DOI: 10.1039/C6CS00424E.

[207] David Dolphin. *The Porphyrins V7: Biochemistry, Part B*. Burlington: Elsevier Science, 2012. ISBN: 9780323145619.

[208] A. Yella, H.-W. Lee, H. N. Tsao, C. Yi, A. K. Chandiran, M. K. Nazeeruddin, E. W.-G. Diau, C.-Y. Yeh, S. M. Zakeeruddin, and M. Gratzel. "Porphyrin-Sensitized Solar Cells with Cobalt(II/III)-Based Redox Electrolyte Exceed 12 Percent Efficiency". In: *Science* 334.6056 (2011), pp. 629–634. DOI: 10.1126/science.1209688.

[209] Jonathan S. Lindsey and David F. Bocian. "Molecules for Charge-Based Information Storage". In: *Accounts of Chemical Research* 44.8 (2011), pp. 638–650. DOI: 10.1021/ar200107x.

[210] Jacob Ducke, Alexander Riss, Alejandro Pérez Paz, Knud Seufert, Martin Schwarz, Manuela Garnica, Angel Rubio, and Willi Auwärter. "Layered Insulator/Molecule/Metal Heterostructures with Molecular Functionality through Porphyrin Intercalation". In: *ACS Nano* (2018). DOI: 10.1021/acsnano.7b08887..

[211] Felix Bischoff, Knud Seufert, Willi Auwärter, Sushobhan Joshi, Saranyan Vijayaraghavan, David Écija, Katharina Diller, Anthoula C. Papageorgiou, Sybille Fischer, Francesco Allegretti, David A. Duncan, Florian Klappenberger, Florian Blobner, Runyuan Han, and Johannes V. Barth. "How Surface Bonding and Repulsive Interactions Cause Phase Transformations: Ordering of a Prototype Macrocyclic Compound on Ag(111)". In: *ACS Nano* 7.4 (2013), pp. 3139–3149. DOI: 10.1021/nn305487c.

[212] K. Diller, F. Klappenberger, M. Marschall, K. Hermann, A. Nefedov, Ch. Wöll, and J. V. Barth. "Self-Metalation of 2H-Tetraphenylporphyrin on Cu(111): An X-ray Spectroscopy Study". In: *The Journal of Chemical Physics* 136.1 (2012), p. 014705. DOI: 10.1063/1.3674165.

[213] Hubertus Marbach. "Surface-Mediated in Situ Metalation of Porphyrins at the Solid–Vacuum Interface". In: *Accounts of Chemical Research* 48.9 (2015), pp. 2649–2658. DOI: 10.1021/acs.accounts.5b00243.

[214] Katharina Diller, Anthoula C. Papageorgiou, Florian Klappenberger, Francesco Allegretti, Johannes V. Barth, and Willi Auwärter. "In Vacuo Interfacial Tetrapyrrole Metallation". In: *Chem. Soc. Rev.* 45.6 (2016), pp. 1629–1656. DOI: 10.1039/C5CS00207A.

[215] W. Paszkowicz, J. B. Pelka, M. Knapp, T. Szyszko, and S. Podsiadlo. "Lattice Parameters and Anisotropic Thermal Expansion of Hexagonal Boron Nitride in the 10-297.5 K Temperature Range". In: *Appl. Phys. A-Mater.* 75.3 (2002), pp. 431–435. DOI: 10.1007/s003390100999.

[216] M. Nonnenmacher, M. P. O'Boyle, and H. K. Wickramasinghe. "Kelvin Probe Force Microscopy". In: *Applied Physics Letters* 58.25 (1991), pp. 2921–2923. DOI: 10.1063/1.105227.

[217] H. O. Jacobs, H. F. Knapp, and A. Stemmer. "Practical Aspects of Kelvin Probe Force Microscopy". In: *Review of Scientific Instruments* 70.3 (1999), pp. 1756–1760. DOI: 10.1063/1.1149664.

[218] Wilhelm Melitz, Jian Shen, Andrew C. Kummel, and Sangyeob Lee. "Kelvin Probe Force Microscopy and Its Application". In: *Surface Science Reports* 66.1 (2011), pp. 1–27. DOI: 10.1016/j.surfrep.2010.10.001.

[219] X. W. Tu, G. Mikaelian, and W. Ho. "Controlling Single-Molecule Negative Differential Resistance in a Double-Barrier Tunnel Junction". In: *Physical Review Letters* 100.12 (2008). DOI: 10.1103/PhysRevLett.100.126807.

[220] Martin Schwarz, Manuela Garnica, David A. Duncan, Alejandro Pérez Paz, Jacob Ducke, Peter S. Deimel, Pardeep K. Thakur, Tien-Lin Lee, Angel Rubio, Johannes V. Barth, Francesco Allegretti, and Willi Auwärter. "Adsorption Conformation and Lateral Registry of Cobalt Porphine on Cu(111)". In: *The Journal of Physical Chemistry C* (2018). DOI: 10.1021/acs.jpcc.7b11705.

[221] Jascha Repp, Gerhard Meyer, Sladjana M. Stojković, André Gourdon, and Christian Joachim. "Molecules on Insulating Films: Scanning-Tunneling Microscopy Imaging of Individual Molecular Orbitals". In: *Physical Review Letters* 94.2 (2005). DOI: 10.1103/PhysRevLett.94.026803.

[222] P. Liljeroth, J. Repp, and G. Meyer. "Current-Induced Hydrogen Tautomerization and Conductance Switching of Naphthalocyanine Molecules". In: *Science* 317.5842 (2007), pp. 1203–1206. DOI: 10.1126/science.1144366.

[223] Takashi Kumagai, Felix Hanke, Sylwester Gawinkowski, John Sharp, Konstantinos Kotsis, Jacek Waluk, Mats Persson, and Leonhard Grill. "Controlling intramolecular hydrogen transfer in a porphycene molecule with single atoms or molecules located nearby". In: *Nature Chemistry* 6.1 (2013), pp. 41–46. ISSN: 1755-4330. DOI: 10.1038/nchem.1804.

[224] Moritz Müller, Katharina Diller, Reinhard J. Maurer, and Karsten Reuter. "Interfacial Charge Rearrangement and Intermolecular Interactions: Density-Functional Theory Study of Free-Base Porphine Adsorbed on Ag(111) and Cu(111)". In: *The Journal of Chemical Physics* 144.2 (2016), p. 024701. DOI: 10.1063/1.4938259.

[225] Matthias Koch, Mark Pagan, Mats Persson, Sylwester Gawinkowski, Jacek Waluk, and Takashi Kumagai. "Direct Observation of Double Hydrogen Transfer via Quantum Tunneling in a Single Porphycene Molecule on a Ag(110) Surface". In: *Journal of the American Chemical Society* 139.36 (2017), pp. 12681–12687. DOI: 10.1021/jacs.7b06905.

[226] Dino Novko, María Blanco-Rey, and Jean Christophe Tremblay. "Intermode Coupling Drives the Irreversible Tautomerization in Porphycene on Copper(111) Induced by Scanning Tunnelling Microscopy". In: *The Journal of Physical Chemistry Letters* 8.5 (2017), pp. 1053–1059. DOI: 10.1021/acs.jpclett.7b00141.

[227] Alissa Wiengarten, Knud Seufert, Willi Auwärter, David Ecija, Katharina Diller, Francesco Allegretti, Felix Bischoff, Sybille Fischer, David A. Duncan, Anthoula C. Papageorgiou, Florian Klappenberger, Robert G. Acres, Thien H. Ngo, and Johannes V. Barth. "Surface-assisted Dehydrogenative Homocoupling of Porphine Molecules". In: *Journal of the American Chemical Society* 136.26 (2014), pp. 9346–9354. DOI: 10.1021/ja501680n.

[228] L. S. Panchakarla, K. S. Subrahmanyam, S. K. Saha, Achutharao Govindaraj, H. R. Krishnamurthy, U. V. Waghmare, and C. N. R. Rao. "Synthesis, Structure, and Properties of Boron- and Nitrogen-Doped Graphene". In: *Advanced Materials* 6 (2009), NA–NA. DOI: 10.1002/adma.200901285.

[229] Liangti Qu, Yong Liu, Jong-Beom Baek, and Liming Dai. "Nitrogen-Doped Graphene as Efficient Metal-Free Electrocatalyst for Oxygen Reduction in Fuel Cells". In: *ACS Nano* 4.3 (2010), pp. 1321–1326. DOI: 10.1021/nn901850u.

[230] Dehui Deng, Xiulian Pan, Liang Yu, Yi Cui, Yeping Jiang, Jing Qi, Wei-Xue Li, Qiang Fu, Xucun Ma, Qikun Xue, Gongquan Sun, and Xinhe Bao. "Toward N-Doped Graphene via Solvothermal Synthesis". In: *Chemistry of Materials* 23.5 (2011), pp. 1188–1193. ISSN: 0897-4756. DOI: 10.1021/cm102666r.

[231] Zhiqiang Luo, Sanhua Lim, Zhiqun Tian, Jingzhi Shang, Linfei Lai, Brian MacDonald, Chao Fu, Zexiang Shen, Ting Yu, and Jianyi Lin. "Pyridinic N Doped Graphene: Synthesis, Electronic Structure, and Electrocatalytic Property". In: *Journal of Materials Chemistry* 21.22 (2011), p. 8038. ISSN: 0959-9428. DOI: 10.1039/c1jm10845j.

[232] Jiong Lu, Pei Shan Emmeline Yeo, Yi Zheng, Hai Xu, Chee Kwan Gan, Michael B. Sullivan, A. H. Castro Neto, and Kian Ping Loh. "Step Flow versus Mosaic Film Growth in Hexagonal Boron Nitride". In: *Journal of the American Chemical Society* 135.6 (2013), pp. 2368–2373. DOI: 10.1021/ja3117735.

[233] Alexandre Tkatchenko and Matthias Scheffler. "Accurate Molecular van der Waals Interactions from Ground-State Electron Density and Free-Atom Reference Data". In: *Physical Review Letters* 102.7 (2009), p. 073005. DOI: 10.1103/PhysRevLett.102.073005.

[234] Jaime Gómez Díaz, Yun Ding, Ralph Koitz, Ari P. Seitsonen, Marcella Iannuzzi, and Jürg Hutter. "Hexagonal Boron Nitride on Transition Metal Surfaces". In: *Theor. Chem. Acc.* 132.4 (2013), p. 1350. DOI: 10.1007/s00214-013-1350-z.

[235] Ralph Koitz, Ari P. Seitsonen, Marcella Iannuzzi, and Jürg Hutter. "Structural and Electronic Properties of a Large-Scale Moiré Pattern of Hexagonal Boron Nitride on Cu(111) studied with density functional theory". In: *Nanoscale* 5.12 (2013), p. 5589. DOI: 10.1039/C3NR00709J.

[236] Frank Jensen. "The Basis Set Convergence of Spin−Spin Coupling Constants Calculated by Density Functional Methods". In: *Journal of Chemical Theory and Computation* 2.5 (2006), pp. 1360–1369. ISSN: 1549-9618. DOI: 10.1021/ct600166u.

[237] Jascha Repp, Gerhard Meyer, Karl-Heinz Rieder, and Per Hyldgaard. "Site Determination and Thermally Assisted Tunneling in Homogenous Nucleation". In: *Physical Review Letters* 91.20 (2003), p. 206102. DOI: 10.1103/PhysRevLett.91.206102.

[238] Sarah Hurst Petrosko, Robert Johnson, Henry White, and Chad A. Mirkin. "Nanoreactors: Small Spaces, Big Implications in Chemistry". In: *Journal of the American Chemical Society* 138.24 (2016), pp. 7443–7445. DOI: 10.1021/jacs.6b05393.

[239] P. E. Blöchl. "Projector Augmented-Wave Method". In: *Physical Review B* 50.24 (1994), pp. 17953–17979. DOI: 10.1103/PhysRevB.50.17953.

[240] G. Kresse and J. Hafner. "Ab Initio Molecular Dynamics for Liquid Metals". In: *Physical Review B* 47.1 (1993), pp. 558–561. DOI: 10.1103/PhysRevB.47.558.

[241] G. Kresse and J. Hafner. "Norm-Conserving and Ultrasoft Pseudopotentials for First-Row and Transition Elements". In: *Journal of Physics: Condensed Matter* 6.40 (1994), pp. 8245–8257. DOI: 10.1088/0953-8984/6/40/015.

[242] G. Kresse and J. Furthmüller. "Efficient Iterative Schemes for ab Initio Total-Energy Calculations Using a Plane-Wave Basis Set". In: *Physical Review B* 54.16 (1996), pp. 11169–11186. DOI: 10.1103/PhysRevB.54.11169.

[243] G. Kresse and D. Joubert. "From Ultrasoft Pseudopotentials to the Projector Augmented-Wave Method". In: *Physical Review B* 59.3 (1999), pp. 1758–1775. DOI: 10.1103/PhysRevB.59.1758.

[244] John P. Perdew, Kieron Burke, and Matthias Ernzerhof. "Generalized Gradient Approximation Made Simple". In: *Physical Review Letters* 77.18 (1996), pp. 3865–3868. DOI: 10.1103/PhysRevLett.77.3865.

[245] Angshuman Nag, Kalyan Raidongia, Kailash P. S. S. Hembram, Ranjan Datta, Umesh V. Waghmare, and C. N. R. Rao. "Graphene Analogues of BN: Novel synthesis and properties". In: *ACS Nano* 4.3 (2010), pp. 1539–1544. DOI: 10.1021/nn9018762.

[246] W. Tang, E. Sanville, and G. Henkelman. "A Grid-Based Bader Analysis Algorithm Without Lattice Bias". In: *Journal of Physics: Condensed Matter* 21.8 (2009), p. 084204. DOI: 10.1088/0953-8984/21/8/084204.

[247] Zheng Liu, Lulu Ma, Gang Shi, Wu Zhou, Yongji Gong, Sidong Lei, Xuebei Yang, Jiangnan Zhang, Jingjiang Yu, Ken P. Hackenberg, Aydin Babakhani, Juan-Carlos Idrobo, Robert Vajtai, Jun Lou, and Pulickel M. Ajayan. "In-Plane Heterostructures of Graphene and Hexagonal Boron Nitride with Controlled Domain Sizes". In: *Nature Nanotechnology* 8.2 (2013), pp. 119–124. ISSN: 1748-3387. DOI: 10.1038/nnano.2012.256.

[248] Zheng Liu, Yongji Gong, Wu Zhou, Lulu Ma, Jingjiang Yu, Juan Carlos Idrobo, Jeil Jung, Allan H. MacDonald, Robert Vajtai, Jun Lou, and Pulickel M. Ajayan. "Ultrathin high-temperature oxidation-resistant coatings of hexagonal boron nitride". In: *Nature Communications* 4 (2013), p. 2541. ISSN: 2041-1723. DOI: 10.1038/ncomms3541.

[249] Xuemei Li, Jun Yin, Jianxin Zhou, and Wanlin Guo. "Large Area Hexagonal Boron Nitride Monolayer as Efficient Atomically Thick Insulating Coating Against Friction and Oxidation". In: *Nanotechnology* 25.10 (2014), p. 105701. ISSN: 0957-4484. DOI: 10.1088/0957-4484/25/10/105701.

[250] F.H.P.M. Habraken, E.Ph. Kieffer, and G. A. Bootsma. "A Study of the Kinetics of the Interactions of O2 and N2O with a Cu(111) Surface and of the Reaction of CO with Adsorbed Oxygen Using AES, LEED and Ellipsometry". In: *Surface Science* 83.1 (1979), pp. 45–59. DOI: 10.1016/0039-6028(79)90479-5.

[251] L. H. Dubois. "Oxygen Chemisorption and Cuprous Oxide Formation on Cu(111): A High Resolution EELS Study". In: *Surface Science* 119.2-3 (1982), pp. 399–410. DOI: 10.1016/0039-6028(82)90306-5.

[252] H. Niehus. "Surface Reconstruction of Cu (111) upon Oxygen Adsorption". In: *Surface Science* 130.1 (1983), pp. 41–49. DOI: 10.1016/0039-6028(83)90258-3.

[253] R. W. Judd, P. Hollins, and J. Pritchard. "The Interaction of Oxygen with Cu(111): Adsorption, Incorporation and Reconstruction". In: *Surface Science* 171.3 (1986), pp. 643–653. DOI: 10.1016/0039-6028(86)91065-4.

[254] J. Haase and H.-J. Kuhr. "Reconstruction and Relaxation of the Oxygen-Covered Cu(111) Surface: A SEXAFS Study". In: *Surface Science* 203.3 (1988), pp. L695–L699. DOI: 10.1016/0039-6028(88)90084-2.

[255] S. M. Thurgate and P. J. Jennings. "Effects of Oxygen Adsorption on the LEED Fine Structure Features of Cu(001), Cu(110), Cu(111) and Ni(001)". In: *Surface Science* 131.2-3 (1983), pp. 309–320. DOI: 10.1016/0039-6028(83)90280-7.

[256] F. Jensen, F. Besenbacher, E. Lægsgaard, and I. Stensgaard. "Oxidation of Cu(111): Two New Oxygen Induced Reconstructions". In: *Surface Science* 259.3 (1991), pp. L774–L780. DOI: 10.1016/0039-6028(91)90550-C.

[257] Aloysius Soon, Mira Todorova, Bernard Delley, and Catherine Stampfl. "Surface Oxides of the Oxygen–Copper System: Precursors to the Bulk Oxide Phase?" In: *Surface Science* 601.24 (2007), pp. 5809–5813. DOI: 10.1016/j.susc.2007.06.062.

[258] F. Jensen, F. Besenbacher, and I. Stensgaard. "Two New Oxygen Induced Reconstructions on Cu(111)". In: *Surface Science* 269-270 (1992), pp. 400–404. DOI: 10.1016/0039-6028(92)91282-G.

[259] T. Matsumoto, R. A. Bennett, P. Stone, T. Yamada, K. Domen, and M. Bowker. "Scanning Tunneling Microscopy Studies of Oxygen Adsorption on Cu(111)". In: *Surface Science* 471.1-3 (2001), pp. 225–245. DOI: 10.1016/S0039-6028(00)00918-3.

[260] Aloysius Soon, Mira Todorova, Bernard Delley, and Catherine Stampfl. "Oxygen Adsorption and Stability of Surface Oxides on Cu(111): A First-Principles Investigation". In: *Physical Review B* 73.16 (2006). DOI: 10.1103/PhysRevB.73.165424.

[261] F. Wiame, V. Maurice, and P. Marcus. "Initial Stages of Oxidation of Cu(111)". In: *Surface Science* 601.5 (2007), pp. 1193–1204. DOI: 10.1016/j.susc.2006.12.028.

[262] Anneli Önsten, Mats Göthelid, and Ulf O. Karlsson. "Atomic Structure of Cu2O(111)". In: *Surface Science* 603.2 (2009), pp. 257–264. DOI: 10.1016/j.susc.2008.10.048.

[263] Stefano Gottardi, Kathrin Müller, Luca Bignardi, Juan Carlos Moreno-López, Tuan Anh Pham, Oleksii Ivashenko, Mikhail Yablonskikh, Alexei Barinov, Jonas Björk, Petra Rudolf, and Meike Stöhr. "Comparing Graphene Growth on Cu(111) versus Oxidized Cu(111)". In: *Nano Letters* 15.2 (2015), pp. 917–922. ISSN: 1530-6984. DOI: 10.1021/nl5036463.

[264] Fan Yang, YongMan Choi, Ping Liu, Jan Hrbek, and José A. Rodriguez. "Autocatalytic Reduction of a Cu 2 O/Cu(111) Surface by CO: STM, XPS, and DFT Studies †". In: *The Journal of Physical Chemistry C* 114.40 (2010), pp. 17042–17050. DOI: 10.1021/jp1029079.

[265] Piran R. Kidambi, Raoul Blume, Jens Kling, Jakob B. Wagner, Carsten Baehtz, Robert S. Weatherup, Robert Schloegl, Bernhard C. Bayer, and Stephan Hofmann. "In Situ Observations during Chemical Vapor Deposition of Hexagonal Boron Nitride on Polycrystalline Copper". In: *Chemistry of Materials* 26.22 (2014), pp. 6380–6392. ISSN: 0897-4756. DOI: 10.1021/cm502603n.

[266] André Gourdon. "On-Surface Covalent Coupling in Ultrahigh Vacuum". In: *Angewandte Chemie International Edition* 47.37 (2008), pp. 6950–6953. DOI: 10.1002/anie.200802229.

[267] Grégory Franc and André Gourdon. "Covalent Networks Through On-Surface Chemistry in Ultra-High Vacuum: State-of-the-Art and Recent Developments". In: *Physical chemistry chemical physics : PCCP* 13.32 (2011), pp. 14283–14292. DOI: 10.1039/c1cp20700h.

[268] Carlos-Andres Palma and Paolo Samorì. "Blueprinting Macromolecular Electronics". In: *Nature chemistry* 3.6 (2011), pp. 431–436. ISSN: 1755-4349. DOI: 10.1038/nchem.1043.

[269] Jonas Björk and Felix Hanke. "Towards Design Rules for Covalent Nanostructures on Metal Surfaces". In: *Chemistry (Weinheim an der Bergstrasse, Germany)* 20.4 (2014), pp. 928–934. DOI: 10.1002/chem.201303559.

[270] Robert Lindner and Angelika Kühnle. "On-Surface Reactions". In: *Chemphyschem : a European journal of chemical physics and physical chemistry* 16.8 (2015), pp. 1582–1592. DOI: 10.1002/cphc.201500161.

[271] Leopold Talirz, Pascal Ruffieux, and Roman Fasel. "On-Surface Synthesis of Atomically Precise Graphene Nanoribbons". In: *Advanced materials (Deerfield Beach, Fla.)* 28.29 (2016), pp. 6222–6231. DOI: 10.1002/adma.201505738.

[272] André Gourdon. *On-Surface Synthesis*. Cham: Springer International Publishing, 2016. ISBN: 978-3-319-26598-8. DOI: 10.1007/978-3-319-26600-8.

[273] Yuanqin He, Manuela Garnica, Felix Bischoff, Jacob Ducke, Marie-Laure Bocquet, Matthias Batzill, Willi Auwärter, and Johannes V. Barth. "Fusing Tetrapyrroles to Graphene Edges by Surface-Assisted Covalent Coupling". In: *Nature Chemistry* 9 (2016), pp. 33–38. ISSN: 1755-4330. DOI: 10.1038/nchem.2600.

[274] Antje Richter, Andrea Floris, Ralf Bechstein, Lev Kantorovich, and Angelika Kühnle. "On-Surface Synthesis on a Bulk Insulator Surface". In: *Journal of physics. Condensed matter : an Institute of Physics journal* 30.13 (2018), p. 133001. DOI: 10.1088/1361-648X/aab0b9.

[275] Leonhard Grill, Matthew Dyer, Leif Lafferentz, Mats Persson, Maike V. Peters, and Stefan Hecht. "Nano-architectures by covalent assembly of molecular building blocks". In: *Nature Nanotechnology* 2.11 (2007), pp. 687–691. ISSN: 1748-3387. DOI: 10.1038/nnano.2007.346.

[276] Rico Gutzler, Hermann Walch, Georg Eder, Stephan Kloft, Wolfgang M. Heckl, and Markus Lackinger. "Surface Mediated Synthesis of 2D Covalent Organic Frameworks: 1,3,5-tris(4-bromophenyl)benzene on graphite(001), Cu(111), and Ag(110)". In: *Chemical communications (Cambridge, England)* 29 (2009), pp. 4456–4458. DOI: 10.1039/b906836h.

[277] Jinming Cai, Pascal Ruffieux, Rached Jaafar, Marco Bieri, Thomas Braun, Stephan Blankenburg, Matthias Muoth, Ari P. Seitsonen, Moussa Saleh, Xinliang Feng, Klaus Müllen, and Roman Fasel. "Atomically Precise Bottom-Up Fabrication of Graphene Nanoribbons". In: *Nature* 466.7305 (2010), pp. 470–473. DOI: 10.1038/nature09211.

[278] L. Lafferentz, V. Eberhardt, C. Dri, C. Africh, G. Comelli, F. Esch, S. Hecht, and L. Grill. "Controlling On-Surface Polymerization by Hierarchical and Substrate-Directed Growth". In: *Nature chemistry* 4.3 (2012), pp. 215–220. ISSN: 1755-4349. DOI: 10.1038/nchem.1242.

[279] Johanna Eichhorn, Damian Nieckarz, Oliver Ochs, Debabrata Samanta, Michael Schmittel, Pawel Jerzy Szabelski, and Markus Lackinger. "On-Surface Ullmann Coupling: The Influence of Kinetic Reaction Parameters on the Morphology and Quality of Covalent Networks". In: *ACS Nano* 8.8 (2014), pp. 7880–7889. DOI: 10.1021/nn501567p.

[280] Sören Zint, Daniel Ebeling, Tobias Schlöder, Sebastian Ahles, Doreen Mollenhauer, Hermann A. Wegner, and André Schirmeisen. "Imaging Successive Intermediate States of the On-Surface Ullmann Reaction on Cu(111): Role of the Metal Coordination". In: *ACS Nano* 11.4 (2017), pp. 4183–4190. DOI: 10.1021/acsnano.7b01109.

[281] C. Glaser. "Beiträge zur Kenntniss des Acetenylbenzols". In: *Berichte der deutschen chemischen Gesellschaft* 2.1 (1869), pp. 422–424. DOI: 10.1002/cber.186900201183.

[282] Siemsen, Livingston, and Diederich. "Acetylenic Coupling: A Powerful Tool in Molecular Construction". In: *Angewandte Chemie (International ed. in English)* 39.15 (2000), pp. 2632–2657.

[283] Haigang Zhang, W. D. Xiao, Jinhai Mao, Haitao Zhou, Geng Li, Yi Zhang, Liwei Liu, Shixuan Du, and H.-J. Gao. "Host–Guest Superstructures on Graphene-Based Kagome Lattice". In: *The Journal of Physical Chemistry C* 116.20 (2012), pp. 11091–11095. DOI: 10.1021/jp3020244.

[284] Johanna Eichhorn, Wolfgang M. Heckl, and Markus Lackinger. "On-Surface Polymerization of 1,4-Diethynylbenzene on Cu(111)". In: *Chemical communications (Cambridge, England)* 49.28 (2013), pp. 2900–2902. DOI: 10.1039/c3cc40444g.

[285] Hong-Ying Gao, Jörn-Holger Franke, Hendrik Wagner, Dingyong Zhong, Philipp-Alexander Held, Armido Studer, and Harald Fuchs. "Effect of Metal Surfaces in On-Surface Glaser Coupling". In: *The Journal of Physical Chemistry C* 117.36 (2013), pp. 18595–18602. DOI: 10.1021/jp406858p.

[286] Hong-Ying Gao, Hendrik Wagner, Dingyong Zhong, Jörn-Holger Franke, Armido Studer, and Harald Fuchs. "Glaser Coupling at Metal Surfaces". In: *Angewandte Chemie (International ed. in English)* 52.14 (2013), pp. 4024–4028. DOI: 10.1002/anie.201208597.

[287] Hong-Ying Gao, Dingyong Zhong, Harry Mönig, Hendrik Wagner, Philipp-Alexander Held, Alexander Timmer, Armido Studer, and Harald Fuchs. "Photochemical Glaser Coupling at Metal Surfaces". In: *The Journal of Physical Chemistry C* 118.12 (2014), pp. 6272–6277. DOI: 10.1021/jp411889e.

[288] Florian Klappenberger, Yi-Qi Zhang, Jonas Björk, Svetlana Klyatskaya, Mario Ruben, and Johannes V. Barth. "On-Surface Synthesis of Carbon-Based Scaffolds and Nanomaterials Using Terminal Alkynes". In: *Accounts of chemical research* 48.7 (2015), pp. 2140–2150. DOI: 10.1021/acs.accounts.5b00174.

[289] Sigrid Weigelt, Carsten Busse, Christian Bombis, Martin M. Knudsen, Kurt V. Gothelf, Thomas Strunskus, Christof Wöll, Mats Dahlbom, Bjørk Hammer, Erik Laegsgaard, Flemming Besenbacher, and Trolle R. Linderoth. "Covalent Interlinking of an Aldehyde and an Amine on a Au(111) Surface in Ultrahigh Vacuum". In: *Angewandte Chemie (International ed. in English)* 46.48 (2007), pp. 9227–9230. DOI: 10.1002/anie.200702859.

[290] Sigrid Weigelt, Carsten Busse, Christian Bombis, Martin M. Knudsen, Kurt V. Gothelf, Erik Laegsgaard, Flemming Besenbacher, and Trolle R. Linderoth. "Surface Synthesis of 2D Branched Polymer Nanostructures". In: *Angewandte Chemie (International ed. in English)* 47.23 (2008), pp. 4406–4410. DOI: 10.1002/anie.200705079.

[291] Nikolas A. A. Zwaneveld, Rémy Pawlak, Mathieu Abel, Daniel Catalin, Didier Gigmes, Denis Bertin, and Louis Porte. "Organized Formation of 2D Extended Covalent Organic Frameworks at Surfaces". In: *Journal of the American Chemical Society* 130.21 (2008), pp. 6678–6679. DOI: 10.1021/ja800906f.

[292] Matthias Treier, Neville V. Richardson, and Roman Fasel. "Fabrication of Surface-Supported Low-Dimensional Polyimide Networks". In: *Journal of the American Chemical Society* 130.43 (2008), pp. 14054–14055. DOI: 10.1021/ja805342n.

[293] Johannes C. Hermann, Juliette Pradon, Jeremy N. Harvey, and Adrian J. Mulholland. "High Level QM/MM Modeling of the Formation of the Tetrahedral Intermediate in the Acylation of Wild Type and K73A Mutant TEM-1 Class A Beta-Lactamase". In: *The journal of physical chemistry. A* 113.43 (2009), pp. 11984–11994. DOI: 10.1021/jp9037254.

[294] Oualid Ourdjini, Rémy Pawlak, Mathieu Abel, Sylvain Clair, Liang Chen, Nathalie Bergeon, Michel Sassi, Vincent Oison, Jean-Marc Debierre, Roland Coratger, and Louis Porte. "Substrate-Mediated Ordering and Defect Analysis of a Surface Covalent Organic Framework". In: *Physical Review B* 84.12 (2011), p. 2480. DOI: 10.1103/PhysRevB.84.125421.

[295] Thomas Faury, Sylvain Clair, Mathieu Abel, Frédéric Dumur, Didier Gigmes, and Louis Porte. "Sequential Linking To Control Growth of a Surface Covalent Organic Frame-

work". In: *The Journal of Physical Chemistry C* 116.7 (2012), pp. 4819–4823. DOI: 10.1021/jp300417g.

[296] Petra Fesser, Cristian Iacovita, Christian Wäckerlin, Saranyan Vijayaraghavan, Nirmalya Ballav, Kara Howes, Jean-Paul Gisselbrecht, Maura Crobu, Corinne Boudon, Meike Stöhr, Thomas A. Jung, and François Diederich. "Visualizing the Product of a Formal Cycloaddition of 7,7,8,8-Tetracyano-P-Quinodimethane (TCNQ) to an Acetylene-Appended Porphyrin by Scanning Tunneling Microscopy on Au(111)". In: *Chemistry (Weinheim an der Bergstrasse, Germany)* 17.19 (2011), pp. 5246–5250. DOI: 10.1002/chem.201100733.

[297] Fabian Bebensee, Christian Bombis, Sundar-Raja Vadapoo, Jacob R. Cramer, Flemming Besenbacher, Kurt V. Gothelf, and Trolle R. Linderoth. "On-Surface Azide-Alkyne Cycloaddition on Cu(111): Does It "Click" in Ultrahigh Vacuum?" In: *Journal of the American Chemical Society* 135.6 (2013), pp. 2136–2139. DOI: 10.1021/ja312303a.

[298] Oscar Díaz Arado, Harry Mönig, Hendrik Wagner, Jörn-Holger Franke, Gernot Langewisch, Philipp Alexander Held, Armido Studer, and Harald Fuchs. "On-Surface Azide-Alkyne Cycloaddition on Au(111)". In: *ACS Nano* 7.10 (2013), pp. 8509–8515. DOI: 10.1021/nn4022789.

[299] Philipp Rahe, Robert Lindner, Markus Kittelmann, Markus Nimmrich, and Angelika Kühnle. "From Dewetting to Wetting Molecular Layers: C60 on CaCO3(1014) as a Case Study". In: *Physical chemistry chemical physics : PCCP* 14.18 (2012), pp. 6544–6548. DOI: 10.1039/c2cp40172j.

[300] Philipp Rahe, Markus Kittelmann, Julia L. Neff, Markus Nimmrich, Michael Reichling, Philipp Maass, and Angelika Kühnle. "Tuning Molecular Self-Assembly on Bulk Insulator Surfaces by Anchoring of the Organic Building Blocks". In: *Advanced materials (Deerfield Beach, Fla.)* 25.29 (2013), pp. 3948–3956. DOI: 10.1002/adma.201300604.

[301] Markus Kittelmann, Philipp Rahe, Markus Nimmrich, Christopher M. Hauke, André Gourdon, and Angelika Kühnle. "On-Surface Covalent Linking of Organic Building Blocks on a Bulk Insulator". In: *ACS Nano* 5.10 (2011), pp. 8420–8425. DOI: 10.1021/nn2033192.

[302] Markus Kittelmann, Markus Nimmrich, Robert Lindner, André Gourdon, and Angelika Kühnle. "Sequential and Site-Specific On-Surface Synthesis on a Bulk Insulator". In: *ACS Nano* 7.6 (2013), pp. 5614–5620. DOI: 10.1021/nn402018w.

[303] Robert Lindner, Philipp Rahe, Markus Kittelmann, André Gourdon, Ralf Bechstein, and Angelika Kühnle. "Substrate Templating Guides the Photoinduced Reaction of C60 on Calcite". In: *Angewandte Chemie (International ed. in English)* 53.30 (2014), pp. 7952–7955. DOI: 10.1002/anie.201309128.

[304] A. Richter, V. Haapasilta, C. Venturini, R. Bechstein, A. Gourdon, A. S. Foster, and A. Kühnle. "Diacetylene Polymerization on a Bulk Insulator Surface". In: *Physical chemistry chemical physics : PCCP* 19.23 (2017), pp. 15172–15176. DOI: 10.1039/c7cp01526g.

[305] Antje Richter, Manuel Vilas-Varela, Diego Peña, Ralf Bechstein, and Angelika Kühnle. "Homocoupling of Terminal Alkynes on Calcite (10.4)". In: *Surface Science* (2017). DOI: 10.1016/j.susc.2017.12.012.

[306] Claudius Morchutt, Jonas Björk, Sören Krotzky, Rico Gutzler, and Klaus Kern. "Covalent coupling via dehalogenation on Ni(111) supported boron nitride and graphene". In: *Chemical communications (Cambridge, England)* 51.12 (2015), pp. 2440–2443. DOI: 10.1039/c4cc07107g.

[307] Wei Zhao, Lei Dong, Chao Huang, Zaw Myo Win, and Nian Lin. "Cu- and Pd-Catalyzed Ullmann Reaction on a Hexagonal Boron Nitride Layer". In: *Chemical communications (Cambridge, England)* 52.90 (2016), pp. 13225–13228. DOI: 10.1039/c6cc05029h.

[308] Xiaobo Lu, Wei Yang, Shuopei Wang, Shuang Wu, Peng Chen, Jing Zhang, Jing Zhao, Jianling Meng, Guibai Xie, Duoming Wang, Guole Wang, Ting Ting Zhang, Kenji Watanabe, Takashi Taniguchi, Rong Yang, Dongxia Shi, and Guangyu Zhang. "Graphene Nanoribbons Epitaxy on Boron Nitride". In: *Applied Physics Letters* 108.11 (2016), p. 113103. DOI: 10.1063/1.4943940.

[309] Lirong Xu, Lili Cao, Zongxia Guo, Zeqi Zha, and Shengbin Lei. "Side-Functionalized Two-Dimensional Polymers Synthesized via On-Surface Schiff-Base Coupling". In: *Chemical communications (Cambridge, England)* 51.41 (2015), pp. 8664–8667. DOI: 10.1039/c5cc02232k.

[310] Luciano Colazzo, Francesco Sedona, Alessandro Moretto, Maurizio Casarin, and Mauro Sambi. "Metal-Free on-Surface Photochemical Homocoupling of Terminal Alkynes". In: *Journal of the American Chemical Society* 138.32 (2016), pp. 10151–10156. DOI: 10.1021/jacs.6b03589.

[311] Lirong Xu, Yanxia Yu, Jianbin Lin, Xin Zhou, Wei Quan Tian, Damian Nieckarz, Pawel Szabelski, and Shengbin Lei. "On-Surface Synthesis of Two-Dimensional Imine Polymers with a Tunable Band Gap: A Combined STM, DFT and Monte Carlo Investigation". In: *Nanoscale* 8.16 (2016), pp. 8568–8574. DOI: 10.1039/c5nr07663c.

[312] Reinhard Berger, Manfred Wagner, Xinliang Feng, and Klaus Müllen. "Polycyclic Aromatic Azomethine Ylides: A Unique Entry to Extended Polycyclic Heteroaromatics". In: *Chemical science* 6.1 (2015), pp. 436–441. DOI: 10.1039/c4sc02793k.

[313] Xiao-Ye Wang, Marcus Richter, Yuanqin He, Jonas Björk, Alexander Riss, Raju Rajesh, Manuela Garnica, Felix Hennersdorf, Jan J. Weigand, Akimitsu Narita, Reinhard Berger, Xinliang Feng, Willi Auwärter, Johannes V. Barth, Carlos-Andres Palma, and Klaus Müllen. "Exploration of Pyrazine-Embedded Antiaromatic Polycyclic Hydrocarbons Generated by Solution and On-Surface Azomethine Ylide Homocoupling". In: *Nature Communications* 8.1 (2017), p. 1948. ISSN: 2041-1723. DOI: 10.1038/s41467-017-01934-1.

[314] Rolf Huisgen. "1,3-Dipolar Cycloadditions. Past and Future". In: *Angewandte Chemie International Edition in English* 2.10 (1963), pp. 565–598. ISSN: 0570-0833. DOI: 10.1002/anie.196305651.

[315] Albert Padwa and William H. Pearson. *Synthetic Applications of 1,3-Dipolar Cycloaddition Chemistry Toward Heterocycles and Natural Products*. Vol. 59. The Chemistry of Heterocyclic Compounds. Hoboken, New Jersey: John Wiley & Sons, 2003.

[316] R. Beugelmans, L. Benadjila-Iguertsira, and G. Roussi. "The Reactivity of Benzyldimethylamine N-Oxide on Treatment with Strong Bases". In: *Journal of the Chemical Society, Chemical Communications* 10 (1982), p. 544. DOI: 10.1039/c39820000544.

[317] Albert Padwa, William Dent, Hildegard Nimmesgern, M. K. Venkatramanan, and George S. K. Wong. "Utilization of Phenylthio Substituted Amines for the Synthesis of Pyrrolidines". In: *Chemische Berichte* 119.3 (1986), pp. 813–828. DOI: 10.1002/cber.19861190305.

[318] S. D. Kahn, W. J. Hehre, and J. A. Pople. "Hartree-Fock Descriptions of 1,3-dipoles. Zwitterions, 1,3-Diradicals, or Hypervalent Species?" In: *Journal of the American Chemical Society* 109.6 (1987), pp. 1871–1873. DOI: 10.1021/ja00240a053.

[319] Luis R. Domingo, Eduardo Chamorro, and Patricia Perez. "Understanding the High Reactivity of the Azomethine Ylides in [3 + 2] Cycloaddition Reactions". In: *Letters in Organic Chemistry* 7.6 (2010), pp. 432–439. ISSN: 15701786. DOI: 10.2174/157017810791824900.

[320] Daniel H. Ess and K. N. Houk. "Theory of 1,3-Dipolar Cycloadditions: Distortion/Interaction and Frontier Molecular Orbital Models". In: *Journal of the American Chemical Society* 130.31 (2008), pp. 10187–10198. DOI: 10.1021/ja800009z.

[321] Benoit Braida, Christof Walter, Bernd Engels, and Philippe C. Hiberty. "A Clear Correlation between the Diradical Character of 1,3-Dipoles and their Reactivity Toward Ethylene or Acetylene". In: *Journal of the American Chemical Society* 132.22 (2010), pp. 7631–7637. DOI: 10.1021/ja100512d.

[322] Jean-Pierre Fleury, Jean-Paul Schoeni, Daniel Clerin, and Hans Fritz. "Aza-2-Dièenes-1,3. 2. Synthèse et Structure d'un Ylure d'Azométhine Stable". In: *Helvetica Chimica Acta* 58.7 (1975), pp. 2018–2026. DOI: 10.1002/hlca.19750580716.

[323] Christian Rømming, Per Kolsaker, E. Kulonen, Adam Deutsch, and Takao Matsuno. "The Crystal Structure of Dicyano-1-methyl-3H-Isoindoleninium Methylide". In: *Acta Chemica Scandinavica* 32b (1978), pp. 679–682. DOI: 10.3891/acta.chem.scand.32b-0679.

[324] L. Toupet and Y. Délugeard. "1-(1-Morpholino-1-Cyclohexen-6-Ylideneammonio)-1-Cyano-2-Methoxy-2-Oxoethanide. A Stable Azomethine Ylide". In: *Acta Crystallographica Section B Structural Crystallography and Crystal Chemistry* 35.8 (1979), pp. 1935–1936. ISSN: 05677408. DOI: 10.1107/S0567740879008190.

[325] John J. D'Amico, B. Ray Stults, Peter G. Ruminski, and Karl V. Wood. "Synthesis of 1-Cyano-2-Methylisoindole. A New Route to Isoindoles". In: *Journal of Heterocyclic Chemistry* 20.5 (1983), pp. 1283–1286. DOI: 10.1002/jhet.5570200527.

[326] Ronald Grigg, John F. Malone, Theeravat Mongkolaussavaratana, and Sunit Thianpatanagul. "Cycloaddition Reaction Relevant to the Mechanism of the Ninhydrin Reaction. X-Ray Crystal Structure of Protonated Ruhemann's Purple, a Stable 1,3-Dipole". In: *Journal of the Chemical Society, Chemical Communications* 5 (1986), p. 421. DOI: 10.1039/c39860000421.

[327] Kazuo Achiwa, Yoshiyasu Terao, and Masahiro Aono. "New Generation of 1,3-Dipoles from Organosilicon Compounds and Syntheses of Heterocycles". In: *Heterocycles* 27.4 (1988), p. 981. DOI: 10.3987/REV-87-375.

[328] Eloisa Lopez-Calle, Manfred Keller, and Wolfgang Eberbach. "Access to Isolable Azomethine Ylides by Photochemical Transformation of 2,3-Dihydroisoxazoles". In: *European Journal of Organic Chemistry* 2003.8 (2003), pp. 1438–1453. DOI: 10.1002/ejoc.200390203.

[329] Philip Allway and Ronald Grigg. "Chiral Co(II) and Mn(II) Catalysts for the 1,3-Dipolar Cycloaddition Reactions of Azomethine Ylides Derived from Arylidene Imines of Glycine". In: *Tetrahedron Letters* 32.41 (1991), pp. 5817–5820. ISSN: 00404039. DOI: 10.1016/S0040-4039(00)93563-9.

[330] Wenzhong Gao, Xumu Zhang, and Malati Raghunath. "Cu(I)-Catalyzed Highly Exo-Selective and Enantioselective 3 + 2 Cycloaddition of Azomethine Ylides with Acrylates". In: *Organic letters* 7.19 (2005), pp. 4241–4244. DOI: 10.1021/ol0516925.

[331] Xiao-Hua Chen, Qiang Wei, Shi-Wei Luo, Han Xiao, and Liu-Zhu Gong. "Organocatalytic Synthesis of Spiropyrrolidin-3,3'-Oxindoles with High Enantiopurity and Structural Diversity". In: *Journal of the American Chemical Society* 131.38 (2009), pp. 13819–13825. DOI: 10.1021/ja905302f.

[332] Ichiro Oura, Kenta Shimizu, Kenichi Ogata, and Shin-Ichi Fukuzawa. "Highly Endo-Selective and Enantioselective 1,3-Dipolar Cycloaddition of Azomethine Ylide with Alpha-Enones Catalyzed by a Silver(I)/ThioClickFerrophos Complex". In: *Organic letters* 12.8 (2010), pp. 1752–1755. DOI: 10.1021/ol100336q.

[333] T. Yokoyama, S. Yokoyama, T. Kamikado, Y. Okuno, and S. Mashiko. "Selective Assembly on a Surface of Supramolecular Aggregates with Controlled Size and Shape". In: *Nature* 413.6856 (2001), pp. 619–621. DOI: 10.1038/35098059.

[334] Yoshishige Okuno, Takashi Yokoyama, Shiyoshi Yokoyama, Toshiya Kamikado, and Shinro Mashiko. "Theoretical Study of Benzonitrile Clusters in the Gas Phase and Their Adsorption onto a Au(111) Surface". In: *Journal of the American Chemical Society* 124.24 (2002), pp. 7218–7225. DOI: 10.1021/ja011744v.

[335] Stefano Gottardi, Kathrin Müller, Juan Carlos Moreno-López, Handan Yildirim, Ute Meinhardt, Milan Kivala, Abdelkader Kara, and Meike Stöhr. "Cyano-Functionalized Triarylamines on Au(111): Competing Intermolecular versus Molecule/Substrate Interactions". In: *Advanced Materials Interfaces* 1.1 (2014), p. 1300025. ISSN: 21967350. DOI: 10.1002/admi.201300025.

[336] Sebastian Stepanow, Nian Lin, Dietmar Payer, Uta Schlickum, Florian Klappenberger, Giorgio Zoppellaro, Mario Ruben, Harald Brune, Johannes V. Barth, and Klaus Kern. "Surface-Assisted Assembly of 2D Metal–Organic Networks That Exhibit Unusual Threefold Coordination Symmetry". In: *Angewandte Chemie* 119.5 (2007), pp. 724–727. ISSN: 00448249. DOI: 10.1002/ange.200603644.

[337] U. Schlickum, R. Decker, F. Klappenberger, G. Zoppellaro, S. Klyatskaya, M. Ruben, I. Silanes, A. Arnau, K. Kern, H. Brune, and J. V. Barth. "Metal-organic honeycomb nanomeshes with tunable cavity size". In: *Nano Letters* 7.12 (2007), pp. 3813–3817. ISSN: 1530-6984. DOI: 10.1021/nl072466m.

[338] Peter A. Wood, Simon J. Borwick, David J. Watkin, W. D. Samuel Motherwell, and Frank H. Allen. "Dipolar CN-...-CN Interactions in Organic Crystal Structures: Database Analysis and Calculation of Interaction Energies". In: *Acta crystallographica. Section B, Structural science* 64.Pt 3 (2008), pp. 393–396. ISSN: 0108-7681. DOI: 10.1107/S0108768108010239.

[339] W. Chen, V. Madhavan, T. Jamneala, and M. F. Crommie. "Scanning Tunneling Microscopy Observation of an Electronic Superlattice at the Surface of Clean Gold". In: *Physical Review Letters* 80.7 (1998), pp. 1469–1472. DOI: 10.1103/PhysRevLett.80.1469.

[340] Yuanqin He. *PhD Thesis*. 2017.

[341] A. Das, S. Pisana, B. Chakraborty, S. Piscanec, S. K. Saha, U. V. Waghmare, K. S. Novoselov, H. R. Krishnamurthy, A. K. Geim, A. C. Ferrari, and A. K. Sood. "Monitoring Dopants by Raman Scattering in an Electrochemically Top-Gated Graphene Transistor". In: *Nature nanotechnology* 3.4 (2008), pp. 210–215. DOI: 10.1038/nnano.2008.67.

[342] Yu-Ming Lin, Keith A. Jenkins, Alberto Valdes-Garcia, Joshua P. Small, Damon B. Farmer, and Phaedon Avouris. "Operation of Graphene Transistors at Gigahertz Frequencies". In: *Nano Letters* 9.1 (2009), pp. 422–426. ISSN: 1530-6984. DOI: 10.1021/nl803316h.

[343] Lei Liao, Yung-Chen Lin, Mingqiang Bao, Rui Cheng, Jingwei Bai, Yuan Liu, Yongquan Qu, Kang L. Wang, Yu Huang, and Xiangfeng Duan. "High-Speed Graphene Transistors With a Self-Aligned Nanowire Gate". In: *Nature* 467.7313 (2010), pp. 305–308. DOI: 10.1038/nature09405.

[344] Yanqing Wu, Yu-Ming Lin, Ageeth A. Bol, Keith A. Jenkins, Fengnian Xia, Damon B. Farmer, Yu Zhu, and Phaedon Avouris. "High-Frequency, Scaled Graphene Transistors on Diamond-Like Carbon". In: *Nature* 472.7341 (2011), pp. 74–78. DOI: 10.1038/nature09979.

[345] Woo Jong Yu, Zheng Li, Hailong Zhou, Yu Chen, Yang Wang, Yu Huang, and Xiangfeng Duan. "Vertically Stacked Multi-Heterostructures of Layered Materials for Logic Transistors and Complementary Inverters". In: *Nature Materials* 12.3 (2013), pp. 246–252. DOI: 10.1038/nmat3518.

[346] Yan Wang, Zhiqiang Shi, Yi Huang, Yanfeng Ma, Chengyang Wang, Mingming Chen, and Yongsheng Chen. "Supercapacitor Devices Based on Graphene Materials". In: *The Journal of Physical Chemistry C* 113.30 (2009), pp. 13103–13107. DOI: 10.1021/jp902214f.

[347] Chenguang Liu, Zhenning Yu, David Neff, Aruna Zhamu, and Bor Z. Jang. "Graphene-Based Supercapacitor with an Ultrahigh Energy Density". In: *Nano letters* 10.12 (2010), pp. 4863–4868. DOI: 10.1021/nl102661q.

[348] Kai Zhang, Li Li Zhang, X. S. Zhao, and Jishan Wu. "Graphene/Polyaniline Nanofiber Composites as Supercapacitor Electrodes". In: *Chemistry of Materials* 22.4 (2010), pp. 1392–1401. ISSN: 0897-4756. DOI: 10.1021/cm902876u.

[349] Linh T. Le, Matthew H. Ervin, Hongwei Qiu, Brian E. Fuchs, and Woo Y. Lee. "Graphene Supercapacitor Electrodes Fabricated by Inkjet Printing and Thermal Reduction of Graphene Oxide". In: *Electrochemistry Communications* 13.4 (2011), pp. 355–358. ISSN: 13882481. DOI: 10.1016/j.elecom.2011.01.023.

[350] Chun Xian Guo and Chang Ming Li. "A Self-Assembled Hierarchical Nanostructure Comprising Carbon Spheres and Graphene Nanosheets for Enhanced Supercapacitor Performance". In: *Energy & Environmental Science* 4.11 (2011), p. 4504. DOI: 10.1039/c1ee01676h.

[351] Xiao-Chen Dong, Hang Xu, Xue-Wan Wang, Yin-Xi Huang, Mary B. Chan-Park, Hua Zhang, Lian-Hui Wang, Wei Huang, and Peng Chen. "3D Graphene-Cobalt Oxide Electrode for High-Performance Supercapacitor and Enzymeless Glucose Detection". In: *ACS Nano* 6.4 (2012), pp. 3206–3213. DOI: 10.1021/nn300097q.

[352] Yongmin He, Wanjun Chen, Xiaodong Li, Zhenxing Zhang, Jiecai Fu, Changhui Zhao, and Erqing Xie. "Freestanding Three-Dimensional Graphene/MnO2 Composite Networks as Ultralight and Flexible Supercapacitor Electrodes". In: *ACS Nano* 7.1 (2013), pp. 174–182. DOI: 10.1021/nn304833s.

[353] Brian Seger and Prashant V. Kamat. "Electrocatalytically Active Graphene-Platinum Nanocomposites. Role of 2-D Carbon Support in PEM Fuel Cells". In: *The Journal of Physical Chemistry C* 113.19 (2009), pp. 7990–7995. DOI: 10.1021/jp900360k.

[354] R. Imran Jafri, N. Rajalakshmi, and S. Ramaprabhu. "Nitrogen Doped Graphene Nanoplatelets as Catalyst Support for Oxygen Reduction Reaction in Proton Exchange Membrane Fuel Cell". In: *Journal of Materials Chemistry* 20.34 (2010), p. 7114. ISSN: 0959-9428. DOI: 10.1039/c0jm00467g.

[355] Yongye Liang, Yanguang Li, Hailiang Wang, Jigang Zhou, Jian Wang, Tom Regier, and Hongjie Dai. "Co_3O_4 Nanocrystals on Graphene as a Synergistic Catalyst for Oxygen Reduction Reaction". In: *Nature Materials* 10.10 (2011), pp. 780–786. DOI: 10.1038/nmat3087.

[356] Ermete Antolini. "Graphene as a New Carbon Support for Low-Temperature Fuel Cell Catalysts". In: *Applied Catalysis B: Environmental* 123-124 (2012), pp. 52–68. DOI: 10.1016/j.apcatb.2012.04.022.

[357] Xuejun Zhou, Jinli Qiao, Lin Yang, and Jiujun Zhang. "A Review of Graphene-Based Nanostructural Materials for Both Catalyst Supports and Metal-Free Catalysts in PEM Fuel Cell Oxygen Reduction Reactions". In: *Advanced Energy Materials* 4.8 (2014), p. 1301523. ISSN: 16146832. DOI: 10.1002/aenm.201301523.

[358] G. Giovannetti, P. A. Khomyakov, G. Brocks, V. M. Karpan, van den Brink, J., and P. J. Kelly. "Doping Graphene with Metal Contacts". In: *Physical Review Letters* 101.2 (2008). DOI: 10.1103/PhysRevLett.101.026803.

[359] N. Srivastava, Qin Gao, M. Widom, R. M. Feenstra, Shu Nie, K. F. McCarty, and I. V. Vlassiouk. "Low-Energy Electron Reflectivity of Graphene on Copper and other Substrates". In: *Physical Review B* 87.24 (2013). DOI: 10.1103/PhysRevB.87.245414.

[360] I. Pletikosić, M. Kralj, P. Pervan, R. Brako, J. Coraux, A. T. N'diaye, C. Busse, and T. Michely. "Dirac Cones and Minigaps for Graphene on Ir(111)". In: *Physical Review Letters* 102.5 (2009), p. 056808. DOI: 10.1103/PhysRevLett.102.056808.

[361] Matthew Yankowitz, Jiamin Xue, Daniel Cormode, Javier D. Sanchez-Yamagishi, K. Watanabe, T. Taniguchi, Pablo Jarillo-Herrero, Philippe Jacquod, and Brian J. LeRoy. "Emergence of Superlattice Dirac Points in Graphene on Hexagonal Boron Nitride". In: *Nature Physics* 8.5 (2012), pp. 382–386. ISSN: 1745-2473. DOI: 10.1038/nphys2272.

[362] C. R. Dean, L. Wang, P. Maher, C. Forsythe, F. Ghahari, Y. Gao, J. Katoch, M. Ishigami, P. Moon, M. Koshino, T. Taniguchi, K. Watanabe, K. L. Shepard, J. Hone, and P. Kim. "Hofstadter's Butterfly and the Fractal Quantum Hall Effect in Moiré Superlattices". In: *Nature* 497.7451 (2013), pp. 598–602. DOI: 10.1038/nature12186.

[363] L. A. Ponomarenko, R. V. Gorbachev, G. L. Yu, D. C. Elias, R. Jalil, A. A. Patel, A. Mishchenko, A. S. Mayorov, C. R. Woods, J. R. Wallbank, M. Mucha-Kruczynski, B. A. Piot, M. Potemski, I. V. Grigorieva, K. S. Novoselov, F. Guinea, V. I. Fal'ko, and A. K. Geim. "Cloning of Dirac Fermions in Graphene Superlattices". In: *Nature* 497.7451 (2013), pp. 594–597. DOI: 10.1038/nature12187.

[364] N. Levy, S. A. Burke, K. L. Meaker, M. Panlasigui, A. Zettl, F. Guinea, Neto, A. H. C., and M. F. Crommie. "Strain-Induced Pseudo-Magnetic Fields Greater Than 300 Tesla in Graphene Nanobubbles". In: *Science* 329.5991 (2010), pp. 544–547. DOI: 10.1126/science.1191700.

[365] C. Wang, Y. Liu, L. Li, and H. Tan. "Anisotropic Thermal Conductivity of Graphene Wrinkles". In: *Nanoscale* 6.11 (2014), pp. 5703–5707. DOI: 10.1039/C4NR00423J.

[366] Jiutao Li, Wolf-Dieter Schneider, Richard Berndt, and S. Crampin. "Electron Confinement to Nanoscale Ag Islands on Ag(111): A Quantitative Study". In: *Physical Review Letters* 80.15 (1998), pp. 3332–3335. DOI: 10.1103/PhysRevLett.80.3332.

[367] Jascha Repp, Gerhard Meyer, and Karl-Heinz Rieder. "Snell's Law for Surface Electrons: Refraction of an Electron Gas Imaged in Real Space". In: *Physical Review Letters* 92.3 (2004), p. 036803. DOI: 10.1103/PhysRevLett.92.036803.

[368] Philipp Leicht, Lukas Zielke, Samuel Bouvron, Riko Moroni, Elena Voloshina, Lukas Hammerschmidt, Yuriy S. Dedkov, and Mikhail Fonin. "In Situ Fabrication of Quasi-Free-Standing Epitaxial Graphene Nanoflakes on Gold". In: *ACS Nano* 8.4 (2014), pp. 3735–3742. DOI: 10.1021/nn500396c.

[369] Thomas Olsen and Kristian S. Thygesen. "Random Phase Approximation Applied to Solids, Molecules, and Graphene-Metal Interfaces: From van der Waals to Covalent Bonding". In: *Physical Review B* 87.7 (2013), p. 920. DOI: 10.1103/PhysRevB.87.075111.

[370] Ivor Lončarić and Vito Despoja. "Benchmarking van der Waals Functionals with Noncontact RPA Calculations on Graphene-Ag(111)". In: *Physical Review B* 90.7 (2014), p. 207. DOI: 10.1103/PhysRevB.90.075414.

[371] A. Garcia-Lekue, T. Balashov, M. Olle, G. Ceballos, A. Arnau, P. Gambardella, D. Sanchez-Portal, and A. Mugarza. "Spin-Dependent Electron Scattering at Graphene Edges on Ni(111)". In: *Physical review letters* 112.6 (2014), p. 066802. DOI: 10.1103/PhysRevLett.112.066802.

[372] B. Borca, S. Barja, M. Garnica, D. Sánchez-Portal, V. M. Silkin, E. V. Chulkov, C. F. Hermanns, J. J. Hinarejos, A. L. Vázquez de Parga, A. Arnau, P. M. Echenique, and R. Miranda. "Potential Energy Landscape for Hot Electrons in Periodically Nanostructured Graphene". In: *Physical review letters* 105.3 (2010), p. 036804. DOI: 10.1103/PhysRevLett.105.036804.

[373] P. A. Khomyakov, G. Giovannetti, P. C. Rusu, G. Brocks, van den Brink, J., and P. J. Kelly. "First-Principles Study of the Interaction and Charge Transfer between Graphene and Metals". In: *Physical Review B* 79.19 (2009). DOI: 10.1103/PhysRevB.79.195425.

[374] K. H. Gundlach. "Zur Berechnung des Tunnelstroms durch eine Trapezförmige Potentialstufe". In: *Solid-State Electronics* 9.10 (1966), pp. 949–957. DOI: 10.1016/0038-1101(66)90071-2.

[375] G. Binnig, K. Frank, H. Fuchs, N. Garcia, B. Reihl, H. Rohrer, F. Salvan, and A. Williams. "Tunneling Spectroscopy and Inverse Photoemission: Image and Field States". In: *Physical Review Letters* 55.9 (1985), pp. 991–994. DOI: 10.1103/PhysRevLett.55.991.

[376] J. H. Coombs and J. K. Gimzewski. "Fine Structure in Field Emission Resonances at Surfaces". In: *Journal of Microscopy* 152.3 (1988), pp. 841–851. DOI: 10.1111/j.1365-2818.1988.tb01457.x.

[377] J. Gadzuk. "Single-Atom Point Source for Electrons: Field-Emission Resonance Tunneling in Scanning Tunneling Microscopy". In: *Physical Review B* 47.19 (1993), pp. 12832–12839. DOI: 10.1103/PhysRevB.47.12832.

[378] E. V. Chulkov, V. M. Silkin, and P. M. Echenique. "Image Potential States on Metal Surfaces: Binding Energies and Wave Functions". In: *Surface Science* 437.3 (1999), pp. 330–352. DOI: 10.1016/S0039-6028(99)00668-8.

[379] Marina Pivetta, François Patthey, Massimiliano Stengel, Alfonso Baldereschi, and Wolf-Dieter Schneider. "Local Work Function Moiré Pattern on Ultrathin Ionic Films: NaCl on Ag(100)". In: *Physical Review B* 72.11 (2005), p. 1621. DOI: 10.1103/PhysRevB.72.115404.

[380] C. D. Ruggiero, T. Choi, and J. A. Gupta. "Tunneling Spectroscopy of Ultrathin Insulating Films: CuN on Cu(100)". In: *Applied Physics Letters* 91.25 (2007), p. 253106. DOI: 10.1063/1.2825595.

[381] C. L. Lin, S. M. Lu, W. B. Su, H. T. Shih, B. F. Wu, Y. D. Yao, C. S. Chang, and Tien T. Tsong. "Manifestation of Work Function Difference in High Order Gundlach Oscillation". In: *Physical Review Letters* 99.21 (2007). DOI: 10.1103/PhysRevLett.99.216103.

[382] Lingmei Kong, Cameron Bjelkevig, Sneha Gaddam, Mi Zhou, Young Hee Lee, Gang Hee Han, Hae Kyung Jeong, Ning Wu, Zhengzheng Zhang, Jie Xiao, P. A. Dowben, and Jeffry A. Kelber. "Graphene/Substrate Charge Transfer Characterized by Inverse Photoelectron Spectroscopy". In: *The Journal of Physical Chemistry C* 114.49 (2010), pp. 21618–21624. DOI: 10.1021/jp108616h.

[383] Ke Xu, Peigen Cao, and James R. Heath. "Scanning Tunneling Microscopy Characterization of the Electrical Properties of Wrinkles in Exfoliated Graphene Monolayers". In: *Nano letters* 9.12 (2009), pp. 4446–4451. DOI: 10.1021/nl902729p.

[384] Vitor M. Pereira, A. H. Castro Neto, H. Y. Liang, and L. Mahadevan. "Geometry, Mechanics, and Electronics of Singular Structures and Wrinkles in Graphene". In: *Physical review letters* 105.15 (2010), p. 156603. DOI: 10.1103/PhysRevLett.105.156603.

[385] Wenjuan Zhu, Tony Low, Vasili Perebeinos, Ageeth A. Bol, Yu Zhu, Hugen Yan, Jerry Tersoff, and Phaedon Avouris. "Structure and Electronic Transport in Graphene Wrinkles". In: *Nano letters* 12.7 (2012), pp. 3431–3436. DOI: 10.1021/nl300563h.

[386] Borislav Vasić, Amaia Zurutuza, and Radoš Gajić. "Spatial Variation of Wear and Electrical Properties Across Wrinkles in Chemical Vapour Deposition Graphene". In: *Carbon* 102 (2016), pp. 304–310. DOI: 10.1016/j.carbon.2016.02.066.

[387] E. N. Voloshina, Yu. S. Dedkov, S. Torbrügge, A. Thissen, and M. Fonin. "Graphene on Rh(111): Scanning tunneling and atomic force microscopies studies". In: *Applied Physics Letters* 100.24 (2012), p. 241606. DOI: 10.1063/1.4729549.

[388] Mark P. Boneschanscher, Joost van der Lit, Zhixiang Sun, Ingmar Swart, Peter Liljeroth, and Daniël Vanmaekelbergh. "Quantitative atomic resolution force imaging on epitaxial graphene with reactive and nonreactive AFM probes". In: *ACS Nano* 6.11 (2012), pp. 10216–10221. DOI: 10.1021/nn3040155.

[389] E. N. Voloshina, E. Fertitta, A. Garhofer, F. Mittendorfer, M. Fonin, A. Thissen, and Yu S. Dedkov. "Electronic Structure and Imaging Contrast of Graphene Moiré on Metals". In: *Scientific Reports* 3 (2013), p. 1072. DOI: 10.1038/srep01072.

[390] Sascha Koch, Daniele Stradi, Enrico Gnecco, Sara Barja, Shigeki Kawai, Cristina Díaz, Manuel Alcamí, Fernando Martín, Amadeo Lopez Vázquez de Parga, Rodolfo Miranda, Thilo Glatzel, and Ernst Meyer. "Elastic Response of Graphene Nanodomes". In: *ACS Nano* 7.4 (2013), pp. 2927–2934. DOI: 10.1021/nn304473r.

[391] Hans Peter Koch, Robert Laskowski, Peter Blaha, and Karlheinz Schwarz. "Adsorption of Small Gold Clusters on the h-BN/Rh(111) Nanomesh". In: *Physical Review B* 86.15 (2012). DOI: 10.1103/PhysRevB.86.155404.

[392] Andrea Resta, Thomas Leoni, Clemens Barth, Alain Ranguis, Conrad Becker, Thomas Bruhn, Patrick Vogt, and Guy Le Lay. "Atomic Structures of Silicene Layers Grown on Ag(111): Scanning Tunneling Microscopy and Noncontact Atomic Force Microscopy Observations". In: *Scientific Reports* 3 (2013), p. 2399. DOI: 10.1038/srep02399.

[393] Z. Majzik, M. Rachid Tchalala, M. Svec, P. Hapala, H. Enriquez, A. Kara, A. J. Mayne, G. Dujardin, P. Jelínek, and H. Oughaddou. "Combined AFM and STM Measurements of a Silicene Sheet Grown on the Ag(111) Surface". In: *Journal of physics. Condensed matter : an Institute of Physics journal* 25.22 (2013), p. 225301. DOI: 10.1088/0953-8984/25/22/225301.

[394] Yuriy Dedkov and Elena Voloshina. "Multichannel Scanning Probe Microscopy and Spectroscopy of Graphene Moiré Structures". In: *Physical chemistry chemical physics : PCCP* 16.9 (2014), pp. 3894–3908. DOI: 10.1039/C3CP54541E.

[395] Zhixiang Sun, Sampsa K. Hämäläinen, Jani Sainio, Jouko Lahtinen, Daniël Vanmaekelbergh, and Peter Liljeroth. "Topographic and Electronic Contrast of the Graphene Moiré on Ir(111) Probed by Scanning Tunneling Microscopy and Noncontact Atomic Force Microscopy". In: *Physical Review B* 83.8 (2011). DOI: 10.1103/PhysRevB.83.081415.

[396] Sampsa K. Hämäläinen, Mark P. Boneschanscher, Peter H. Jacobse, Ingmar Swart, Katariina Pussi, Wolfgang Moritz, Jouko Lahtinen, Peter Liljeroth, and Jani Sainio. "Structure and local variations of the graphene moiré on Ir(111)". In: *Physical Review B* 88.20 (2013). DOI: 10.1103/PhysRevB.88.201406.

[397] Carsten Busse, Predrag Lazić, Rabie Djemour, Johann Coraux, Timm Gerber, Nicolae Atodiresei, Vasile Caciuc, Radovan Brako, Alpha T. N'Diaye, Stefan Blügel, Jörg Zegenhagen, and Thomas Michely. "Graphene on Ir(111): Physisorption with Chemical Modulation". In: *Physical Review Letters* 107.3 (2011). DOI: 10.1103/PhysRevLett.107.036101.

[398] Fabien Jean, Tao Zhou, Nils Blanc, Roberto Felici, Johann Coraux, and Gilles Renaud. "Topography of the Graphene/Ir(111) Moiré Studied by Surface X-ray Diffraction". In: *Physical Review B* 91.24 (2015). DOI: 10.1103/PhysRevB.91.245424.

[399] B. de La Torre, M. Ellner, P. Pou, N. Nicoara, Rubén Pérez, and J. M. Gómez-Rodríguez. "Atomic-Scale Variations of the Mechanical Response of 2D Materials Detected by Noncontact Atomic Force Microscopy". In: *Physical review letters* 116.24 (2016), p. 245502. DOI: 10.1103/PhysRevLett.116.245502.

[400] W. Allers, A. Schwarz, U.D Schwarz, and R. Wiesendanger. "Dynamic Scanning Force Microscopy at Low Temperatures on a van der Waals Surface: Graphite (0001)". In: *Applied Surface Science* 140.3-4 (1999), pp. 247–252. DOI: 10.1016/S0169-4332(98)00535-2.

[401] H. Hölscher, A. Schwarz, W. Allers, U. D. Schwarz, and R. Wiesendanger. "Quantitative Analysis of Dynamic-Force-Spectroscopy Data on Graphite(0001) in the Contact and Noncontact Regimes". In: *Physical Review B* 61.19 (2000), pp. 12678–12681. DOI: 10.1103/PhysRevB.61.12678.

[402] Stefan Hembacher, Franz J. Giessibl, Jochen Mannhart, and Calvin F. Quate. "Revealing the Hidden Atom in Graphite by Low-Temperature Atomic Force Microscopy". In: *Proceedings of the National Academy of Sciences* 100.22 (2003), pp. 12539–12542. DOI: 10.1073/pnas.2134173100.

[403] Makoto Ashino, Alexander Schwarz, Timo Behnke, and Roland Wiesendanger. "Atomic-Resolution Dynamic Force Microscopy and Spectroscopy of a Single-Walled Carbon Nanotube: Characterization of Interatomic van der Waals Forces". In: *Physical Review Letters* 93.13 (2004), p. 136101. DOI: 10.1103/PhysRevLett.93.136101.

[404] Shigeki Kawai and Hideki Kawakatsu. "Surface-Relaxation-Induced Giant Corrugation on Graphite (0001)". In: *Physical Review B* 79.11 (2009). DOI: 10.1103/PhysRevB.79.115440.

[405] Shigeki Kawai, Thilo Glatzel, Sascha Koch, Bartosz Such, Alexis Baratoff, and Ernst Meyer. "Ultrasensitive Detection of Lateral Atomic-Scale Interactions on Graphite (0001) via Bimodal Dynamic Force Measurements". In: *Physical Review B* 81.8 (2010). DOI: 10.1103/PhysRevB.81.085420.

[406] Martin Ondráček, Pablo Pou, Vít Rozsíval, Cesar González, Pavel Jelínek, and Rubén Pérez. "Forces and Currents in Carbon Nanostructures: Are We Imaging Atoms?" In: *Physical review letters* 106.17 (2011), p. 176101. DOI: 10.1103/PhysRevLett.106.176101.

[407] Joost van der Lit, Mark P. Boneschanscher, Daniël Vanmaekelbergh, Mari Ijäs, Andreas Uppstu, Mikko Ervasti, Ari Harju, Peter Liljeroth, and Ingmar Swart. "Suppression of Electron-Vibron Coupling in Graphene Nanoribbons Contacted via a Single Atom". In: *Nature Communications* 4 (2013), p. 2023. ISSN: 2041-1723. DOI: 10.1038/ncomms3023.

[408] Isabel Fernández Torrente, Katharina J. Franke, and Jose Ignacio Pascual. "Spectroscopy of C 60 Single Molecules: The Role of Screening on Energy Level Alignment". In: *Journal of Physics: Condensed Matter* 20.18 (2008), p. 184001. DOI: 10.1088/0953-8984/20/18/184001.

[409] Arieh Aviram and Mark A. Ratner. "Molecular Rectifiers". In: *Chemical Physics Letters* 29.2 (1974), pp. 277–283. ISSN: 00092614. DOI: 10.1016/0009-2614(74)85031-1.

[410] M. A. Reed. "Conductance of a Molecular Junction". In: *Science* 278.5336 (1997), pp. 252–254. DOI: 10.1126/science.278.5336.252.

[411] Abraham Nitzan and Mark A. Ratner. "Electron Transport in Molecular Wire Junctions". In: *Science* 300.5624 (2003), pp. 1384–1389. DOI: 10.1126/science.1081572.

[412] Michael Galperin, Mark A. Ratner, Abraham Nitzan, and Alessandro Troisi. "Nuclear Coupling and Polarization in Molecular Transport Junctions: Beyond Tunneling to Function". In: *Science* 319.5866 (2008), pp. 1056–1060. DOI: 10.1126/science.1146556.

[413] Leif Lafferentz, Francisco Ample, Hao Yu, Stefan Hecht, Christian Joachim, and Leonhard Grill. "Conductance of a Single Conjugated Polymer as a Continuous Function of its Length". In: *Science* 323.5918 (2009), pp. 1193–1197. DOI: 10.1126/science.1168255.

[414] Kasper Moth-Poulsen and Thomas Bjørnholm. "Molecular Electronics with Single Molecules in Solid-State Devices". In: *Nature nanotechnology* 4.9 (2009), pp. 551–556. DOI: 10.1038/nnano.2009.176.

[415] Behtash Behin-Aein, Deepanjan Datta, Sayeef Salahuddin, and Supriyo Datta. "Proposal for an All-Spin Logic Device with Built-In Memory". In: *Nature nanotechnology* 5.4 (2010), pp. 266–270. DOI: 10.1038/nnano.2010.31.

[416] Alpha T. N'Diaye, Sebastian Bleikamp, Peter J. Feibelman, and Thomas Michely. "Two-Dimensional Ir Cluster Lattice on a Graphene Moiré on Ir(111)". In: *Physical Review Letters* 97.21 (2006), p. 215501. DOI: 10.1103/PhysRevLett.97.215501.

[417] Peter J. Feibelman. "Pinning of Graphene to Ir(111) by Flat Ir Dots". In: *Physical Review B* 77.16 (2008). DOI: 10.1103/PhysRevB.77.165419.

[418] Alpha T. N'Diaye, Raoul van Gastel, Antonio J. Martínez-Galera, Johann Coraux, Hichem Hattab, Dirk Wall, Heringdorf, Frank-J Meyer zu, Michael Horn-von Hoegen, José M. Gómez-Rodríguez, Bene Poelsema, Carsten Busse, and Thomas Michely. "In Situ Observation of Stress Relaxation in Epitaxial Graphene". In: *New Journal of Physics* 11.11 (2009), p. 113056. ISSN: 1367-2630. DOI: 10.1088/1367-2630/11/11/113056.

[419] Jan Knudsen, Peter J. Feibelman, Timm Gerber, Elin Grånäs, Karina Schulte, Patrick Stratmann, Jesper N. Andersen, and Thomas Michely. "Clusters Binding to the Graphene Moiré on Ir(111): X-ray Photoemission Compared to Density Functional Calculations". In: *Physical Review B* 85.3 (2012). DOI: 10.1103/PhysRevB.85.035407.

[420] Kerstin Donner and Peter Jakob. "Structural Properties and Site Specific Interactions of Pt with the Graphene/Ru(0001) Moiré Overlayer". In: *The Journal of Chemical Physics* 131.16 (2009), p. 164701. DOI: 10.1063/1.3246166.

[421] Zihao Zhou, Feng Gao, and D. Wayne Goodman. "Deposition of Metal Clusters on Single-Layer Graphene/Ru(0001): Factors that Govern Cluster Growth". In: *Surface Science* 604.13-14 (2010), pp. L31–L38. DOI: 10.1016/j.susc.2010.03.008.

[422] M. Sicot, S. Bouvron, O. Zander, U. Rüdiger, Yu. S. Dedkov, and M. Fonin. "Nucleation and Growth of Nickel Nanoclusters on Graphene Moiré on Rh(111)". In: *Applied Physics Letters* 96.9 (2010), p. 093115. DOI: 10.1063/1.3341176.

[423] Jinhai Mao, Haigang Zhang, Yuhang Jiang, Yi Pan, Min Gao, Wende Xiao, and H-J Gao. "Tunability of Supramolecular Kagome Lattices of Magnetic Phthalocyanines Using Graphene-Based Moire Patterns as Templates". In: *Journal of the American Chemical Society* 131.40 (2009), pp. 14136–14137. DOI: 10.1021/ja904907z.

[424] Yi-Qi Zhang, Nenad Kepčija, Martin Kleinschrodt, Katharina Diller, Sybille Fischer, Anthoula C. Papageorgiou, Francesco Allegretti, Jonas Björk, Svetlana Klyatskaya, Florian Klappenberger, Mario Ruben, and Johannes V. Barth. "Homo-Coupling of Terminal Alkynes on a Noble Metal Surface". In: *Nature Communications* 3 (2012), p. 1286. ISSN: 2041-1723. DOI: 10.1038/ncomms2291.

[425] Romana Baltic, Marina Pivetta, Fabio Donati, Christian Wäckerlin, Aparajita Singha, Jan Dreiser, Stefano Rusponi, and Harald Brune. "Superlattice of Single Atom Magnets on Graphene". In: *Nano letters* 16.12 (2016), pp. 7610–7615. DOI: 10.1021/acs.nanolett.6b03543.

[426] Dimitris Mousadakos, Marina Pivetta, Harald Brune, and Stefano Rusponi. "Sm Cluster Superlattice on Graphene/Ir(111)". In: *New Journal of Physics* 19.12 (2017), p. 123021. ISSN: 1367-2630. DOI: 10.1088/1367-2630/aa83e6.

[427] Maurizia Palummo, Conor Hogan, Francesco Sottile, Paolo Bagalá, and Angel Rubio. "Ab Initio Electronic and Optical Spectra of Free-Base Porphyrins: The Role of Electronic Correlation". In: *The Journal of Chemical Physics* 131.8 (2009), p. 084102. DOI: 10.1063/1.3204938.

[428] Ismaila Dabo, Andrea Ferretti, Cheol-Hwan Park, Nicolas Poilvert, Yanli Li, Matteo Cococcioni, and Nicola Marzari. "Donor and Acceptor Levels of Organic Photovoltaic Compounds from First Principles". In: *Physical chemistry chemical physics : PCCP* 15.2 (2013), pp. 685–695. DOI: 10.1039/C2CP43491A.

[429] Tianchao Niu, Miao Zhou, Jialin Zhang, Yuanping Feng, and Wei Chen. "Growth Intermediates for CVD Graphene on Cu(111): Carbon Clusters and Defective Graphene". In: *Journal of the American Chemical Society* 135.22 (2013), pp. 8409–8414. DOI: 10.1021/ja403583s.

[430] Hugo Dil, Jorge Lobo-Checa, Robert Laskowski, Peter Blaha, Simon Berner, Jürg Osterwalder, and Thomas Greber. "Surface Trapping of Atoms and Molecules with Dipole Rings". In: *Science* 319.5871 (2008), pp. 1824–1826. DOI: 10.1126/science.1154179.

[431] Haifeng Ma, Thomas Brugger, Simon Berner, Yun Ding, Marcella Iannuzzi, Jürg Hutter, Jürg Osterwalder, and Thomas Greber. "Nano-Ice on Boron Nitride Nanomesh: Accessing Proton Disorder". In: *ChemPhysChem* 11.2 (2010), pp. 399–403. ISSN: 14394235. DOI: 10.1002/cphc.200900857.

[432] Fabian Schulz, Robert Drost, Sampsa K. Hämäläinen, and Peter Liljeroth. "Templated Self-Assembly and Local Doping of Molecules on Epitaxial Hexagonal Boron Nitride". In: *ACS Nano* 7.12 (2013), pp. 11121–11128. DOI: 10.1021/nn404840h.

[433] F. Schiller, M. Ruiz-Osés, J. E. Ortega, P. Segovia, J. Martínez-Blanco, B. P. Doyle, V. Pérez-Dieste, J. Lobo, N. Néel, R. Berndt, and J. Kröger. "Electronic Structure of C60 on Au(887)". In: *The Journal of Chemical Physics* 125.14 (2006), p. 144719. DOI: 10.1063/1.2354082.

[434] Jan M. Englert, Christoph Dotzer, Guang Yang, Martin Schmid, Christian Papp, J. Michael Gottfried, Hans-Peter Steinrück, Erdmann Spiecker, Frank Hauke, and Andreas Hirsch. "Covalent Bulk Functionalization of Graphene". In: *Nat Chem* 3.4 (2011), pp. 279–286. DOI: 10.1038/nchem.1010.

[435] Lin Gan, Jian Zhou, Fen Ke, Hang Gu, Danna Li, Zonghai Hu, Qiang Sun, and Xuefeng Guo. "Tuning the Properties of Graphene Using a Reversible Gas-Phase Reaction". In: *NPG Asia Materials* 4.11 (2012), e31–e31. DOI: 10.1038/am.2012.58.

[436] Vasilios Georgakilas, Michal Otyepka, Athanasios B. Bourlinos, Vimlesh Chandra, Namdong Kim, K. Christian Kemp, Pavel Hobza, Radek Zboril, and Kwang S. Kim. "Functionalization of Graphene: Covalent and Non-Covalent Approaches, Derivatives and Applications". In: *Chemical reviews* 112.11 (2012), pp. 6156–6214. DOI: 10.1021/cr3000412.

[437] Elena Bekyarova, Santanu Sarkar, Feihu Wang, Mikhail E. Itkis, Irina Kalinina, Xiaojuan Tian, and Robert C. Haddon. "Effect of Covalent Chemistry on the Electronic Structure and Properties of Carbon Nanotubes and Graphene". In: *Accounts of Chemical Research* 46.1 (2013), pp. 65–76. DOI: 10.1021/ar300177q.

[438] Chun Kiang Chua and Martin Pumera. "Covalent Chemistry on Graphene". In: *Chemical Society reviews* 42.8 (2013), pp. 3222–3233. ISSN: 1460-4744. DOI: 10.1039/C2CS35474H.

[439] Hong Ying Mao, Yun Hao Lu, Jia Dan Lin, Shu Zhong, Andrew Thye Shen Wee, and Wei Chen. "Manipulating the Electronic and Chemical Properties of Graphene via Molecular Functionalization". In: *Progress in Surface Science* 88.2 (2013), pp. 132–159. ISSN: 00796816. DOI: 10.1016/j.progsurf.2013.02.001.

[440] M. Lattelais and M.-L. Bocquet. "Cycloaddition of Metal Porphines on Metal-Supported Graphene: A Computational Study". In: *The Journal of Physical Chemistry C* 119.17 (2015), pp. 9234–9241. DOI: 10.1021/jp512247n.

[441] Simon J. Altenburg, Marie Lattelais, Bin Wang, Marie-Laure Bocquet, and Richard Berndt. "Reaction of Phthalocyanines with Graphene on Ir(111)". In: *Journal of the American Chemical Society* 137.29 (2015), pp. 9452–9458. DOI: 10.1021/jacs.5b05558.

[442] H. G. Zhang, J. T. Sun, T. Low, L. Z. Zhang, Y. Pan, Q. Liu, J. H. Mao, H. T. Zhou, H. M. Guo, S. X. Du, F. Guinea, and H.-J. Gao. "Assembly of Iron Phthalocyanine and Pentacene Molecules on a Graphene Monolayer Grown on Ru(0001)". In: *Physical Review B* 84.24 (2011). DOI: 10.1103/PhysRevB.84.245436.

[443] Murray Campbell, A.Joseph Hoane, and Feng-hsiung Hsu. "Deep Blue". In: *Artificial Intelligence* 134.1-2 (2002), pp. 57–83. ISSN: 00043702. DOI: 10.1016/S0004-3702(01)00129-1.

[444] Avron Barr and Edward Feigenbaum. *The Handbook of Artificial Intelligence*. 2014. ISBN: 9781483214375.

[445] David Silver, Aja Huang, Chris J. Maddison, Arthur Guez, Laurent Sifre, George van den Driessche, Julian Schrittwieser, Ioannis Antonoglou, Veda Panneershelvam, Marc Lanctot, Sander Dieleman, Dominik Grewe, John Nham, Nal Kalchbrenner, Ilya Sutskever, Timothy Lillicrap, Madeleine Leach, Koray Kavukcuoglu, Thore Graepel, and Demis Hassabis. "Mastering the Game of Go with Deep Neural Networks and Tree Search". In: *Nature* 529.7587 (2016), pp. 484–489. DOI: 10.1038/nature16961.

[446] Jean-François Bonnefon, Azim Shariff, and Iyad Rahwan. "The Social Dilemma of Autonomous Vehicles". In: *Science* 352.6293 (2016), pp. 1573–1576. DOI: 10.1126/science.aaf2654.

[447] Sandhya Samarasinghe. *Neural Networks for Applied Sciences and Engineering: From Fundamentals to Complex Pattern Recognition*. Boca Raton, FL: Auerbach Publications, 2007. ISBN: 9781420013061.

[448] Martin T. Hagan, Howard B. Demuth, Mark Hudson Beale, and Orlando de Jesús. *Neural Network Design*. 2nd ed. [S. l.: s. n.], 2016. ISBN: 0971732116.

[449] Chi-hau Chen, ed. *Handbook of Pattern Recognition and Computer Vision*. 5th edition. New Jersey et al.: World Scientific, 2016. ISBN: 978-9814656528.

[450] Joyce Liu. "In Your Face: China's all-seeing state". In: *BBC* 2017 (10.12.2017). URL: http://www.bbc.com/news/av/world-asia-china-42248056/in-your-face-china-s-all-seeing-state.

[451] Yilun Wang Michal Kosinski. "Deep Neural Networks are More Accurate than Humans at Detecting Sexual Orientation from Facial Images." In: *Journal of Personality and Social Psychology* ().

[452] Scott T. Brady, George J. Siegel, R. Wayne Albers, and D. L. Price. *Basic Neurochemistry: Principles of Molecular, Cellular, and Medical Neurobiology*. Eighth edition. Waltham, Massachusets and Oxford: Academic Press / Elsevier, 2012. ISBN: 9780080959016.

[453] Rainer Waser and Masakazu Aono. "Nanoionics-Based Resistive Switching Memories". In: *Nature Materials* 6.11 (2007), pp. 833–840. DOI: 10.1038/nmat2023.

[454] Yingpu Bi and Gongxuan Lu. "Morphology-Controlled Preparation of Silver Nanocrystals and Their Application in Catalysis". In: *Chemistry Letters* 37.5 (2008), pp. 514–515. ISSN: 0366-7022. DOI: 10.1246/cl.2008.514.

[455] Y. Sun and Y. Xia. "Large-Scale Synthesis of Uniform Silver Nanowires Through a Soft, Self-Seeding, Polyol Process". In: *Advanced Materials* 14.11 (2002), p. 833. DOI: 10.1002/1521-4095(20020605)14:11{\textless}833::AID-ADMA833{\textgreater}3.0.CO;2-K.

[456] Benjamin Wiley, Yugang Sun, Brian Mayers, and Younan Xia. "Shape-Controlled Synthesis of Metal Nanostructures: The Case of Silver". In: *Chemistry (Weinheim an der Bergstrasse, Germany)* 11.2 (2005), pp. 454–463. DOI: 10.1002/chem.200400927.

[457] Jie-Jun Zhu, Cai-Xia Kan, Jian-Guo Wan, Min Han, and Guang-Hou Wang. "High-Yield Synthesis of Uniform Ag Nanowires with High Aspect Ratios by Introducing the Long-Chain PVP in an Improved Polyol Process". In: *Journal of Nanomaterials* 2011.2-3 (2011), pp. 1–7. DOI: 10.1155/2011/982547.

[458] K. Terabe, T. Hasegawa, T. Nakayama, and M. Aono. "Quantized Conductance Atomic Switch". In: *Nature* 433.7021 (2005), pp. 47–50. DOI: 10.1038/nature03190.

[459] Xin Guo, Christina Schindler, Stephan Menzel, and Rainer Waser. "Understanding The Switching-Off Mechanism in Ag+ Migration Based Resistively Switching Model Systems". In: *Applied Physics Letters* 91.13 (2007), p. 133513. DOI: 10.1063/1.2793686.

[460] Tsuyoshi Hasegawa, Takeo Ohno, Kazuya Terabe, Tohru Tsuruoka, Tomonobu Nakayama, James K. Gimzewski, and Masakazu Aono. "Learning abilities achieved by a single solid-state atomic switch". In: *Advanced materials (Deerfield Beach, Fla.)* 22.16 (2010), pp. 1831–1834. DOI: 10.1002/adma.200903680.

[461] Audrius V. Avizienis, Henry O. Sillin, Cristina Martin-Olmos, Hsien Hang Shieh, Masakazu Aono, Adam Z. Stieg, and James K. Gimzewski. "Neuromorphic Atomic Switch Networks". In: *PloS one* 7.8 (2012), e42772. DOI: 10.1371/journal.pone.0042772.

[462] Tomonobu Nakayama, Osamu Kubo, Yoshitaka Shingaya, Seiji Higuchi, Tsuyoshi Hasegawa, Chun-Sheng Jiang, Taichi Okuda, Yuji Kuwahara, Kazuhiro Takami, and Masakazu Aono. "Development and Application of Multiple-Probe Scanning Probe Microscopes". In: *Advanced materials (Deerfield Beach, Fla.)* 24.13 (2012), pp. 1675–1692. DOI: 10.1002/adma.201200257.

[463] Tomonobu Nakayama, Yoshitaka Shingaya, and Masakazu Aono. "Multiple-Probe Scanning Probe Microscopes for Nanoarchitectonic Materials Science". In: *Japanese Journal of Applied Physics* 55.11 (2016), 1102A7. DOI: 10.7567/JJAP.55.1102A7.

[464] Seiji Higuchi, Hiromi Kuramochi, Osamu Kubo, Shintaro Masuda, Yoshitaka Shingaya, Masakazu Aono, and Tomonobu Nakayama. "Angled Long Tip to Tuning Fork Probes for Atomic Force Microscopy in Various Environments". In: *The Review of scientific instruments* 82.4 (2011), p. 043701. ISSN: 1089-7623. DOI: 10.1063/1.3569765.

[465] Rintaro Higuchi, Yoshitaka Shingaya, and Tomonobu Nakayama. "Resistance of Single Polyaniline Fibers and their Junctions Measured by Double-Probe Atomic Force Microscopy". In: *Japanese Journal of Applied Physics* 55.8S1 (2016), 08NB09. DOI: 10.7567/JJAP.55.08NB09.

[466] Ruisong Ma, Qing Huan, Liangmei Wu, Jiahao Yan, Wei Guo, Yu-Yang Zhang, Shuai Wang, Lihong Bao, Yunqi Liu, Shixuan Du, Sokrates T. Pantelides, and Hong-Jun Gao. "Direct Four-Probe Measurement of Grain-Boundary Resistivity and Mobility in Millimeter-Sized Graphene". In: *Nano letters* 17.9 (2017), pp. 5291–5296. DOI: 10.1021/acs.nanolett.7b01624.

[467] Marek Kolmer, Piotr Olszowski, Rafal Zuzak, Szymon Godlewski, Christian Joachim, and Marek Szymonski. "Two-Probe STM Experiments at the Atomic Level". In: *Journal of physics. Condensed matter : an Institute of Physics journal* 29.44 (2017), p. 444004. DOI: 10.1088/1361-648X/aa8a05.

[468] Eleanor C. Demis, Renato Aguilera, Kelsey Scharnhorst, Masakazu Aono, Adam Z. Stieg, and James K. Gimzewski. "Nanoarchitectonic Atomic Switch Networks for Unconventional Computing". In: *Japanese Journal of Applied Physics* 55.11 (2016), 1102B2. DOI: 10.7567/JJAP.55.1102B2.

[469] Gabriel Vasilescu. *Electronic Noise and Interfering Signals: Principles and Applications*. Signals and communication technology. Berlin: Springer-Verlag, 2005. ISBN: 3540265104.

[470] H. Nyquist. "Thermal Agitation of Electric Charge in Conductors". In: *Physical Review* 32.1 (1928), pp. 110–113. DOI: 10.1103/PhysRev.32.110.

[471] J. B. Johnson. "Thermal Agitation of Electricity in Conductors". In: *Physical Review* 32.1 (1928), pp. 97–109. DOI: 10.1103/PhysRev.32.97.

[472] W. Schottky. "Über spontane Stromschwankungen in verschiedenen Elektrizitätsleitern". In: *Annalen der Physik* 362.23 (1918), pp. 541–567. DOI: 10.1002/andp.19183622304.

[473] Ya.M. Blanter and M. Büttiker. "Shot Noise in Mesoscopic Conductors". In: *Physics Reports* 336.1-2 (2000), pp. 1–166. DOI: 10.1016/S0370-1573(99)00123-4.

[474] Seiji Higuchi, Osamu Kubo, Hiromi Kuramochi, Masakazu Aono, and Tomonobu Nakayama. "A Quadruple-Scanning-Probe Force Microscope for Electrical Property Measurements of Microscopic Materials". In: *Nanotechnology* 22.28 (2011), p. 285205. ISSN: 0957-4484. DOI: 10.1088/0957-4484/22/28/285205.

Acknowledgment

In the end, I would like to thank everybody who contributed to this work and supported me during this time.

First of all, I want to thank Willi Auwärter for supervising my thesis and giving me the opportunity to join his group. Thanks to Alex Riss, for the work together in the lab and the support with the data evaluation and interpretation. I thank Johannes Barth, that I could work on his equipment and Knud Seufert for his help to keep the experimental set up running.

A special thanks goes to the lunch group, Martin Uphoff, Andreas Walz, Felix Bischoff, Tobias Paintner, Tobias Kaposi, Domenik Zimmermann, Sabine Synkule, Mathias Pörtner, Eduardo Rascon, Karolina Stoiber, Peter Feulner, Aleksandr Baklanov, Maryam Ebrahimi, Reza Kakavandi, and Alex Riss, which created some culinary highlights and saved me from the mensa „food“.

I'm thankful for the support and expertise of Karl Eberle, Reinhold Schneider, Max Glanz, Peter Feulner and Hartmut Schlichting. Furthermore, I thank Viktoria Blaschek for the excellent help with all the organizational tasks.

I thank Franz Giessibl and his group for the experienced help with the AFM setup.

I thank Tomonobu Nakayama for hosting me in his group and giving me insights to the research ambitions within the MANA network. I thank Rintaro Higuchi, Yoshitaka Shingaya, Thien Ngo, and Hatori Kayoko for their welcoming and help, in a way that I had a great time in Japan.

Finally, I thank my family, which supported me during my studies and my PhD and of course my girlfriend Mannnu.